FEMTOSECOND NONLINEARITIES IN InGaAsP DIODE LASERS

by

Katherine Lavin Hall

B.A., Wellesley College
(1984)

S.M., Massachusetts Institute of Technology
(1990)

Submitted to the
Department of Electrical Engineering and Computer Science
in partial fulfillment of the
requirements for the degree of

Doctor of Philosophy

at the

Massachusetts Institute of Technology

May 1993

Signature of Author _____
Department of Electrical Engineering and Computer Science
May 13, 1993

Certified by _____
Erich P. Ippen
Thesis Advisor

Accepted by _____
Campbell Searle
Chairman, Department Committee on Graduate Students

FEMTOSECOND NONLINEARITIES IN InGaAsP DIODE LASERS

by

Katherine Lavin Hall

Submitted to the
Department of Electrical Engineering and Computer Science
on May 13, 1993 in partial fulfillment of the requirements
for the degree of Doctor of Philosophy.

Abstract

Semiconductor optical amplifiers are receiving increasing attention for possible applications to broadband optical communication and switching systems. In this thesis we report the results of an extensive experimental study of the ultrafast gain and refractive index nonlinearities in 1.5 μm InGaAsP laser diode amplifiers. The temporal resolution afforded by the femtosecond optical pulses used in these experiments allows us to study carrier interactions with other carriers as well as carrier interactions with the lattice.

The 100-200 fs optical pulses used in the pump-probe experiments are generated by an Additive Pulse Modelocked color center laser. The measured group velocity dispersion in the diodes ranged from -0.6 to -0.95 μm^{-1}. Differences in the group velocity for TE- and TM-polarized pulses suggested that cross-polarized pump-probe pulses walk off from each other in the diode. This walk-off can diminish the time resolution of some experiments. A novel heterodyne pump-probe technique was developed to distinguish collinear, copolarized, pump and probe pulses that were nominally at the same wavelength. Comparing cross-polarized and copolarized pump-probe results yielded new information about the physical mechanisms responsible for nonlinear gain in the diodes. We observed a gain compression across the entire bandwidth of the diode, associated with carrier heating. The hot carrier distribution cooled back to the lattice temperature with a 0.6 to 1.0 ps time constant, depending on the device structure. In addition, we observed a 0.1 to 0.25 ps delay in onset of carrier heating. Large gain compression due to two photon absorption was also observed. A small portion of the nonlinear gain is attributed to spectral hole burning. Pulsewidth-dependent output saturation energies were explained by a rate equation model that included the effect of carrier heating. Measurements of pump-induced probe phase changes revealed index nonlinearities due to delayed carrier heating and an instantaneous electronic, or virtual process.

Thesis Advisor: Erich P. Ippen
Title: Elihu Thomson Professor of Electrical Engineering

To my boys, Dave and Tommy.

And to Marsh. We still miss you every day.

Acknowledgements

First and foremost I thank Professor Erich Ippen for his unwavering support. For almost six years, he has been my guardian and my guide, advising me as much about life as about science. He is the greatest teacher I have ever known. He has given me freedom and encouragement to grow as a scientist and as a person. He has never steered me wrong.

Thank you, Professor Haus. I will miss our early morning conversations. They gave me an even bigger jolt than that first cup of coffee, and as anyone who's ever tasted the group coffee knows... Thanks are also due to Professor Jim Fujimoto, for his interest and help over the years. I appreciate the time Professor Fonstad spent as a thesis reader and as a member of my oral committee.

I am grateful to Donna Gale, Cindy Kopf and Mary Aldridge for doing all the work that keeps our group together and running smoothly.

As for the optics group, there are many people whose names I would like to tarnish by acknowledging them here. Mike LaGasse was cynical, but often correct. I'm not sure I'd be here today had it not been for those closed-door conversations about how blind everyone else can be. Mary Phillips has been a true friend from the start. Besides that, she has taught me a thing or two about power supplies. I enjoyed spending time with Stuey Brorson despite his constant predictions of GEC. Thanks are also due to Janice Huxley, Morris Kesler and Bob Schoenlein for showing me the ropes. Jannik Mark and I spent many long hours in the lab together and he remains a good friend. It was a privilege to work with Yinchieh Lai, whose contributions to the diode saturation experiments were invaluable.

Charlie Hultgren and I have spent way too much time together. From him I learned that problem sets can be done in one night, that the most important equations rhyme, and that there is little that distinguishes madmen from geniuses. From me he should learn to spend more than $5 on a haircut. Gadi Lenz has been my partner in crime for the past three years and he has taught me that all problems can be solved numerically with 1 line of code, and that a $5 haircut is better than nothing. Keren Bergman has been a caring and a loyal friend. Her unique view of the world is matched only by her inability to articulate that view. The P.C. will be safe in her hands. To the other students and visiting scientists who have helped me and have become my friends, Kazunori Naganuma, Jerome Paye, Antonio Mecozzi, Franz Kartner, Jerry Chen, Steve Cheng, Jay Damask,

Ali Darwish, Chris (Curtis) Doerr, Dave Dougherty, Siegfried Fleischer, Farzana Khatri, John Moores, Lynn Nelson, Malini Ramaswamy, Chi-Kuang Sun, Kohichi Tamura and Nick Ulman, thank you. It has been an education and a pleasure to work with all of you.

I will always owe a debt of gratitude to my friends at Bell Labs. Bob Jopson has inspired me more than he will ever know or may want to admit. Tingyi Li has provided much appreciated avuncular encouragement and advice. Ted Darcie made sure I was never lonely. We solved all sorts of problems over peanuts and beer. I am lucky to count Pat and Carla Iannone, Greg and Judy Raybon, and Matt and Andrea Whalen as close friends. Besides great technical advice, I am thankful to Uzi Koren, Gadi Eisenstein and Jay Wiesenfeld for providing the devices studied in this thesis.

To my sisters from Wellesley College and beyond, you have been my touchstones. I hold Liz Marshall personally responsible for diverting me from politics to science. Thank you for years of honesty, friendship and support. Professor Leslie Kolodziejski has been a late and great addition to my list of favorite women. Nothing is drab when Leslie is around.

I am grateful for the support of a Joint Services Electronics Program (JSEP) Fellowship.

I can honestly say that none of what is described in this thesis would have been possible or worthwhile had it not been for my family. My mother is the kindest, most courageous person I know. Whatever I may achieve is owed to her. My brothers and sisters are my best friends. Thank you Michael and Lisa, Peggy and Todd, Patrick and Laura, Jennifer, and Danny. I can't think of the Harrisons as in-laws, they're much too nice for that. Thank you Jean, Virg and Jim, Kate and Martha, for making me part of the family. I thank my grandparents, Peg and Jim McLaughlin, their love has always been unconditional. They have taught me that there is nothing in this world more important than family.

Dave's father, Marsh, was like a father to me. He will always be with us.

Dave, you are my foundation. Everything I have is yours. I can't begin to thank you for all the patience, support, encouragement and love that has brought us here. I can't wait for the day people say, "I went to grad school with his wife".

Finally, I am thankful for my son, Thomas Mulcahy Harrison (Tommy). He has brought us nothing but joy since the day he was born.

Contents

List of Figures

List of Tables

Chapter 1

Introduction

Semiconductor optical amplifiers are of interest for possible applications to broadband optical communication and switching systems. Of particular interest are InGaAsP devices that can be tailored to the communication bands of 1.3 and 1.5 μm [1] [2]. While much is known about their linear and small signal characteristics, the physical mechanisms responsible for their nonlinear and dynamical properties are still debated. The nonlinear properties of these active semiconductor waveguides are of interest for several reasons. They influence the modulation response and mode stability of diode lasers [3], they limit speed and produce cross talk between multiplexed signals in optical amplifiers [4] [5] [6] [7], and they may be useful for the design of nonlinear optical waveguide modulators and switches [8] [9] [10]. Dynamic changes in carrier population, limited in speed by the carrier lifetime, are responsible for many of the observed effects. However, experiments on GaAs devices have shown that nonequilibrium changes in the carrier energy distribution are also important [11] [12].

In this thesis, we report the results of an extensive experimental study of the ultrafast gain and refractive index nonlinearities in InGaAsP diode lasers and amplifiers operating in the 1.5 μm region of the spectrum. Time domain studies are performed using the 100-200 fs pulses generated by an Additive Pulse Mode-locked laser. First, standard pump-probe [13] and pulse echo [14] techniques are used to characterize the gain nonlinearities and group velocity dispersion in these long wavelength lasers. Second, the pulsewidth-dependent saturation behavior is investigated. Third, a novel heterodyne pump-probe technique is demonstrated

that yields new information regarding the physical mechanisms responsible for nonlinear gain and index. Finally, the work is summarized and conclusions are presented.

The thesis is organized in the following manner. Chapter 2 contains a summary of the semiconductor physics necessary to understand the nonlinearities we measure. The density of states and the Fermi function are discussed. Linear gain and loss coefficients are shown to depend on carrier density and carrier temperature. A rate equation model is used to describe carrier and photon density changes. Physical mechanisms responsible for nonlinear gain and their time domain signatures are discussed. The linear and nonlinear refractive index, related to the gain by a Kramers-Kronig (KK) transformation, are described. Finally, the laser structures studied in this work, bulk V-groove, multiple quantum well (MQW), and strained-layer (SL) MQW, are described.

Chapter 3 contains a description of the Additive Pulse Modelocked (APM) color center laser used as the source for the experiments. This laser produces 100-200 fs pulses, tunable around 1.5 μm, at a repetition rate of 100 MHz. The optical pulses are between 1.1 and 1.3 times transform-limited, assuming a $\text{sech}^2(t)$ pulseshape. Average powers for the APM color center laser are typically $\sim$ 100 mW.

Chapter 4 contains a study of the effects of group velocity dispersion (GVD) on short pulse propagation in these diodes. Group velocity dispersion is measured via a pulse echo technique. TE- and TM-polarized results are presented for active and passive, bulk and MQW waveguides. Values of $-\lambda\frac{d^2n_{eff}}{d\lambda^2}$ from -0.60 to -0.95 μm^{-1} are measured. Critical pulsewidths less than 100 fs are calculated for diodes less than 1 mm long.

Chapter 5 contains a review of the pump-probe technique and of the first measurements of gain nonlinearities in bulk and MQW diode laser amplifiers at 1.5 μm. These results show gain nonlinearities due to carrier heating, two photon absorption (TPA) and an ultrafast effect. The physical mechanism responsible for the ultrafast effect will be determined in Chapter 7. A pump-probe technique where nonlinearities are measured as changes in the diode junction voltage is demonstrated. The results of these pump-probe experiments confirm the importance of carrier heating and TPA to the nonlinear gain.

Chapter 6 describes the short pulse saturation behavior of bulk and MQW

diodes biased in the gain regimes. The measured output saturation energies are pulsewidth dependent. This behavior is modeled by including the effects of carrier heating in the rate equations as described in Chapter 2. Using this model, the predicted differences in the output saturation energies for 150 fs and 15 ps pulses agree very well with the measured differences.

Chapter 7 discusses a novel heterodyne pump-probe technique in which the pump and probe pulses have parallel polarizations and are nominally at the same wavelength but are still distinguishable. This technique can improve the time resolution of some experiments by circumventing the group velocity walk-off associated with orthogonally polarized pump and probe pulses (determined in Chapter 4), and it allows the study of anisotropy in the waveguide nonlinearity. Comparing copolarized and cross-polarized pump-probe transmission results in SLMQW diodes indentifies a delay in the onset of carrier heating. Also, a small nonlinear component is revealed whose amplitude flips sign at the transparency point. This component is attributed to spectral hole burning. The heterodyne technique is extended to measure index nonlinearities in the diodes. These measurements show refractive index nonlinearities due to carrier heating and an instantaneous electronic, or virtual process.

Chapter 8 contains a review of the experimental results described in the thesis. The applicability of these active waveguides to all-optical switching are discussed. Other reported measurements of gain and index nonlinearities in InGaAsP diode lasers are reviewed and future experiments are proposed. Finally, conclusions are presented.

Chapter 2

Semiconductor Lasers

2.1 Introduction

Semiconductor diode lasers are compact and efficient sources of coherent optical radiation. First demonstrated in 1962 [15] [16] [17] [18], they have many practical applications in the marketplace. Perhaps their most common application is in compact disc players. Cheap and reliable semiconductor lasers with rather modest performance characteristics can also be found in laser printers and the ever popular laser pointers. However, the lasers we are interested in studying are high-performance long wavelength lasers to be used in high-speed optical communication and computing systems. These long-wavelength InGaAsP lasers, operating in the 1.3 μm-1.5 μm region of the spectrum, are attractive because those wavelengths correspond to the low loss and low dispersion regimes in optical fibers.

A simplified picture of a semiconductor laser is shown in Figure 2.1. The diode consists of a semiconductor waveguide sandwiched in the middle of a p-n junction. Waveguiding is achieved by placing a high refractive index core or active region material between two lower refractive index cladding materials. This design is fortuitous in that the low index cladding layers that give the waveguiding also create a potential well for the active region and help confine the carriers injected by forward biasing the p-n junction. As we shall see later in this chapter, carriers injected into the diode active region pump the material and can provide

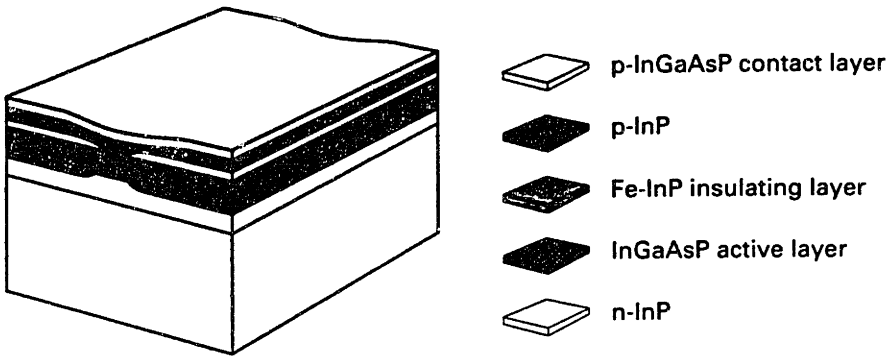

Figure 2.1: Schematic of a semiconductor laser chip. (from Reference [19])

gain. The mirrors for the laser cavity are formed by cleaving the semiconductor material perpendicular to the waveguide. The refractive index difference between the semiconductor material, n_0=3.4, and the surrounding air, creates the mirrors. When these cleaved facets are anti-reflection coated, the device is referred to as an optical amplifier. The main differences between the laser and the amplifier are the elimination of longitudinal standing wave effects and the unclamped carrier densities in the amplifier.

In this chapter, we will discuss the operation of semiconductor diode lasers. We will derive the density of states for 3-dimensional and 2-dimensional systems and discuss the carrier distributions which are governed by Fermi-Dirac statistics. Using the density of states and the Fermi-Dirac functions, we will calculate the linear gain and loss in these diodes. We will model the gain, and its effect on laser performance phenomenologically using a set of rate equations. We will discuss the effects of nonlinear gain on the high-speed modulation response of these diodes. The refractive index, related to the gain by a Kramers-Kronig transformation, will also be described. With an understanding of the physical mechanisms that are responsible for linear gain and index, we will go on to discuss the origins of nonlinearities in the gain and index. Finally, the last section of this thesis will be

devoted to laser design and performance. The three types of diode lasers studied in this thesis, bulk V-groove, multiple quantum well (MQW), and strained-layer (SL) MQW, will be described and the advantages of the different structures will be discussed.

2.2 Gain

The simplest description of gain in semiconductor lasers is that of a two-level energy system with an energy gap, $E_{gap} = \hbar\omega$ [1] [20]. In this oversimplified picture, the transition probabilities are governed only by the relative carrier densities in the two states. For instance, if the density of carriers in the lower energy state is higher than the density of carriers in the upper state, the probability that a photon of energy E_{gap} will cause a transition from the lower to the upper state is greater than the probability that it will cause a transition from the upper to the lower state. Stated another way, stimulated absorption is more probable than stimulated emission. The intensity of the photon field decreases while passing through the medium because on average, photons are being absorbed. If the upper state carrier density is greater than the lower state carrier density, stimulated emission is more probable than stimulated absorption and the optical intensity increases while traveling through the medium. Increasing the optical intensity corresponds to gain. In semiconductor materials, there are bands of energy levels, rather than the simplified two levels we have considered here. Therefore, to understand gain in these semiconductor diodes, we must understand how the carriers, electrons and holes, are distributed in this band of energy levels.

The 3-dimensional electron density, defined as the number of electrons allowed in a given region of k-space is given by [21]

$$n = \frac{k^3}{3\pi^2}. \tag{2.1}$$

To determine the density of electronic levels in the material $\rho(E)dE$, given by the number of energy levels in an energy range δE, we use the dispersion relation for the electrons to relate k to E and find

$$\rho(E) = dn/dE = \frac{1}{2\pi^2}\left(\frac{2m^*}{\hbar^2}\right)^{3/2} E^{1/2}. \tag{2.2}$$

This simple method for determining the density of energy levels in a semiconductor gives an accurate description of many important material characteristics. For instance, the density of states for electrons and holes in a 3-dimensional semiconductor can be determined by the method we have just described. We specify the dimensionality of the system because the calculated k-space volume was assumed to be a sphere. The density of states for the electrons is given by

$$\rho_c(E) = \frac{1}{2\pi^2}\left(\frac{2m_e^*}{\hbar^2}\right)^{3/2} (E - E_c)^{1/2}, \tag{2.3}$$

where E_c is the conduction band minimum and m_e^* is the effective mass of the electron. As we discussed previously, the gain in semiconductor materials is viewed in terms of two bands of energy levels rather than two single energy levels. (The effect of all other bands is neglected.) This density of states (levels) for electrons is equivalent to the band of upper states and is called the conduction band. The valence band, equivalent to the density of states for the holes, describes the band of lower states and is given by

$$\rho_v(E) = \frac{1}{2\pi^2}\left(\frac{2m_h^*}{\hbar^2}\right)^{3/2} (E_v - E)^{1/2}, \tag{2.4}$$

where E_v is the valence band maximum and m_h^* is the effective mass for the holes. In our calculations that utilize the 3-dimensional density states, we will always assume the bands are parabolic. This assumption breaks down for energies high above the conduction band minimum or below the valence band maximum, for highly doped materials, and for high carrier densities. The difference in the parabolicity of the conduction and valence bands is simply a function of the different electron and hole masses.

This parabolic density of states for the electrons and holes is the result of the dispersion relation and the 3-D counting of available k-states. In quantum well structures, where the electrons and holes are confined to planes of motion, we count the 2-D availability of k-states and find that

$$n = \frac{k^2}{2\pi} \tag{2.5}$$

so that

$$\rho_{2D}(E) = \frac{m}{\pi\hbar^2}. \tag{2.6}$$

Note that the 3-D density of states is parabolic in E but the 2-D density of states is constant is E. Here we have assumed that only one electron or hole level is contained in the quantum well. If more than one level is contained in the well, then the density of states consists of a series of steps spaced by l^2 where l is the integer that labels the level (l=1 for first electron level, l=2 for second electron level, and so on).

The density of states defines how many states exist at a given energy E. The probability that a given energy state is actually occupied is given by the Fermi function, $f(E)$. The Fermi function is simply a probability density function given by

$$f(E) = \frac{1}{[1 + e^{(E-E_F)/k_BT}]}, \tag{2.7}$$

where we adopt the convention that $\mu = E_F$ where μ is the chemical potential, E_F is the quasi-Fermi energy, k_B is Boltzmann's constant and T is the temperature. Note that $f(E_F)$=1/2. The density of carriers in the bands is given by

$$N = \int_{-\infty}^{\infty} f_c(E)\rho_c(E)dE \tag{2.8}$$

for electrons in the conduction band, and

$$P = \int_{-\infty}^{\infty} f_v(E)\rho_v(E)dE \tag{2.9}$$

for holes in the valence band. The Fermi functions for the electrons and holes are

$$f_c(E_1) = \frac{1}{[1 + e^{(E_1-E_{Fc})/k_BT_e}]} \tag{2.10}$$

and

$$f_v(E_2) = \frac{1}{[1 + e^{(E_2 - E_{Fv})/k_B T_h}]}, \tag{2.11}$$

where E_1 is an energy level in the conduction band, E_2 is an energy level in the valence band, E_{Fc} and T_c are the quasi-Fermi energy and temperature for electrons and E_{Fv} and T_h are the quasi-Fermi energy and temperature for holes. In the steady state, T_e=T_h=T. These Fermi functions give the probability that a given state is occupied by an electron. The probability that the same state is unoccupied, or is occupied by a hole, is given by $(1 - f(E))$.

We return to our original description of gain in semiconductor diodes. There we stated that the transition probability was related to the carrier density. Gain was associated with a higher carrier density in the upper energy state than in the lower energy state. If we consider the transition between two energy levels, E_1 in the conduction band and E_2 in the valence band, the rate of stimulated absorption of a photon of energy $E_{12} = E_1 - E_2$ is given by

$$r_{21} = B f_v(E_2)(1 - f_c(E_1))P(E_{21}). \tag{2.12}$$

$P(E_{21})$ is the photon density and B is the transition probability given by

$$B = \frac{\pi q^2 \hbar}{m^{*2} \epsilon_0 n_g^2 E_{21}} |M|^2, \tag{2.13}$$

where $|M|$ is the momentum matrix element, ϵ_0 is the permittivity of free space, and n_g is the group index. Physically, absorption takes an electron from an occupied state in the valence band, $f_v(E_2)$, and excites it to an empty state in the conduction band,$(1 - f_c(E_1))$. The rate of stimulated emission is given by

$$r_{12} = B f_c(E_1)(1 - f_v(E_2))P(E_{21}). \tag{2.14}$$

Stimulated emission takes an electron from an occupied state in the conduction band, $f_c(E_1)$ and drives it to an empty state in the valence band, $(1 - f_v(E_2))$. Because B is the same in the equation for stimulated emission and stimulated

absorption, the stimulated transition direction is determined by the relative carrier concentrations in the two energy levels.

As we stated previously, the incident photon density, $P(E_{21})$ experiences gain when, the rate of stimulated emission exceeds the rate of stimulated absorption, $r_{12} - r_{21} > 0$. The gain can be related to the net stimulated emission rate by

$$g(E_{21}) = \frac{r_{12} - r_{21}}{P(E_{21})v_g} = \frac{B(f_c(E_1) - f_v(E_2))}{c/n_g}, \tag{2.15}$$

where $v_g = c/n_g$ is the group velocity. Again note that to experience gain, $f_c(E_1) > f_v(E_2)$. This condition for gain does not require that the concentration of electrons exceed the concentration of holes, only that the occupational probability of E_1 exceed the occupational probability of E_2. The total number of carriers in the conduction band and valence band are equal and the quasineutrality condition, $N = P$, is not violated.

Because there are many combinations of energy levels in the conduction and valence bands that satisfy the condition, $E = E_1 - E_2$, to find the total gain we must sum Eq. (2.15) over all levels separated by E. Then, the gain in the semiconductor material is given by

$$g(E) = \frac{\pi q^2 \hbar}{\epsilon_0 m^{*2} c n_g E} \int_{-\infty}^{\infty} |M|^2 \rho_v(E_2)\rho_c(E_2 + E)\left[f_c(E_2 + E) - f_v(E_2)\right] dE_2 \tag{2.16}$$

where E_2 is the energy state in the valence band and $E_1 = E_2 + E$ is the energy of the state in the conduction band. Figure 2.2 shows the gain curve calculated for a bulk, V-groove InGaAsP diode laser at a carrier density of $N = 1.8 \times 10^{18}$ cm^{-3}. Other parameters used to calculate the gain curve are given in Table 2.1. Single photons with energies less than the band gap or equal to the electron-hole quasi-Fermi energy separation, do not, on average, stimulate transitions. However, photons with energies less than the quasi-Fermi energy separation for electrons and holes (but greater than the the band-gap energy) on average stimulate emission and experience gain. Photons with energies larger than the quasi-Fermi energy separation stimulate absorption. For the gain curve shown in Figure 2.2, the gain regime extends from E_{gap} to $E_{gap} + 78$ meV. $E = E_{gap} + 78$ meV is defined at the transparency point. At this point, stimulated emission and stimulated absorption

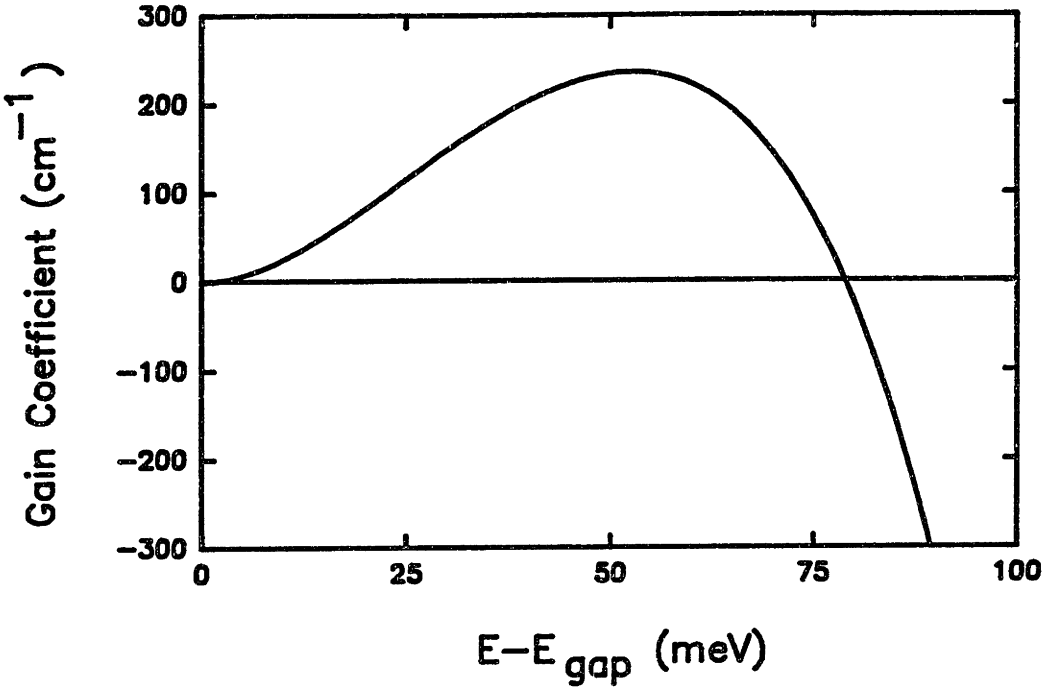

Figure 2.2: Typical gain curve for an InGaAsP bulk laser. The parameters used to calculate this curve are summarized in Table 2.1.

are equally probable and the gain coefficient is zero. This transparency energy is equal to the separation between quasi-Fermi energies for electrons and holes, $E_{trans} = E_{Fc} - E_{Fv}$. The absorption (or loss regime) includes all energies E greater than $E_{gap} + 78$ meV. In this regime the gain coefficient is negative.

Note that the gain curve we have shown in Figure 2.2 depends sensitively on many parameters. First, it depends on the assumed carrier density, N. The steady state injected carrier density is used to determine the quasi-Fermi energy for the carriers via Eq. (2.8). This quasi-Fermi energy, in the context of the Fermi function, $f(E)$, determines the occupational probability and is used to calculate the gain. The carrier density can be changed by current injection or by optical excitation. Figure 2.3 shows a series of gain curves calculated for different carrier densities ranging from 0.7×10^{18} cm^{-3} to 3.0×10^{18} cm^{-3}. In this case we have held the electron and hole temperatures fixed at room temperature, T=300 K. (Also, we have not included carrier density dependent band-gap renormalization in these calculations.) All the calculated gain curves in this chapter are for the bulk, V-groove lasers. In the pump-probe experiments that we will be describing in the later chapters of this thesis, we measure the optically-induced gain changes

as a function of bias current (carrier density) applied to the diode. In Figure 2.4 we show the gain coefficient at a given energy as a function of carrier density. Note that the gain coefficient changes rapidly in the absorption regime but levels off in the gain regime. This effective saturation of the gain coefficient will have important consequences in the data interpretation that follows.

Holding the carrier density fixed and changing the carrier temperature will also affect the calculated gain curves. This effect arises from the temperature dependence of the Fermi function. In Figure 2.5 (a) the carrier density is 1.8×10^{18} cm^{-3} (which gives a peak gain coefficient commonly quoted in the literature [1]) and the holes and electrons are at T=300 K (solid line). We can change the temperature of just one of the carrier distributions to see how it affects the gain. The dashed curves shows the calculated gain when the holes are heated to T_h= 320 K (T_e=300 K) and the dotted curve shows the gain when the electrons are heated to T_e=320 K (T_h=300 K). Note that even this small change in carrier temperature affects the gain significantly. Figure 2.5 (b) shows the difference between the room temperature gain and the hot electron (dotted line) and hot hole (dashed line) gain. Note that the hot carrier induced gain change is relatively small for energies just above the band-edge. Also note that the gain change due to heating the hole distribution is smaller than the gain change due to heating the electrons. This difference can be attributed to differences in mass. However, for energies near the band edge, the gain change due to the hot holes is the dominant effect.

Figure 2.6 shows the calculated gain coefficient as a function of excess photon energy when both the holes and electrons are heated. Heating the carriers compresses the gain and shifts the gain peak to longer wavelengths (lower energies). In the dashed curve, the electrons and holes have a temperature $T_e = T_h$=320 K. The peak gain coefficient has dropped from 240 cm^{-1} to 180 cm^{-1}. In the dotted curve, the carrier temperature has been increased to 340 K and the peak gain coefficient is 140 cm^{-1}. The gain coefficient at the peak wavelength for the room temperature gain curve is 120 cm^{-1}. Thus, heating the carrier distribution by 40 K, with respect to the lattice, decreases the diode gain by about a factor of 2.

There are a number of assumptions that have been made in the calculation described above. First, we have assumed that the k-selection rule is not obeyed. Near the band-edge, and for high carrier densities, this assumption is valid. Second, we have not considered the effect of the carrier-concentration-dependent energy band

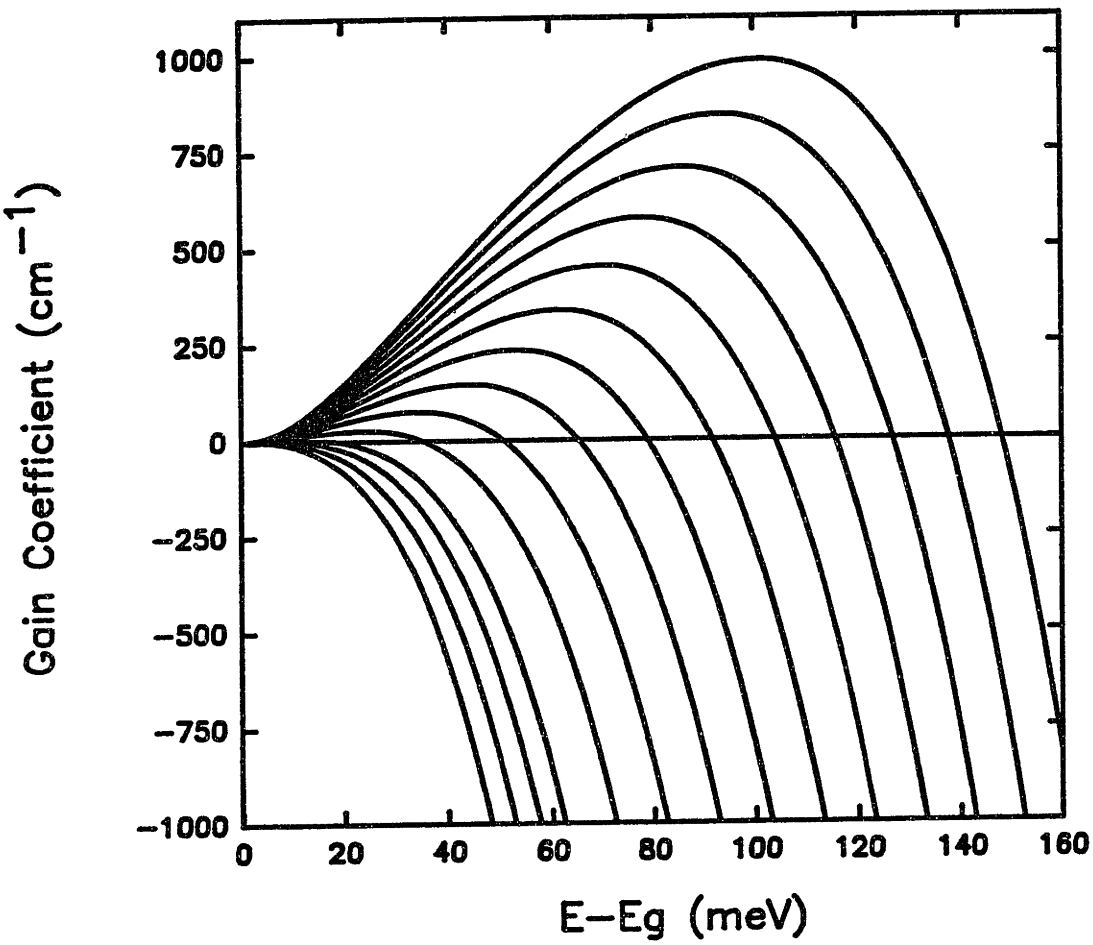

Figure 2.3: Calculated gain curves as a function of excess energy above the band gap. The carrier densities are $N \times 10^{18}$ cm^{-3} = 0.7, 0.8, 0.9, 1.0, 1.2, 1.4, 1.6, 1.8, 2.0, 2.2, 2.4, 2.6, 2.8 and 3.0. $T_e = T_h$=300 K.

NAME	SYMBOL	VALUE	UNITS
Planck's Constant	$\hbar$	6.6 E-13	meV-sec
Electronic Charge	q	1.6 E-19	coul
Free Space Permitivity	$\varepsilon 0$	8.8 E-17	coul/mV-cm
Boltzmann's Constant	k_B	0.08617	meV/K
Room Temperature	T	300	K
Index	n	3.6	
Band Gap Energy	E_g	750	meV
Split-off Band Energy	Δ	312	meV
Free Electron Mass	m0	5.7 E -13	$\frac{\text{meV-sec}^2}{\text{cm}^2}$
Conduction Band Mass	me	0.041 m0	$\frac{\text{meV-sec}^2}{\text{cm}^2}$
Heavy Hole Mass	mh	0.62 m0	$\frac{\text{meV-sec}^2}{\text{cm}^2}$
Light Hole Mass	ml	0.05 m0	$\frac{\text{meV-sec}^2}{\text{cm}^2}$
Valence Band Mass	mv	0.63 m0	$\frac{\text{meV-sec}^2}{\text{cm}^2}$

Table 2.1: Parameters used in the calculations in this chapter.

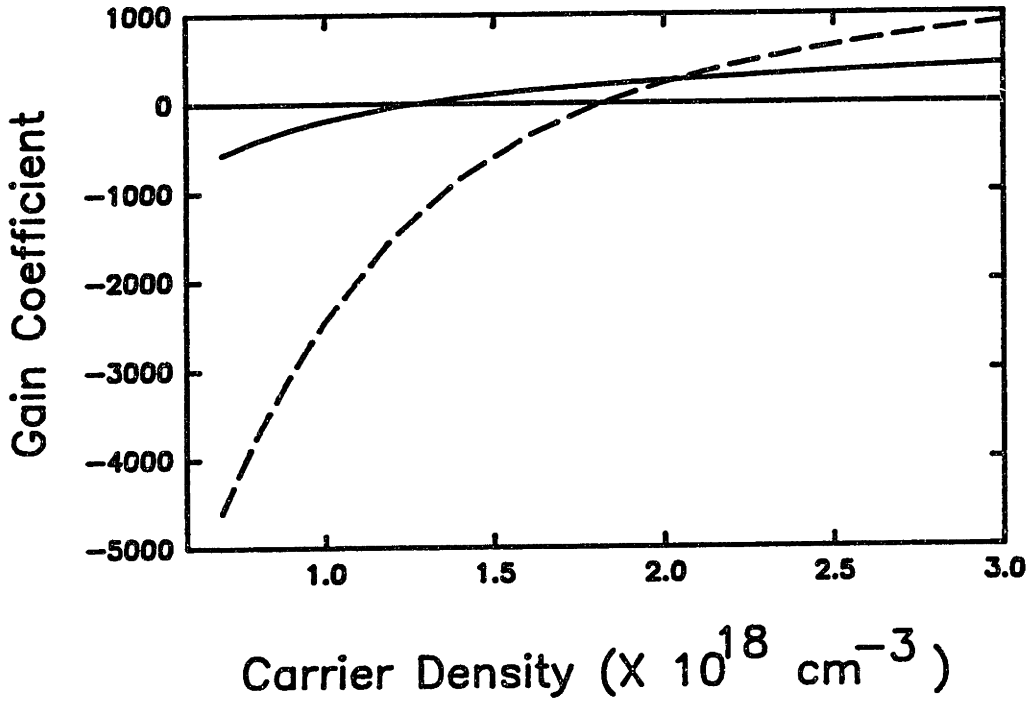

Figure 2.4: Gain coefficient at a given excess energy (30 meV-solid line, and 50 meV-dashed line) as a function of carrier density.

gap reduction. In these long wavelength lasers, the band gap renormalization is assumed to be the same as in GaAs [1], ΔE_{gap}(in eV)= (-1.6 $\times 10^{-8}$)($P^{1/3} + N^{1/3}$). Note that this renormalization does not affect the value of the peak gain but merely shifts the band edge and possibly the peak wavelength. Third, the active regions in our diodes are almost intrinsic and we have not considered the effects of band-tail states. Finally, we have assumed that the valence and conduction bands are purely parabolic. Note that for energies well above the band-edge, it is not valid to use the parabolic band approximation or to ignore the k-selection rules. Despite these many approximations, our calculations are in good agreement with previous calculations reported in the literature [22] [23] [24].

2.2.1 Carrier Dynamics

With an understanding of the physical mechanisms responsible for linear gain in these semiconductor diodes, we can consider the proposed sources for the nonlinear gain. Traditionally, we have discussed the carrier dynamics due to interband effects, intraband effects, and diffusion effects. In general, diffusion and nonradia-

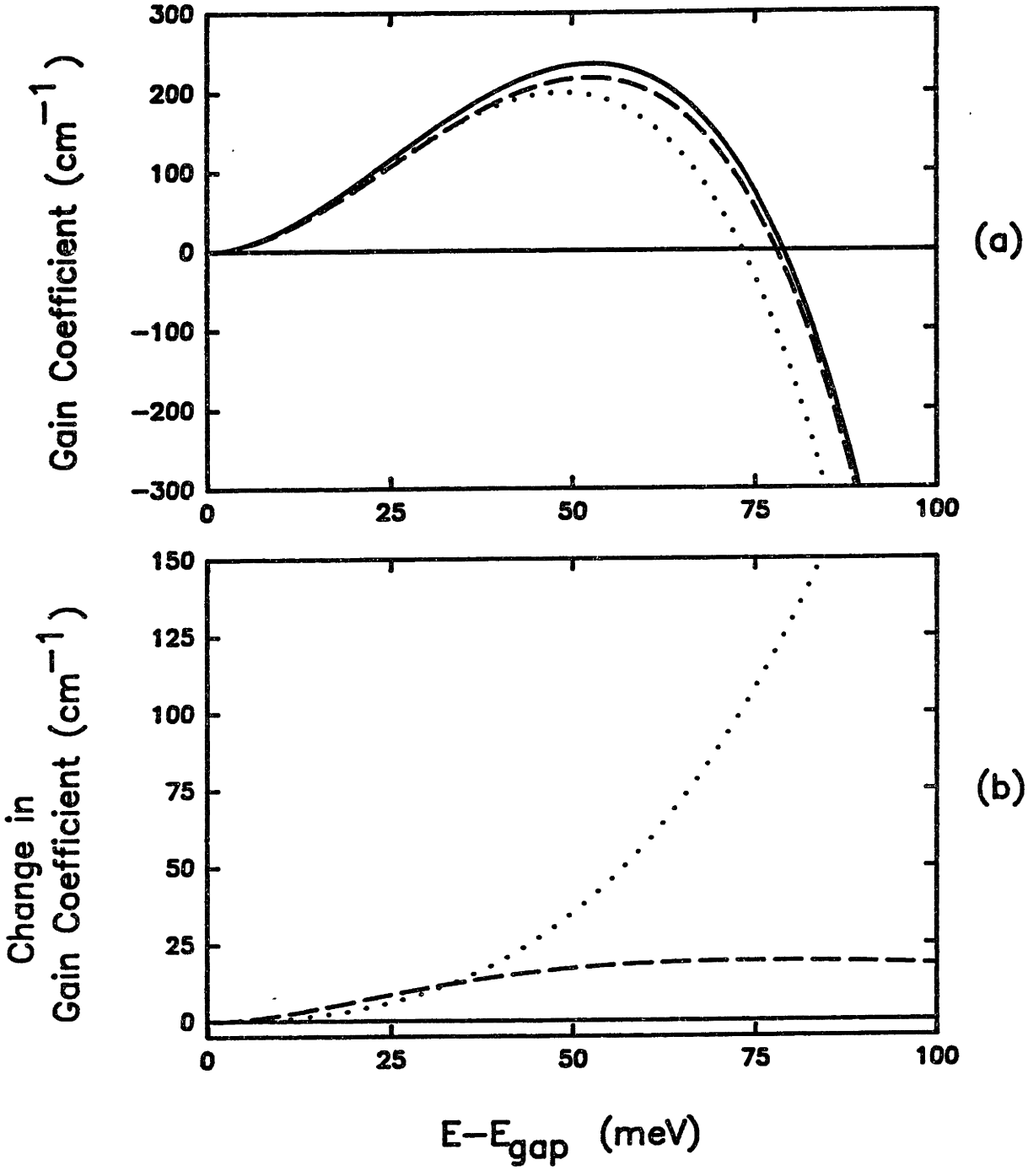

Figure 2.5: Calculated gain curves with N=1.8 × 10^{18} cm^{-3} and $T_e = T_h$=300 K (solid line), T_e=300 K and T_h=310 K (dashed line) and T_e=310 K and T_h=300 K (dotted line). In (b) the dashed line shows the difference between the room temperature gain curve and the hot hole gain curve. The dotted lines shows the difference between the room temperature gain curve and the hot electron gain curve.

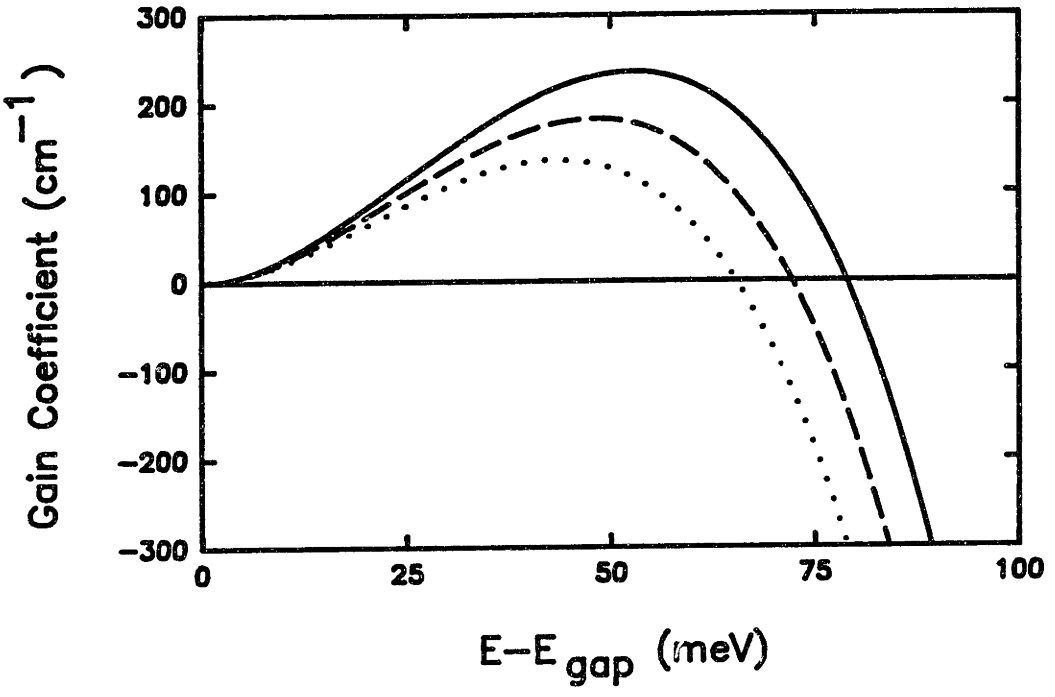

Figure 2.6: Calculated gain curves versus excess energy above the band-gap for a variety of carrier temperatures. The temperatures used are $T_e = T_h$=300 K (solid line), 320 K (dashed line) and 340 K (dotted line).

tive recombination are not considered to be important effects in the subpicosecond gain nonlinearities we investigate using pump-probe experiments. However, many recent experiments have suggested that these effects can be significant, at least on the time scale of a few picoseconds.

Stimulated absorption and emission induced by an optical pulse will instantaneously change the carrier population. In the case of stimulated absorption, the increased carrier density will relax back to its equilibrium concentration via spontaneous emission, on a nanosecond time scale [1]. In pump-probe experiments, which typically measure the 10 ps time interval around the pulse, this nanosecond recovery is not observed. Instead, the change in gain due to pump-induced carrier density changes appears as a step change in gain (see Figure 5.3). However, it has been suggested recently that nonradiative recombination and carrier diffusion may increase the carrier density relaxation rate [25] [26]. At high carrier densities, recombination in the diode active region can be dominated by Auger recombination. Auger recombination requires a number of simultaneous particle interactions and is therefore highly dependent on the carrier density, $R_a = CN^3$,

where R_a is the Auger recombination rate, N is the carrier density and C is the Auger coefficient. An example of an Auger process is energy released when an electron and hole recombine being transferred to another electron (or hole) which is excited to a high energy state in the band. This highly excited carrier will relax back to thermal equilibrium via phonon emission. For the InGaAsP material system, C is on the order of 5×10^{-29} cm^6/s [27] [28]. At high carrier densities, $N > 5 \times 10^{18}$ cm^{-3}, Auger recombination can reduce the upper state lifetime to a few hundred picoseconds [27]. This nonradiative recombination can become an important effect in optical amplifiers because the unclamped carrier densities can be as high as 5×10^{18} cm^{-3} [25]. However, a gain recovery time of 300-400 ps is still too slow to be observed in our pump-probe experiments.

Recently, measured lifetimes as short as 100 ps have been observed in traveling-wave semiconductor amplifiers. These lifetimes have been attributed to a combination of effects, Auger recombination and spatial hole burning [25] [26]. Spatial hole burning occurs because some portion of the injected bias current leaks around the active region and pumps the cladding layers of the diode. These cladding layers have a different band-gap than the active region and do not provide gain. However, carriers in this region can diffuse into the active region where the carrier density has been depleted by the optical field. A typical diffusion length depends on a number of parameters such as the active layer width, the cladding layer width and the mode confinement factor. However, the carrier density gradient is usually assumed to extend approximately 1 μm into the cladding regions. Even with these relatively small diffusion distances, measurements in a bulk V-groove amplifier at 1.3 μm have suggested that carriers diffusing from the cladding "storage regions" shortens the gain recovery time to 100 ps. Again, we are interested in studying the subpicosecond dynamics in these diodes. On a typical pump-probe delay scale of 10 ps, even a 100 ps recovery time will produce an insignificant signal. We will not consider the spatial hole burning effects due to longitudinal standing waves because by antireflection coating our diodes we have eliminated the standing wave effects.

Another diffusion effect that has recently been proposed as a cause of nonlinear gain in semiconductor quantum well diodes is the so-called "well-barrier hole burning" [29] [30] [31] [32] [33] [34] [35]. Quantum well active regions consist of a series of wells and barriers embedded in a carrier confinement layer. Carriers that

are removed from the bottom of the quantum well can be replenished by carriers diffusing across this confinement layer and dropping into the wells. The time constant associated with this effect is structure dependent. For typical confinement layer widths of 0.8 nm-3 nm, diffusion times of 2-10 ps have been measured [32] via a pump-probe technique. These carrier transit dynamics recovering with time constants on the order of a few picoseconds might be expected to contribute to the pump-probe signals we measure. However, we do not observe significant contributions from these diffusion effects. The most probable explanation for the difference between our results and those of Weiss et al. [32], is that our pump-probe pulses are shorter (150 fs vs. 400 fs) and therefore can preferentially excite the nonlinearities with the faster time constants. Also, our experiments are performed at lower injection currents (carrier densities), where the importance of Auger recombination and carrier gradient induced diffusion are reduced.

Presumably, the nonlinearities associated with carrier transit and capture times can be minimized by careful design of the diode's active region. However, there are nonlinearities that are more fundamental in that they are associated with the semiconductor material, not the diode structure. One such nonlinearity is spectral hole burning. In an inhomogeneously broadened gain medium, the stimulated transitions are wavelength dependent so that only resonant or near-resonant transitions are allowed. In a semiconductor laser, this implies that only electrons and holes in a certain energy range are available for gain or absorption. In the gain regime, an optical beam will stimulate emission, but the electrons and holes will be removed from a limited energy range, creating a "hole" in the carrier distribution. In the absorption regime, carriers will be generated within a limited range, bleaching a "hole" in the absorption. These holes are created by stimulated transitions so that at the transparency point, where stimulated emission and stimulated absorption are equally probable, there is no spectral hole burning. At high carrier densities, such as are present in a semiconductor diode laser, the holes in the carrier distribution persist until carrier-carrier scattering redistributes the total density of carriers into a Fermi distribution. In semiconductor materials at high carrier densities, the carrier-carrier scattering time is thought to be less than 100 femtoseconds [36] [37] [38].

In the time domain, gain and absorption nonlinearities due to spectral hole burning have a well-defined signature. The transient change in gain due to spectral

hole burning should have the same sign as the step change in gain due to stimulated transitions because the hole is burned by stimulated transitions. However, the hole will disappear quickly as the carriers reach an intermediate thermalized distribution via carrier-carrier scattering. As the hole fills in and the carriers reach this intermediate thermalized distribution, the gain or absorption exhibits a partial recovery. Total recovery will not be achieved until carriers removed (or added) by the stimulated transitions have been replenished by the injection current (or depleted by spontaneous emission). This recovery time is the upper state lifetime for the material ($\sim$ 1 ns, at our carrier densities).

Nonequilibrium carrier heating is another nonlinearity that is fundamental to the semiconductor gain medium. As we have seen in the previous section, heating the carrier distribution decreases the gain in the diode. The carrier distribution can be heated by a number of mechanisms. Free carrier absorption (FCA) and two-photon absorption (TPA) can create highly energetic carriers in both the conduction and valence bands. Through carrier-carrier scattering, these "hot" carriers can give up their excess energy to the distribution. As a result, the distribution heats up. The distribution will cool back to the lattice temperature via phonon emission. Figure 2.6 shows the calculated gain curves for three different carrier temperatures. Note that heating the carrier distribution reduces the gain across the entire gain bandwidth. Therefore, the time domain signature for carrier heating is different than for spectral hole burning. Regardless of whether the diode is biased in the gain, transparency or absorption regimes, carrier heating causes a transient decrease in gain that recovers on a time scale that is consistent with carrier-phonon scattering times ($\sim$ 200 fs [39]).

Besides FCA and TPA, the carrier distribution can be heated via stimulated transitions. Consider the gain curve shown in Figure 2.7(a) ($N = 1.8 \times 10^{18}$ cm^{-3}). The dashed line shows the average energy of the carrier distribution and the dotted line shows the electron-hole quasi-Fermi energy difference (E_{trans}). Carriers occupying energy levels below the average energy are said to be cold, while those occupying levels above the average energy are said to be hot. Photons with excess energies between 0 and E_{trans} will stimulate emission, removing cold electrons and holes from the distributions. Removing cold carriers effectively heats the distribution. Photons with energies between E_{trans} and $< E >$ will stimulate absorption, creating cold carriers. Photons with energies greater than $< E >$ will

stimulate absorption and create hot carriers. This process heats the distributions. Note that the relative position of the average energy $< E >$, calculated according to

$$< E >= \frac{\int_{-\infty}^{\infty} f(E)\rho(E)EdE}{N}, \tag{2.17}$$

and the electron-hole quasi-Fermi energy separation, E_{trans}, depends on the carrier density. However, even when the average energy is greater than the transparency energy, there is a set of photon energies for which stimulated transitions will cool the distributions. In Figure 2.7(b) ($N = 4.0 \times 10^{18}$ cm^{-3}) we show a distribution where $< E >$ is less than E_{trans}. In this case, photon energies between 0 and $< E >$ stimulate emission and heat the distributions. Excess photon energies between $< E >$ and E_{trans}, stimulated emission and remove hot carriers. In this case, stimulated emission effectively cools the distributions. Again, in the highly absorbing regime, (excess photon energies greater than E_{trans}), stimulated absorption creates hot carriers and heats the distributions.

Of FCA, TPA and stimulated transitions, it is not clear a priori which mechanism for heating the carriers is dominant. Typically the stimulated transition probability is orders of magnitude larger than the FCA probability. However, each FCA event changes the total energy of the distribution by almost 1 eV, the single photon energy. Each stimulated transition will change the total energy by only a few meV. To investigate the relative importance of these two effects, we would like to find a way to turn one of the effects off. As we have discussed previously, there are no net stimulated transitions induced by photons with excess energies equal to the transparency energy. Therefore, we can perform experiments at the transparency point to investigate the relative importance of these two effects. Also, we can perform experiments at photon energies below the band-gap. Below-band photons can cause FCA but can not stimulate transitions. Note that FCA can only heat the distribution. Stimulated transitions, however, can heat or cool the distribution. Therefore, we might want to investigate the possibility of carrier cooling and an associated transient increase in gain in these diodes. Figure 2.8 shows the average energy and the quasi-Fermi energy for the (a) electrons and (b) holes, as a function of carrier density. Figure 2.9 shows the difference between the electron and hole quasi-Fermi energies and the average energies. Note that for

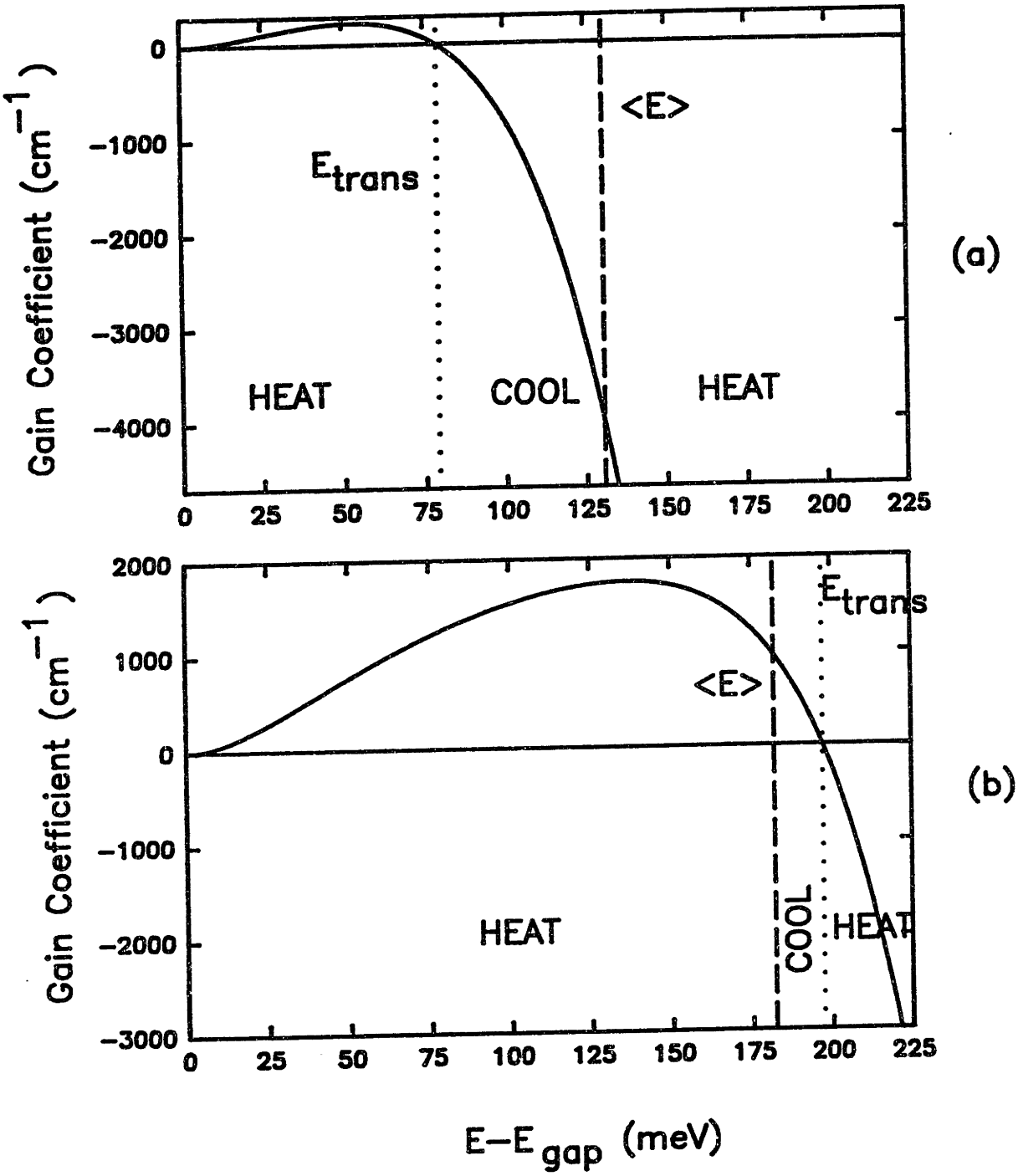

Figure 2.7: Calculated gain curve versus excess photon energy along with the position of the average energy (dashed line) of the distributions, $< E >$, for (a) $N = 1.8 \times 10^{18}$ cm^{-3} and (b) $N = 4 \times 10^{18}$ cm^{-3}. The dotted line shows the position of E_{trans}.

carrier densities less than $\sim 3 \times 10^{18}$ cm^{-3}, the average energy is larger than the quasi-Fermi energy separation. Then, stimulated absorption may be expected to cool the carrier distribution. However, as we shall see in Chapters 5 and 7, carrier cooling has not been observed in these InGaAsP diodes.

Two photon absorption (TPA) is not really a gain nonlinearity because it is relatively insensitive to the carrier density and the optical wavelength. However, it is a significant portion of the total nonlinear response of the InGaAsP diodes. It is common to consider the effects of TPA when the energy separation between two levels or two bands is greater than the single photon energy. In this case, the single photon energy is below-band and can not stimulate transitions. A second order process in which two photons combine, with energy $E = 2E_{photon}$, may now be able to stimulate a real transition between the two levels. The TPA coefficient is much smaller than the stimulated transition coefficient and the TPA probability is intensity dependent. A simplified propagation equation for the optical intensity is given by

$$\frac{dI}{dz} = -\alpha I - \beta I^2 \tag{2.18}$$

where I is the intensity, α is the stimulated loss (gain) coefficient, β is the TPA coefficient and z is the direction of propagation. In the low intensity limit or for $\beta << \alpha/I$, the linear loss dominates and TPA is usually ignored. However, it is important to realize that TPA occurs even when the photon energy is above band. In fact, as we tune from below- to above- band, the linear absorption coefficient will change dramatically, but the TPA coefficient will be relatively unaffected [40]. The TPA coefficient in our waveguides has been measured to be ~ 20 GW/cm^2 [41] [42]. In a pump-probe experiment where the pump powers are low enough that higher order processes can be ignored, the TPA signal will scale linearly with pump power, as will the other nonlinearities we have discussed in this chapter. Therefore, attenuating the signal to reduce the TPA signal will reduce the signal due to the other nonlinearities as well.

As we shall see in Chapters 5 and 7, in our experiments we observe gain nonlinearities due to carrier heating, spectral hole burning and TPA. The time domain signatures of these three effects are quite different. TPA always removes photons from the optical field and shows up as an instantaneous gain compression

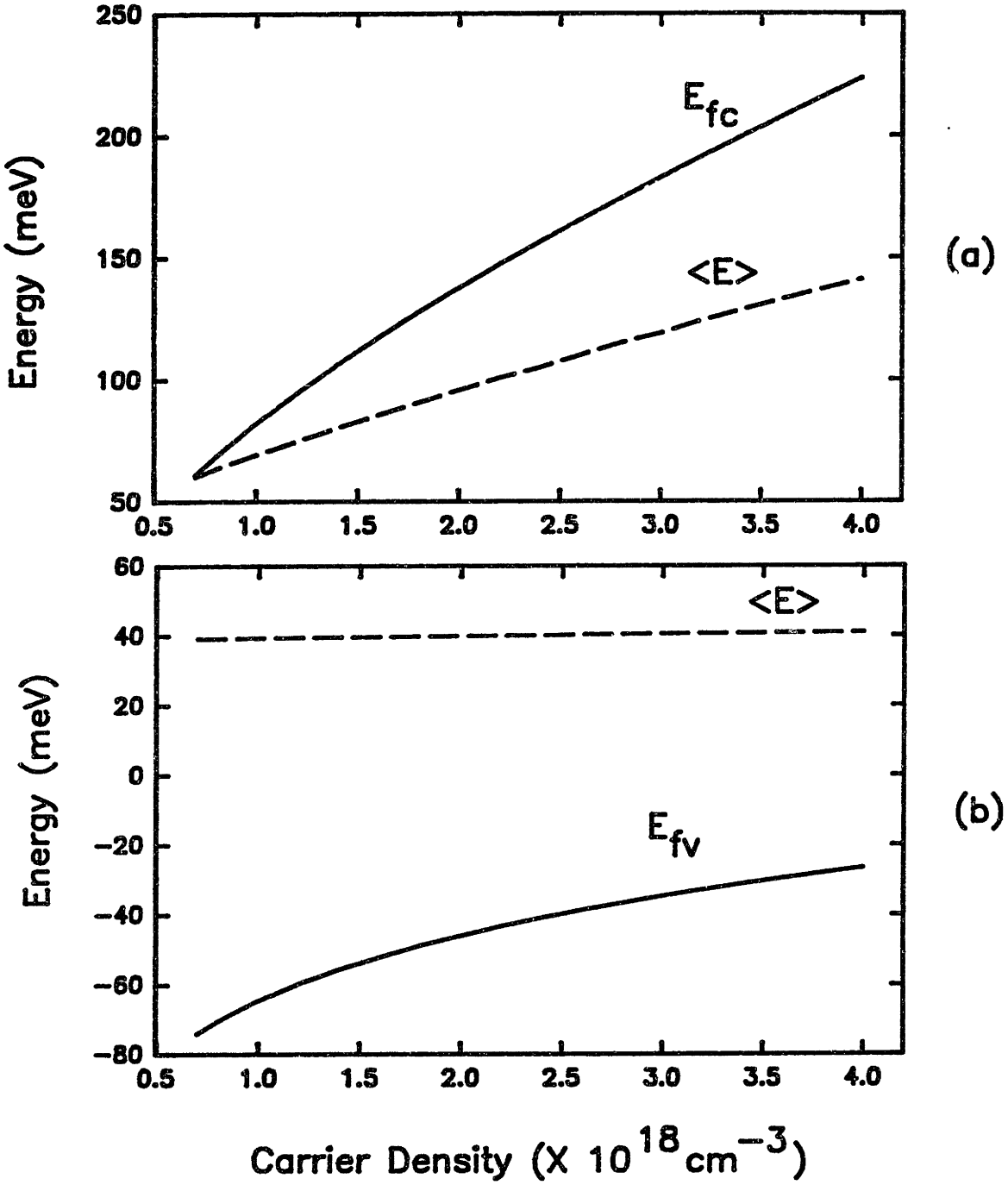

Figure 2.8: Values of the average energy (dashed lines), $< E >$, and the quasi-Fermi energy (solid lines) for (a) electrons and (b) holes as a function of carrier density.

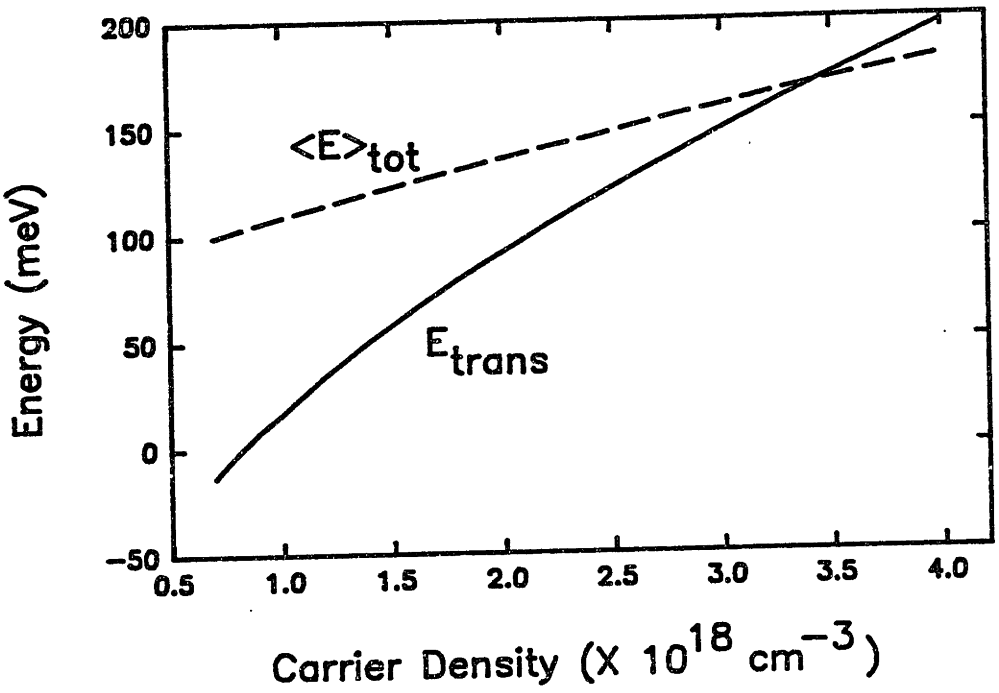

Figure 2.9: Values of the differences in average energies (dashed line) and quasi-Fermi energies (solid line), E_{trans}, for electrons and holes.

at zero time delay. Spectral hole burning should have a fast recovery time and its amplitude will change sign at the transparency point. The sign change should mimic that of the step change in gain due to stimulated carrier population changes. Carrier heating can cause transient increases or decreases in gain, depending on the relative heating efficiency of FCA and stimulated transitions, and depending on the value of the average energy of the distribution compared to the difference in the electron and hole quasi-Fermi energies. In our diodes only carrier heating has been observed. In the next section, we will discuss the rate equation model for carriers and photons in the semiconductor diode active region. We will show that the gain nonlinearities may be incorporated into these equations in a variety of ways.

2.3 Rate Equations

The carrier density, N, and the photon density, S, in the diode active region can be modeled by the rate equations

$$\frac{dN}{dt} = \frac{I}{qV} - \frac{N}{\tau_s} - g(N - N_t)S \tag{2.19}$$

and

$$\frac{dS}{dt} = \frac{-S}{\tau_p} + g\Gamma(N - N_t)S + \frac{\beta_s N}{\tau_s} \tag{2.20}$$

where I is the injection current, V is the volume of the active region, q is the electronic charge, N_t is the carrier density at transparency, g is the differential gain (dg_0/dN), Γ is the mode confinement factor, β_s is the spontaneous emission factor, τ_p is the photon lifetime in the cavity, and τ_s is the upper state lifetime. The small signal gain coefficient, g_0, plotted in Figures 2.2, 2.3, etc., is equivalent to $g(N - N_t)$ in Eq. (2.19). Note that when $N > N_t$, the gain is positive and when $N < N_t$, the gain is negative (absorption). These rate equations, or some variation thereof, can be used to describe many of the performance characteristics of semiconductor diode lasers. For instance, below threshold the photon density is approximately zero and the steady state ($\frac{d}{dt} = 0$) carrier density for a given bias current can be found via

$$N = \frac{I\tau_s}{qV}. \tag{2.21}$$

Also, we can determine the threshold current for the diode,

$$I_{th} = \left[\frac{qV}{\tau_s}\right](N_{ss} - (g\Gamma\tau_p)^{-1}) \tag{2.22}$$

where N_{ss} is the steady-state carrier density, and losses due to finite mirror reflectivity, FCA, and scattering are included in τ_p.

The rate equations we have described above are accurate in the small signal regime. However, in the regime where gain nonlinearities become important, these equations are no longer adequate. Traditionally, these equations have been modified to include the effects of nonlinear gain compression by multiplying the differential gain coefficient by a term $(1-\epsilon_{nl}S)$, where ϵ_{nl} is related to the nonlinear gain compression [3]. This term was introduced to explain the damping of the relaxation oscillation resonance in the high-speed response of typical diode lasers.

This rate equation model for the high-speed modulation response of diode lasers led to the introduction of a "universal relationship between resonant frequency and damping rate" [43], or the "K-factor", as a measure of gain nonlinearities in semiconductor diodes. The K-factor is given by,

$$K = \frac{\gamma}{f_0^2} \tag{2.23}$$

where γ is the damping rate and f_0 is the relaxation oscillation (or resonant) frequency. The K-factor can be related to the nonlinear gain coefficient, ϵ_{nl} via

$$K = 4\pi^2 \left(\tau_p + \frac{\epsilon_{nl}}{g} \right) = \frac{2\sqrt{2}\pi}{f_{max}^{3dB}} \tag{2.24}$$

where f_{max}^{3dB} is the maximum frequency at which the measured response has been reduced by a factor of 2 [44]. Recent experiments have shown that the K-factor is neither universal [45] [46] [47] [48] [49], nor constant [35] [50]. While the K-factor may be a convenient number to use to characterize the modulation response at low powers, it can not be used to predict or determine the magnitude or the origin of the gain nonlinearities.

In our work, we have taken a slightly different approach. Based on experimental results that show that the dominant gain nonlinearity in these diodes is due to carrier heating, and on the calculated results which show that heating the carrier distribution effectively reduces the carrier density at a given photon energy, we model the gain nonlinearity as a third energy level. This level is "pumped" by FCA and the carrier lifetime for this level is the measured carrier cooling time, ~ 1 ps. Using this model, the rate equations become

$$\frac{dN}{dt} = \frac{I}{qV} - \frac{N}{\tau_s} - g(N - N_t - \Delta N_h)S \tag{2.25}$$

and

$$\frac{d(\Delta N_h)}{dt} = \gamma_h \alpha_{fc} N - \frac{\Delta N_h}{\tau_h}, \tag{2.26}$$

where α_{fc} is the FCA coefficient, ΔN_h is the effective carrier density change due to carrier heating, τ_h is the carrier cooling time constant and γ_h is the efficiency factor that relates the number of FCA events to the actual gain reduction due to heating. Comparing this formalism to the traditional modeling of nonlinear gain we find

$$\Delta N_h = \epsilon S(N - N_t). \tag{2.27}$$

Note that for modest injected carrier densities, where the average energy is much greater than the quasi-Fermi energy separation, E_{trans}, Eq. (2.27) gives a good description of the effect of carrier heating due to stimulated transitions. That is, in the gain regime, where $N > N_t$, cold carriers are removed by stimulated emission which effectively heats the distribution and increases ΔN_h. However, in the absorption regime where $N < N_t$, cold carriers are created, which effectively cools the distribution and reduces ΔN_h. The analogy breaks down when we consider the FCA induced heating. As we mentioned before, FCA always heats the distribution and reduces the gain. In Chapter 6, we extend this rate equation model to include the effects of FCA in heating the distribution. Also, we model the so-called "ultrafast" nonlinearity that opposes the effect of carrier heating as a fourth level, with a 100-250 fs lifetime. As we shall see in Chapter 6, this rate equation model is an accurate predictor of the saturation behavior in these diodes.

2.4 Index

The gain (g_0) and index (n) in the semiconductor materials are related to the imaginary and real parts of the susceptibility tensor

$$\chi(\omega) = \chi'(\omega) - j\chi''(\omega) \tag{2.28}$$

where

$$\sqrt{1+\chi} = \sqrt{\frac{\epsilon}{\epsilon_0}} = n - j\left(\frac{\lambda g_0}{4\pi}\right) \tag{2.29}$$

and where $\chi(\omega)$ is related to the polarization, $\mathcal{P}$, via

$$\mathcal{P} = \epsilon_0 \chi \mathcal{E} \tag{2.30}$$

where ϵ_0 is the permittivity of free space and $\mathcal{E}$ is the electric field. These real and imaginary parts of the susceptibility tensor are related by a Kramers-Kronig (KK) transformation. If we call g_0 the linear gain coefficient and n the refractive index, then the KK transformation tells us that [51]

$$\mathrm{n}(\omega) = 1 + \left[\frac{c}{\pi}\right] \int_0^\infty \frac{g_0(\omega')}{\omega'^2 - \omega^2} d\omega'. \tag{2.31}$$

A perturbational change in gain (or absorption), Δg_0, will have an associated change in index given by

$$\Delta\mathrm{n}(\omega) = \left[\frac{c}{\pi}\right] \int_0^\infty \frac{\Delta g_0(\omega')}{\omega'^2 - \omega^2} d\omega'. \tag{2.32}$$

Note that if an induced gain change is symmetric around some center wavelength, ω_0, the corresponding change in index at ω_0 is zero ($\Delta\mathrm{n}(\omega_0)$=0).

Referring back to the nonlinear gain changes discussed in Section 2.2, we can predict the associated nonlinear changes in refractive index given by the KK transform. For instance, the change in gain due to changes in the carrier population can be calculated via

$$\Delta g_0 = g_0(E, N_1) - g_0(E, N_2) \tag{2.33}$$

where $g_0(E, N_i)$ is the gain curve derived for a carrier density of N_i. This change in gain can be substituted into Eq. (2.32) to determine the change in refractive index due to carrier population changes. Figure 2.10 shows the computed change in refractive index (a) for a given change in gain (b). The gain changes are calculated for carrier density changes of $\Delta N = +0.02 \times 10^{18}$ cm^{-3} (solid line), -0.02×10^{18} cm^{-3} (dashed line), -0.05×10^{18} cm^{-3} (dotted line), and -0.07×10^{18} cm^{-3} (dashed-dotted line) around N=1.8 $\times 10^{18}$ cm^{-3} [52] [53]. Note that for excess photon energies near the band-gap, increasing the carrier density decreases the refractive index and vice versa. Also note that the index changes extend below

the band-edge. These results are in agreement with previously published results for GaAs diodes [52] [54] [55] [56].

We can also calculate the Δg_0's due to carrier heating. Figure 2.11 shows the computed change in (a) refractive index and (b) gain for carrier temperature changes (electrons and holes) of +10 K (solid line), +20 K (dashed line), +30 K (dotted line) and +40 K (dashed-dotted line). From these calculations of gain and index changes for carrier density and carrier temperature changes, we can calculate the linewidth enhancement factors. For carrier density changes, the linewidth enhancement factor or α is defined as [57]

$$\alpha = -\frac{\delta\chi_r/\delta N}{\delta\chi_i/\delta N} \tag{2.34}$$

where χ is the complex susceptibility and N is the carrier density. As we mentioned before, the real and imaginary parts of the complex susceptibility are related to the refractive index and the gain. As a result, α is commonly written as

$$\alpha = -\frac{4\pi}{\lambda}\frac{\delta n/\delta N}{\delta g/\delta N}. \tag{2.35}$$

Figure 2.12 (a) shows the calculated values of α as a function of excess photon energy above the band gap. Very near the band-edge, $\delta g/\delta N$ is small and the magnitude of α diverges. This behavior has been observed previously [58] [59]. Changes in gain and index also accompany changes in the carrier temperature. Therefore, an α parameter that quantifies the relative gain and index changes induced by a carrier temperature change, α_T, is given by [60] [61]

$$\alpha_T = -\frac{\delta\chi_r/\delta T}{\delta\chi_i/\delta T} = -\frac{4\pi}{\lambda}\frac{\delta n/\delta T}{\delta g/\delta T}. \tag{2.36}$$

Figure 2.12 (b) shows the calculated α_T for the carrier temperature induced gain and index changes shown in Figure 2.11. This calculation agrees qualitatively with the values of α_T predicted previously [62]. It is difficult to use the measured values of Δg and Δn to compute the different α parameters and then compare them to the theoretical predictions because we can not accurately determine our

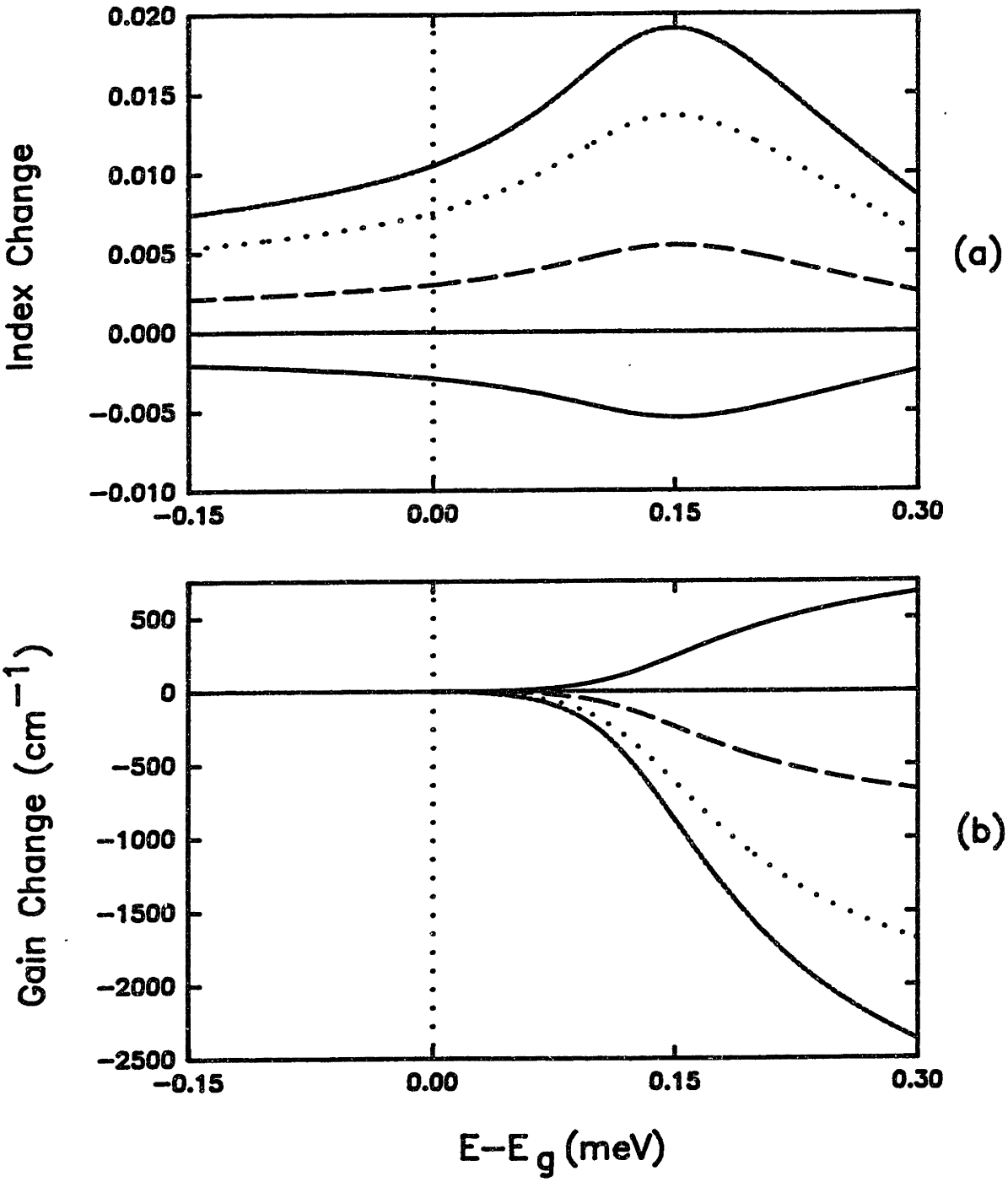

Figure 2.10: Computed change in (a) index and (b) gain for carrier density changes $\Delta N = +0.02\times10^{18}$ cm^{-3} (solid line), -0.02×10^{18} cm^{-3} (dashed line), -0.05×10^{18} cm^{-3} (dotted line), and -0.07×10^{18} cm^{-3} (dashed-dotted line) around N=1.8 $\times10^{18}$ cm^{-3}. The electrons and holes are at room temperature in these calculations.

experimental excess photon energy. However, it is interesting to note that for a given excess photon energy, the calculated values of α_T are always smaller than α. This behavior is consistent with the results presented in Reference [52] . We point out that the α's calculated for the different carrier density and carrier temperature changes shown in Figures 2.10 and 2.11 are similar and can not be distinguished on the scale shown in Figure 2.12.

TPA and other instantaneous absorption effects such as the optical Stark effect are expected to contribute to the nonlinear refractive index, n_2. There have been some calculations performed using the KK transform to relate calculated nonlinear pump-probe spectra to this instantaneous nonlinear refractive index [51] [63]. However, experimental studies have yet to distinguish which instantaneous gain nonlinearities are contributing to the index nonlinearites. The below band measurements in AlGaAs devices suggest that TPA and the optical Stark effect are important [64] [65] [66]. These results agree qualitatively with the above-band measurements in AlGaAs diode lasers [67].

Few experimental and theoretical results exist that observe or predict the effects of spectral hole burning on the nonlinear refractive index. The reason is that the shape and the size of the spectral holes that may be burned are not well understood and therefore difficult to model. However, if the k-selection rules hold, and if the hole is symmetric around some center wavelength, ω_0, then the corresponding refractive index change at ω_0 will be zero. Illustrations of this basic property of the KK transform can be found in many texts [59] [68] [69].

2.5 InGaAsP Diodes

Semiconductor laser chips are waveguides with active cores. In the heterostructure lasers we will study, the active region is sandwiched between two higher-band gap, lattice-matched semiconductor materials. These higher band-gap cladding layers serve two purposes. First, they help confine injected carriers (electrons and holes) to the active layer. Electrons and holes recombine in the depletion region of the p-n junction to provide gain. Poor carrier confinement leads to higher threshold currents and heating of the laser chip. Second, the lower refractive index of these cladding layers creates the waveguide that confines the optical mode to the active layer. Without this waveguiding, the optical mode would radiate out into the

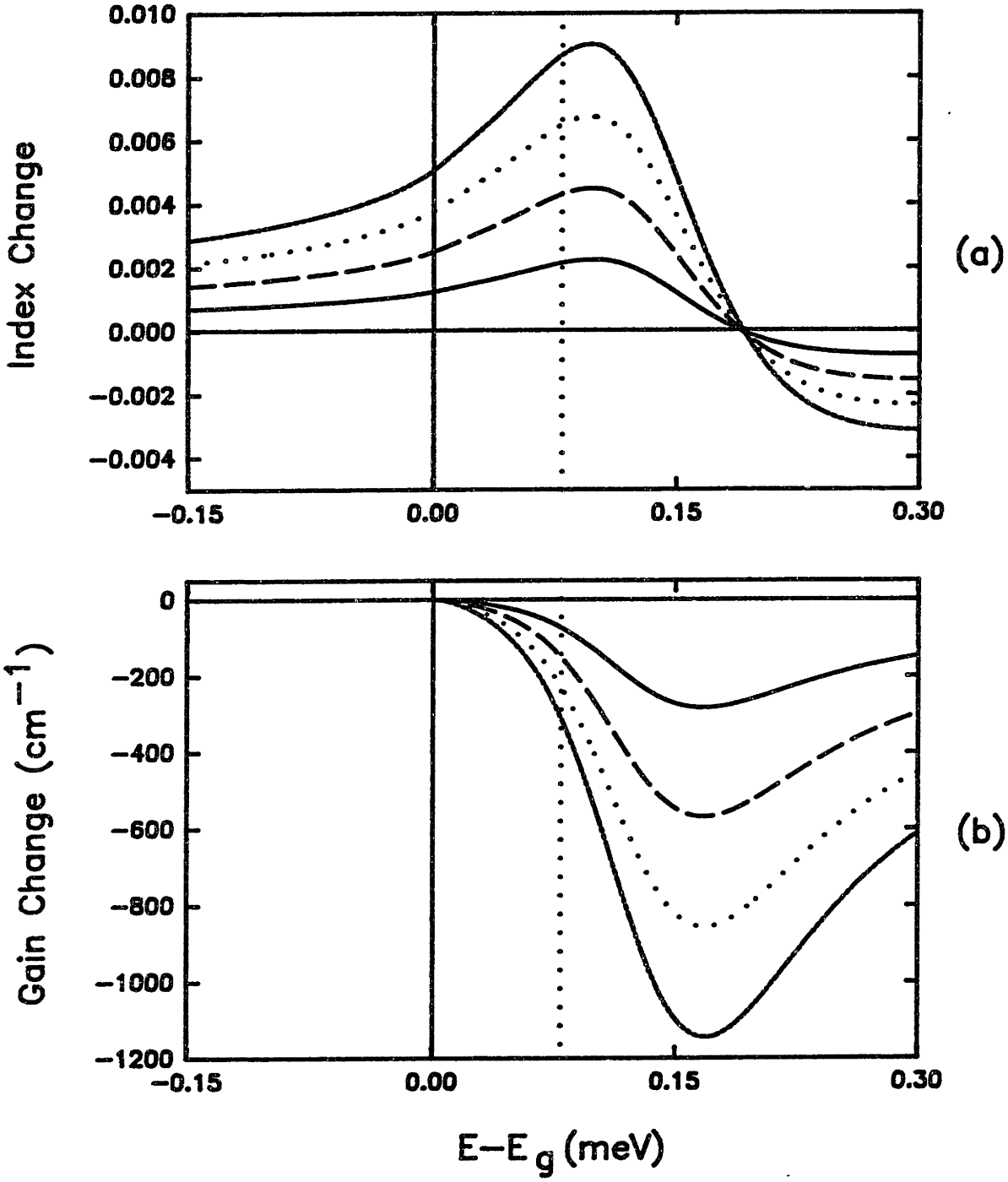

Figure 2.11: Computed change in (a) refractive index and (b) gain for carrier temperature changes (electrons and holes) of +10 K (solid line), +20 K (dashed line), +30 K (dotted line) and +40 K (dashed-dotted line). The carrier density in this calculation is $N = 1.8 \times 10^{18}$ cm^{-3}. The dotted vertical line shows the position of E_{trans} at room temperature.

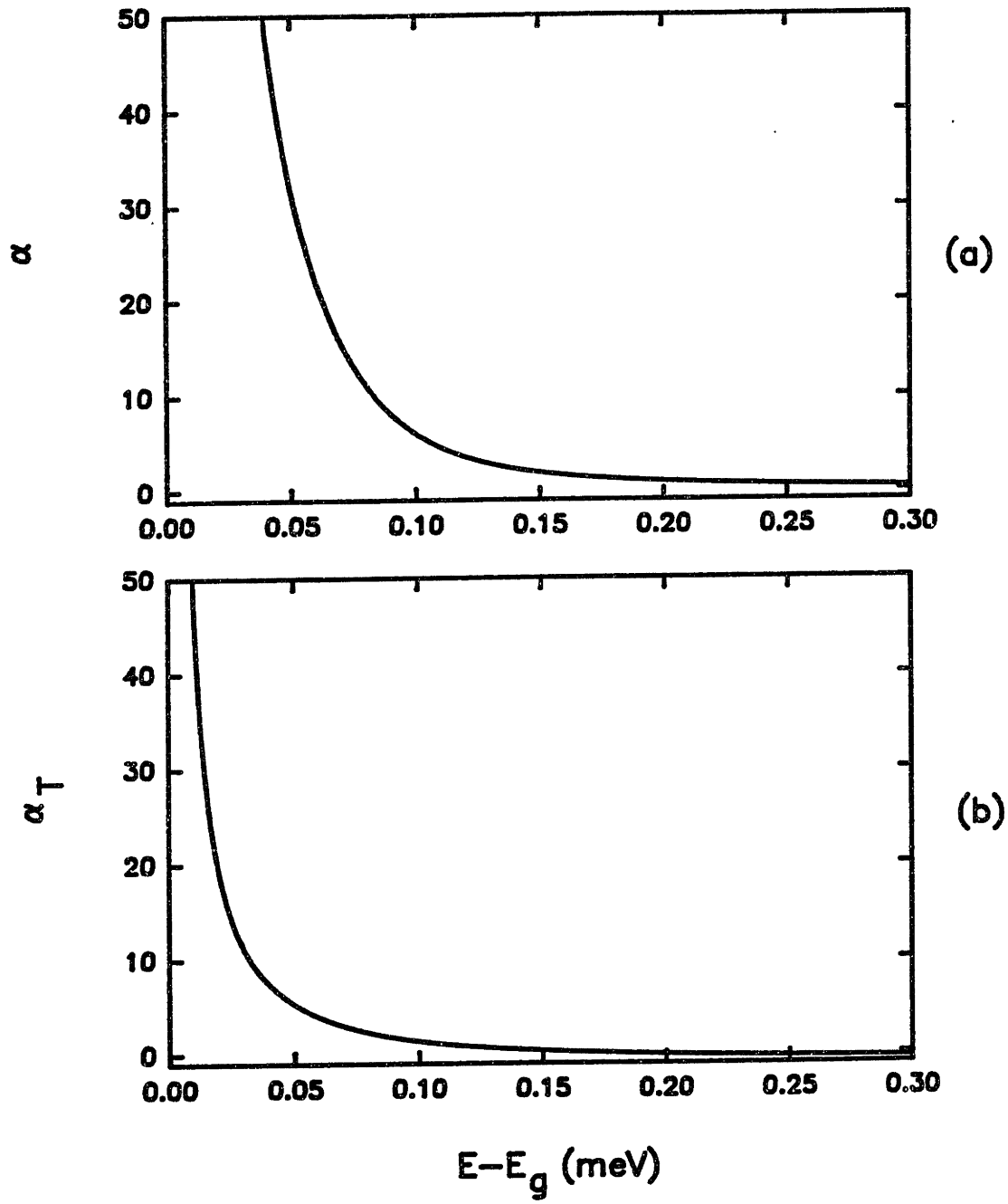

Figure 2.12: Calculated values of (a) α, the linewidth enhancement factor and (b) α_T as a function of excess photon energy. These values of α correspond to the gain and index changes shown in (a) Figure 2.10 and (b) Figure 2.11.

lossy, unpumped cladding regions of the semiconductor chip. Feedback is provided by cleaving facets perpendicular to the active waveguide. The semiconductor-air interface reflectivity is approximately 35%. This reflectivity can be altered by depositing coatings on the laser facets. In our work, anti-reflection coatings are deposited on at least one facet of the semiconductor diode [70].

The dimensions of the active region are chosen with many competing performance characteristics in mind. For instance, broad active cross-sections provide high gain but multi-transverse mode operation. We will study single transverse mode diodes where the width of the active region is 1-3 μm and the thickness is $\sim$ 0.1 μm. The active region lengths are typically between 200 μm and 900 μm. In general, chip lengths are chosen with a particular application in mind. For instance, vertical cavity surface emitting lasers (VCSEL's) have active regions that are so short, only one longitudinal mode of the cavity falls under the gain curve. Longer active lengths in conventional edge-emitting diodes are usually chosen to minimize the effective loss. For the measurements we perform, the length of the diode active region is important because it determines the amplitude of dispersive effects on short pump-probe pulse propagation. Also, our pump-probe signals are integrated over the entire length of the diode.

In our experiments, we study three different diode structures. One structure, shown in Figure 2.13, is the channelled-substrate buried heterostructure (CSBH) InGaAsP/InP V-groove laser [71]. After etching the V-groove, four epitaxial layers are grown, an n-doped InP buffer layer, an InGaAsP active layer, a p-doped InP layer and a p-doped InGaAsP contact layer. The first and third layers create the p-n junction. The electrical contacts to the chip are at the top and bottom of the chip as shown in Figure 2.13. The current flow is perpendicular to the layers. The emission wavelength of the active region is determined by the relative mole fractions in the $In_{1-x}Ga_xAs_yP_{1-y}$ layer (see Figure 2.14). Typical active region dimensions for these diodes are 0.2 $\times$ 2.5 μm. In this thesis, we will refer to these diode structures as bulk diodes because the gain characteristics of the active region can be modeled using the bulk, 3-dimensional representation of the crystal lattice.

The second structure we will study is a separate confinement heterostructure (SCH) quantum well laser. These diodes offer many advantages over the more conventional bulk lasers. They have lower threshold currents, higher quantum

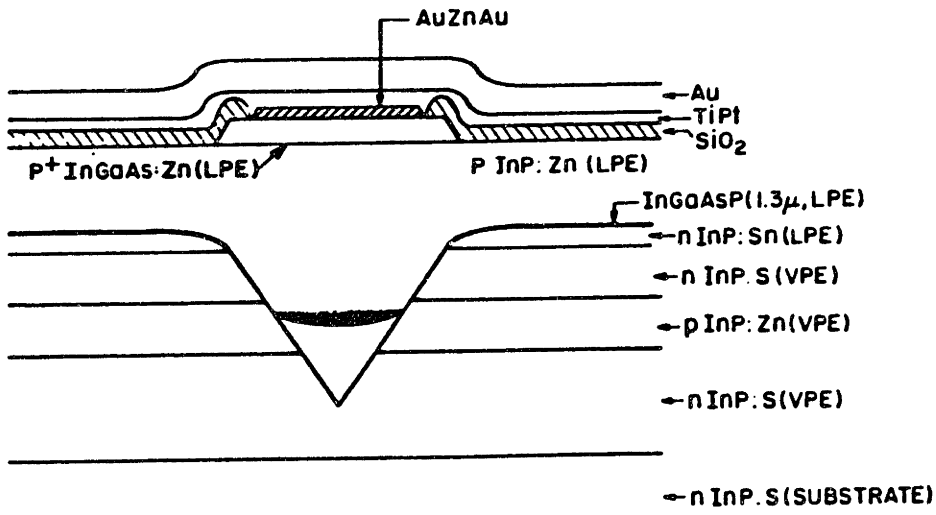

Figure 2.13: Cross section of the channelled-substrate buried heterostructure laser. (From Ref. [71].)

efficiencies and lower internal losses [72]. A schematic description of the laser is given in Figure 2.15. The active region is comprised of four narrow (80 Å each) InGaAs wells separated by 300 Å barriers (λ_{bar}=1.3 μm). The carriers are confined to the active region by the semi-insulating blocked planar buried heterostructure (SIPBH) design [73]. Note that the carriers are injected from the sides of the diode as shown in Figure 2.15 (b), and the current flow is perpendicular to the layers.

We will use pump-probe experiments to study the gain and index nonlinearities in these bulk and multiple quantum well (MQW) diodes. In the context of the pump-probe experiments, quantities like threshold current, internal loss and quantum efficiency are unimportant. For our studies, there are two important differences between the bulk and the MQW diodes. The first is the difference in the mode confinement factor. The mode confinement factor, Γ, is a measure of the fraction of the optical field that overlaps the active region. For the bulk diode, with an active region area of 0.2 $\times$ 2.5 μm = 0.5 μm^2, Γ=0.30 [1]. In the MQW diode, the active region area is much smaller and can be approximated by 4 (wells) $\times$ 8 nm/well $\times$ 2 μm =0.065 μm^2, and Γ=0.05. The mode confinement factor is

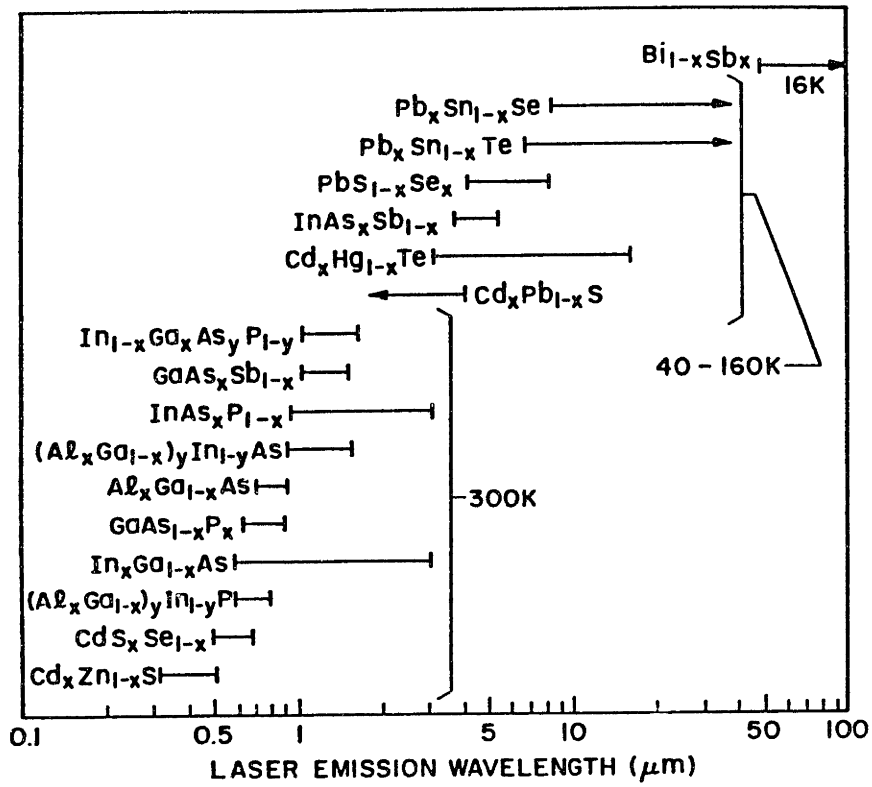

Figure 2.14: Wavelength range of semiconductor lasers covered by different material systems. (From Ref. [1].)

important because it relates the measured amplitude of nonlinearities induced in the active region to nonlinearities induced in the cladding. For instance, we might expect TPA, which is relatively independent of carrier density and pump-probe wavelength, to occur in the cladding as well as the active regions of the diodes. However, nonlinear effects like carrier heating and spectral hole burning should only occur in the electrically-"pumped" region (active region) of the diode. The pump-probe pulses will induce and sense nonlinearities across the entire spatial extent of the mode. However, in the bulk diodes, the ratio of the nonlinear signals generated in the cladding to those generated in the active region should be less than for the MQW diodes. This is because, relatively speaking, the mode samples more cladding in the MQW diodes. Therefore, we might expect TPA, for example, to be a larger portion of the total nonlinear response for the MQW diode than for the bulk diode.

The other important difference between the MQW and bulk diodes is that the degeneracy of the heavy hole and light hole bands at the Brillouin zone center is lifted by quantum confinement. It is well known that the energy levels for a particle in a quantum well depend on the mass. In these diodes, the heavy

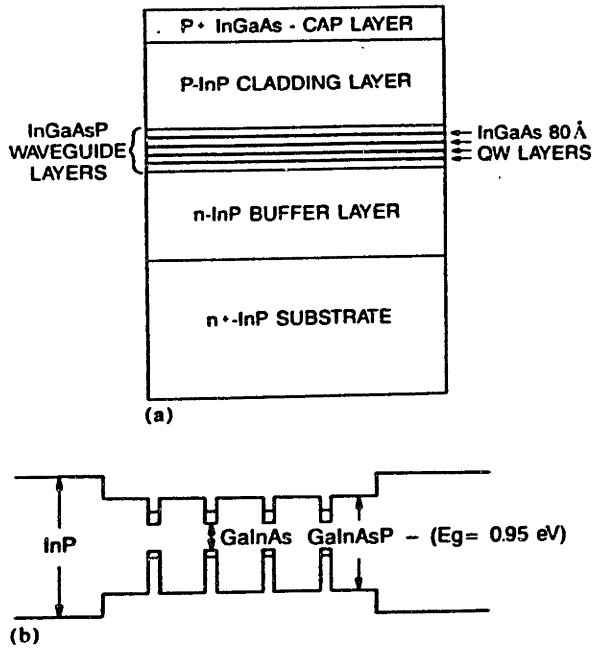

Figure 2.15: Schematic description of the SCH QW laser. (a) the layer structure; (b) the band diagram. (From Ref. [72].)

hole (hh) and light hole (lh) bands are split. Therefore, the hh-electron (hh-e) transition wavelength is longer than the lh-electron (lh-e) transition wavelength. Also, this separation of the heavy hole and light hole bands accentuates the importance of the polarization selection rules. The polarization selection rules state that at the Brillouin zone center, TM-polarized (perpendicular to the QW layers) light can not stimulate hh-e transitions. However, lh-e transitions are allowed. TE-polarized light (parallel to the QW layers) can stimulate both hh-e and lh-e transitions [74]. These polarization selection rules hold for bulk as well as MQW diodes but they have little impact on the gain in bulk diodes because the hh and lh bands are degenerate. In those diodes, the gain material can be considered isotropic. Any polarization anisotropy that is observed can be traced to the asymmetry of the waveguide [75].

We will see in our pump-probe experiments that the gain in the MQW diodes can be considered isotropic as well. There are a number of reasons why the polarization selection rules are relatively unimportant in these diodes. First, the energy separation between the light hole and heavy hole bands is small compared to the energy bandwidth of the pump-probe pulses. Therefore, both TE-polarized

and TM-polarized pulses can cause stimulated transitions, TPA and FCA. Second, the polarization selection rules are only strictly true at k=0. For other values in k-space, there are no strictly forbidden transitions. Experimentally, we have not observed a polarization-dependence of the measured responses in the MQW diodes.

The third type of diode we study, the strained-layer multiple-quantum- well (SLMQW) diode, is very sensitive to the polarization selection rules because of the large energy separation between the lh and hh bands ($\sim$ 100 meV [76] [77]). These structures are SIPBH lasers with narrow strained quantum well regions (Figure 2.16). The active region consists of four 2.5 nm thick $In_{0.77}Ga_{0.23}As$ quantum wells with 1.53 % compressive strain sandwiched between 9 nm thick lattice matched InGaAsP barriers. The active region width is approximately 2.5 μm. The measured emission peaks are at 1.53 μm for the TE mode and 1.38 μm for the TM mode [78]. Again, the polarization-dependence of the emission peaks is due to the polarization selection rules and the large energy sub-band separation between the lh and hh bands in these diodes. The gain is clearly not isotropic. In fact, pump-probe pulses (with center wavelengths near 1.5 μm) that are TM-polarized are below band and do not experience gain. However, TE-polarized pulses, with center wavelengths near 1.5 μm can stimulate hh-e transitions and see gain.

In this chapter, we have discussed the semiconductor physics relevant to gain in diode lasers and amplifiers. We have calculated the carrier density dependence and the carrier temperature dependence of the gain coefficients. The time evolution of the carrier and photon densities has been modeled by rate equations. The index changes, related to the gain changes by a Kramers-Kronig transformation, have been calculated for changes in carrier density and carrier temperature. Also, we have discussed the mechanisms responsible for gain and index nonlinearites and have described how these nonlinearities will appear in the pump-probe experiments that follow. Finally, we have given a brief description of the three diode structures, bulk, MQW and SLMQW, that will be studied in this thesis.

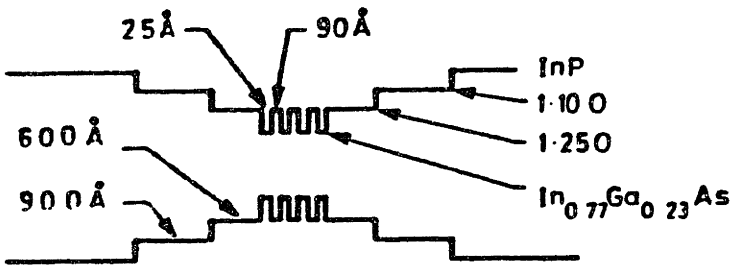

Figure 2.16: Band diagram of the strained-layer multiple quantum well device. (Ref. [78].)

Chapter 3

Additive Pulse Modelocked (APM) F-Center Laser

3.1 Introduction

There is a great deal of interest in lasers that can produce ultrashort pulses at 1.5 μm, both as sources for fiber optic communication systems and as diagnostic tools. Until 1987, short pulse generation in this wavelength region had been accomplished by actively modelocking InGaAsP diode lasers [79] and by soliton formation in fibers [80]. Since that time, a number of new modelocking schemes have been demonstrated. Passively modelocked color center lasers with intracavity multiple quantum well saturable absorbers have produced pulses as short as 275 fs, tunable from 1.59 μm to 1.7 μm [81]. Very recently, passively modelocked erbium doped fiber lasers, producing 77 fs pulses, have been demonstrated [82]. Optical pulsewidths of approximately 100 fs duration are optimal for our pump-probe investigations because they are the shortest pulses that will propagate through the diode without experiencing significant pulse broadening. In our lab, we have developed a modelocked source, based on the original soliton laser, that produces 100 fs pulses tunable near 1.5 μm. The Additive Pulse Modelocked, or APM, color center laser consists of a synchronously-pumped color center laser

coupled to a nonlinear auxiliary cavity [83] [84] [85]. In the APM scheme, pulses in the auxiliary cavity experience an intensity dependent phase shift. The interferometric addition of pulses from the main cavity and phase-shifted pulses from the auxiliary cavity produces the pulse shortening. As a result, the auxiliary cavity in the APM laser can contain any medium (positive dispersion fiber, negative dispersion fiber, semiconductor waveguide, etc.) with an instantaneous refractive index nonlinearity. In this chapter, we will discuss the operating principles and design of the APM KCl:Tl color center laser.

3.2 Operating Principles

The color center laser is synchronously pumped by a cw-modelocked Nd:YAG laser that produces $\sim$ 100 ps pulses at an average power of 5-6 W. The Nd:YAG laser cavity is 1.5 m long corresponding to a pulse repetition rate of 100 MHz. The optical resonator consists of a concave HR (highly-reflective) rear mirror and a convex front mirror. The cavity is unstable by design and only becomes stable when an intracavity focussing element is included. Intracavity focussing is achieved via thermal lensing in the Nd:YAG rod. For normal flashlamp currents, the YAG rod approximates a 30 cm focal length lens [86]. An aperture in the cavity forces the laser to oscillate in the TEM_{00} mode.

The gain material in the color center laser is a KCl:Tl^0 crystal. This crystal is composed of color centers, electron or hole trapping defects that produce the optical absorption and emission bands in insulating crystals [87] [88]. These defects are produced by irradiating the crystal with high-energy (2 MeV) electrons while the crystal is immersed in liquid nitrogen. The crystal must be kept cold to prevent the defects from "walking out" from the sites where they are induced. Typical irradiation current densities are 5 $\mu A/cm^2$. The laser-active color centers are efficient for two reasons. First, the gain has a large cross-section, $\sigma = 3 \times 10^{-16}$ cm^2 because the emission band represents a fully allowed transition. Second, the gain is homogeneously broadened so that all the centers contribute energy to the lasing mode. The absorption is homogeneously broadened as well so that all centers may be pumped by a laser operating in the pump band. The peak of one of the absorption bands is 1.06 μm which is why the laser is pumped by a Nd:YAG laser.

Figure 3.1 shows the color center laser with the auxiliary cavity. The design is that of a folded, astigmatically compensated cavity [88]. Mirrors M1 and M2 are contained within the vacuum enclosure that provides the thermal isolation for the cold finger and that protects the crystal surfaces from condensation. A lens and and the substrate of mirror M1 combine to form a thick lens with an effective focal length of 33 mm that focusses the pump beam onto the laser crystal. The crystal is held by a cold finger at a distance from M1 determined by the stability criterion for the cavity [89]. Mirrors M3, M4 and M0 are outside the vacuum enclosure and are arranged in a folded configuration to save table space. The output coupler, M0, has a reflectivity of 80 %. The color-center cavity length is matched to the Nd:YAG cavity length (1.5 m). The synch-pumped pulses from the color center laser are typically 20 ps in duration. The laser can be tuned from 1.46 μm to 1.58 μm using a birefringent tuning plate [90]. Typical output powers range from 20-300 mW.

The auxiliary cavity, measured from M0, is 1.5 m long to match the cavity length of the color center and Nd:YAG lasers. A beamsplitter directs 50 % of the output power to the auxiliary cavity. The beam transmitted by the beamsplitter is the output beam from the APM color center laser. Light in the auxiliary cavity is coupled by a 10 cm focal length convex lens and graded index (GRIN) lens combination into a 40 cm length of dispersion-shifted, non-polarization-preserving fiber. Dispersion-shifted fiber is used because it has a smaller core diameter, 5 μm, than standard 9 μm fiber, (AT&T 5D), yielding a higher nonlinearity for the same input power. The output end of the fiber is butt-coupled to a gold mirror. The reflected light travels back through the fiber and lenses and is split at the beamsplitter. The power transmitted by the beamsplitter (P_{FIBER}) is used to monitor the linear phase of the auxiliary cavity. The fiber is glued (5-minute epoxy), under tension, to a piezoelectric transducer (PZT). Coarse adjustments to the auxiliary cavity length can be made manually by translating the stage that holds the GRIN lens and input fiber end. The length of the auxiliary cavity can be controlled precisely by applying a voltage to the PZT and stretching the fiber.

The simple picture that describes APM is that of two pulses interfering. One pulse, circulating in the main color center cavity, is modeled as having a constant phase. The other pulse circulates in the auxiliary cavity. The pulses can be overlapped at a common mirror. The linear phase difference between the pulses is

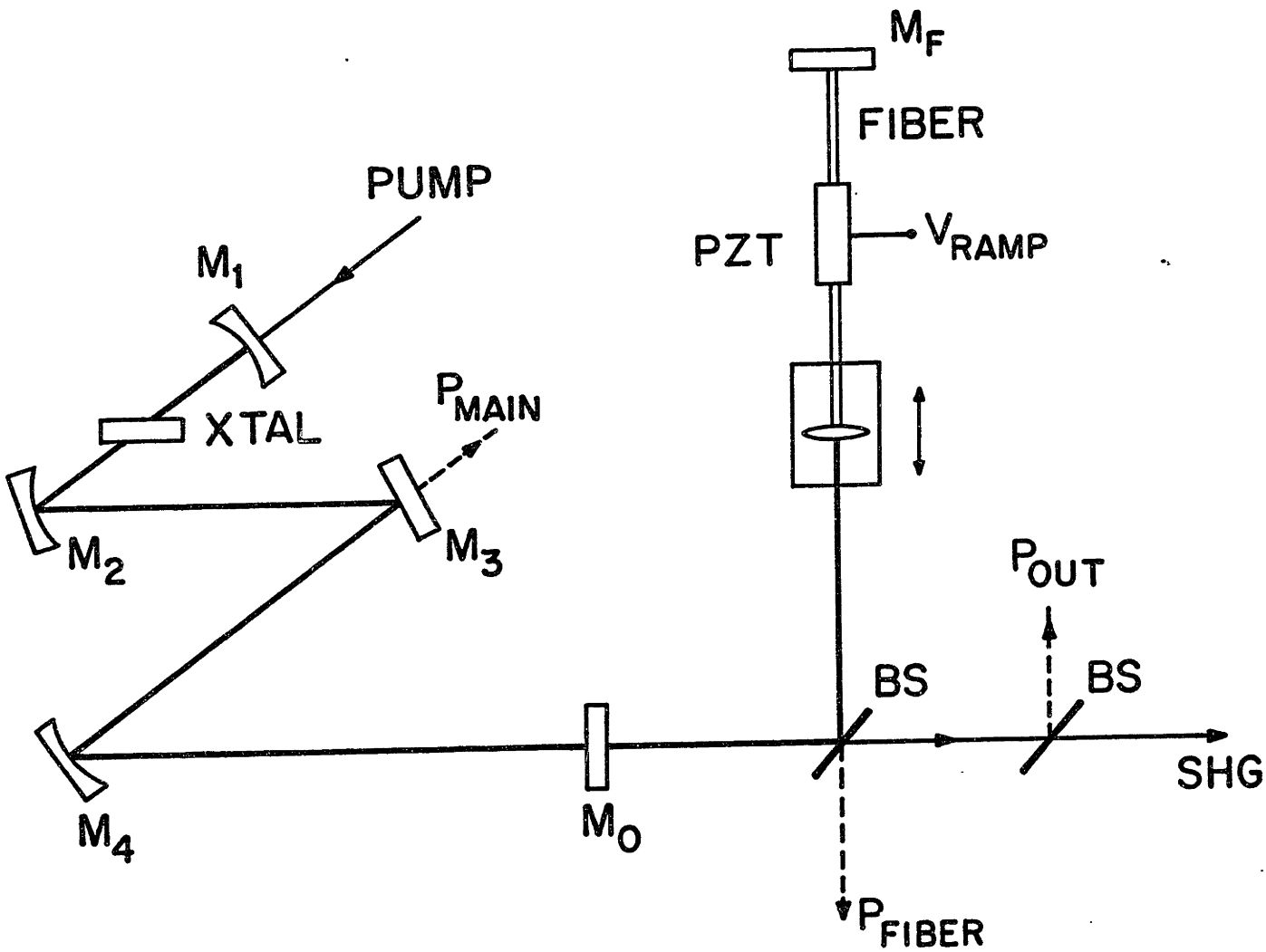

Figure 3.1: Schematic of the color center laser with the auxiliary cavity.

set by the relative lengths of the two cavities. If the two cavity lengths are exactly matched, the two pulses are in phase and interfere constructively. If the round trip auxiliary cavity length is changed by $\lambda/2$, the two pulses will be out of phase and will interfere destructively. Besides this linear phase shift, pulses circulating in the auxiliary cavity experience an intensity dependent (nonlinear) phase shift in the optical fiber. The nonlinear phase shift, $\Delta\Phi(t)$, due to self-phase modulation in the optical fiber, is given by

$$\Delta\Phi(t) = \left(\frac{2\pi n_2 L}{\lambda}\right) I(t) \tag{3.1}$$

where L is the fiber length, λ is the center wavelength of the optical pulses, $n_2 = 3.2 \times 10^{-16}$ cm^2/W [91], and $I(t)$ is the intensity profile of the pulse. Thus, the peak of the optical pulse is shifted in phase relative to the wings. Then, if the linear phase difference between the two cavities is π, so that the wings of the pulses are out of phase and interfere destructively, the peaks of the pulses will be closer in phase and can interfere constructively. It was this interferometric pulse subtraction in the wings and pulse addition at the peaks that lead to the name, Additive Pulse Modelocking.

In our laser, we think of the two pulses interfering at the laser output coupler M0. The pulses from the two coupled cavities will interfere in the time domain as long as there is some overlap of the pulse envelopes. A 100 fs pulse at 1.5 μm is approximately 20 cycles long. Therefore, as long as the laser cavity and auxiliary cavity lengths are within 30 μm of each other (round-trip), the pulses from the two cavities will interfere. To study the effects of pulse interference, we monitor the power in the main laser cavity, P_{MAIN}, the output power, P_{OUT}, and the amount of second-harmonic generated as a function of auxiliary cavity length. Figure 3.2 shows the measured powers and SHG as the cavity length is ramped from -6μm to $+6\mu$m. The sinusoidal variation in powers P_{MAIN} and P_{OUT} is also observed in power P_{FIBER}. The slight discontinuity in the top two power-versus-length scans is associated with perfect matching of the two cavity lengths. The peaks of the P_{MAIN} sine wave correspond to the pulse reflected back from the auxiliary cavity being in phase with the pulse circulating in the main cavity. Then the two pulses add constructively at the mirror and the overall power in the main cavity is increased. These points represent effective increases in M0 reflectivity

and occur simultaneously with minima in the output power. Likewise, when the effective reflectivity of M0 is lowered, the output power increases, corresponding to destructive interference of the two pulses at M0. The amplitude of the SHG signal is inversely proportional to the output pulse width. Note that short pulse operation is achieved only over a finite range of cavity detunings.

Characterizing the stability ranges for short pulse operation in these lasers has been an active area of research [92] [93] [94]. It is clear from Figure 3.2 that the relative detuning of the cavity lengths must be maintained in order to achieve stable modelocking. We stabilize the cavity detuning using a scheme designed by Mitschke and Mollenauer [95]. A detector is placed after the beamsplitter to monitor P_{FIBER}. This average power will fluctuate as the cavity detuning fluctuates. However, there will be a specific power level (reference level) that corresponds to the auxiliary cavity phase bias that supports APM. A home-made circuit compares the real power level to the reference level and the difference signal is used to drive the PZT attached to the fiber. Stretching the fiber with the PZT changes the length of the auxiliary cavity and allows us to lock the optical phase that supports APM. Figure 3.3 shows the intensity autocorrelation traces of the (a) synch-pumped and (b) APM laser pulses. In this case, the pulses have been shortened from 25 ps to 130 fs by the APM technique, a factor of almost 200.

3.3 Tricks

Like all state-of-the-art equipment, the APM color center laser has idiosyncrasies that must be acknowledged. The most important thing to remember when designing an auxiliary cavity is to eliminate all reflections. It has been theoretically predicted that extraneous reflections in the auxiliary cavity may keep an APM laser from self-starting [96] [97]. In fact, extraneous reflections may keep the laser from modelocking at all. For example, replacing the beamsplitter in Figure 3.1 with a variable beamsplitter, consisting of a half-wave plate and a polarization beamsplitting cube, made it impossible to APM the color center laser. The optics had all been anti-reflection (AR) coated for 1.5 μm, reducing the reflection coefficient at each face from 4% to 1%. Also, the reflectivity of the variable beamsplitter was adjusted to match that of the plate beamsplitter. However, the synch-pumped

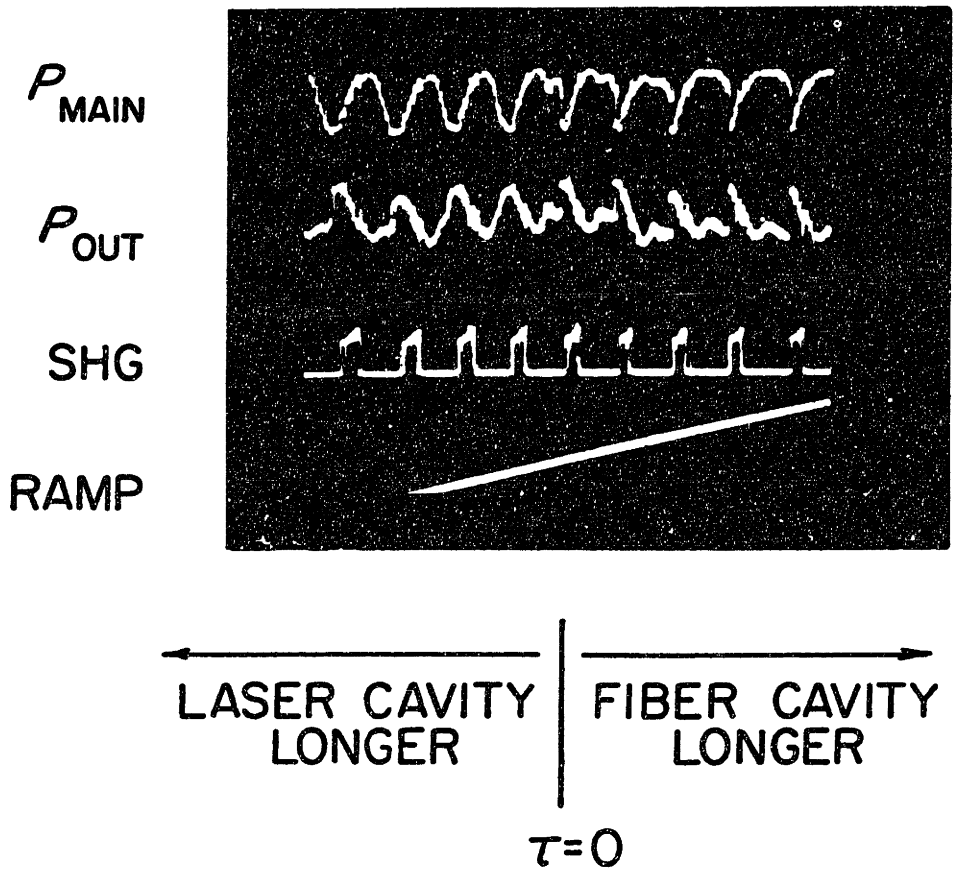

Figure 3.2: Variations of laser cavity power P_{MAIN}, output power, P_{OUT}, and second harmonic generation, SHG, as a function of cavity length detuning.

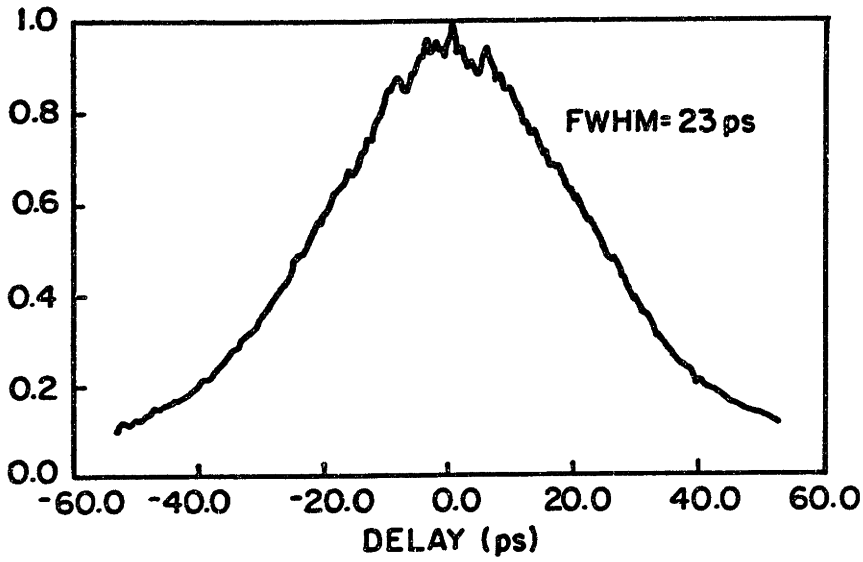

(a)

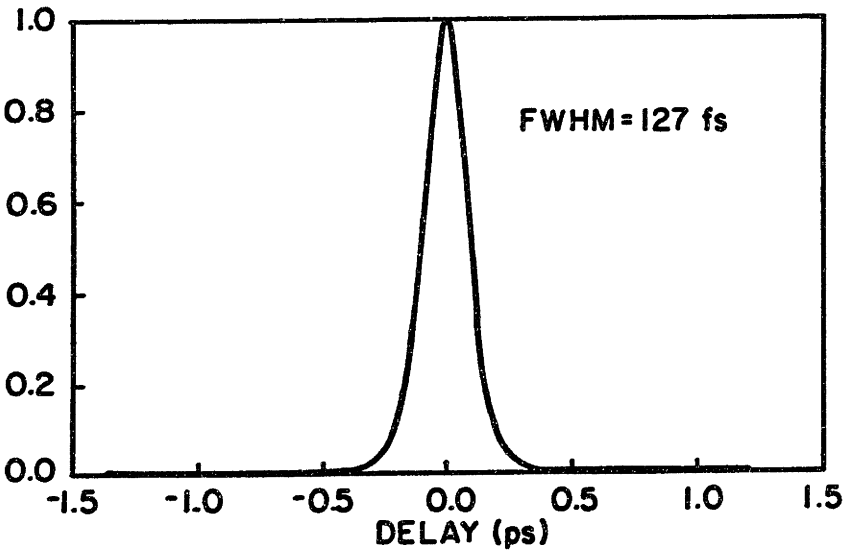

(b)

Figure 3.3: Intensity autocorrelation traces of the (a) synch-pumped and (b) APM laser pulses.

pulses would not shorten. Using a microscope objective to couple to the fiber in the auxiliary cavity had a similar effect.

There are many ways to eliminate reflections in the auxiliary cavity. First, minimize the number of optical components in the cavity because even AR-coated optics reflect. Commercial coatings typically reduce the glass-air interface reflectivity from 4% to 1%. Beware of microscope objectives. They have three lenses (6 reflecting surfaces) inside the housing. Second, tilt the optical components so that the transmitted and reflected beams are not collinear. Third, use index matching fluid between glass components when possible. In our set-up, the GRIN lens is AR-coated on the input face (from the color center laser) and the output face is uncoated. Index matching fluid is inserted between the GRIN lens and the fiber endface. To further reduce the reflections from the fiber endface, we bevel it at 8^0. For light coupled into the fiber, beveling the endface will direct the reflected light away from the cavity axis. For light exiting the endface, the amount of reflected power that is recaptured by the core is -60 dBm.

Maintaining the color center laser is an art all its own [88]. The crystal is replaced about once a year. Usually the laser fails because the crystal itself has degraded and the power levels have become unacceptably low or the vacuum fails. Every time the crystal is replaced, the APM changes personalities. However, experimenting with parameters such as the beamsplitter reflection/transmission ratio, the auxiliary cavity fiber length, and the birefringent tuning plate, eventually returns the laser to stable operation. The APM performance is only weakly dependent on the synch-pumped performance of the color center laser and the modelocked performance of the Nd:YAG laser. Amplitude fluctuations on the Nd:YAG pulses translate to amplitude fluctuations on the APM pulses, but the small-signal pump-probe experiments are relatively insensitive to amplitude fluctuations as high as 20% of the total average power. Slow drifts in the length of the Nd:YAG laser broaden the output modelocked pulses and therefore the color center synch-pumped pulses. However, APM is such a strong modelocking mechanism that 100-150 fs pulses will build up even from very broad color center pulses. On occasion, this laser has self-started. In self-starting, the Nd:YAG modelocker is turned off and the pulses build up from noise. This behavior has only been observed at high output powers from the color center laser (average $P_{OUT} > 300$ mW).

Finally, we point out that the tuning range of the synch-pumped laser has not been maintained under APM operation. The APM laser can be tuned from approximately 1.48 μm to 1.52 μm. Tuning to even longer wavelengths produces pulses that are broader and that have wings. This behavior is not well understood and will be the subject of future investigations.

In conclusion, we have discussed the operating principles of Additive Pulse Modelocking. We have described an APM source consisting of a synchronously pumped color center laser coupled to a nonlinear external cavity that produces tunable, subpicosecond pulses near 1.5 μm. The APM color center laser is an excellent source for our pump-probe experiments for many reasons. First, it produces 100-200 fs, transform-limited pulses, tunable near 1.5 μm. Second, using an external stabilization circuit, stable pulses are produced for hours at a time. Third, the average output power is high enough to supply many picojoules of pulse energy to the pump and probe pulses. Finally, the pulses are clean and pedestal-free, allowing us to perform high resolution temporal studies of InGaAsP diode lasers and amplifiers.

Chapter 4

Group Velocity Dispersion

4.1 Introduction

Before we can investigate the gain and refractive index nonlinearities in these diode amplifiers via pump-probe measurements, we must study the effects that cause pulse distortion. As we will describe in Chapter 5, pump-probe results are fit by convolving an assumed impulse response function, $h(t)$, with the experimentally determined autocorrelation function, $G^2(t-\tau)$. If the pump-probe pulses are distorted as they travel through the diode, the autocorrelation function is not an accurate representation of the pulse in the diode and the mathematical fitting procedure breaks down. Therefore, it is important to start our experimental investigations by comparing the pulses before and after they travel through the diode, to verify that the diode introduces no significant pulse distortion. In this chapter, we will investigate the effect of group velocity dispersion on short pulse propagation in these diodes. We will present the first time-domain measurements of the group velocity dispersion in bulk and multiple quantum well (MQW) InGaAsP devices at 1.5 μm.

Group velocity dispersion (GVD), defined as the second derivative of the propagation constant with respect to frequency, $\frac{d^2\beta}{d\omega^2}$, is an important quantity because it describes limitations in the propagation and generation of short pulses in semiconductor diode lasers and amplifiers. In the frequency domain, GVD can affect experiments by limiting the phase matching bandwidth and by creating an arti-

ficial spectral hole. In the time domain, GVD can cause pulse broadening, and polarization-dependent group velocities can cause orthogonally polarized pulses to walk-off from each other. Both pulse broadening and pulse walk-off limit the time resolution of the measurements.

We begin by noting that the semiconductor material is polarizable and can be modeled as an ensemble of dipole oscillators. Then, following the description of Butcher and Cotter [69], we say that in the presence of an electric field, these dipoles oscillate according to

$$F = m\left[\frac{d^2x}{dt^2} + 2\Gamma\frac{dx}{dt} + \Omega^2 x - (\psi^{(2)}x^2 + \psi^{(3)}x^3 + ...)\right] = -qE \tag{4.1}$$

where Ω is the resonance frequency, Γ is the damping constant and x is the displacement of the dipole charge from its equilibrium position. If we assume that the applied electric field causes only small displacements of the charges, then the dipole's response to the field is linear and we can ignore the anharmonic terms ($\psi^{(2)}x^2$, etc.). If E is sinusoidal

$$E(t) = E_0\cos(\omega t), \tag{4.2}$$

then

$$x = -\frac{qE}{2m}\frac{e^{-j\omega t}}{[\Omega^2 - 2j\Gamma\omega - \omega^2]} + c.c. \tag{4.3}$$

where *c.c.* denotes the complex conjugate. The polarization, P is given by

$$P = \epsilon_0\chi E = -Nqx \tag{4.4}$$

where N is the density of oscillating dipoles, ϵ_0 is the permittivity of free space, and χ is the linear susceptibility,

$$\chi = \frac{Nq^2}{\epsilon_0 m}\left[\frac{1}{\Omega^2 - 2j\Gamma\omega - \omega^2}\right]. \tag{4.5}$$

The refractive index, n, is given by

$$n(\omega) = \Re e\sqrt{1+\chi} \tag{4.6}$$

and is frequency dependent. For our discussion, it is more convenient to consider the wavelength dependence of the refractive index as opposed to the frequency dependence, so we define the GVD as $-\lambda\frac{d^2n_{eff}}{d\lambda^2}$, rather than $\frac{d^2\beta}{d\omega^2}$. The wavelength dependence of the refractive index is important for short pulse propagation because the different wavelength components contained in the spectral bandwidth of the pulse travel at different speeds. This effect can cause pulse broadening or narrowing, depending on the size and the sign of the wavelength dependence and whether or not the pulse is chirped.

In the experiments described in this chapter, we measure the wavelength dependence of the pulse round-trip transit time. The pulse energy, or pulse envelope, travels at the group velocity, v_g, which is related to the propagation constant, β, via

$$\frac{1}{v_g} = \frac{d\beta}{d\omega} = \frac{d\beta}{d\lambda}\frac{d\lambda}{d\omega} = \frac{n_g}{c} \tag{4.7}$$

where $\beta = 2\pi n_{eff}(\lambda)/\lambda$, $d\omega = (\frac{-2\pi c}{\lambda^2})d\lambda$ and n_g is the group index. The effective index, n_{eff}, can be thought of as a weighted average of the core and cladding indices and can be determined using the effective index approximation [98]. Substituting for β, we get

$$n_g = n_{eff}\left(1 - \frac{\lambda}{n_{eff}}\frac{dn_{eff}}{d\lambda}\right), \tag{4.8}$$

The pulse round-trip transit time in the diode is related to the group velocity and the group index via,

$$\tau_g = \frac{2l}{v_g} = \left(\frac{2l}{c}\right)n_g. \tag{4.9}$$

Dispersion in the group velocity can be characterized by,

$$\frac{dn_g}{d\lambda} = \left(\frac{c}{2l}\right)\frac{d\tau_g}{d\lambda} = -\lambda\frac{d^2n_{eff}}{d\lambda^2}, \tag{4.10}$$

where $\frac{d\tau_g}{d\lambda}$ is the wavelength dependence of the pulse round-trip time in the diode.

4.2 Experiments

The first measurements of GVD in semiconductor diodes were performed in the frequency domain. In those experiments, the variation in the longitudinal mode spacing was measured for 0.8 μm AlGaAs devices [99] [100] [101] and 1.5 μm InGaAsP[102][103] devices. More recently, the GVD in 1.3 μm InGaAsP diode lasers was measured by an envelope phase shift technique [104] and an interferometric technique [105]. A discussion of the limitations of these various techniques can be found in Reference [105]. The time domain measurements, or pulse echo measurements, were first performed by Kesler et al., on AlGaAs diodes [14] at 0.8 μm. In our experiment, we extend the pulse echo technique to measure the GVD for both TE- and TM-polarized pulses at 1.5 μm [106].

The experimental setup is shown in Figure 4.1. The tunable, 100 fs pulses generated by the Additive Pulse Modelocked (APM) color center laser pass through a half-wave plate and are coupled into a short length of dispersion shifted fiber that is terminated with a microlens. The fiber microlens couples the optical pulses into the diode laser active region and a microscope objective couples them out. Each pulse that enters the diode will be partially reflected at the facets and will experience some gain so that the output contains a sequence of pulses spaced by the diode round-trip time. This pulse sequence is then passed through a second half-wave plate and is cross-correlated with a gating pulse. The cross-correlation of the output pulse sequence for the bulk, V-groove laser is shown in Figure 4.2. In this case, the pulse center wavelength was 1.521 μm and the diode was 475 μm long.

By varying the pulse center wavelength and measuring the resulting change in pulse round-trip time, we can determine the dispersion in the group index. Figure 4.3 (a) shows two pulse sequences, one for a pulse center wavelength of 1.520μm (solid line) and the other for a pulse center wavelength of 1.492 μm (dashed line). Notice the small but measurable difference in the pulse echo spacing as a function of wavelength. Figure 4.3 (b) shows the pulse sequences for TE-polarized (solid lines) and TM-polarized (dashed lines) pulse trains with the same pulse center

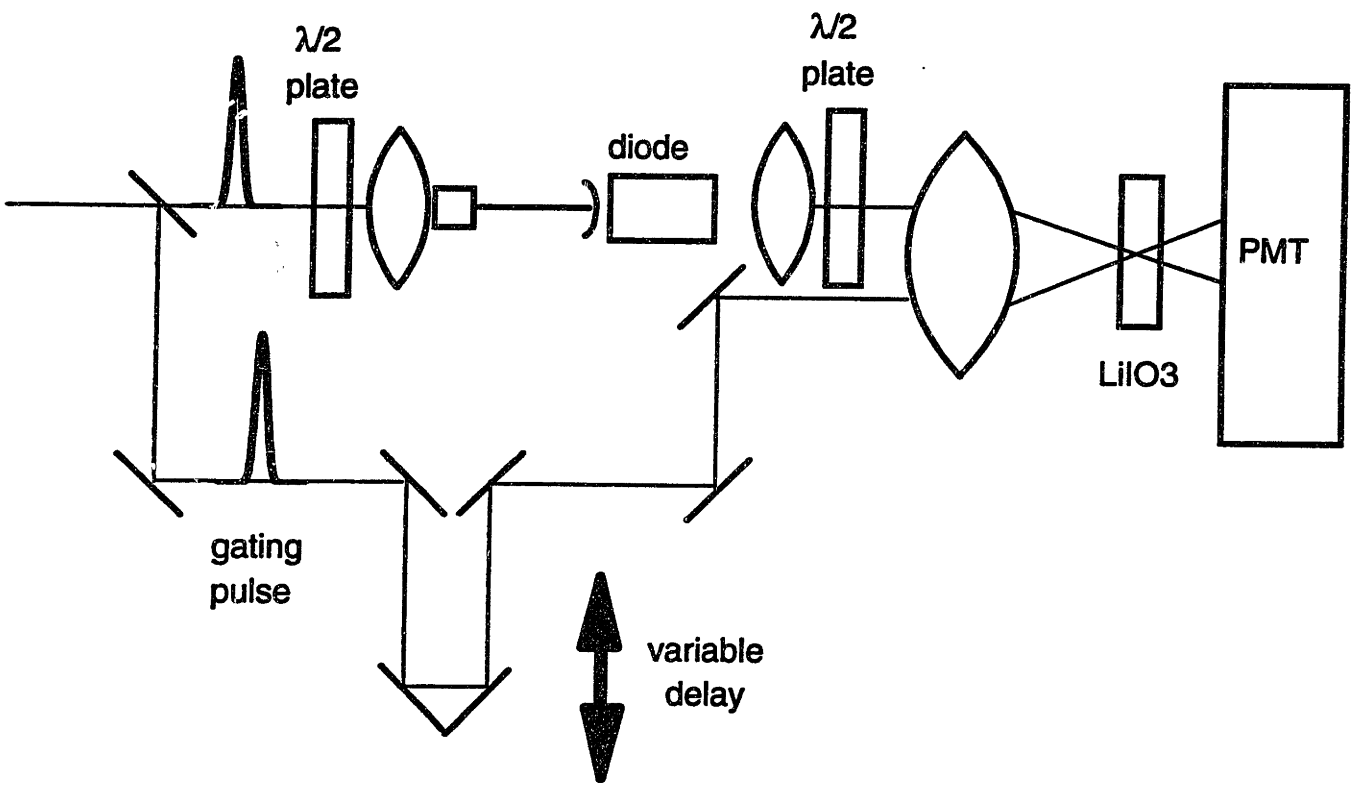

Figure 4.1: Schematic of the pulse echo experiment.

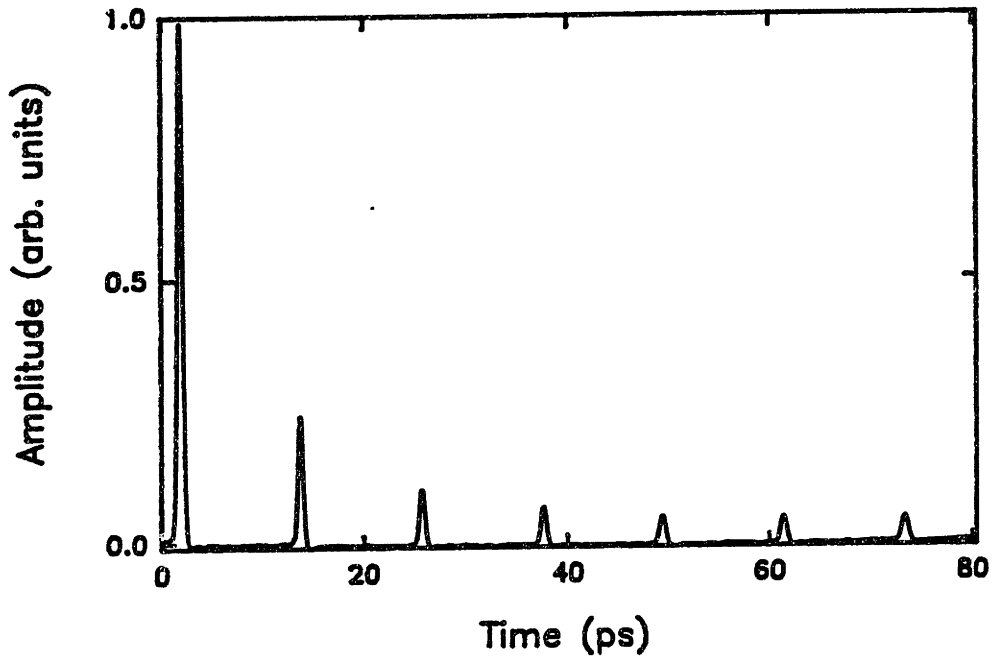

Figure 4.2: Cross-correlation of the output pulse train produced by a single pulse incident on an uncoated, 475 μm long, bulk, V-groove laser diode. In this case the diode bias current was 40 mA (I_{th}=20 mA), the pulse center wavelength was 1.521 μm, and the pulse was TE polarized.

wavelength. The difference in the group velocity is clear.

Figure 4.4 shows the measured round-trip time for pulses having TE and TM polarizations, for the bulk and the MQW diodes, as a function of wavelength. In these experiments, the bulk laser was 475 μm long and the MQW laser was 900 μm long. The measurements were performed on the diodes when they were biased above threshold so that we could resolve many echoes. Therefore, the carrier density was relatively independent of current. The effects of carrier induced index changes on waveguide anisotropy and GVD are small [55] and are neglected. As described previously, the slope of the lines in these plots, $\frac{\Delta t}{\Delta \lambda}$, gives the dispersion of the group index and the corresponding group velocity dispersion via Eq. (4.10). Notice that the slopes of the lines are similar for both diode structures and for both polarizations. This result implies that the group velocity dispersion is similar in both diodes. However, the difference in the round-trip transit times for the TE and TM polarizations, implies that the group velocity itself is polarization dependent. This polarization dependence of the group velocity has been observed

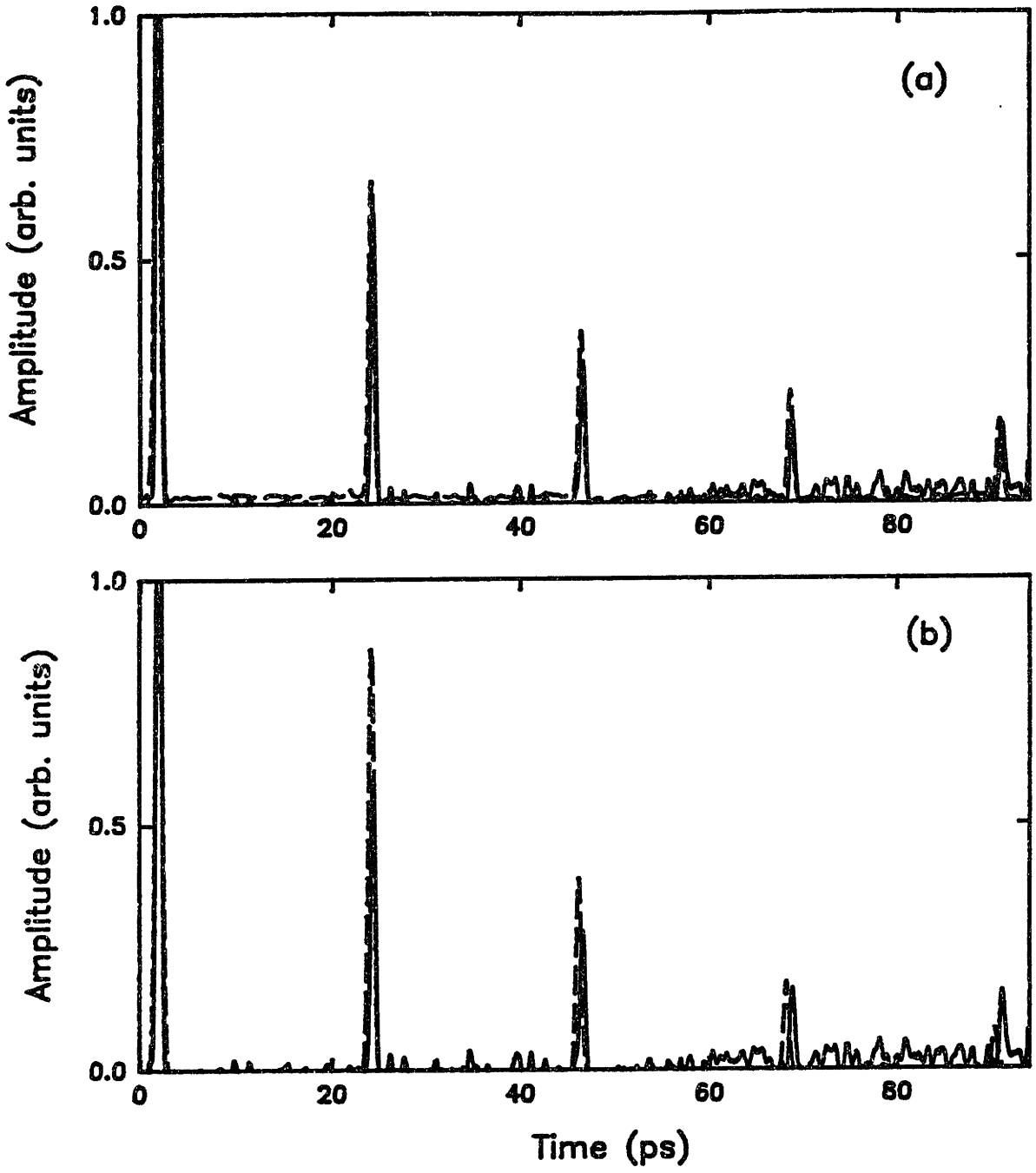

Figure 4.3: Cross-correlation of the output pulse train produced by a single pulse with (a)center wavelength = 1.520 μm (solid line) and 1.492 μm (dashed line) and with (b) TE-polarized pulses (solid line) and TM-polarized pulses (dashed lines). In (a), the pulses are TE-polarized in both cases and in (b), the center wavelength is 1.52 μm in both cases.

in bulk diodes at 1.3 μm [105] and has been attributed to differences in waveguide dispersion for the two polarizations.

The effect of GVD on pulse broadening can be determined in the following manner. Assume that the electric field incident on the waveguide can be described in the time domain by a Gaussian,

$$E(t, z = 0) = e^{(-(2ln2)t^2)/\tau_{in}^2}. \tag{4.11}$$

The intensity full width at half maximum (FWHM) of this pulse is τ_{in}. In the frequency domain, this short pulse can be described as a superposition of different frequencies centered around ω_0. If the Fourier transform of $E(t, z = 0)$ is $E(\omega, z = 0)$, then after traveling a distance l in a dispersive medium, where each frequency has experienced a different phase shift, the field is described by $E(\omega, l) = E(\omega, 0)e^{-j\beta(\omega)l}$, where $\beta(\omega)$ can be expanded in a Taylor series

$$\beta = \beta_0 + \frac{d\beta_0}{d\omega}(\omega - \omega_0) + \frac{1}{2}\frac{d^2\beta_0}{d\omega^2}(\omega - \omega_0)^2 + ... \tag{4.12}$$

Transforming $E(\omega, l)$ back to the time domain yields a Gaussian pulse with a FWHM of

$$\tau_{out} = \tau_{in}\sqrt{1 + (\tau_c/\tau_{in})^4}. \tag{4.13}$$

The critical pulsewidth, τ_c, is given by

$$\tau_c = \sqrt{\frac{(2ln2)\lambda^2 l}{\pi c^2}(\lambda\frac{d^2 n_{eff}}{d\lambda^2})} = \sqrt{\frac{(2ln2)\lambda^2 l}{\pi c^2}(\text{GVD})}. \tag{4.14}$$

A pulse of width τ_c will broaden by a factor of $\sqrt{2}$ after passing through the medium. Table 4.1 summarizes the measured values of $\frac{\Delta t}{\Delta \lambda}$ and the calculated values for GVD and critical pulsewidth for the two diodes. In Figure 4.5 (solid line) we show the calculated output pulsewidth versus input pulsewidth for a waveguide with a critical pulsewidth of 75 fs. The dotted and dashed lines in Figure 4.5 show the calculated pulse broadening when τ_c=50 fs and τ_c=100 fs

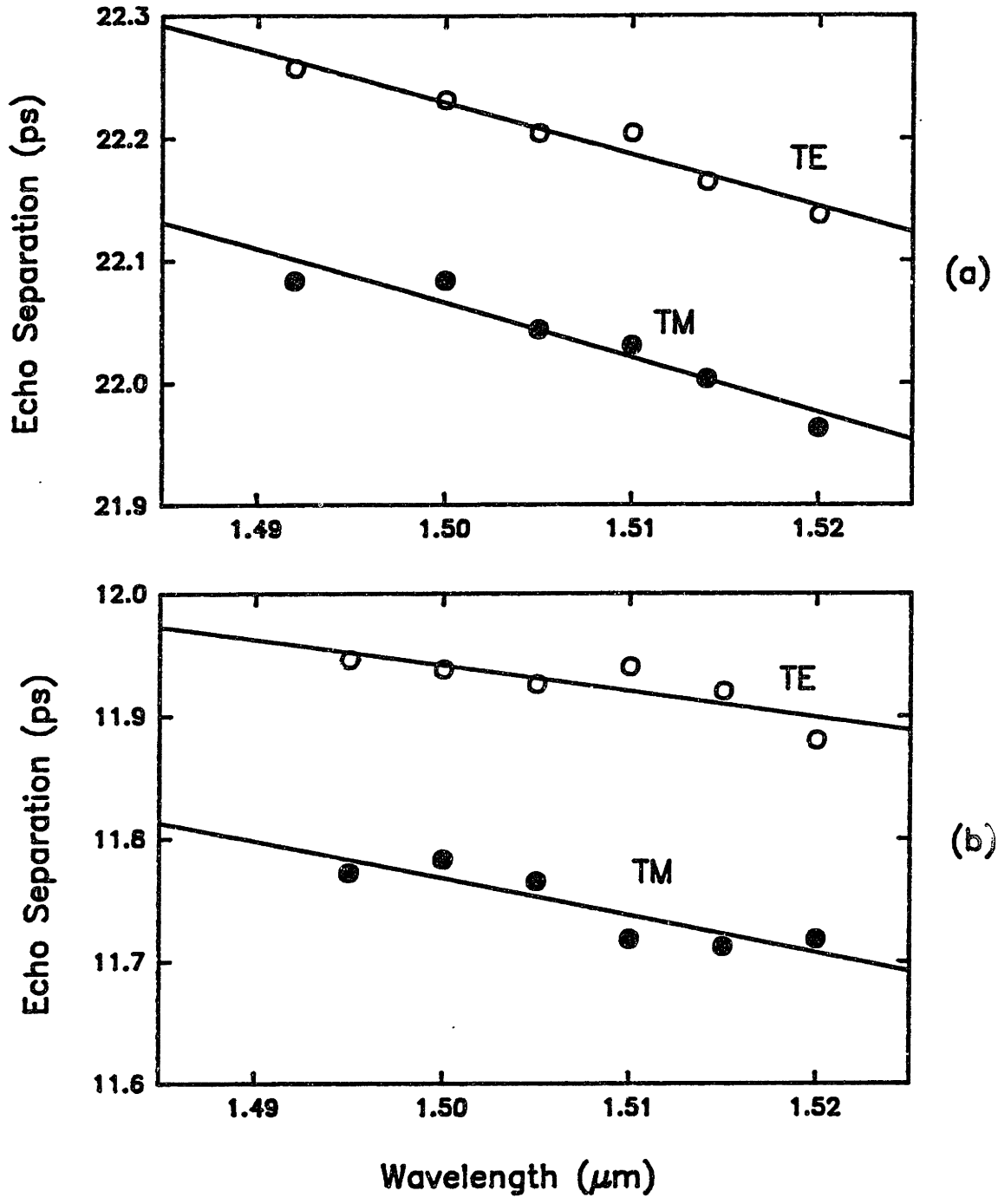

Figure 4.4: Measured transit time through the diode as a function of pulse center wavelength for (a) a 900 μm long MQW laser and (b) a 475 μm long bulk V-groove laser. The open circles are values for TE-polarized pulses and the solid circles are values for TM-polarized pulses.

Diode	L	$\left.\frac{\Delta t}{\Delta\lambda}\right\|_{TE}$	$\left.\frac{\Delta t}{\Delta\lambda}\right\|_{TM}$	$\left.-\lambda\frac{d^2 n_{eff}}{d\lambda^2}\right\|_{TE}$	$\left.-\lambda\frac{d^2 n_{eff}}{d\lambda^2}\right\|_{TM}$	$\tau_c\|_{TE}$	$\tau_c\|_{TM}$
Bulk	475μm	-2.0 fs/nm	-3.0 fs/nm	-0.63 μm^{-1}	-0.95 μm^{-1}	58 fs	71 fs
MQW	900μm	-4.2 fs/nm	-4.5 fs/nm	-0.71 μm^{-1}	-0.74 μm^{-1}	84 fs	86 fs

Table 4.1: Measured values of $\frac{\Delta t}{\Delta\lambda}$ and calculated values of the group velocity dispersion and the critical pulsewidth for the bulk V-groove and MQW devices. Results are presented for both the TE and TM polarizations.

respectively. Note that for typical pulses used in the pump-probe experiments (τ_{in}=150 fs) there is negligible pulse broadening in these diodes.

Figure 4.6 compares the autocorrelation (solid line) for a 104 fs input pulse, with the cross-correlation (dashed line) of that pulse after traveling once through (a) all the components in the optical path except the diode and (b) all the optical components in the path, including the MQW diode. We have calculated the pulsewidths assuming a Gaussian pulseshape so that we can compare our results to the critical pulsewidth theory. Notice that in Figure 4.6 (a), the pulse was broadened by $\sim$ 15 fs by the optics. After passing through the optics and the MQW diode, the pulsewidth has been broadened to 160 fs (Figure 4.6(b)). If we use the measured value of GVD to obtain a critical pulsewidth, and then predict the output pulsewidth, based on the dispersion in the diode alone, we expect τ_{out} = 125 fs for an input pulsewidth of τ_{in} = 104 fs. The difference between the measured and calculated values is due in part to pulse broadening in the optics. If we calculate the critical pulsewidth as the geometric mean of the critical pulsewidth for the optics (77 fs) and the critical pulsewidth for the diode (85 fs), we obtain a critical pulsewidth of τ_c = 115 fs. This value predicts an output pulsewidth of 155 fs for τ_{in} = 104 fs, in much better agreement with

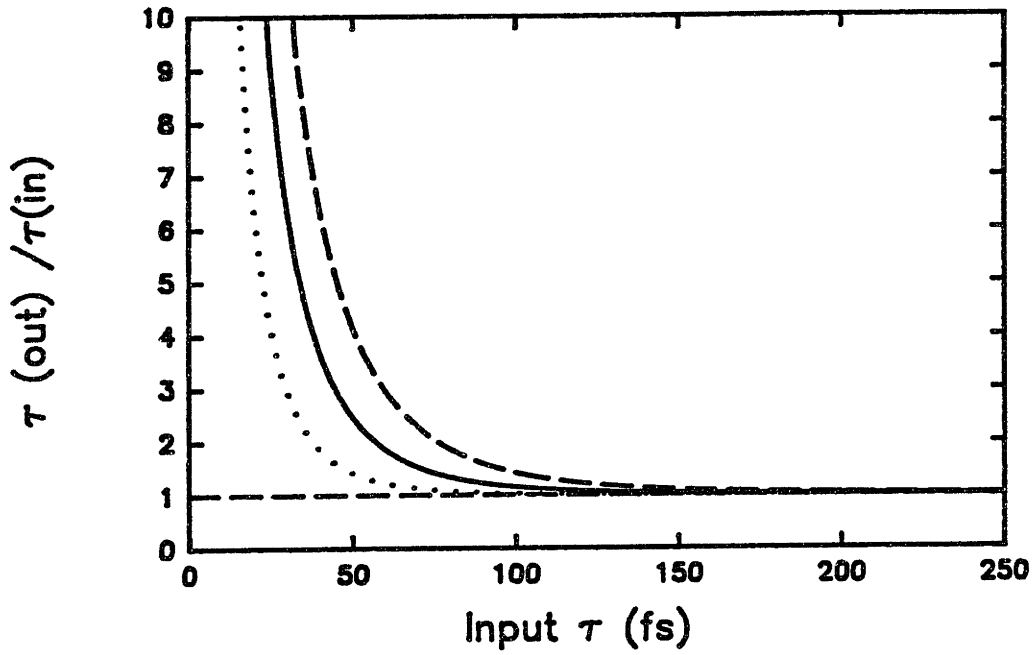

Figure 4.5: Output pulsewidth versus input pulsewidth for a waveguide with a critical pulsewidth of 50 fs (dotted line), 75 fs (solid line) and 100 fs (dashed line).

the measured value. The remainder of the difference is most likely the result of pulsewidth fluctuations (10 fs pulse-to-pulse), the deviation of the pulse shape from Gaussian and the deviation of the pulse spectrum from transform limit.

In Figure 4.6 we have shown the cross-correlation for a pulse polarized parallel to the active layer (TE mode) of the diode. The measured cross-correlation for a pulse polarized in the orthogonal direction (TM mode) showed similar amounts of pulse broadening. This similarity is consistent with the fact that the critical pulsewidth is approximately the same for both polarizations. We have also measured the pulse broadening from echo to echo in the bulk diodes and the results are consistent with the measured values of GVD. In making this comparison, it should be noted that τ_c scales as $\sqrt{nL}$ where L is the diode length and n is the number of transits.

The difference in the group velocity for TE- and TM-polarized pulses means that orthogonally polarized pump-probe pulses walk-off from each other as they pass through the diode. This walk-off effectively broadens the pump-probe pulse and limits the time resolution of the experiments. It can be shown that this pulse broadening due to pump-probe pulse walk-off can be accounted for by convolving

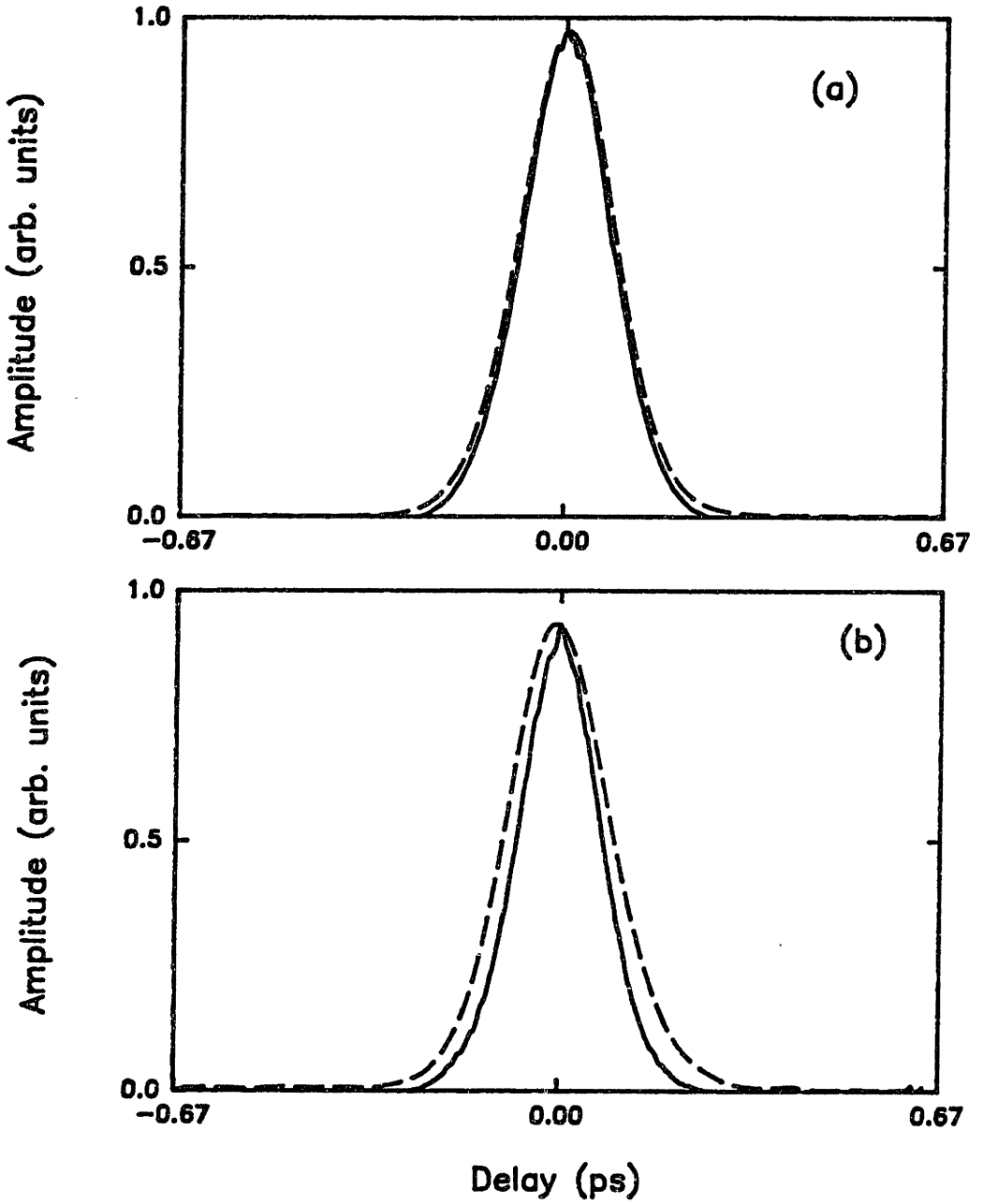

Figure 4.6: (a) Autocorrelation (solid line) of the incident pulse (τ=104 fs) and cross-correlation (dashed line) of the output pulse (τ= 120 fs) after traveling through the optics in the set-up. (b) Autocorrelation (solid line) of the incident pulse and cross-correlation (dashed line) of the pulse (τ=160 fs) after traveling through the optics described in (a) and the MQW diode.

the input pulse with a square pulse of duration equal to the single-pass walk-off. In our diodes, there is a pump-probe walk-off of approximately 100 fs. For the pulses used in our experiment, the effective pulse broadening due to walk-off is less than 10 % [107]. Larger relative changes in effective pulsewidth are expected for longer diodes and shorter pump-probe pulses.

Finally, we point out that this pulse echo technique is perfectly general and can be used on any waveguide sample. For example, we have measured the GVD of passive waveguide samples cleaved from a monolithic extended cavity laser [108]. Figure 4.7 shows the cross-correlation of the output pulse train when the laser center wavelength was 1.492 μm (solid line) and 1.530 μm (dashed line). The echo spacing was very close because the waveguide samples were short, L=130 μm. Also, only a few echoes were visible, probably because the signal was attenuated by loss in the waveguide. On this timescale, there was no measurable wavelength dependence of the echo spacing. Comparing autocorrelation traces with cross-correlation traces of the second and third echo pulses, also shows no measurable effects of GVD on pulses in such a short sample (Figure 4.8). In order to see the effects of GVD on pulses in these waveguides, we had to study pulse broadening in longer devices.

Figure 4.9 shows a schematic of the waveguide we have measured. The device consists of a 1.03 cm long 1.3 μm quaternary layer, passive waveguide segment, sandwiched between two 650 μm MQW InGaAs/InGaAsP active regions. The MQW active regions are similar to those measured and described in the previous section of this chapter. Pulse echo experiments were not performed on this diode because of the large echo spacing ($\sim$ 7 cm) compared to the travel of the Klinger stepping stage ($\sim$ 10 cm) used to set the delay between the two arms of the autocorrelator. Rather, we characterized the GVD by measuring the pulse broadening in the device. Note that the pulse broadening we measure includes that due to the active as well as the passive waveguide sections. Figure 4.10 shows the autocorrelation (solid line) of the incident pulse and the cross-correlation (dashed line) of the pulse after traveling through the waveguide. The decorrelated pulsewidth of 420 fs suggests that the critical pulsewidth for this diode is τ_c= 260 fs. This value yields $-\lambda\frac{d^2n_{eff}}{d\lambda^2}$= $-$0.6 μm^{-1}. Thus, the GVD in this device is comparable to that measured for the diode lasers we described previously. Note that this value of GVD is consistent with the fact that we observed no pulse broadening even after

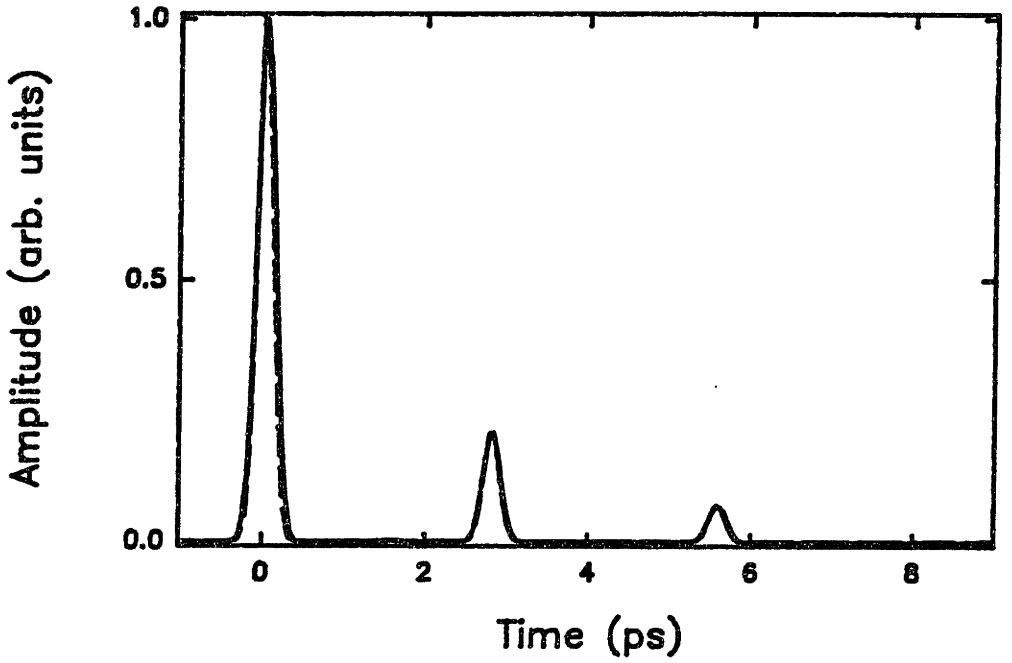

Figure 4.7: Cross-correlation of the output pulse train from a passive waveguide segment for input pulses with center wavelengths of 1.492 μm (solid line) and 1.530 μm (dashed line). The pulses are TE-polarized. The waveguide length is 130 μm.

2.5 round-trips in the 130 μm long device (Figure 4.8). The calculated critical pulsewidth for a 650 μm device (5 trips through a 130 μm long sample) is τ_c= 65 fs. If the input pulsewidth was 180 fs, the output pulsewidth should have been 181.5 fs, a negligible difference.

4.3 Discussion

To compare our results to theory, we performed a simple numerical calculation of the GVD for a waveguide structure using well-known expressions [109]. Using the formalism outlined in Reference [109], the total dispersion for the structure is expressed as the sum of the material dispersion, the waveguide dispersion, the composite profile dispersion, and a remainder term. The remainder term includes all the terms in the expression for the total dispersion that could not be clearly and singularly identified with one of the other three types of dispersion. For the sake of discussion, and to compare the relative importance of the different types of

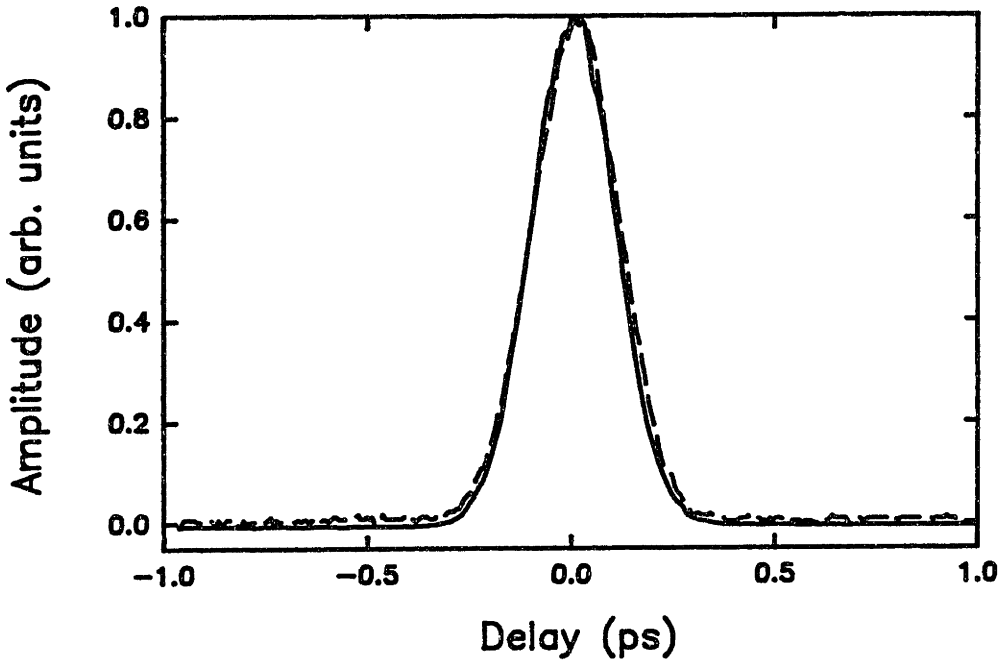

Figure 4.8: Autocorrelation (solid line) of the input pulse and cross-correlation (dashed line) of the second echo pulse shown in Figure 4.7. The second echo has traveled through the diode 5 times, ($\sim$ 650 μm), and has experienced no measurable broadening.

dispersion, we give the expressions for these separate dispersion terms. However, the numerical calculation solves the equation for the total dispersion. Also, we assumed that the geometrical parameters of the structures [44] [71] justified the use of the effective index method in calculating the dispersion for the waveguide. This assumption allowed us to model the devices as symmetric, one-dimensional waveguides [98]. This approximation was reasonable because of the large aspect ratio of the core region. The analysis for the bulk versus the MQW device differed in the assumed values for the active region thickness. Also, an effective material dispersion in the MQW waveguide was calculated by considering the quantum wells, the confinement layer, and the cladding layer separately. The dispersion in these different regions was weighted according to width, and averaged, and this weighted material dispersion was used to describe the core region [107].

The material dispersion was calculated using semi-empirical expressions for the wavelength dependence of the refractive index of InGaAsP alloys [109] [110]. These calculated values were then assumed to contribute to the net material dispersion

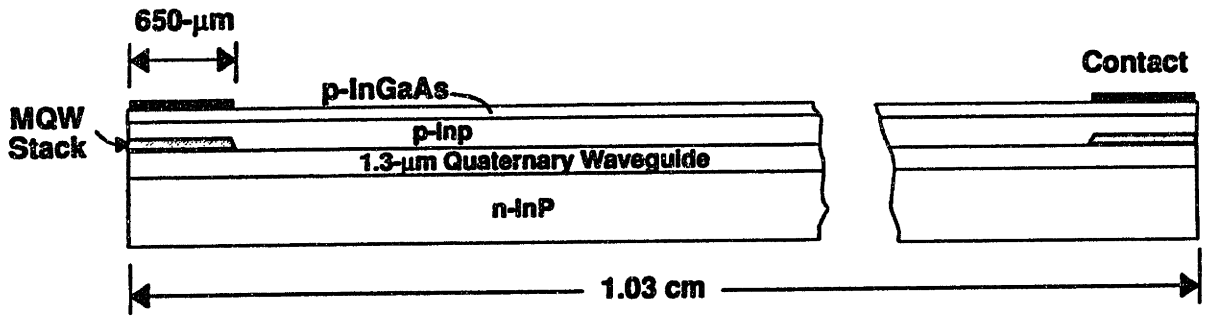

Figure 4.9: Schematic of the monolithic extended cavity laser.

according to

$$-\lambda(d^2 n_{eff}/d\lambda^2)_{mat} = \lambda(\Gamma\frac{d^2 n_1}{d\lambda^2} + (1-\Gamma)\frac{d^2 n_2}{d\lambda^2}) \tag{4.15}$$

where n_1 is the refractive index of the core, n_2 is the refractive index of the cladding, and Γ is the power confinement factor. This so-called composite material dispersion is a weighted average of the material dispersion coefficients of the core and cladding materials. The weighting is determined by the proportion of the optical power carrier in each region. The material dispersion of each region is determined by the wavelength dependence of the refractive index. In this formalism, the waveguide dispersion, which depends on the average index difference between the core and the cladding, and the core diameter, is given by

$$-\lambda(d^2 n_{eff}/d\lambda^2)_{wg} = \frac{{m_1}^2\Delta}{\lambda n_{eff}} v\frac{d^2(bv)}{dv^2} \tag{4.16}$$

where m_1 is the core group index, Δ is the relative index difference between core and cladding, v is the normalized frequency and b is the normalized propagation

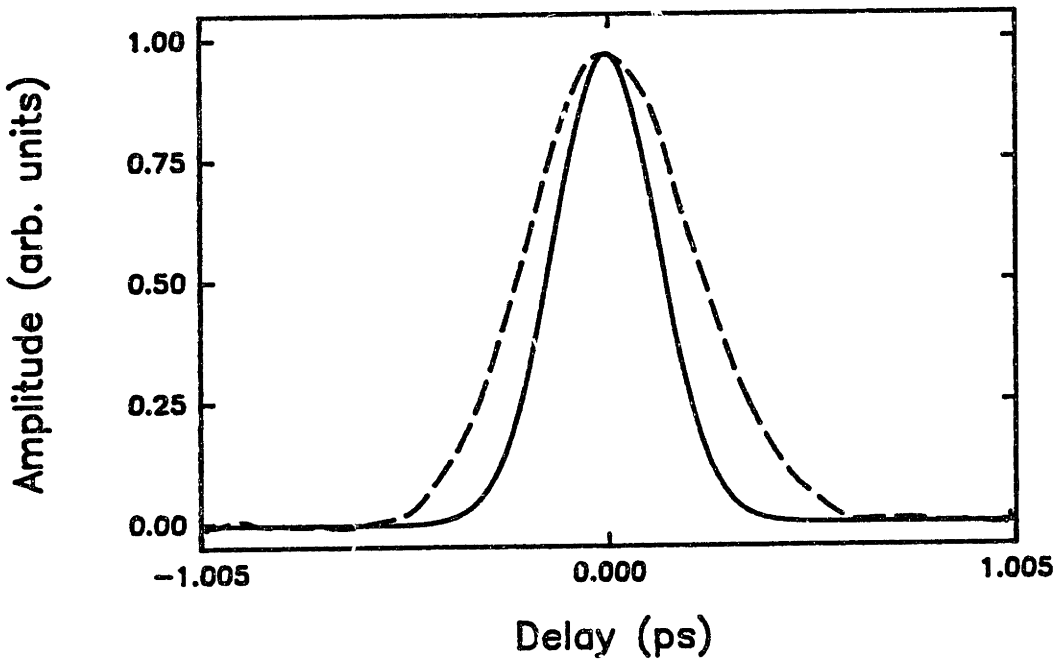

Figure 4.10: Autocorrelation (solid line) and cross-correlation (dashed line) traces of the pulses before and after traveling through the diode. The input pulsewidth is 180 fs and the decorrelated output pulsewidth is 420 fs.

constant. Note that all the terms that depend on Δ, the relative index difference, are grouped into this waveguide dispersion term. Defining the waveguide dispersion in this manner neglects the importance of the terms that result from the wavelength dependence of the relative index difference, Δ'. These terms are grouped in the composite profile dispersion term. It is called composite profile dispersion because it depends on the index profile of the core and cladding regions and it is given by

$$-\lambda(d^2 n_{eff}/d\lambda^2)_{cpd} = \frac{{n_1}^2\Delta'}{n_{eff}}\left(\frac{\lambda\Delta'}{4\Delta} - \frac{m_1}{n_1}\right)[2(\Gamma - b) + v\frac{d^2(bv)}{dv^2}] \qquad (4.17)$$

where $\Delta' = d\Delta/d\lambda$. In a less explicit formalism, the GVD_{wg} and the GVD_{cpd} together would be referred to as waveguide dispersion. Finally, there is the contribution referred to as the remainder term, which is a consequence of writing the total dispersion as a sum of components [109]

$$\mathrm{GVD}_{total} = \mathrm{GVD}_{mat} + \mathrm{GVD}_{wg} + \mathrm{GVD}_{cpd} + \mathrm{GVD}_{r}. \tag{4.18}$$

As we pointed out previously, this remainder term is made up of terms that could not be easily categorized and included in any of the previous expressions and is given by

$$\mathrm{GVD}_{r} = -\lambda(d^2 n_{eff}/d\lambda^2)_{r} = -\frac{1}{\lambda n_{eff}}[{m_1}^2 2\Delta(\Gamma - b) - {n_g}^2 + {m_1}^2\Gamma + {m_2}^2(1-\Gamma)]. \tag{4.19}$$

The details of these expressions are explained in [109] and will not be repeated here.

The calculations yielded a total GVD ($-\lambda\frac{d^2 n_{eff}}{d\lambda^2}$) of $-0.46\ \mu\mathrm{m}^{-1}$ for the TE polarization and $-0.47\ \mu\mathrm{m}^{-1}$ for the TM polarization for the bulk laser. In these calculations we assumed that $\Gamma_{TE} \approx \Gamma_{TM} \approx 0.3$ and that the active region thickness was 0.2 μm. The power confinement factor for the two polarizations is not the same, but the calculation is only very weakly dependent on Γ, so the approximation that $\Gamma_{TE} \approx \Gamma_{TM}$ is a good one. It is interesting to note that the calculated GVD is due largely to the material dispersion. As an example, for the bulk diode with pulses TE polarized, the GVD_r term ($-0.02\ \mu\mathrm{m}^{-1}$) was small enough to be neglected and the GVD_{wg} and GVD_{cpd} terms ($1.63\ \mu\mathrm{m}^{-1}$ and $-1.62\ \mu\mathrm{m}^{-1}$) were approximately equal in magnitude and opposite in sign. If material dispersion is the dominant contribution to the total dispersion, then it is reasonable to assume that the GVD should be similar for bulk and MQW devices. For the MQW device, we assume the active region thickness is 0.3 μm [44] and calculate a weighted GVD as described previously. In this case, we obtain GVD values of $-0.516\ \mu\mathrm{m}^{-1}$ and $-0.521\ \mu\mathrm{m}^{-1}$ for the TE and TM polarizations respectively. The agreement between experiment and theory is quite good considering the rough approximations made by the model. Note that the theory predicts that the GVD for the TM mode will be slightly higher than for the TE mode, and that the GVD for the MQW device will be slightly higher than for the bulk device. The theory can also be checked by the round-trip transit time it predicts for the different polarizations. In the case of the bulk diode, the theory predicts that the TE and TM round-trip transit times are 10.6 ps and 10.5 ps respectively. These values are within 10%

of the measured values. The small discrepancy between experiment and theory may be attributed to the fact that we used a purely one-dimensional model, that we oversimplified the active region structure, or that we did not correct for the carrier induced refractive index change.

In summary, we have used time domain (pulse echo) measurements in the 1.5 μm region of the spectrum to determine the GVD in a bulk and a MQW laser for TE and TM polarizations. Also, we have measured the pulse broadening in a 1 cm monolithic extended cavity laser and computed the GVD. The range of values, $-\lambda\frac{d^2n_{eff}}{d\lambda^2} = -0.60$ to -0.95 μm^{-1}, is in reasonable agreement with previously reported values for diode lasers at other wavelengths [14] [102] [105]. We have computed critical pulsewidths of less than 100 fs for the 475 μm long bulk diode and the 900 μm-long MQW diode, and less than 300 fs for the 1 cm-long monolithic device. These results have been confirmed by cross-correlation measurements. These results give us confidence that the pulses used in our pump-probe experiments are not significantly distorted in the time domain after traveling through the waveguide devices under test. Therefore, the experimentally determined autocorrelation function is a good representation of the optical pulse and can be used in the data fitting procedure outlined in Chapter 5. Finally, we have compared our results with a model of dispersion in a simple one-dimensional waveguide and found good agreement between experiment and theory.

Chapter 5

Cross-Polarized Pump-Probe Measurements

5.1 Introduction

Pump-probe experiments are commonly used to characterize the ultrafast dynamics of materials in the time domain [13]. These experiments have found a wide range of applications because the technique itself is rather simple and requires no high-speed detectors. Instead, accurate relative timing between pump and probe pulses is required. At each pump-probe delay setting, many pulses are averaged on the detector, yielding an average value of the probe pulse transmission. As the delay between pump and probe is varied, new values of average probe transmission are measured. Plotting the measured probe transmission versus pump-probe delay gives a map of the ultrafast gain changes as a function of time.

Figure 5.1 shows a pump-probe arrangement used to study ultrafast relaxation processes in bulk samples. The output from a modelocked laser is split at beamsplitter BS1 into two beams, a strong pump and a weak probe. Here we are assuming that the pump and probe are at the same wavelength. One arm, in this case the pump, contains a precision stepping stage, used to set the time delay between the pump and probe pulses. After traveling path lengths that are separate but nearly equal, the pump and probe are focussed by a lens onto the bulk sample as shown. After the sample, a detector is placed in the path of the probe. Data

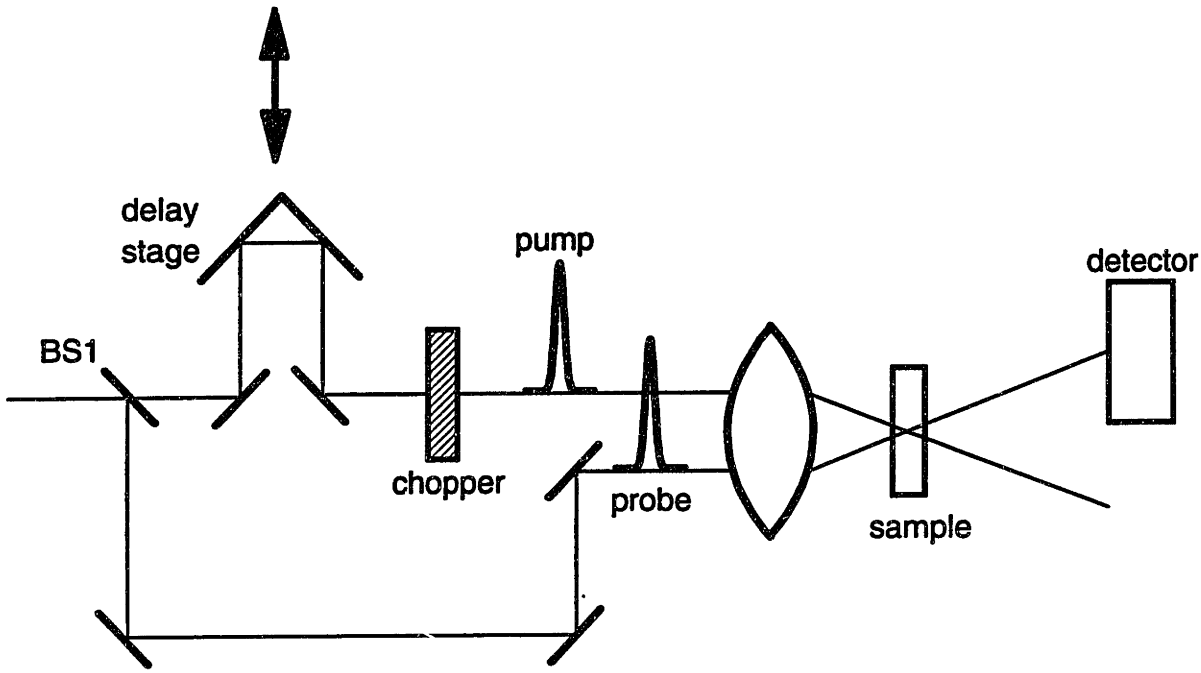

Figure 5.1: Pump-probe set-up with spatially separated beams.

are collected by measuring the probe transmission as a function of pump-probe delay. Note that in this set-up we could also measure the probe reflectance as a function of pump-probe delay [13]. This measurement would yield information about pump-induced refractive index changes in the sample.

The experimental arrangement we have discussed so far is useful for bulk samples and has the advantage that the pump and probe beams are easily distinguishable because they are spatially separated. However, non-collinear beams can not be coupled simultaneously and efficiently to an optical waveguide. Therefore, we must find a way to distinguish between collinear pump and probe beams. Usually, the polarization of one beam is rotated with respect to the other, and a polarizer is placed after the waveguide to select the probe beam for detection. An example of this arrangement is shown in Figure 5.2. The beam from the mode-locked laser is split, at beamsplitter BS1, into a strong pump and a weak probe. The pump arm contains a precision stepping stage, and the probe arm contains a zero-order half-wave plate to rotate the probe polarization by 90° with respect to the pump. A zero-order waveplate is used to minimize pulse broadening. The pump and probe beams are recombined collinearly at the polarization beamsplitting cube (PBS). In our experiments, to increase coupling to the active region

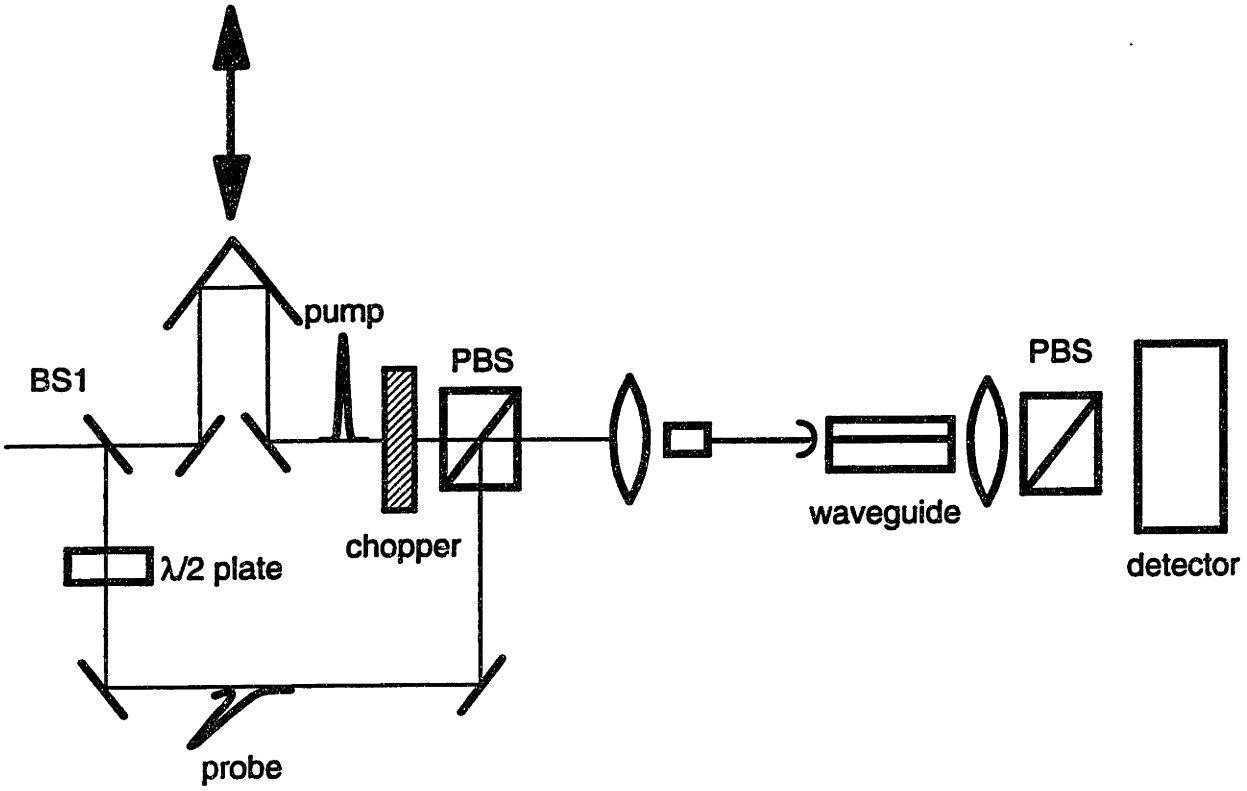

Figure 5.2: Cross-polarized pump-probe set-up for experiments on waveguides.

of the diode, the pump and probe beams are coupled into a short length of dispersion shifted fiber that is terminated with a microlens. The coupling efficiency between the microlensed fiber and the diode active region is approximately 50% and the single-mode fiber insures collinearity of pump and probe beams. There is no measurable pulse broadening in the fiber. A polarizer, placed after the diode, is used to select the probe beam for detection. For all the experiments discussed in this section, unless stated otherwise, the pump beam is TE-polarized and the probe beam is TM-polarized. Also, we will refer to the unstrained, non-quantum well diodes as bulk diodes, even though they are waveguide structures.

In our experiments, the optical signal in the diode is characterized by $S(t)$, the total photon flux. This total photon flux takes the form of a pair of pulses,

$$S(t) = s_{probe}(t) + s_{pump}(t+\tau) = as(t) + s(t+\tau) \tag{5.1}$$

where τ is the delay between the pump and probe pulses, and where we will adopt the convention that the pump pulse is delayed with respect to the probe. The probe intensity is usually much less than the pump intensity, $(0 < a << 1)$. We will show that the measured time-dependent signals are proportional to the

product of the pump and probe pulse intensities. Therefore, a is just a constant scaling factor that we do not bother to carry through.

In its simplest form, the nonlinear change in gain, or the differential gain seen by the second pulse, can be written as

$$\Delta g(t) = \int_{-\infty}^{\infty} h(t-t')S(t')dt' \tag{5.2}$$

where $h(t-t')$ is the response of $\Delta g(t)$ to an impulse of light, and $S(t')$ is the total (pump and probe) photon flux. We point out that the integration, written for analytical convenience from $-\infty$ to ∞, need only be over an interval that is long compared to the response time of the dynamics of interest. Recovery is assumed to be complete between pulse pairs. This change in gain that is induced by the pump-probe pair is also sensed by the pump-probe pair. The induced change in the photon flux, $\Delta S(\tau)$, can be written as

$$\Delta S(\tau) = -\int_{-\infty}^{\infty} [s(t) + s(t+\tau)] \int_{-\infty}^{\infty} h(t-t') [s(t') + s(t'+\tau)] \, dt'dt. \tag{5.3}$$

The change in photon flux is the quantity measured in the pump-probe experiments. However, different pump-probe schemes are sensitive to different components in $\Delta S(\tau)$. We will consider each of the terms in $\Delta S(\tau)$ separately, in order to see which terms contribute to the pump-probe signal that we measure.

Expanding Eq. (5.3), we obtain 4 terms. The first two terms,

$$\int_{-\infty}^{\infty} s(t) \int_{-\infty}^{\infty} h(t-t')s(t')dt'dt \tag{5.4}$$

and

$$\int_{-\infty}^{\infty} s(t+\tau) \int_{-\infty}^{\infty} h(t-t')s(t'+\tau)dt'dt \tag{5.5}$$

represent the signals due to the probe pulse sensing the change in gain caused by the probe, and the pump pulse sensing the change in gain caused by the pump, respectively. Neither of these gain changes depends on the pump-probe delay. Therefore, these signals can only contribute as alterations in the background signal

level. In the case where the pump beam is chopped and lock-in detection is used, the signal represented by Eq. (5.4) is not chopped and not detected. Also, if the pump and probe pulses are distinguishable (e.g. via spatial separation or orthogonal polarizations), the signal represented by Eq. (5.5) can be blocked at the detector. In these kinds of experiments, the measured pump-probe signals are said to be background-free. The remaining terms in the expansion,

$$\int_{-\infty}^{\infty} s(t) \int_{-\infty}^{\infty} h(t-t')s(t'+\tau)dt'dt \tag{5.6}$$

and

$$\int_{-\infty}^{\infty} s(t+\tau) \int_{-\infty}^{\infty} h(t-t')s(t')dt'dt \tag{5.7}$$

represent the signals due to the probe pulse sensing the pump-induced gain change, Eq. (5.6), and the pump pulse sensing the probe-induced gain change Eq. (5.7). Both of these signals depend on τ, the pump-probe delay. In cases where the pump can be blocked at the detector, only the response described by Eq. (5.6) is measured.

In the experiment shown in Figure 5.2, the pump and probe beams are orthogonally polarized and the pump beam is chopped. In this case, the detected signal is given by Eq. (5.6). We use a simple change of variable and show that Eq. (5.6) can be rewritten as

$$\Delta S(\tau) = \int_{-\infty}^{\infty} h(\tau - t)G^{(2)}(t)dt \tag{5.8}$$

where $G^{(2)}(t)$ is the experimentally determined intensity autocorrelation function of the pump-probe pulses. We have written a simple computer program that convolves the measured autocorrelation function with a predicted impulse response function, $h(t)$. We can vary the amplitudes and time constants in the impulse response function to obtain the best fits to the data. One trick in using this simple fitting technique is defining zero pump-probe delay. The zero delay position is not well defined experimentally because the pump and probe pulses travel at different speeds and walk off from each other. An approximate zero delay position can be determined by comparing the pump-induced change in probe transmission

Eq. (5.6) with the probe-induced change in pump transmission Eq. (5.7). These signals are time reversed images of each other. When plotted on the same scale, their intersection gives a good estimate of zero time delay. Finally, real changes in probe transmission can be measured by chopping the probe (rather than the pump) and repeating the experiments described above.

The simple calculation of the photoinduced absorption described above is incomplete because it does not consider the interaction of the pump and probe pulses when they are overlapped in time. When overlapped, the pump and probe interfere and their coherent interaction may affect the measured signals. In that case, the nonlinear change in photon flux, $\Delta S(\tau)$, should contain terms due to the coherent artifact [13]. These terms have been derived in a paper by Vardeny and Tauc [111]. In that paper, the nonlinear changes in probe transmission are related to changes in the third order polarizability and the impulse response function is related to $\chi^{(3)}$, the nonlinear susceptibility. For the case of parallel polarized pump-probe beams, the total change in probe transmission is given by

$$\Delta I_{pr\|} \propto (\gamma_{\|} + \beta_{\|}) \tag{5.9}$$

where

$$\gamma_{\|} = \int dtdt' |s(t-\tau)|^2 h_{xxxx}(t-t') |s(t')|^2 \tag{5.10}$$

and

$$\beta_{\|} = \int dtdt' s^*(t-\tau) s(t) h_{xxxx}(t-t') s^*(t') s(t'-\tau). \tag{5.11}$$

Here, the form of the impulse response function, $h_{xxxx}(t)$, suggests its relation to the appropriate tensor component of the nonlinear susceptibility. Note that for any impulse response function, h_{xxxx}, $\gamma_{\|}(0) = \beta_{\|}(0)$. For orthogonally polarized pump-probe pulses, the total change in probe transmission is proportional to the sum of

$$\gamma_{\perp} = \int dtdt' |s(t-\tau)|^2 h_{xxyy}(t-t') |s(t')|^2 \tag{5.12}$$

and

$$\beta_\perp = \int dt dt' s^*(t-\tau)s(t)h_{xyyz}(t-t')s^*(t')s(t'-\tau). \tag{5.13}$$

Notice that in the case of orthogonally polarized pump-probe beams, $\gamma_\perp$ and $\beta_\perp$ depend on χ_{xxyy} and χ_{xyyz}. Therefore, it is not necessarily true that $\gamma_\perp(0) = \beta_\perp(0)$.

Therefore, in copolarized pump-probe experiments, the nonlinear response is always enhanced by the coherent artifact. The coherent artifact can be removed from the data by subtracting a field autocorrelation function (centered at zero pump-probe delay) with amplitude equal to half the total signal at zero delay. The coherent artifact in cross-polarized data is more complicated because the size of its effect depends on the relation between χ_{xxyy} and χ_{xyyz}. In cross-polarized pump-probe experiments, the interaction of the pump and probe beams causes the total field polarization to change as a function of pump-probe delay. The total field polarization is important because it preferentially excites dipoles with certain momentum vectors. If the dipole dephasing time is fast compared to the optical pulsewidth, then the material has no polarization memory and the coherent artifact is zero [111]. In semiconductor diodes, the dephasing time is assumed to be less than 100 fs [1]. For this reason, the importance of the coherent artifact has often been neglected in cross-polarized pump-probe experiments on semiconductors. This assumption may not be valid for the portion of the cross-polarized signal due to instantaneously recovering effects [112]. In this chapter, we will not consider the possible importance of the coherent artifact in our data. However, in a later chapter (Chapter 7) we will describe how the coherent artifact may be contributing to both copolarized and cross-polarized pump-probe signals.

5.2 Pump-Probe on Waveguides

The waveguides we characterize are active and can be described in three different regimes of operation: absorption, transparency and gain. If the pump energy is greater than the electron-hole quasi-Fermi energy separation, stimulated absorption is more probable than stimulated emission and the diode is operating in the absorption regime. This condition is usually met at low injection currents and short pump-probe wavelengths. Stimulated absorption of the pump creates

electron-hole pairs and increases the carrier density, N. This increase in carrier density persists until the carriers recombine via spontaneous emission. This carrier density change recovers with a time constant of approximately 1 ns [1], the upper state lifetime, τ_s. A probe pulse that travels through the diode after the pump will see a higher carrier density, (because carriers have been added by stimulated absorption of the pump) and experience reduced loss. If the pump energy is less than the electron-hole quasi-Fermi energy separation, then its net effect is to stimulate emission, thereby decreasing the carrier density and the gain experienced by the probe. This condition is normally met at high carrier densities and long pump-probe wavelengths. Since the pump experiences gain, the diode is said to be in the gain regime. However, the probe transmission is lowered if it follows the pump pulse through the diode. The carrier density is replenished by carriers injected by the bias current, on a timescale similar to the upper state lifetime. At the transparency point, the pump energy is equal to the electron-hole quasi-Fermi energy separation. In this case, stimulated emission and stimulated absorption of the pump are equally probable and there is no net pump-induced change in the carrier density. We often call this regime of operation the transparency "point" because unlike the absorption and gain regimes that can be reached by many pump-probe wavelengths and many bias currents, the pump-probe energy equals the electron-hole quasi-Fermi energy separation at only one wavelength for a given bias current (and correspondingly, only one bias current for a given wavelength). The reason the diode is characterized in all three regimes of operation is that information about fast dynamics, occurring near zero time delay, can be gained by knowing whether or not these dynamics have the same sign as the change in transmission due to carrier density changes.

In the impulse response function, $h(t)$, pump-induced carrier density changes are modeled by an exponential term with a time constant of 1 ns. In Figure 5.3, we plot the exponential, $e^{-t/(1ns)}$, on a typical pump-probe time scale, 10 ps. On this short time scale, the exponential does not recover. Therefore, we say that the pump-induced carrier density change causes a "step" change in probe transmission. Mathematically, the unit step function, $u(t)$, is given by

$$u(t-\tau_0) = \begin{cases} 0 & t < \tau_0 \\ 1 & \text{otherwise.} \end{cases} \tag{5.14}$$

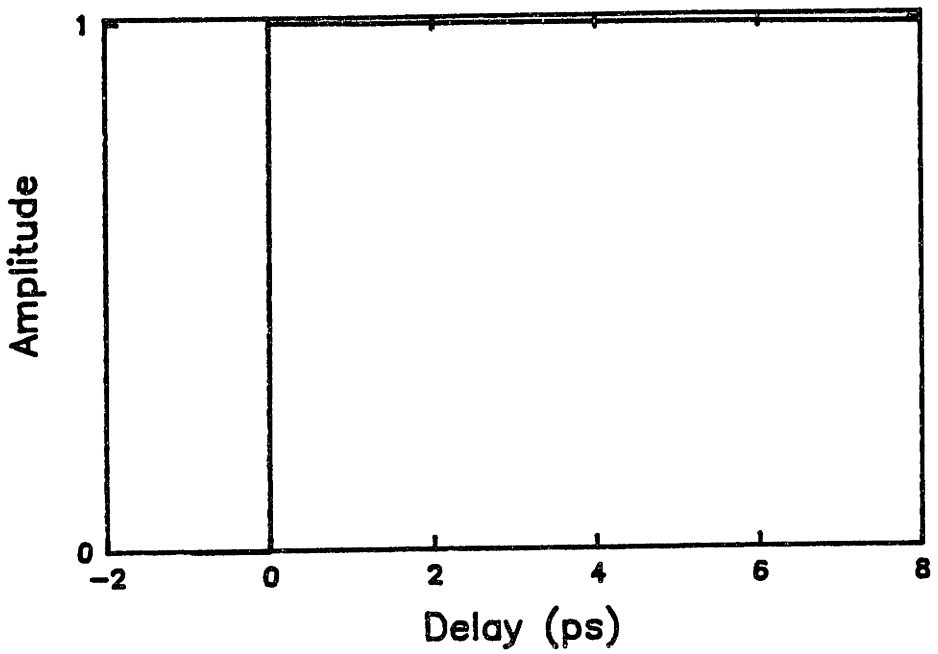

Figure 5.3: The exponential, $e^{-t/1ns}$ as a function of time for a typical pump-probe measurement time scale, 10 ps.

In the data fitting program, this step change in gain is subtracted from the data, and the impulse response function is determined by fitting the ultrafast terms; carrier heating, transient absorption bleaching, and two photon absorption (TPA). Therefore, when we list the impulse response functions used to fit the data in this chapter, they will not contain the term $a_0 u(t)$.

Figure 5.4 shows the diode's gain curve as a function of energy for a carrier density of 1.5×10^{18} cm^{-3}. Note that we can access the three regimes of operation by tuning the pump-probe center wavelength. The three arrows in Figure 5.4 indicate the pump-probe center wavelengths that would access the (a) gain, (b) transparency and (c) absorption regimes. However, the pulsewidth of the APM color center laser is not constant across its tuning range. Therefore, we access the different regimes of operation by changing the bias current to the diode. Changing the bias current changes the steady-state carrier density and the gain seen by the pump and probe pulses. To compensate for these gain changes, we hold the average output power of the pump constant by adjusting a variable attenuator placed before the diode. We have not observed any variation in the measured time constants due to these changes in steady-state carrier density. Figure 5.5

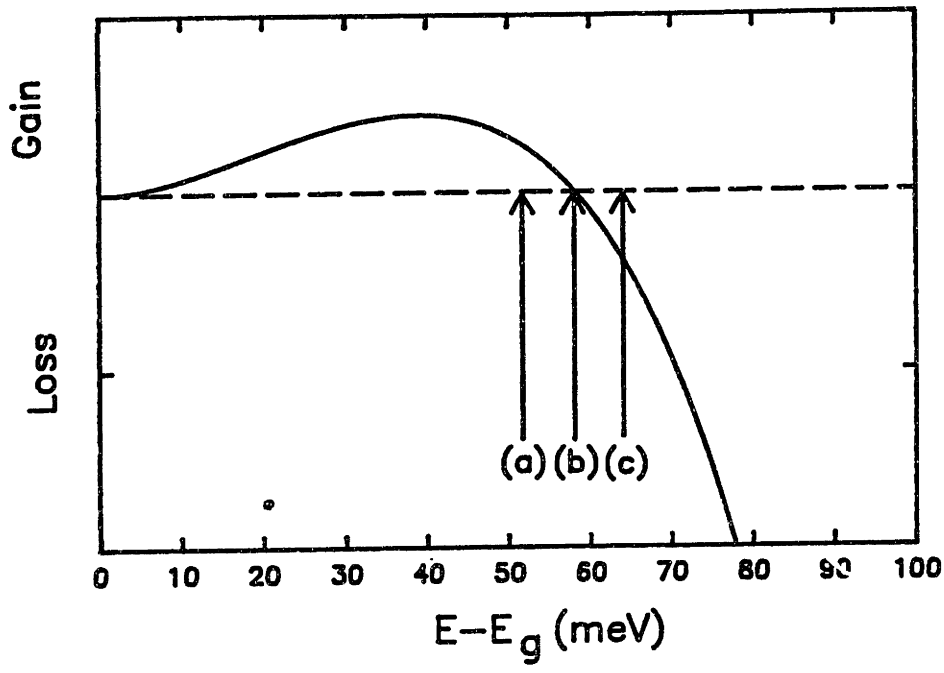

Figure 5.4: Diode gain as a function of energy ($E - E_{gap}$). The 3 arrows indicate the pump-probe wavelength in the (a) gain, (b) transparency and (c) absorption regimes.

shows the diode's gain curve for three applied bias currents (carrier densities). In this calculation, we assume a carrier density at transparency of 1×10^{18} cm^{-3} [1] corresponding to a measured transparency density of 14 mA. Consider a pump-probe center wavelength as indicated by the arrow in Figure 5.4. At bias current I_1 (solid line, 9 mA), there is stimulated absorption of the pump (absorption regime), at I_3 (dotted line, 20 mA) there is stimulated emission caused by the pump (gain regime), and at I_2 (dashed line, 14 mA) there is no carrier density change induced by the pump (transparency regime).

5.2.1 Bulk Diodes

Figure 5.6 (solid lines) shows the measured change in probe transmission as a function of pump-probe delay for the bulk, V-groove diode biased in the three regimes of operation [113] [114]. Keep in mind that the pump and probe are cross-polarized for all the data presented in this chapter. The data are displayed on a time scale that includes negative time delays (probe leads the pump) as well

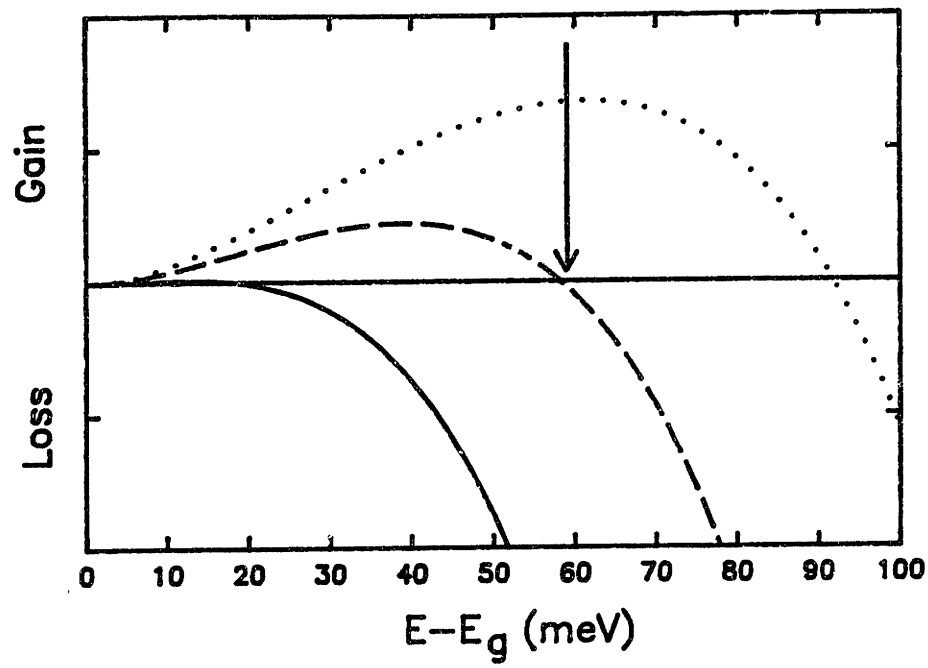

Figure 5.5: Diode gain as a function of energy $(E - E_{gap})$ for 3 bias currents (carrier densities). The arrow shows the pump-probe wavelength.

as positive delays (probe lags the pump). The negative time delays are shown to verify that the system is causal and that there are no strange misalignments in the pump-probe arms that might cause a change in probe transmission in the absence of the pump. In these data, we have varied the bias current to change from the absorption to the gain regime. However, similar results are obtained when the pump-probe wavelength, rather than the bias current, is varied (Figure 5.7 [115] [116]). Notice that for time delays greater than 3 ps, the gain seen by the probe is increased in the absorption regime and decreased in the gain regime. This is the step change in gain due to pump-induced carrier density changes. As expected, in the transparency regime, where stimulated emission and stimulated absorption are equally probable, there is no long-lived change in gain seen by the probe. Notice also, that for each current setting, there is a transient gain compression that recovers with a time constant of approximately 600 fs. Because this dynamic has the same sign in the gain and absorption regimes, and is not zero at the transparency point, it can not be explained by interband transitions alone. Rather, we believe this gain compression is due to a heating of the carrier distribution by stimulated transitions and free carrier absorption. As

was discussed in Chapter 2, heating the carrier distribution reduces the gain in all regimes of diode operation. Another component in the diode's response is observed clearly in the absorption regime. This dynamic, when it is present, acts like an absorption bleaching (transient increase in gain), and recovers with a 100-250 fs time constant. Also, there is an instantaneous gain compression term, present in all three regimes, that we believe is due to two-photon absorption (TPA). This instantaneous gain compression is only weakly dependent on carrier density and wavelength.

The pump-probe data change in both amplitude and shape with variations in current or wavelength [113] [114] [115]. As described previously, we evaluate these changes quantitatively by assuming the diode response can be modeled as an impulse response function consisting of a sum of exponentials with different time constants. The dashed lines in Figure 5.6 show the fits obtained using an impulse response function of the form,

$$h(t) = u(t)[a_1 e^{-t/\tau_1} + a_2 e^{-t/\tau_2}] + a_3\delta(t). \tag{5.15}$$

Here a_1 is the amplitude of the absorption bleaching that recovers with τ_1=200 fs, a_2 is the amplitude of the carrier heating term that recovers with τ_2= 600 fs and $\delta(t)$ models the TPA. All the data shown are fit by keeping τ_1=200 fs and τ_2=600 fs and by varying the a_i's. The impulse response functions that have been used to fit the data are

$$h(t) = 27e^{-t/0.2ps} - 15.5e^{-t/0.6ps} - 1.0\delta(t) \tag{5.16}$$

for the absorption regime,

$$h(t) = 27e^{-t/0.2ps} - 20e^{-t/0.6ps} - 1.0\delta(t) \tag{5.17}$$

for the transparency regime, and

$$h(t) = 29e^{-t/0.2ps} - 25e^{-t/0.6ps} - 1.0\delta(t) \tag{5.18}$$

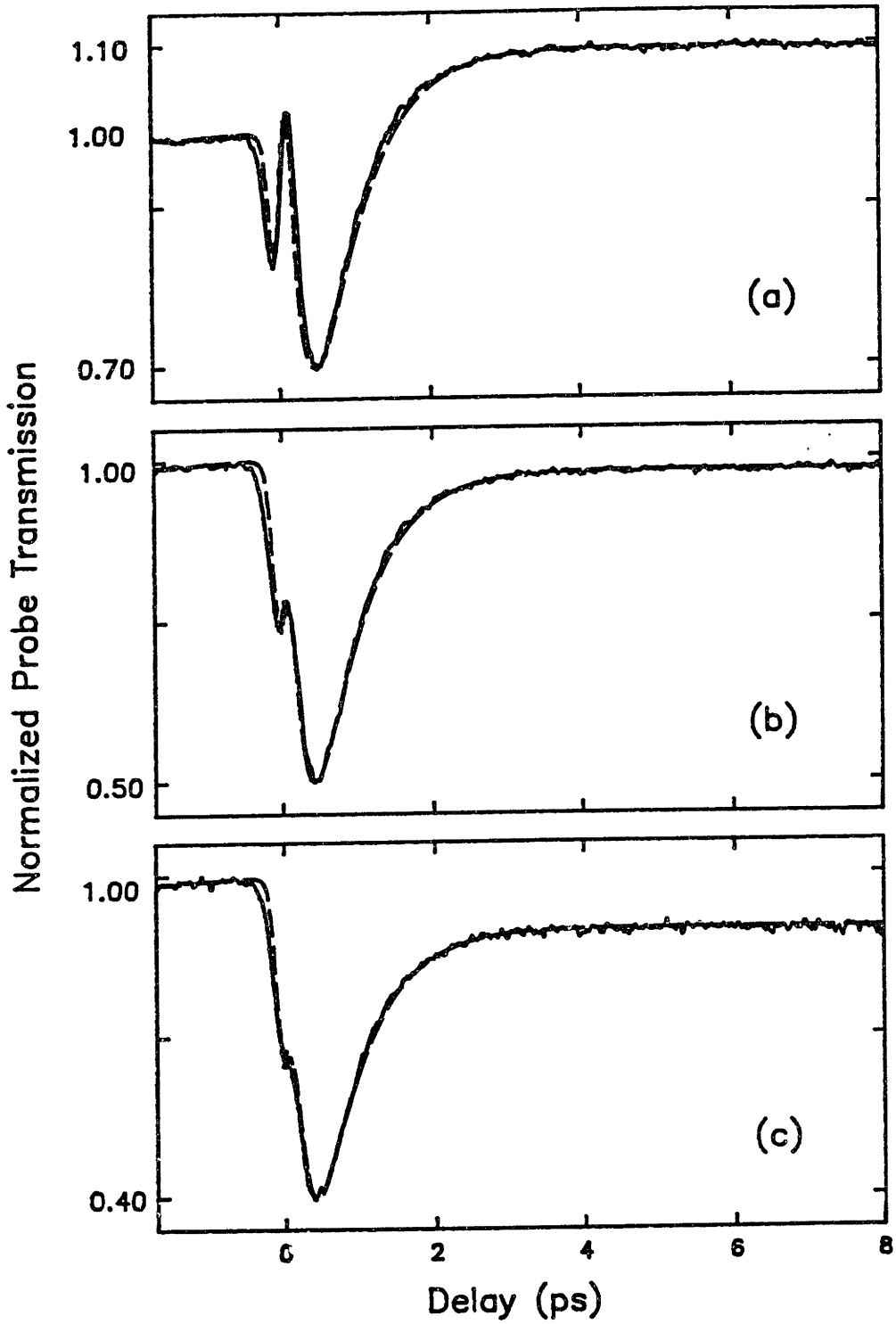

Figure 5.6: Measured change in probe transmission as a function of pump-probe delay for a bulk V-groove diode biased in the three regimes of operation; (a) absorption (I= 12 mA), (b) transparency (I= 14 mA) and (c) gain (I= 16 mA). The pump is TE-polarized and the probe is TM-polarized. The dashed lines show the fits.

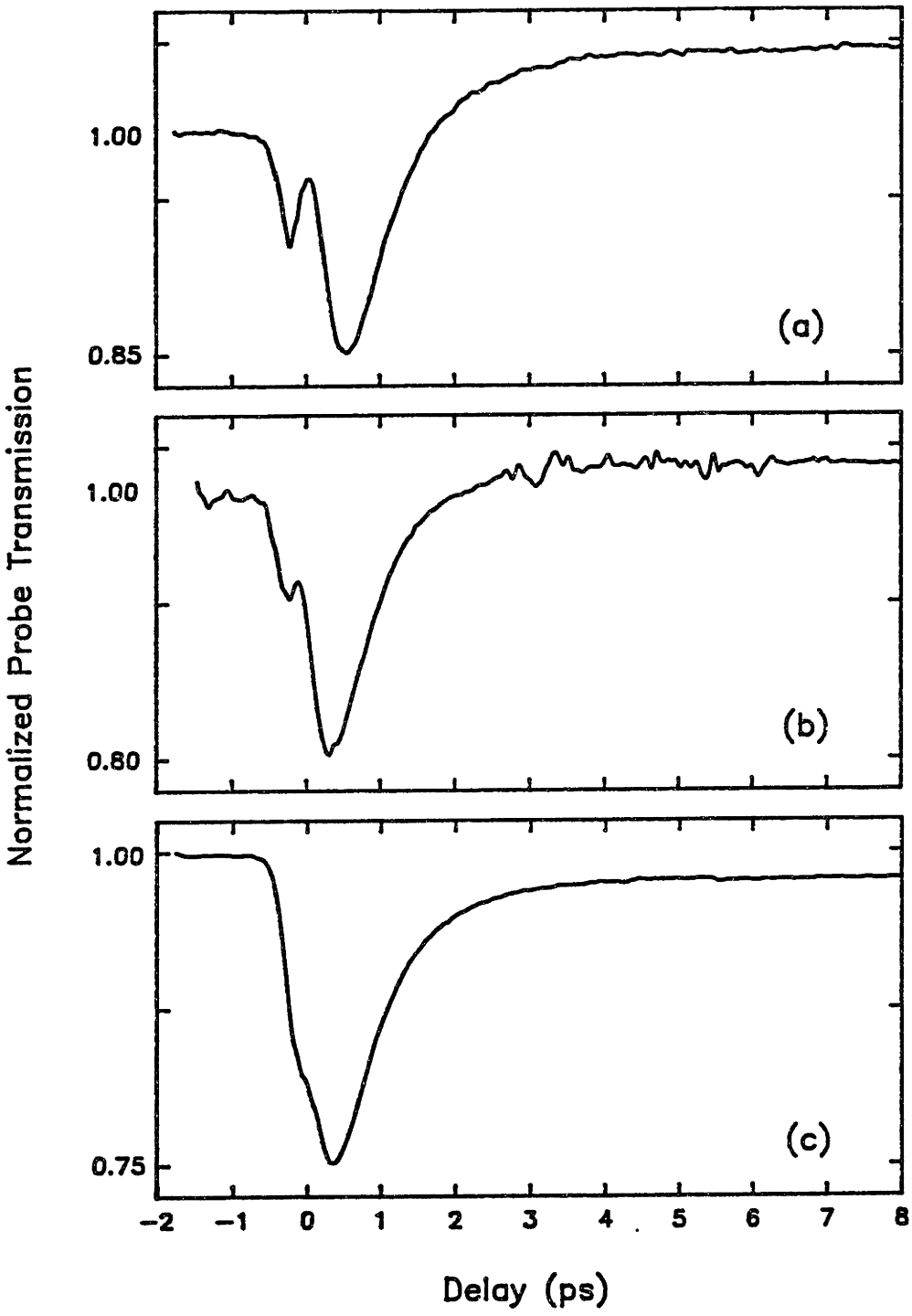

Figure 5.7: Measured change in probe transmission as a function of pump-probe delay for a bulk V-groove diode biased at 10 mA. The pump-probe wavelength is (a) λ=1.490 μm (absorption), (b) λ= 1.495 μm (transparency) and (c) λ=1.50 μm (gain). The pump is TE-polarized and the probe is TM-polarized.

for the gain regime. In Figure 5.8 we show the separate components for the fits of Figure 5.6. Notice that in all three regimes of operation there is a transient absorption bleaching term, but that the amplitude of this term is decreasing, relative to the carrier heating term, as the diode is tuned from the absorption to the gain regime. Also notice that at the transparency point, the carrier heating component and absorption bleaching component have amplitudes that are approximately equal, but opposite in sign. The importance of this behavior will be explained in a later chapter.

The results we have described in this section agree qualitatively with the most recent pump-probe results on AlGaAs diode amplifiers [67]. However, the original results for AlGaAs amplifiers were quite different [11] [12] [60] [67] [117] [118]. In those experiments, no transient absorption bleaching was observed. The biggest difference between the early AlGaAs pump-probe experiments and the more recent ones is the quality of the pump-probe pulses. Recently, experiments have been performed using a modelocked Ti:Sapphire laser that produces 100 fs pulses that are essentially background-free, and nearly transform limited. However, the earlier experiments were performed with pulses that were either longer ($\tau_{FWHM} > 300$ fs) or which contained significant pedestals. We believe that the pump-probe pulse quality was poor enough to obscure faster dynamics that were occurring near zero time delay. The APM color center pulses have always been relatively short ($\tau_{FWHM} < 200$ fs) and nearly transform limited. As a result, all of the reported measurements of gain nonlinearities in InGaAsP diode amplifiers clearly show contributions from TPA and a transient absorption bleaching [42] [113] [114] [115] [116] [119] [120].

5.2.2 Multiple Quantum Well Diodes

Figure 5.9 shows the measured change in probe transmission as a function of pump-probe delay for a MQW diode [72]. The impulse response functions that have been used to fit the data are

$$h(t) = 6.5e^{-t/0.25ps} - 3.7e^{-t/0.7ps} - 1.0\delta(t) \tag{5.19}$$

for the absorption regime,

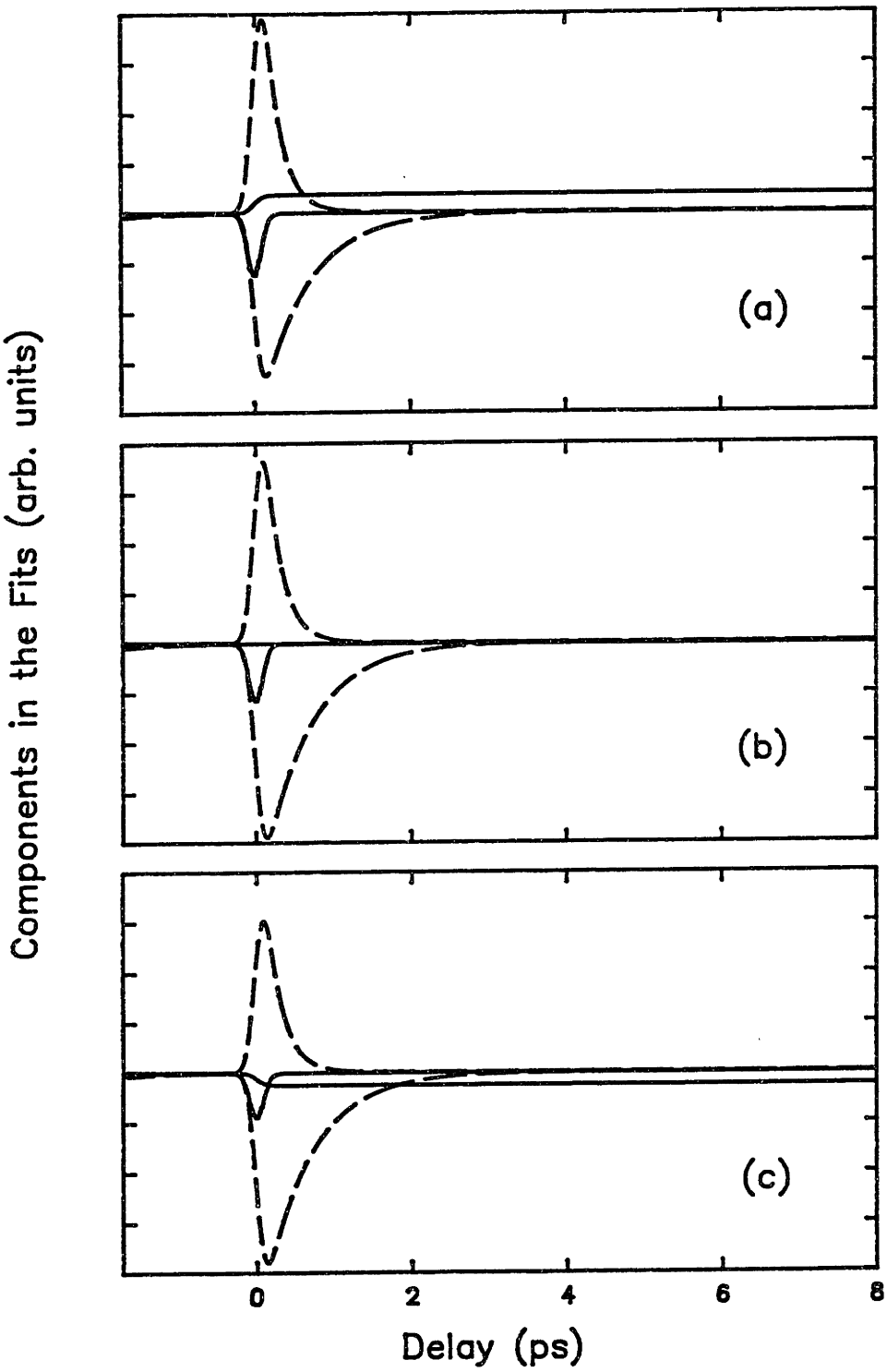

Figure 5.8: Carrier heating, absorption bleaching, step and TPA components separated out from the total fits shown in Figure 5.6. In these plots, the solid lines show the contributions of TPA ($a_3\delta(t)$) and the step change in gain due to stimulated transitions ($a_0u(t)$). The dashed lines show the contributions of the ultrafast absorption bleaching ($a_1e^{-t/\tau_1}u(t)$) and the carrier heating ($a_2e^{-t/\tau_2}u(t)$).

$$h(t) = 5.0e^{-t/0.25ps} - 4.5e^{-t/0.7ps} - 1.0\delta(t) \tag{5.20}$$

for the transparency regime, and

$$h(t) = 3.7e^{-t/0.25ps} - 4.5e^{-t/0.7ps} - 1.0\delta(t) \tag{5.21}$$

for the gain regime. Notice that the instantaneous absorption is a larger percentage of the total signal than it was in the bulk diode. We believe this difference can be explained by the difference in the mode confinement factor for the bulk diode (Γ =0.3) [1] and the MQW diode (Γ=0.05) [72]. TPA is a dynamic that is present in the cladding layer as well as the active layer of the diode. Therefore, TPA happens across the entire spatial mode of the pump-probe field. Gain dynamics, like carrier heating and absorption bleaching, are expected to occur only in the active layer of the diode. A smaller mode confinement factor means that the ratio of the signals due to active layer effects to the signals due to effects happening across the entire spatial extent of the mode is small compared to this same ratio in a diode with a larger mode confinement factor. Relative to the active region signal, TPA is a larger portion of the total response in the MQW diodes than in the bulk diodes but the TPA absorption coefficient, β, calculated in both cases is comparable (20 cm/GW).

Qualitatively, however, the data for the MQW amplifier are the same as for the bulk amplifier. Each regime, absorption, transparency, and gain, is characterized by the step change in transmission. In each regime we observe a fast gain compression, due to carrier heating, that recovers with a 700 fs time constant. Also, in all three regimes there is an absorption bleaching that recovers with a 250 fs time constant. Finally, TPA is present in all regimes of operation.

The similarities in the responses for the bulk and the MQW amplifiers suggest that the complicated dynamics are somewhat independent of the diode structure. The relative amplitudes of the different components in the response may be structure-dependent, but qualitatively, both structures show nonlinearities due to carrier heating, TPA and absorption bleaching. The polarization selection rules discussed in Chapter 2 have negligible effects on our pump-probe results because the heavy hole-light hole energy separation is rather small. Therefore the

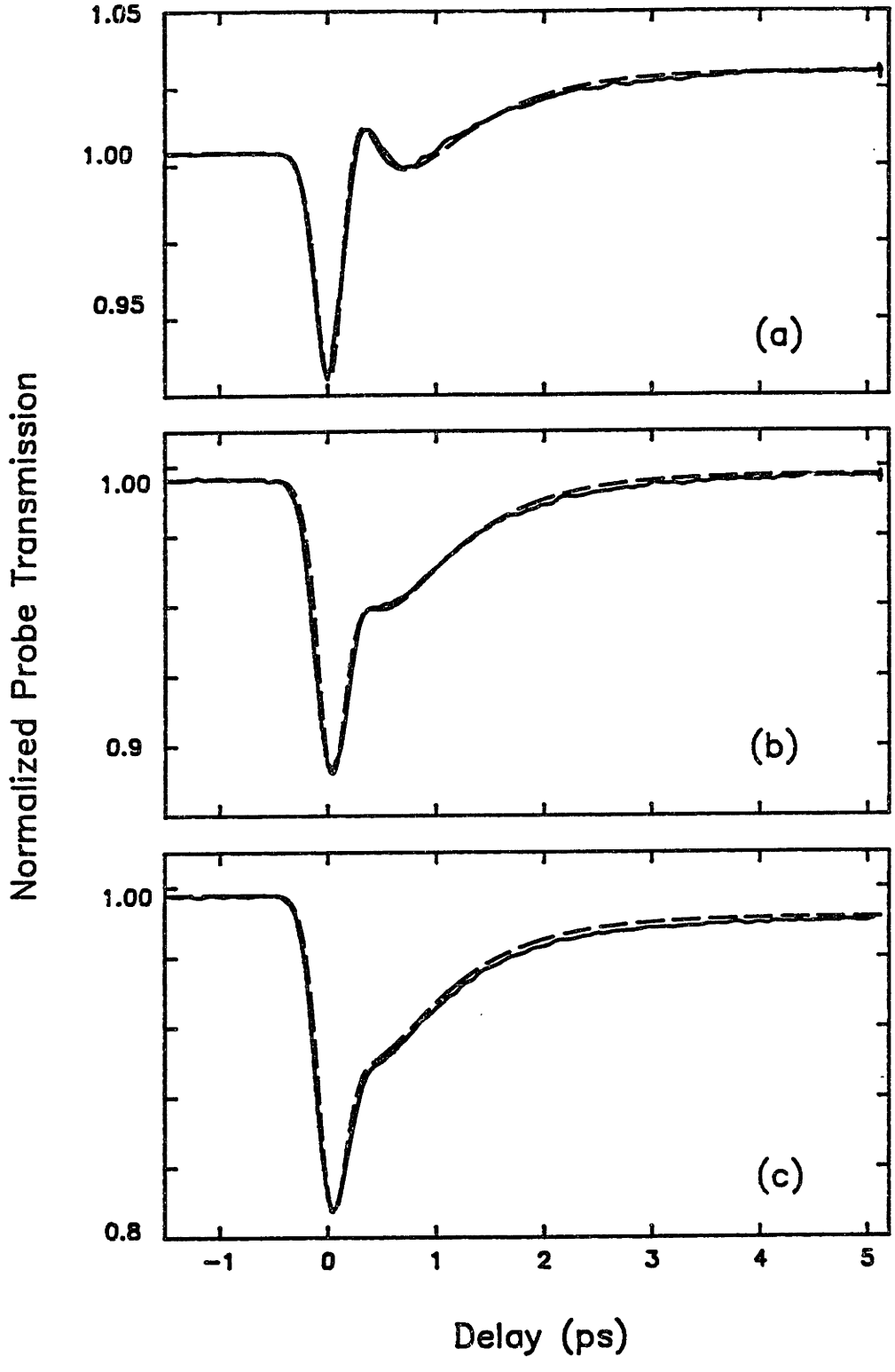

Figure 5.9: Measured change in probe transmission as a function of pump-probe delay for an MQW diode biased in the three regimes of operation; (a) absorption (I= 6 mA), (b) transparency (I= 11 mA) and (c) gain (I = 20 mA). The pump is TE-polarized and the probe is TM-polarized.

pump-probe pulse energy bandwidths are large enough to access both the heavy hole-electron and light hole-electron transitions and the gain appears isotropic. As we will see in a later chapter, the polarization selection rules are very important in MQW diodes with larger heavy hole-light hole energy separations.

5.3 Bias Lead Monitoring

The qualitative similarity between the pump-probe results for bulk and multiple quantum well (MQW) diodes suggests that the measured nonlinearities are not structure-dependent, but are material properties, characteristic of the InGaAs/InGaAsP active regions. To eliminate the possibility of any anomaly in the optical measurement, we have performed pump-probe experiments on these diodes using the diode amplifier to measure its own response [121]. In this experiment, we monitor the pump-induced dynamics by measuring the voltage changes across the active region of the diode as a function of pump-probe delay.

The signals generated in these experiments differ from those in previous pump-probe experiments because we can not distinguish between the orthogonal polarizations. Therefore, we measure both the change in probe transmission due to the pump and the change in pump transmission due to the probe. We assume that the change in the photon flux, described in Section 5.1, is due to a change in carrier density, N. Then, we write the expression for the change in carrier density (population) as

$$\Delta N_t(\tau) = \Delta N(\tau) + \Delta N(-\tau) + \Delta N_0 \tag{5.22}$$

where $\Delta N_t(\tau)$ is the total carrier population change produced by a pulse pair as a function of the pulse pair separation Eq. (5.3). The population change due to stimulated transitions caused by the probe, $s(t)$, in the presence of the nonlinear, time-dependent gain, $\Delta g(t)$, produced by the pump, $s(t+\tau)$, is given by $\Delta N(\tau)$ (defined by Eq. (5.6)). In this formalism, the population change induced by $s(t)$, the probe, and sensed by $s(t+\tau)$, the pump, is $\Delta N(-\tau)$ (Eq. (5.7)). Terms in the response that are independent of pump-probe delay (defined by Eq. (5.4) and Eq. (5.5)) are contained in ΔN_0.

A population change in the active region of the diode causes a voltage change in the electrical measuring circuit [122] [123] [124] [125] [126] [127] [128]. In response to repetitive excitation, the circuit, which responds slowly compared to the diode population dynamics, produces a time-averaged voltage, $\Delta v(\tau)$, that is linearly proportional to $\Delta N(\tau)$. For this reason, the time resolution of the measurement is not limited by device parasitics or details of the detection circuit. Of course the absolute magnitude of the average voltage signal is dependent on device parasitics and the detection circuitry, but we are concerned only with relative voltage changes in our measurements. We will verify experimentally, the linear relation ship between $\Delta N(\tau)$ and $\Delta v(\tau)$.

The experimental set-up is identical to that shown in Figure 5.2 except that the diode is both the device under test and the detector. Figure 5.10 shows the induced junction voltage change as a function of pump-probe delay for various injection current levels. The voltage measurement detects both $\Delta N(\tau)$ and $\Delta N(-\tau)$, and the data are symmetric around zero time delay. Note that in these data, it is difficult to observe clearly the TPA component and the absorption bleaching component of the response. However, all the dynamics measured in previous pump-probe experiments are still represented in these data. For instance, in all three regimes of operation there is a net positive voltage change with a 600 fs recovery time. This time constant agrees with that previously ascribed to carrier heating. In the absorption regime there is a rapid dynamic (absorption bleaching) whose effect is opposite in sign to carrier heating. In the transparency regime, the relative amplitude of this dynamic has decreased but the effect is still evident. Note that the in the symmetrized data, fast dynamics occurring near zero time delay are difficult to quantify.

We can construct predicted curves for the diode voltage measurements by assuming that the diode's gain impulse response, $h(t)$, is that described in the previous section of this chapter, and that $\Delta N(\tau)$ corresponds to the change in probe transmission versus pump-probe delay. This presumes that the signals observed in the optical pump-probe experiments are due to gain changes in the active region of the diode. We obtain $\Delta N(-\tau)$ by reflecting $\Delta N(\tau)$ around the zero delay point (see Section 5.1). Then we add $\Delta N(\tau)$ and $\Delta N(-\tau)$ and the symmetrized sum is compared to the measured traces in Figure 5.10. Figure 5.11 shows the predicted plots of change in junction voltage as a function of pump-

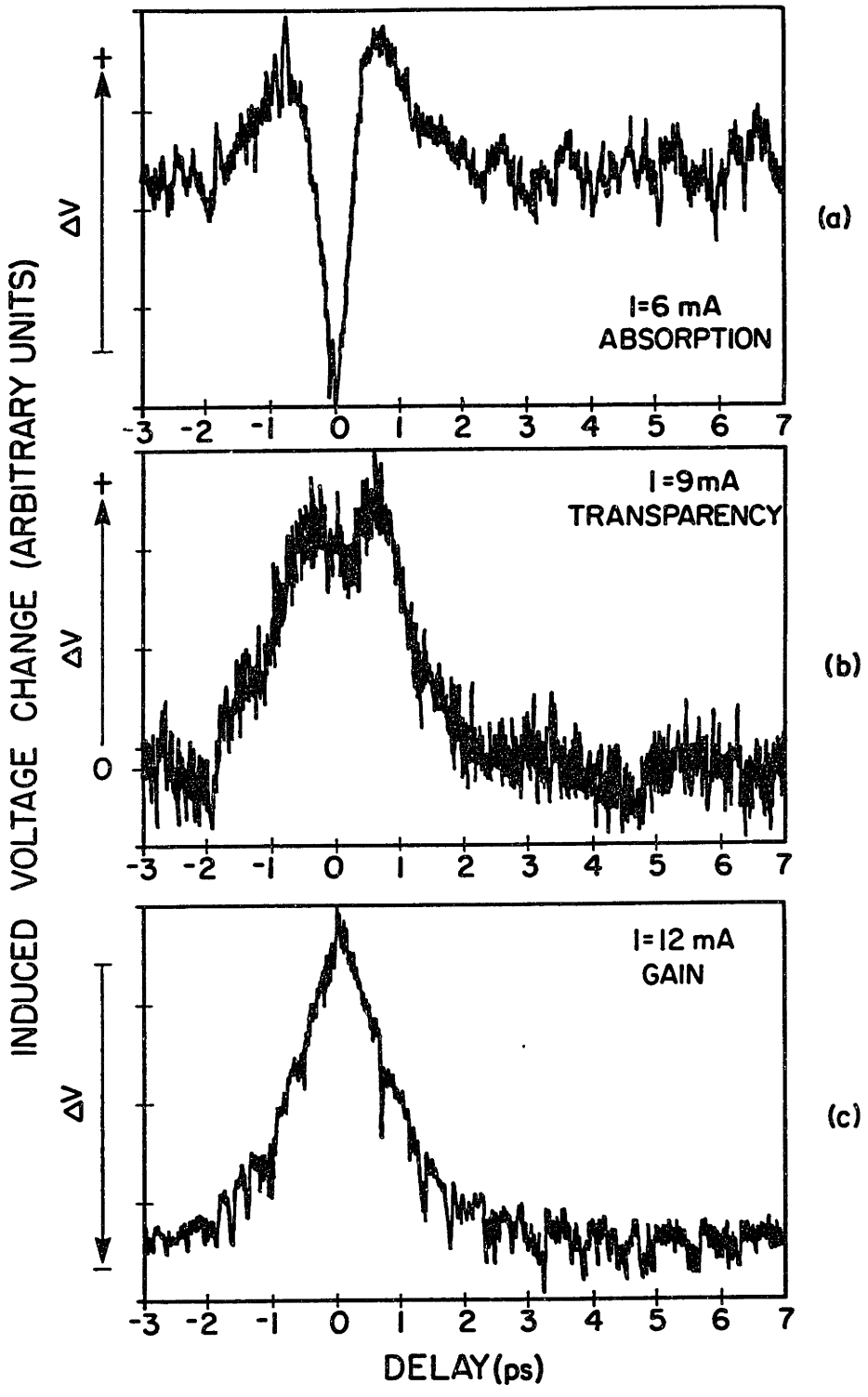

Figure 5.10: Measured change in diode junction voltage as a function of pump-probe delay for the three regimes of operation; (a) absorption (I=6 mA), (b) transparency (I=9 mA) and (c) gain (I= 12 mA).

probe delay in the three regimes of operation. These predictions agree well with the measured plots, indicating that the $h(t)$ deduced from optical pump-probe studies represents nonlinear processes that are characteristic of the active region material and are not sensitive to the diode structure. Note however, that the symmetrized nature of the induced change in diode voltage obscures the fast nonlinearities that were so pronounced in the probe transmission data.

In summary, we have described the importance of the pump-probe technique in measuring ultrafast nonlinearities in active waveguides. We have shown the results of the original time-domain investigations of nonlinearities in bulk and MQW diodes operating at 1.5 μm. In these experiments, orthogonally polarized pump-probe beams are coupled to the active waveguide and a polarizer after the diode is used to select the probe beam for detection. These early experiments suggest that the important contributors to the diodes' nonlinear response are TPA, carrier heating and transient absorption bleaching. To verify that these dynamics are material properties of the active region, (with the exception of TPA which happens across the entire spatial extent of the optical mode), we performed pump-probe experiments where the population changes were measured as changes in diode junction voltage. These experiments yielded symmetrized pump-probe data because the pump and probe were indistinguishable. As a result, fast dynamics happening near zero time delay were obscured.

These experimental results suggest two new areas of study. First, when the diode is biased in the gain regime, TPA and carrier heating (recovering with a subpicosecond time constant) are the dominant nonlinearities. These nonlinearities can be preferentially excited by subpicosecond optical pulses. Therefore, the single-pass gain experienced by a subpicosecond pulse in the amplifier is expected to differ from the single-pass gain experienced by a multipicosecond pulse. Second, our understanding of the nonlinearities is incomplete because we still have no physical explanation for the transient absorption bleaching observed in all three regimes of operation. We will be able to characterize this effect more completely with better time resolution in our experiments. One way to increase the time resolution of these experiments is to eliminate pump-probe pulse walk-off by using co-polarized pump-probe pulses. However, we will need to find some way to distinguish between the pump and probe pulses so that fast dynamics occurring near zero time delay are not obscured. In the next chapter we will study the gain

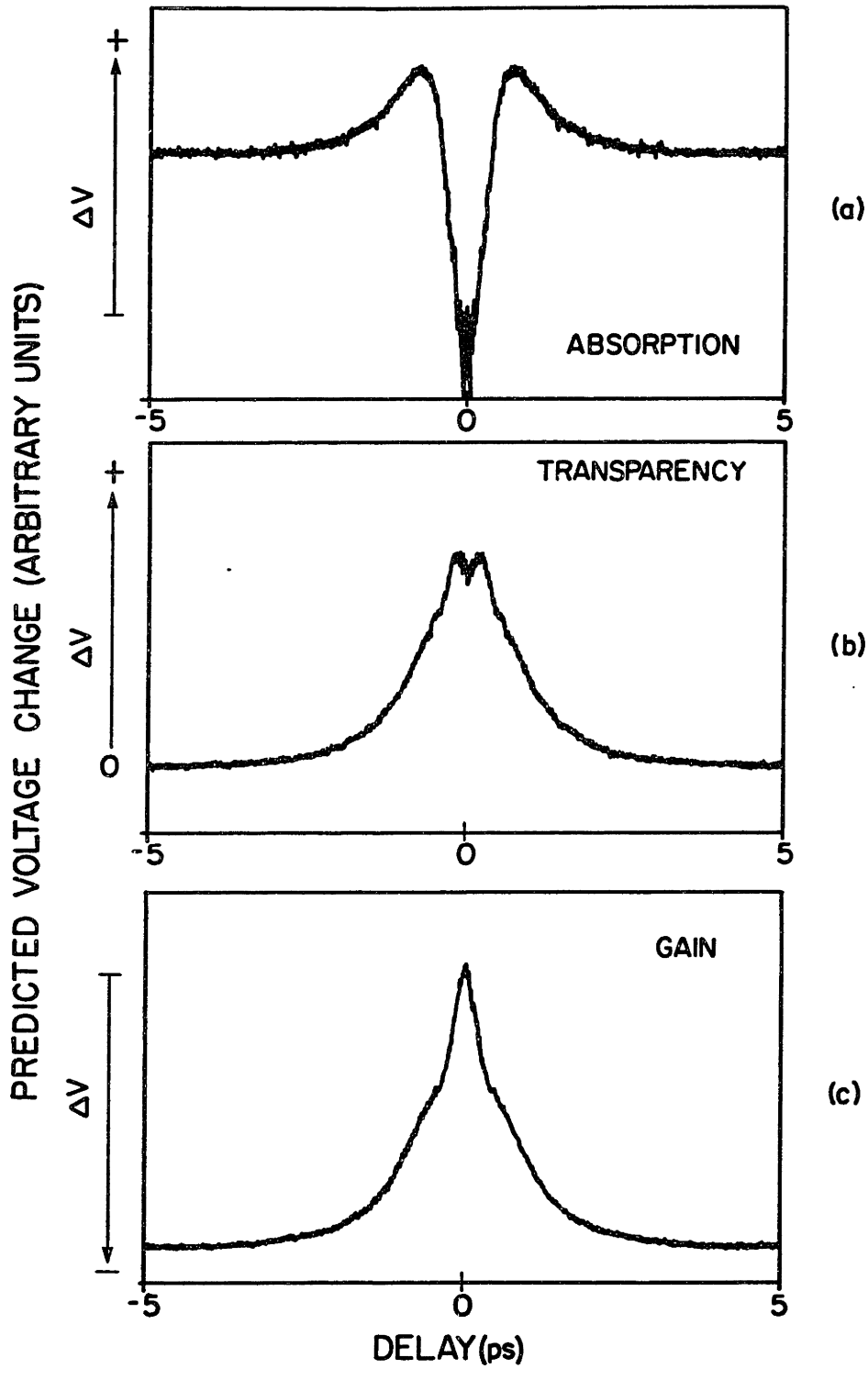

Figure 5.11: Predicted change in diode junction voltage as a function of pump-probe delay for the three regimes of operation; (a) absorption (I=6 mA), (b) transparency (I=9 mA) and (c) gain (I= 12 mA).

saturation behavior for these diodes as a function of input optical pulse width. In the chapter after that, we will describe a novel, heterodyne pump-probe technique that takes advantage of acousto-optic modulator frequency shifting to distinguish between collinear, copolarized pump-probe pulses.

Chapter 6

Short Pulse Gain Saturation

6.1 Introduction

The short pulse amplification properties of semiconductor optical amplifiers are important to the design of future high-speed all-optical networks. As we have discussed in Chapter 5, these amplifiers exhibit large subpicosecond gain nonlinearities. These subpicosecond nonlinearities are expected to influence the gain of femtosecond pulses to a greater extent than they influence the gain of multi-picosecond pulses. In this chapter, we will study the saturation behavior of bulk and multiple quantum well (MQW) optical amplifiers for input pulsewidths of 15 ps and 150 fs. We will show that the measured output saturation intensity is pulsewidth dependent. Also, we will discuss a simple rate equation model based on the pump-probe results that predicts the observed pulsewidth-dependent behavior.

Several groups have studied the amplification of picosecond pulses in InGaAsP optical amplifiers at 1.3 μm and 1.5 μm both experimentally [6] [7] [129] [130] [131] and theoretically [130] [132] [133] [134]. These studies have concentrated on obtaining high output powers and on studying the pulse repetition-rate dependence of the output saturation energy. We will concentrate on comparing the results of saturation measurements for short (150 fs) and long (15 ps) pulses. A similar comparison has been made by Saitoh et al. [131] [133]. Their results suggest

that the output saturation energy depends only on pulse energy (not pulsewidth) and that the effect of carrier heating on pulse energy gain is "negligibly small". However, the short pulses used in their experiments were generated by a mode locked diode laser and had significant pedestals. We believe these authors failed to observe the pulsewidth dependence of the output saturation energy because the broad pedestals made their short pulses (0.49 ps) also, in effect, long pulses (4.4 ps and 21 ps). We will show that the effect of carrier heating on pulse energy gain is significant and can be used to explain the observed pulsewidth dependence of the output saturation energy [42] [119] [120].

6.2 Experiment

The experimental set-up is shown in Figure 6.1. We perform the energy saturation experiments using 15 ps pulses from the synchronously-pumped mode locked color center laser and 150 fs pulses from the same laser in the additive pulse modelocked configuration. The train of pulses from the laser passes through a variable attenuator and is focussed by a microscope objective into a 3 dB coupler made with dispersion-shifted fiber. One output arm of the coupler is terminated with a microlens that is used to achieve high coupling efficiency to the active region of the diode. The other output arm is used to monitor the input power to the diode. By using the two arms of the coupler as the input and the reference, we can normalize out amplitude variations due to drift and beamsteering by the variable attenuator. The coupler arms are short enough, $\sim$ 20 cm, that pulse broadening in the fiber is negligible. After the diode, a microscope objective collects the amplified beam and focusses it onto a detector. We estimate a total coupling loss across the diode of 8 dB. Note that the time between pulses is 10 ns, much longer than the estimated population recovery time of 1 ns in the bulk device [1] and 500 ps in the MQW device [25].

The pulses used in these experiments have negligible pedestals (Figure 3.3). Also, the group velocity dispersion measurements showed that input pulses longer than $\sim$ 100 fs experience no significant change in pulse shape after traveling through the diode, even under conditions of output gain saturation. (We did not study the spectral changes under these conditions.) Figure 6.2 shows the

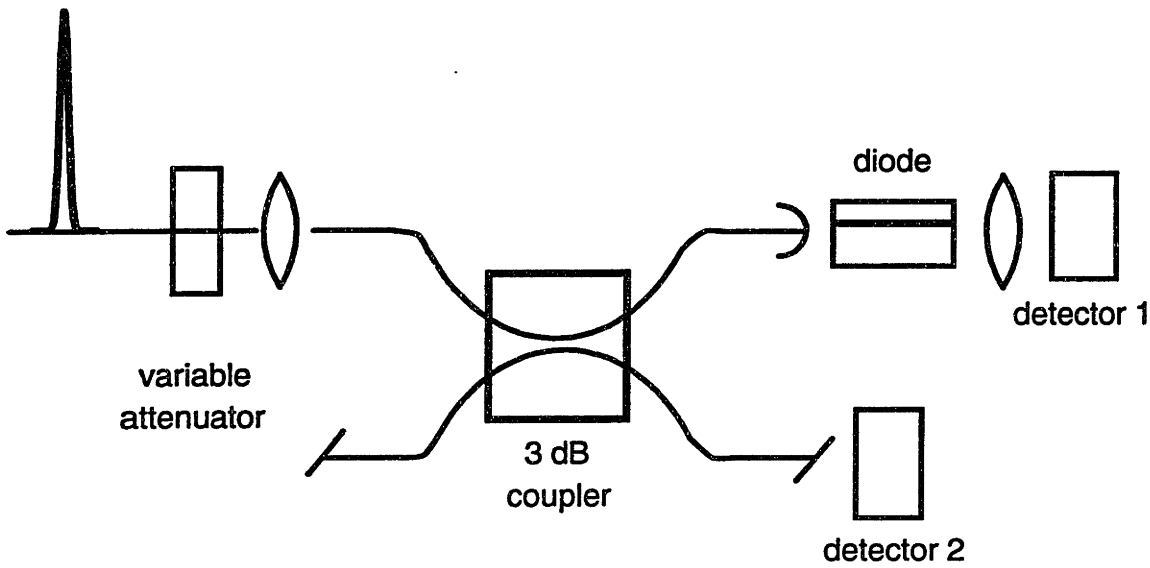

Figure 6.1: Experimental set-up.

amplifier gain as a function of output power for both pulsewidths (150 fs and 15 ps) and for both the (a) bulk, V-groove amplifier and (b) MQW amplifier. The saturation behavior for the long and short pulses is quite different. As expected at low output energies, both pulses experience the same gain. However, at an output energy of 40 fJ, the gain for the 150 fs pulse in the bulk amplifier has decreased by 3 dB while the gain for the 15 ps pulses remains unsaturated. The 15 ps pulses have an output saturation energy of 150 fJ. Likewise, for the MQW amplifier, the 150 fs pulse has an output saturation energy of 200 fJ, compared to 6 pJ for the 15 ps pulse. The output saturation energy is clearly pulsewidth dependent.

Notice that the measured output saturation energies for the MQW amplifier are greater than those for the bulk amplifier. The output saturation energy, E_{3dB}, (for the longer pulses) can be related to the saturation energy [135] [136]

$$E_s = \frac{h\nu A}{g_s \Gamma}, \tag{6.1}$$

via:

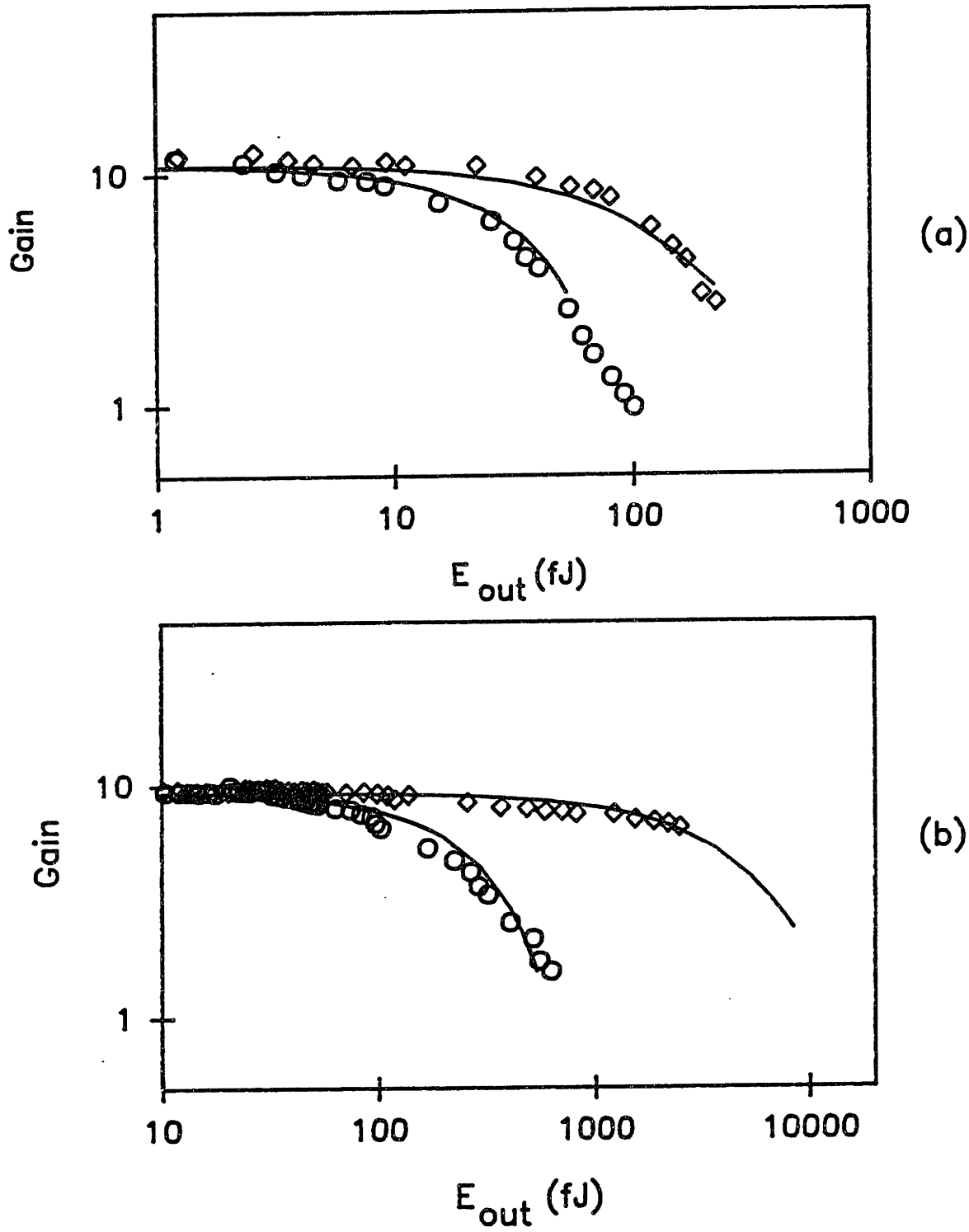

Figure 6.2: Amplifier gain as a function of output energy for pulses with widths of Δt=150 fs (circles) and Δt=15 ps (diamonds). (a) The bulk amplifier bias current was three times threshold and the pulse wavelength was λ=1.515 μm. (b) The MQW amplifier bias was two times threshold and the pulse wavelength was λ= 1.51 μm. The solid lines are theoretical fits obtained from a rate equation model.

$$E_{3dB} = \left[\frac{1.38}{(1+\alpha/g_0)}\right] E_s \tag{6.2}$$

where α is the loss coefficient, g_0 is the small signal gain coefficient, g_s is the differential gain coefficient, Γ is the mode confinement factor and A/Γ is the mode area. The MQW diodes have smaller mode confinement factors but larger differential gain coefficients. Therefore, we might expect similar values for E_s in the two devices. However, α is much smaller in the MQW devices [72], making E_{3dB}(MQW) large compared to E_{3dB}(bulk). We point out that our measured value of E_{3dB}=6 pJ for the MQW device agrees well with a previously measured value of E_{3dB}=5.1 pJ [135]. The output saturation energies for the shorter pulses can be described by similar equations if g_s, the differential gain coefficient, includes the effects of nonlinear gain, $g_s = (g_s + \Delta g)$.

6.3 Discussion

We model the saturation behavior of the diode using rate equations that describe a pulse propagating in a traveling-wave amplifier [137]. These rate equations include the standard expressions for the photon flux and the total carrier density, as well as equations that describe the carrier heating and the transient absorption bleaching observed in the pump-probe results. The effects of carrier heating and absorption bleaching are modeled as other energy levels with time constants that match the experimentally determined recovery times (700 fs for carrier heating and 150 fs for absorption bleaching). The set of rate equations, including the nonlinear effects, can be written as

$$dS/dz = \Gamma[g_s(N - N_t - N_h + N_u) - \alpha_{fc}N]S - \beta S^2, \tag{6.3}$$

$$dN/dt = -g_s(N - N_t - N_h + N_u)S - \frac{N}{\tau_s} + \frac{I}{qV}, \tag{6.4}$$

$$dN_h/dt = \gamma_h \alpha_{fc} NS - \frac{N_h}{\tau_h}, \tag{6.5}$$

$$dN_u/dt = \gamma_u g_s S - \frac{N_u}{\tau_u}. \tag{6.6}$$

Here, S is the photon flux, N is the total carrier density, N_t is the carrier density at transparency, N_h is an effective carrier density change at the emission wavelength caused by carrier heating, N_u is the effective carrier density change caused by the absorption bleaching, Γ is the mode confinement factor, g_s is the differential gain, α_{fc} is the free carrier absorption coefficient, β is an effective two-photon absorption coefficient that depends weakly on N, γ_u determines the relative rate of the absorption bleaching, γ_h represents how efficiently free carrier absorption heats the carrier distribution, τ_s is the upper state lifetime, τ_u is the absorption bleaching time constant and τ_h is the relaxation time of the heated carriers. Carriers are injected into the system via the bias current, I/qV, where I is the applied bias, V is the volume of the active region and q is the electronic charge. We adjust the coefficients of these equations to fit the pump-probe data and then use the model to predict the saturation results.

In the numerical calculations, most of the parameters that are independent of z and t, are taken from the literature. In the case of the bulk diode, we use Γ=0.3, g_s=2.5 $\times$ 10^{-16} cm^2, and N_t=10^{18} cm^{-3} [1]. For the MQW diode, the mode confinement factor is Γ=0.05 [72]. For both diodes, parameters such as τ_h, τ_u, β, α_{fc}, γ_h and γ_u are determined by fitting the pump-probe results. The rate equation model can fit pump-probe data in all three regimes of diode operation, absorption, transparency and gain. We reach the different regimes of diode operation by varying the bias current. These changes in bias current are modeled as changes in the initial value of the carrier density, N, in the numerical fits. Figure 6.3 shows the experimental data and the fit for pump-probe measurements on an unbiased MQW diode. Here, the initial carrier density is zero, and we can determine β, γ_u, and τ_u. The measured recovery time for the transient absorption bleaching is $\sim$ 200 fs.

In fitting the data shown in Figure 6.3, we have assume that the probe intensity is much lower than the pump intensity. We assume an initial value for S and then integrate Eq. (6.4), Eq. (6.5), and Eq. (6.6) with respect to time for a fixed propagation distance, z. This integration yields values for N, N_h, and N_u which are substituted into Eq. (6.3). Then Eq. (6.3) is integrated with respect to z, yielding a new value of S. This process is repeated until z equals the length of the active region. The differential gain in the diode at position z and time t is given by

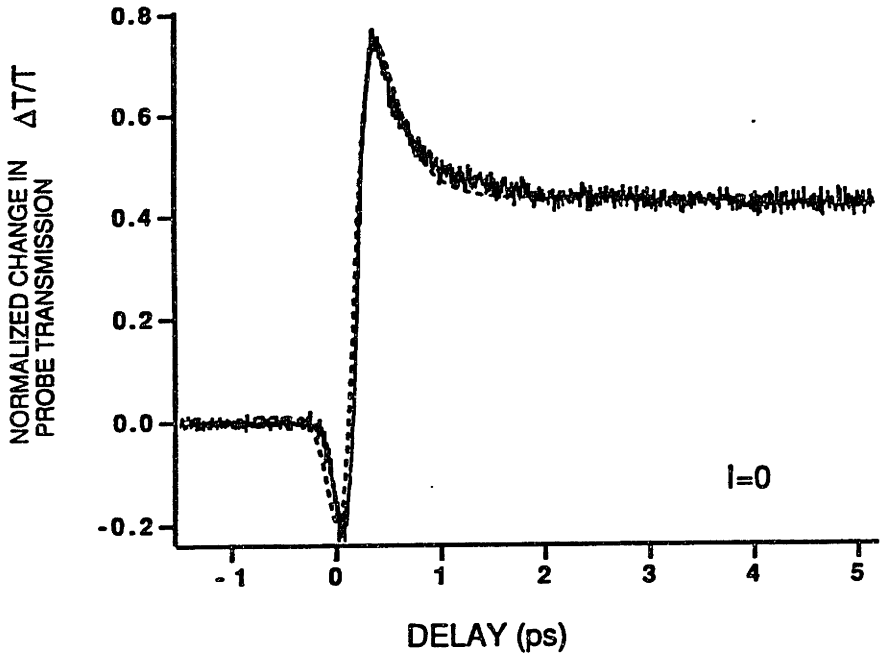

Figure 6.3: Normalized probe transmission (solid line), and fit (dashed line), as a function of pump-probe delay for an unbiased MQW diode. The vertical scale corresponds to a $\sim$ 3 % change in probe transmission.

$$G(t,z) = \Gamma(g_s[N(t,z) - N_t - N_h(t,z) + N_u(t,z)] - \alpha_{fc}N) - \beta S(t,z). \quad (6.7)$$

If we know the differential gain, we can calculate the output probe intensity, $s_o(t-\tau)$, via:

$$s_o(t-\tau) = s_i(t-\tau)e^{(\int_0^{z_0} G(t,z)dz)} \quad (6.8)$$

where $s_i(t-\tau)$ is the input probe intensity and z_0 is the length of the diode, and τ is the delay between the pump and probe pulses. Finally, the gain seen by the probe, which is the quantity we measure, is given by:

$$G_{probe}(\tau) = \frac{\int s_o(t-\tau)dt}{\int s_i(t-\tau)dt}. \quad (6.9)$$

This same fitting procedure is used for pump-probe results with nonzero initial carrier densities. The results of fitting data for the MQW diode in the absorption,

transparency and gain regimes are shown in Figure 6.4. To fit these data, we use $\tau_h = 700$ fs and $\tau_u = 200$ fs. We find that β and γ_u must be adjusted in the different regimes of diode operation to obtain the best possible fits. The fact that these parameters are carrier density dependent suggests that they are not due solely to two-photon absorption and transient absorption bleaching. It is possible, for instance, that some portion of these terms is describing spectral hole burning, a signal whose amplitude should be carrier density dependent. Note that once we have obtained good fits to the pump-probe data, we used exactly those parameters to calculate the saturation energy for the diode.

Figure 6.5 (a) shows the experimental pump-probe results along with the fit for a bulk laser amplifier operating in the gain regime. In this case, the pump-probe pulsewidth is 150 fs. Notice that the gain compression is due mainly to two-photon absorption and carrier heating and that there is little observed transient bleaching of the absorption. However, the absorption bleaching term is still needed to obtain a good fit. If we take the parameters in this fit, and assume an input pump-probe pulsewidth of 15 ps, we obtain the predicted change in probe transmission shown in Figure 6.5 (b). Notice that the ultrafast gain nonlinearities are a significant portion of the 150 fs pulse's gain response, while they are virtually nonexistent in the 15 ps pulse's gain response. We will show that it is these ultrafast nonlinearities that are causing the observed pulsewidth dependence of the gain saturation.

As stated previously, the exact parameters that are used in the rate equation model to fit the pump-probe data in the gain regime are used to calculate the saturation energy for the diode. The only adjustable parameter is N, the initial carrier density. We adjust the initial carrier density to match the observed linear gain. The calculated curves for the output saturation energy are shown as solid lines in Figure 6.2. Notice that the roll-off of the gain curves, as predicted by the theory, is in good agreement with the experiment. These results suggest that carrier heating will play an important role in the amplification of subpicosecond pulses. It is important to note that although the saturated output energy for ultrashort pulses is lower than that for the longer pulses, partial gain recovery following such pulses is very fast ($\sim$ 1 ps). Thus a rapid sequence of ultrashort pulses may be used to extract the same net energy as a long pulse. We also note that the measured output saturation energy should be higher for signal wavelengths

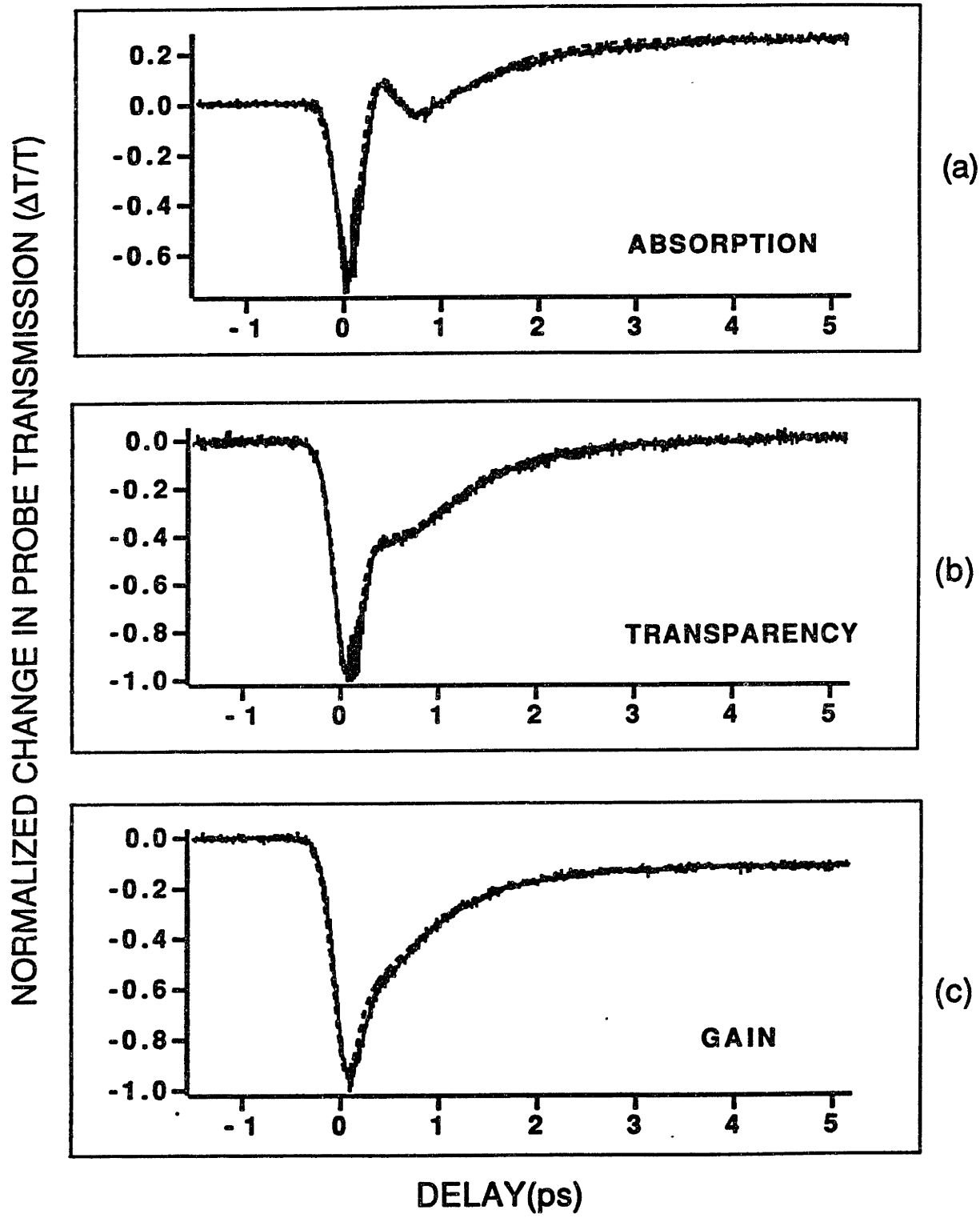

Figure 6.4: Normalized probe transmission (solid lines), along with the fits (dashed line), as a function of pump-probe delay for an MQW diode biased in the (a) absorption, (I = 6 mA), (b) transparency, (I = 10 mA), and (c) gain, (I = 60 mA), regimes. The vertical scale in the gain regime corresponds to a transmission change of $\sim$ 20 %.

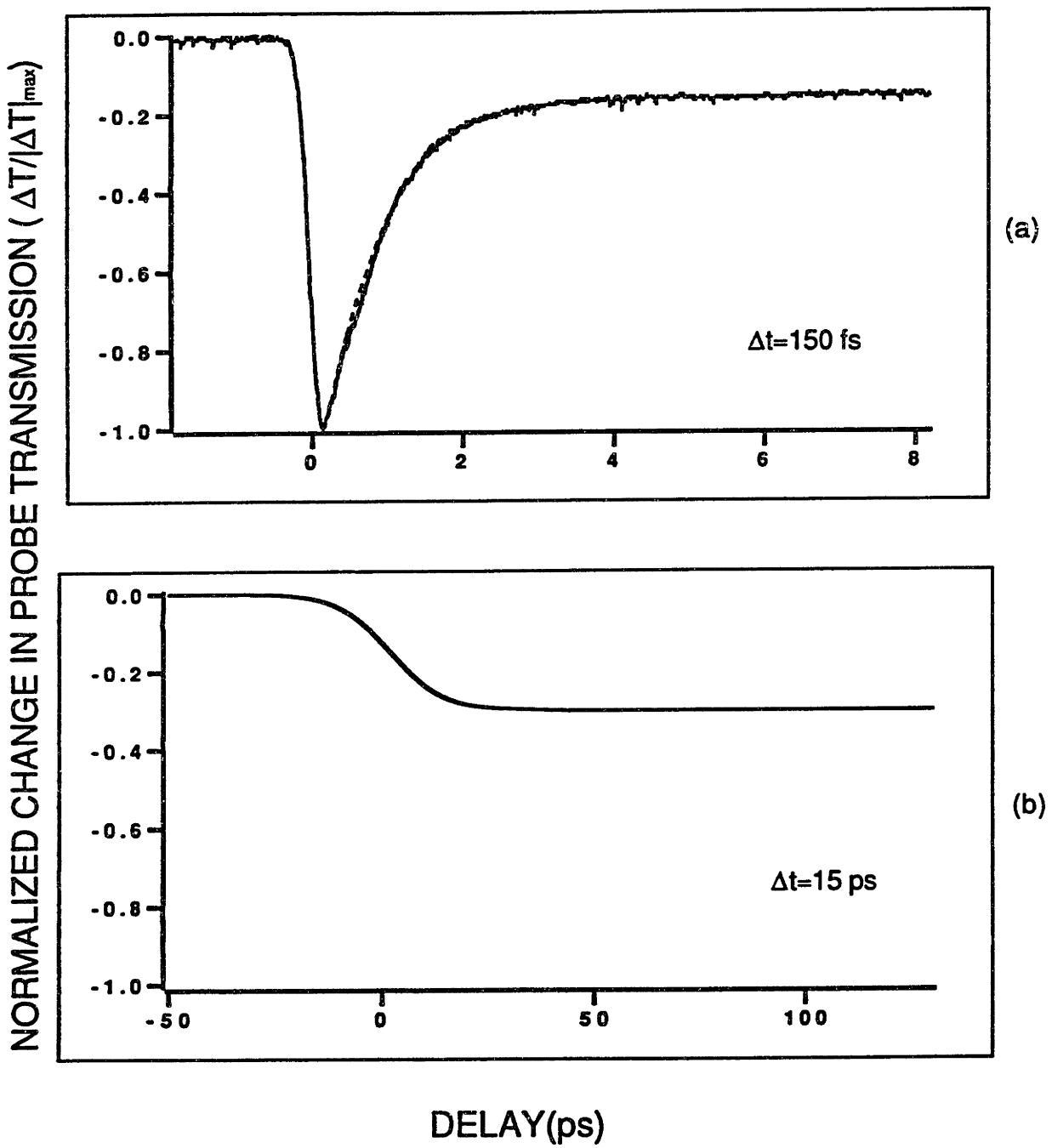

Figure 6.5: (a) Measured (solid line) change in probe transmission as a function of 150 fs-pump-probe delay for a bulk diode biased in the gain regime. The dashed curve shows the fit obtained using the rate equation model. (b) Predicted change in probe transmission versus 15 ps pump-probe delay.

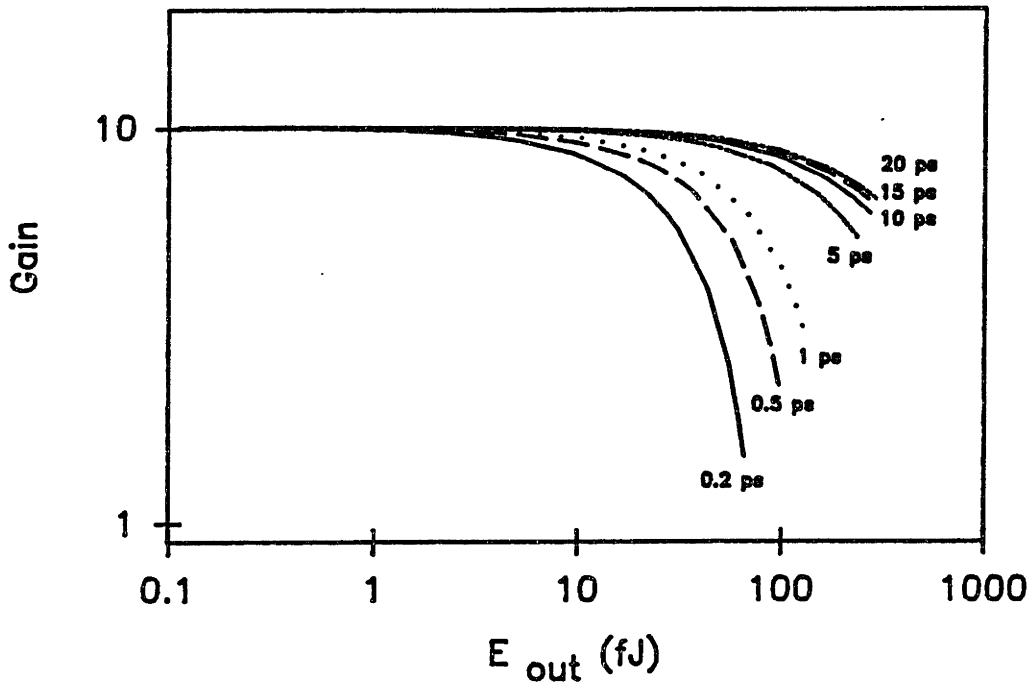

Figure 6.6: Predicted amplifier gain as a function of output energy for pulse widths of Δt = 200 fs (solid line), 500 fs (dashed line), 1 ps (dotted line), 5 ps (dashed-dot-dot line), 10 ps (solid line), 15 ps (dotted line), and 20 ps (dashed-dot-dot line).

close to, or longer than, the diode's peak gain wavelength [138].

Finally, we consider the pulsewidth dependence of the output saturation energy. Figure 6.6 shows the calculated gain curves for a number of pulsewidths between 150 fs and 20 ps. These curves were calculated using the same parameters as in the fits of Figure 6.5 (a). Note that for pulses longer than $\sim$ 10 ps, the carrier heating nonlinearity has negligible influence on the gain. For these longer pulses, the saturation behavior of the diode is pulse energy dependent, not pulsewidth dependent. However, even pulses as long as 5 ps have reduced output saturation intensities due to the carrier heating nonlinearity.

In summary, we have measured the saturation behavior of bulk, V-groove and MQW diodes for short pulses with different pulsewidths. Our results show that the output saturation energy is pulsewidth dependent. Table 6.1 summarizes the measured 3 dB output saturation energies for the two diodes and the two pulsewidths. These results suggests that carrier heating will play an important role in the amplification of subpicosecond pulses. Based on the results of the pump-

DIODE	Length	I (bias)	E (sat-out) Δt = 150 fs	E (sat-out) Δt = 15 ps
BULK	250 μm	3 X I (th)	40 fJ	150 fJ
MQW	400 μm	2 X I (th)	200 fJ	6 pJ

Table 6.1: Summary of results of the measured output saturation energies for bulk and MQW diodes and pulsewidths of $\Delta t = 150$ fs and $\Delta t = 15$ ps.

probe experiments presented in Chapter 5, a rate equation model including the effect of carrier heating has been developed to provide a quantitative explanation for the pulsewidth dependent saturation behavior.

Chapter 7

Heterodyne Pump-Probe Measurements

7.1 Introduction

As we described in Chapter 5, pump-probe experiments provide direct, time-domain measurements of gain [12] [26] [114] [118] and index [61] [64] [67] [139] nonlinearities in optical waveguides. In these experiments, the pump and probe beams must propagate collinearly so they can be coupled to the waveguide. Generally, the pump and probe beams are orthogonally polarized so that a polarizer at the waveguide output can select the probe beam for detection. If the probe beam is polarized parallel to, and is indistinguishable from, the pump beam, background-free measurements are difficult. In this chapter, we will describe a novel pump-probe technique in which the pump and probe have parallel polarizations and are nominally at the same wavelength but are still distinguishable. This technique uses heterodyne detection of frequency-shifted femtosecond pulses to separate the pump and probe signals. It can improve the time resolution of some experiments by circumventing the group velocity walk-off associated with orthogonally polarized pump and probe, and it allows the study of anisotropy in the waveguide nonlinearity.

In the heterodyne technique, three pulses, pump, probe and reference, are generated. The probe and reference pulses are deflected at acousto-optic mod-

ulators (AOM's), and their spectra are upshifted by the AOM drive frequency [59] [140]. Shifting the spectra will allow us to "tag" the probe beam so that it may be distinguished from the pump. In our experiments, the 100 MHz pulse train generated by the APM color center laser contains a 150 fs pulse every 10 ns. We can represent this pulse train in the time domain as the convolution of a 150 fs pulse with a train of delta functions. A schematic of this representation is shown in Figure 7.1 (a). (Note that the axes in this figure are not to scale.) In the frequency domain, the representation is a train of delta functions spaced by 100 MHz, multiplied by the Fourier Transform of the 150 fs pulse. If the optical pulse can be described by a Gaussian in the time domain, then it transforms to a Gaussian in the frequency domain with a full-width-half-maximum (FWHM) of $\Delta\nu = 0.44/(\Delta t) = 3$ THz. Figure 7.1 (b) shows the frequecy domain representation of the pulse train from the color center laser. When this optical pulse train passes through an AOM, the spectra of the deflected pulses are upshifted by f_{rf}, the AOM drive frequency, shown schematically in Figure 7.1 (c). Notice that the total frequency bandwidth of the pulses is broad compared to the delta function spacing so that the amplitudes of the delta functions appear constant. The deflected pulse frequency shift is so small compared to the total pulse bandwidth, we say that the deflected and undeflected beams are nominally at the same wavelength. However, if we overlap these two pulse trains in time and space, we will observe a beat at f_{rf}. We will use this beat frequency to distinguish between pump and probe beams in the heterodyne technique.

An experimental arrangement for the heterodyne pump-probe technique is shown in Figure 7.2. The APM color center laser output beam passes through a fused silica acousto-optic modulator (AOM) that deflects 20% of the power into the probe beam. The fused silica AOM introduces no measurable pulse broadening in the pump and probe pulses, however, it does upshift the spectra of the probe pulses by 39 MHz, the AOM drive frequency. At beamsplitter BS1, power is split between the pump and reference arms. Note that all three beams, pump, probe, and reference have the same polarization. The pump and probe are recombined at BS2. The reference beam passes through a second AOM (made from standard flint glass), where it is deflected and upshifted by 40 MHz. The flint glass does introduce measurable pulse broadening (80 fs pulses broaden to 120 fs), but the reference pulsewidth does not limit the time resolution of the experiment. The

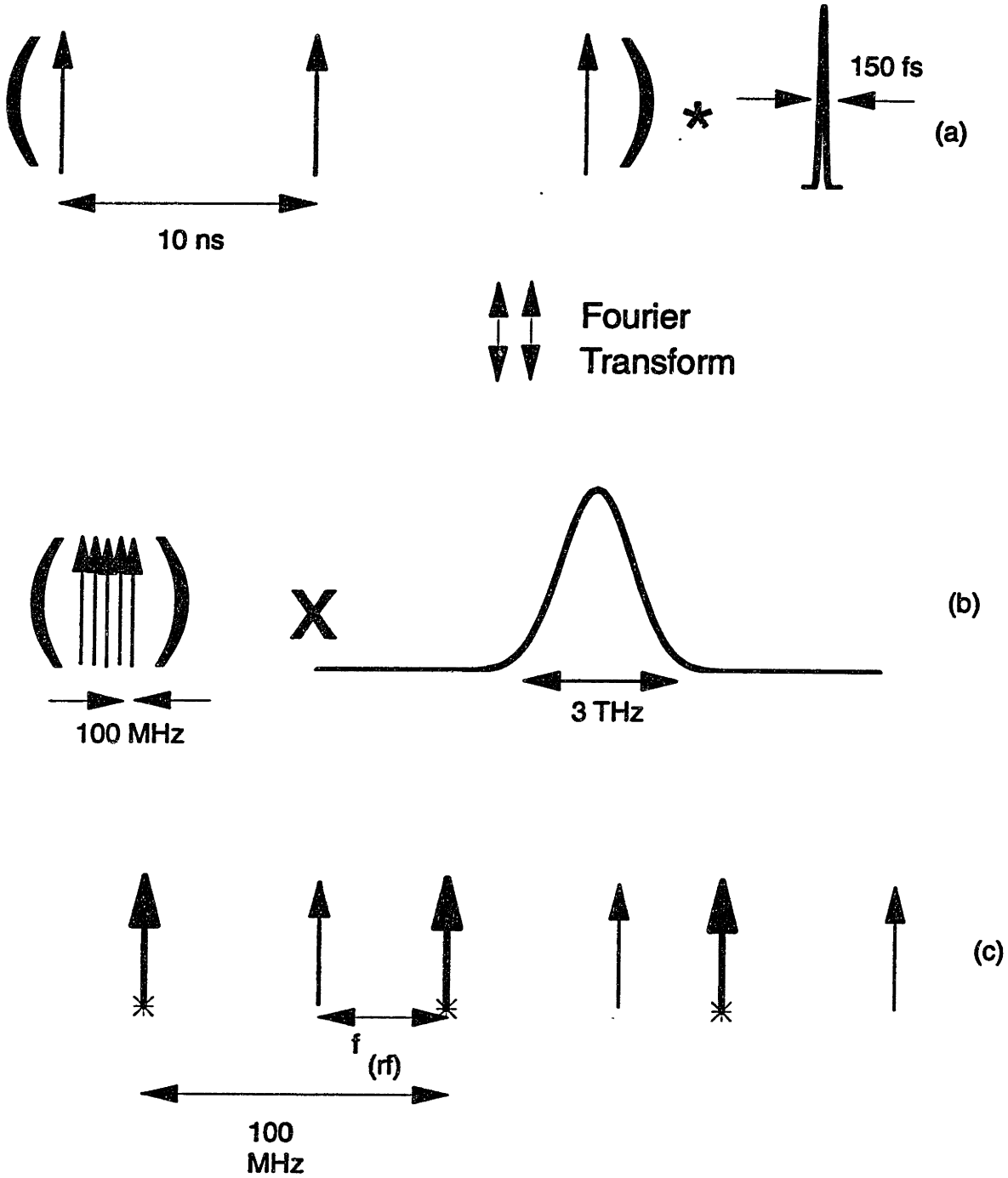

Figure 7.1: Schematic of the pulse train generated by the APM color center laser in the (a) time domain and (b) frequency domain. In (c), we compare the frequency domain representation of the portion of the pulse train that is undeflected by an AOM with the portion that is deflected. Note that the axes are not to scale.

reference beam is recombined with the pump and probe beams at BS3 and all three propagate collinearly to the diode. The reference pulses lead the pump-probe pulses by approximately 600 ps.

This single beam, of three pulses, is coupled to a short length of dispersion shifted fiber and then to the diode amplifier via a fiber microlens. A microscope objective collimates the output beam and directs it to an imbalanced Michelson interferometer where the probe and reference pulses are overlapped in time, at the detector. We use a high-frequency ham radio receiver to monitor the beat frequency between the reference and probe at 1 MHz. We can perform background-free pump-probe experiments by chopping the pump signal at a few kilohertz and passing the output from the radio receiver through a lock-in.

This experimental set-up can be modified to perform measurements where the pump and probe beams are orthogonally polarized by placing a half-wave plate in the pump arm and rotating its polarization by 90°. Note that this modification does not affect the power levels incident on the diode, nor does it affect the heterodyne detection because we are detecting the beat between the reference and the probe. Therefore, we can use the same detection technique for orthogonally-polarized pump-probe experiments. In our experiments, this method produced the same results as those obtained by simply placing a polarizer after the collimating microscope objective and selecting the probe beam for detection (Chapter 5). In the cross-polarized measurements discussed in this chapter, the pump pulses are TM-polarized and the probe pulses are TE-polarized, unless stated otherwise. Also, the pump-probe wavelength is 1.51 μm.

We chose the AOM difference frequency to be 1 MHz so that we could use a standard AM radio as the heterodyne receiver. However, the signals we obtained using this receiver were noisy. Using a spectrum analyzer to detect the 1 MHz beat yielded a much better signal to noise ratio. We found that the filters in the AM radio receiver, which are broad by design (to pass the entire audio band, 20 Hz-20KHz), are too broad to yield clean pump-probe signals. The filters in the spectrum analyzer, by contrast, can be as narrow as a few KHz, just enough to pass the chopped signal. Also, the filters are sharp, with shape factors ($\Delta f_{-3dB}/\Delta f_{-60dB}$) of approximately 2.40. A high-frequency, (ham radio) receiver has filters that are as narrow as, and even sharper than, those in the spectrum analyzer. Also, a ham radio receiver has AM and FM reception at the same

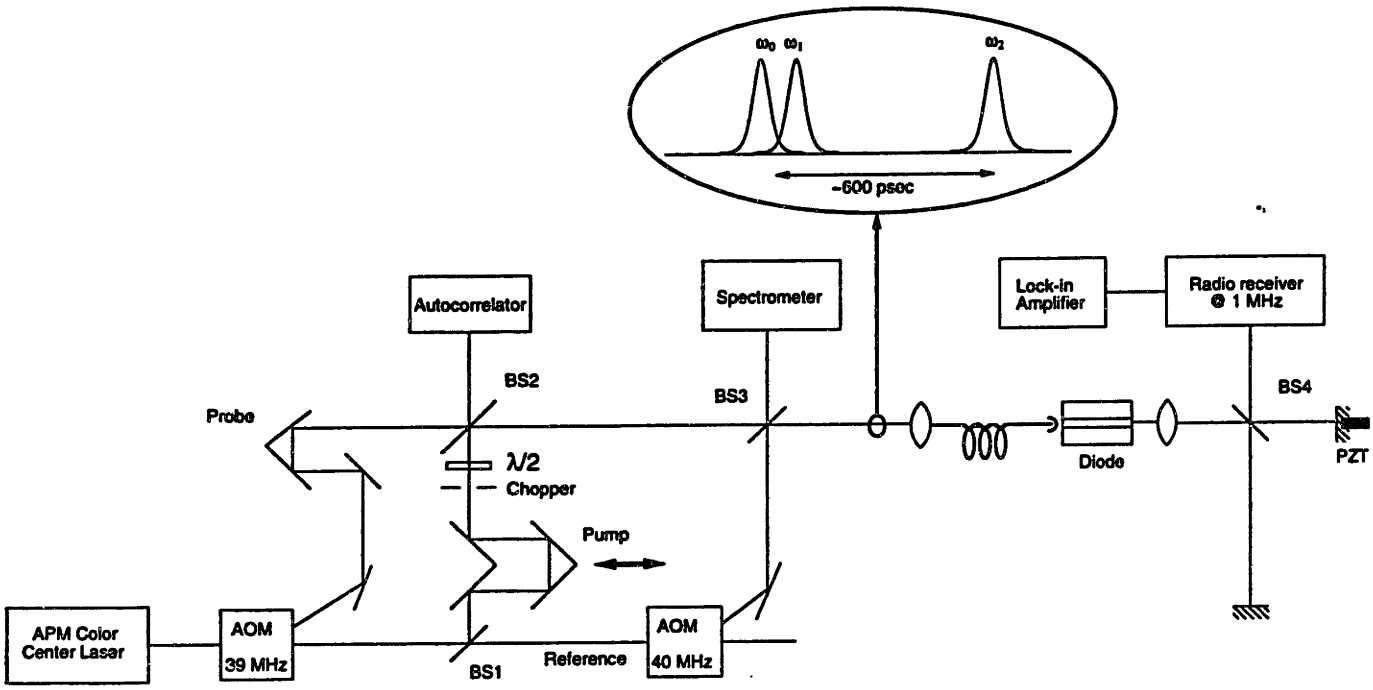

Figure 7.2: Pump-probe set-up for parallel-polarized beams.

frequency, suggesting that both probe amplitude and probe frequency (phase) changes can be detected. Therefore, we chose the ham radio receiver to detect the 1 MHz beat signal in our experiments.

7.2 Gain Nonlinearities

7.2.1 Bulk Diodes

Figure 7.3 shows the measured change in probe transmission as a function of copolarized (dashed lines) pump-probe delay for a bulk [71] diode biased in the absorption, transparency, and gain regimes. In this experiment, we reach the separate regimes of operation by changing the bias current to the diode. These data are best fit by assuming the impulse response functions are

$$h(t) = 18e^{-t/0.2ps} - 10.7e^{-t/0.6ps} - 1.0\delta(t) \tag{7.1}$$

for the absorption regime,

$$h(t) = 17e^{-t/0.2ps} - 10.5e^{-t/0.6ps} - 1.0\delta(t) \tag{7.2}$$

for the transparency regime, and

$$h(t) = 17e^{-t/0.2ps} - 11.5e^{-t/0.6ps} - 1.0\delta(t) \tag{7.3}$$

for the gain regime. For comparison, we also show the change in probe transmission as a function of cross-polarized (solid lines) pump-probe delay in the three regimes of operation. The impulse response functions for the cross-polarized data are given by Eqs. (5.16)-(5.18). Note that for time delays greater than 2 ps, the measured response for the copolarized and cross-polarized beams is essentially the same. We observe gain compression in all three regimes of operation, recovering with a 600 fs time constant. This compression is associated with the hot carrier

distribution cooling back to the lattice temperature. Also, we observe the step changes in probe transmission that are characteristic of the three regimes of operation (Chapter 5). However, for cross-polarized pump-probe results near zero time delay, the fast response (200 fs), associated with a transient absorption bleaching, is washed out. There are a number of possible explanations for the blurring of the response function near zero time delay. First, the group velocity is different for different polarizations so that cross-polarized pump-probe pulses walk off from each other as they travel through the diode. This walk-off limits the time resolution of the measurements and washes out interesting fast dynamics near zero time delay. Second, we expect differences in the amplitude of the coherent coupling term for copolarized and cross-polarized beams. Finally, the difference in the two results may be due to an anisotropy in the waveguide nonlinearity.

The effect of pulse walk-off can be taken into account by cross-correlating the pulse autocorrelation function with a square pulse of duration Δt [106] (Chapter 4),

$$S'(t) = \int_{-\infty}^{\infty} S(t+\tau)W(\tau)d\tau = \int_{0}^{\Delta t} S(t+\tau)d\tau, \tag{7.4}$$

where

$$W(\tau) = \begin{cases} 1 & 0 < \tau < \Delta t \\ 0 & \text{otherwise} \end{cases} \tag{7.5}$$

and Δt is the pulse walk-off. This cross-correlation broadens the impulse response and results in reduced temporal resolution. As an example, we calculate the broadening in our experiment. Our diode is 270 μm long, which gives a single-pass walk-off ($\Delta t = L/\Delta v_g$) of approximately 100 fs [106]. Figure 7.4 (a) shows the copolarized pump-probe data from the gain regime along with the fit (dashed line). Figure 7.4 (b) shows the cross-polarized pump-probe data (solid line) and the predicted curve obtained by convolving the broadened autocorrelation function with the impulse response function determined for the data in Figure 7.4 (a) (Eq. 7.3). If effective pulse broadening due to pump-probe walk-off alone were enough to explain the differences in the data shown in Figure 7.3, the predicted response would match the cross-polarized pump-probe response. Clearly, pulse walk-off alone can not explain the differences in the response.

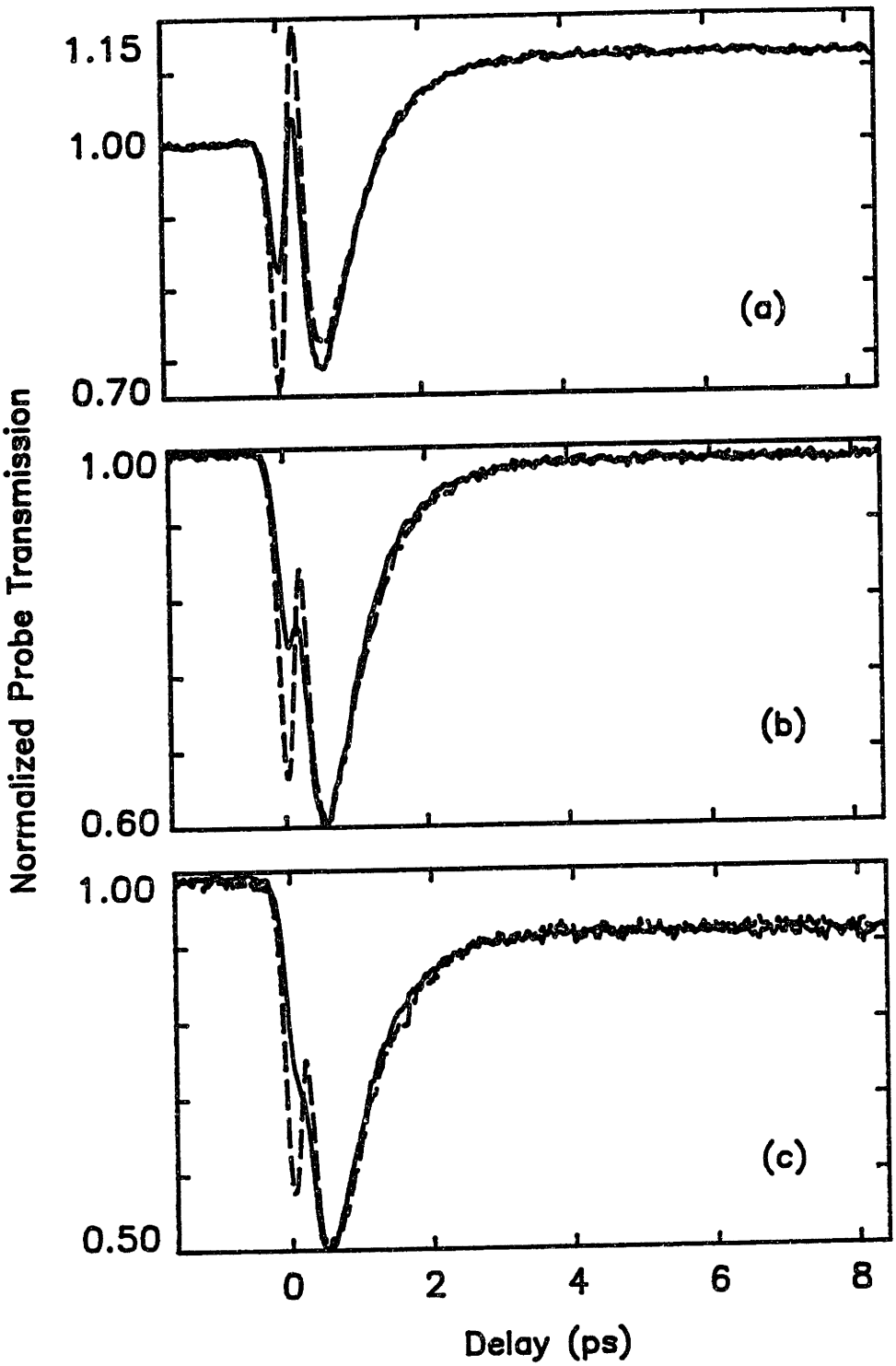

Figure 7.3: Change in probe transmission as a function of copolarized (dashed lines) and cross-polarized (solid lines) pump-probe delay when the bulk diode is biased in the (a) absorption, (b) transparency and (c) gain regimes.

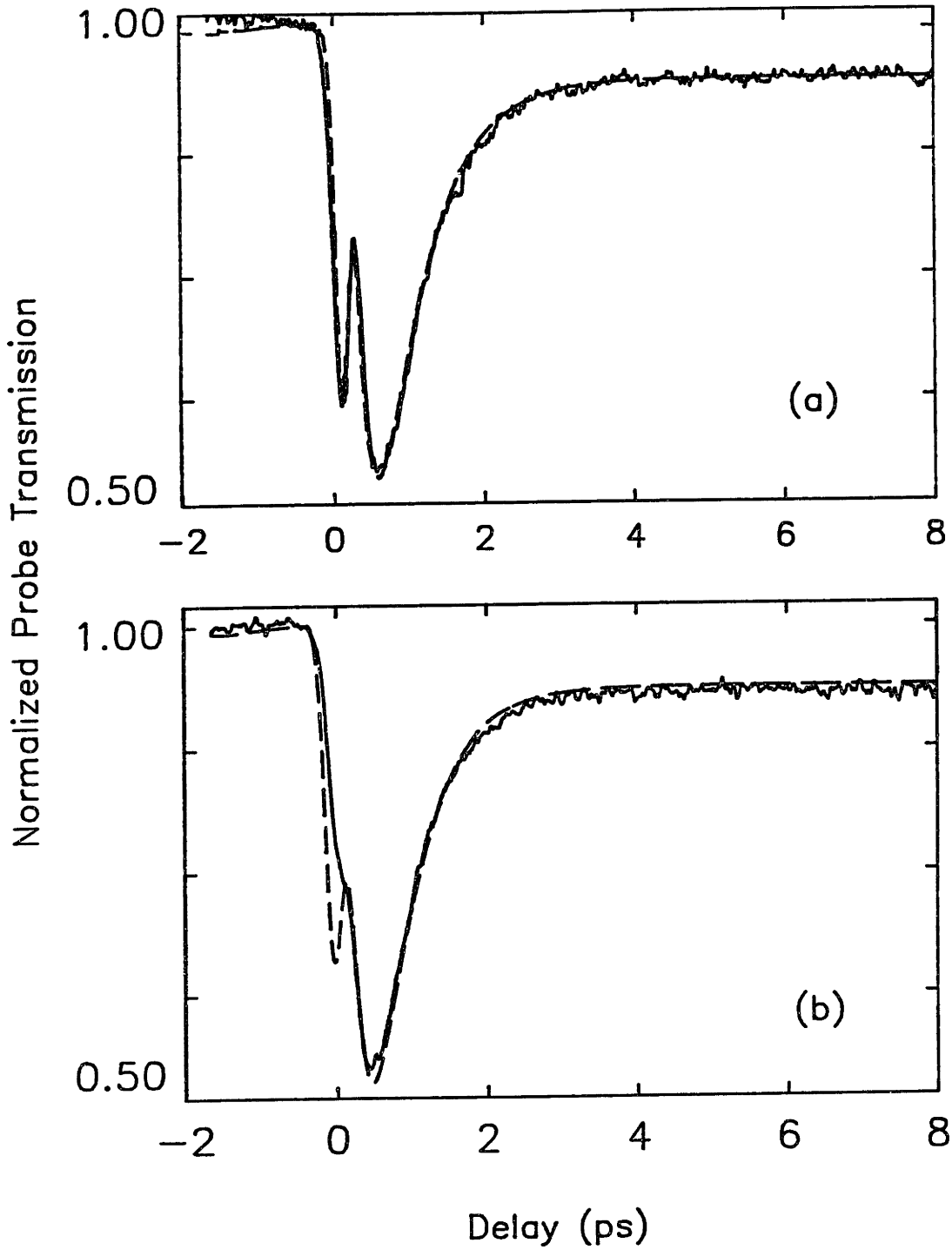

Figure 7.4: (a) Normalized probe transmission (solid line) as a function of copolarized pump-probe delay for a bulk diode biased in the gain regime along with the fit (dashed line). (Data is the same as in Figure 7.3 (c).) (b) Cross-polarized data (solid line) from Figure 7.3 (c) along with the fit (dashed line) predicted by convolving the broadened autocorrelation function with the impulse response function determined in (a).

The coherent coupling term contributes to the copolarized pump-probe data and may contribute to the cross-polarized data as well. As we explained previously (Chapter 5), the coherent artifact is always present in copolarized data, and the amplitude of this term at zero time delay is well-defined, $\gamma_{\parallel}(t = 0) = \beta_{\parallel}(t = 0)$. However, the importance of the coherent artifact in the cross-polarized data is less clear. Previous experiments have shown that the coherent artifact can be neglected in cross-polarized pump-probe experiments where the optical pulsewidth is greater than the dipole dephasing time and the response has a measurable time constant [111]. However, coherent artifacts have been observed in cross-polarized experiments when the response is instantaneous [112]. Our cross-polarized pump-probe responses are a sum of terms with measurable time constants and an instantaneous term. Since the dipole dephasing time is much shorter than the optical pulsewidth, there should be no coherent artifact associated with the terms that have measurable time constants. However, there may be a coherent artifact in the instantaneous component (TPA) of the response.

Initially, we will consider the coherent artifact in the copolarized data only. In this case, the shape and the amplitude of the coherent coupling term is well defined. Figure 7.5 shows the copolarized pump-probe data from Figure 7.3 (c) with the coherent artifact removed (dashed line). The cross-polarized pump-probe data is shown for comparison (solid line). If we assume that half of the TPA component in the cross-polarized data is due to coherent coupling, and we subtract the coherent term from the total response, we obtain the dash-dotted curve shown in Figure 7.5. It is clear from this comparison that coherent coupling alone can not explain the differences between the copolarized and cross-polarized results.

We can predict the the combined effect of the pump-probe pulse walk-off and the coherent artifact by convolving a broadened autocorrelation function with the impulse response function that fits the copolarized data after the coherent term has been removed. Figure 7.6 shows the response predicted by these combined effects (dashed line) along with the cross-polarized data (from Figure 7.3 (c)) (solid line) for comparison. Again we note that the predicted response does not agree with the measured response. There are a number of possible explanations. First, any uncertainty in the definition of the zero pump-probe delay point will lead to uncertainties in the size of the coherent artifact that is subtracted from the

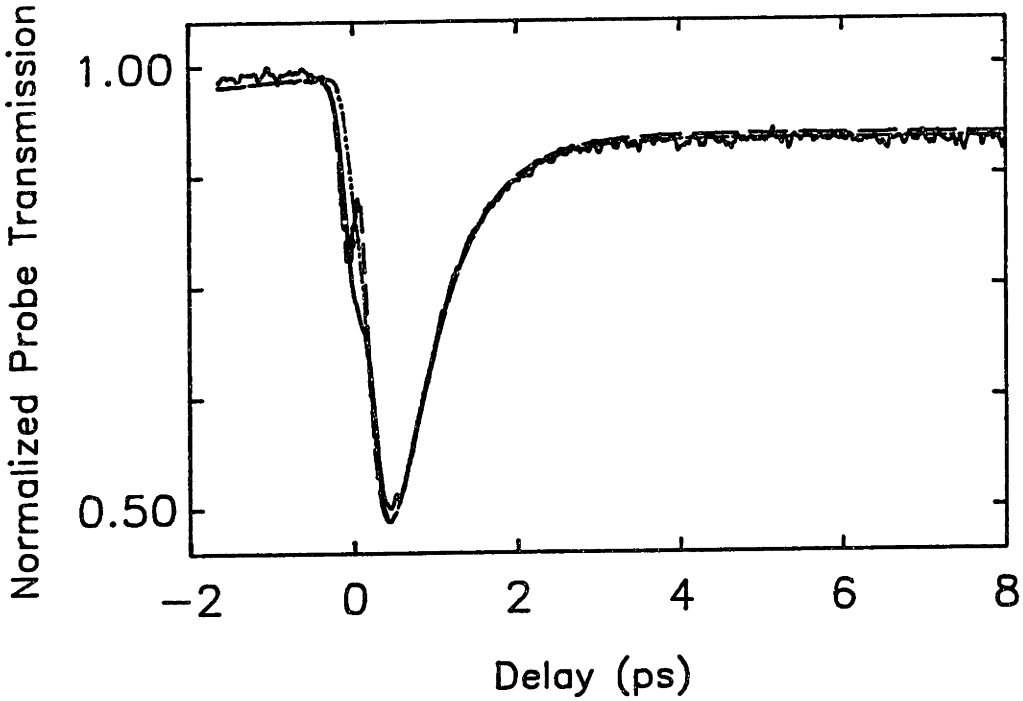

Figure 7.5: Measured change in probe transmission as a function of cross-polarized pump-probe delay (solid line). The dashed line shows the copolarized data after the coherent artifact has been subtracted. The diode bias conditions are given in Figure 7.3 (c).

signal. Second, in calculating the coherent artifact, we used the experimentally determined intensity autocorrelation function rather than the field autocorrelation function. This is not a bad approximation when the pulses are nearly transform limited. Third, we have assumed that all the dynamics we measure are due to free carriers, and that the material can be considered isotropic. We have no experimental proof for this assumption. Finally, we may be measuring anisotropy in the waveguide nonlinearity.

7.2.2 Strained-Layer Multiple Quantum Well Diodes

We can use this heterodyne technique to study the gain nonlinearities in more complicated diode structures like the strained-layer multiple quantum well (SLMQW) devices [78] (Chapter 2). The measured emission peaks for these diodes are 1.53 μm for the TE mode and 1.38 μm for the TM mode [78]. The emission peaks are polarization dependent because the selection rules state that heavy hole-electron

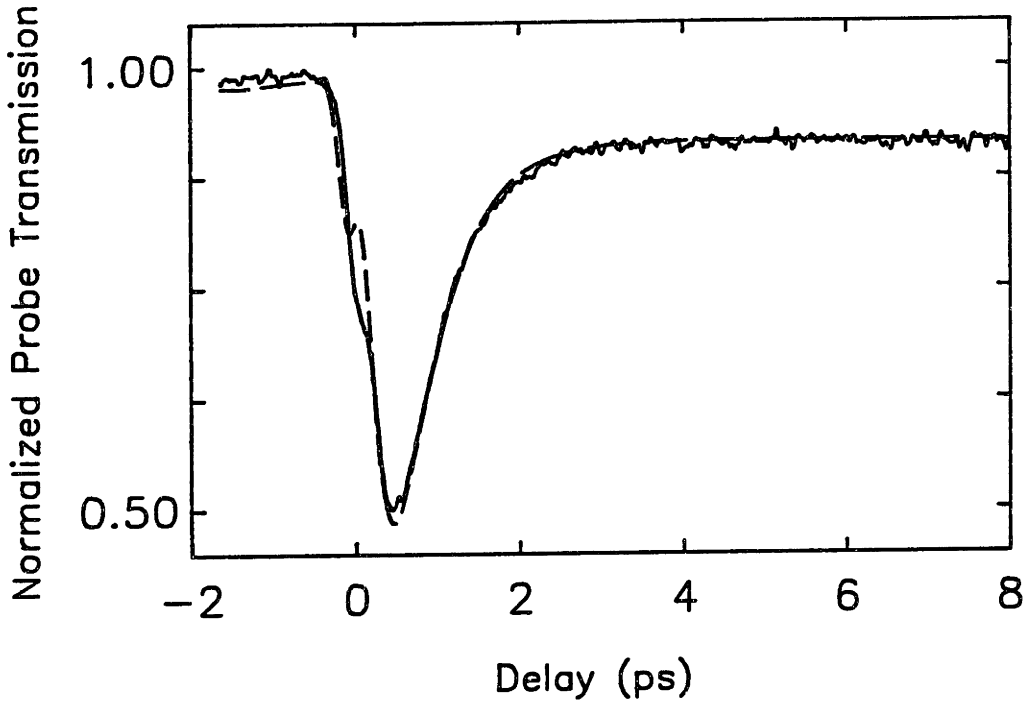

Figure 7.6: Measured change in probe transmission as a function of cross-polarized pump-probe delay (solid line). The dashed line shows the response predicted by convolving a broadened intensity autocorrelation function with the impulse response function describing the copolarized data after the coherent artifact has been removed. The diode bias conditions are given in Figure 7.3 (c).

(hh-e) and light hole-electron (lh-e) transitions are allowed for TE polarized light (parallel to the quantum well layers), whereas hh-e transitions are forbidden for TM polarized light (orthogonal to the layers) [74]. The quantum well energy levels and the allowed transitions are shown schematically in Figure 7.7. While the polarization selection rules are only strictly true at the Brillouin zone center, the effects of band mixing are weak at modest applied bias currents. The weak band mixing at modest applied bias currents will be verified experimentally.

Figure 7.8 shows the measured change in probe transmission as a function of copolarized pump-probe delay for the diode biased in the absorption, transparency and gain regimes [141] [142]. We reach these separate regimes by changing the bias current to the diode. The results for TE polarized pump and probe are shown by the solid lines and the results for TM polarized pump and probe are shown by the dashed lines. The TM polarized results show only an instantaneous absorption due to two-photon absorption (TPA). No other dynamics are observed because

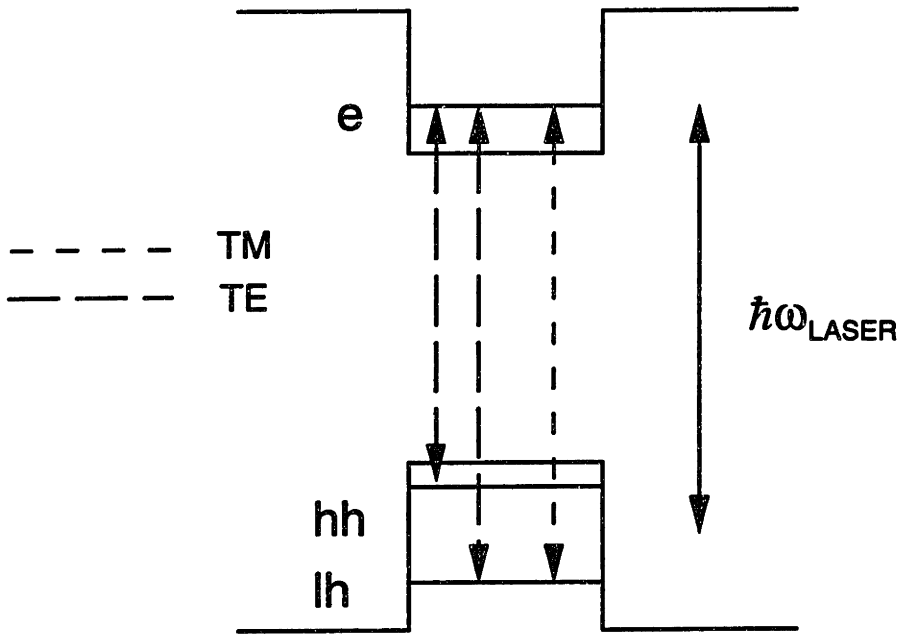

Figure 7.7: Schematic of the energy levels and allowed transitions in a strained quantum well. Note that the pump-probe pulse energy is below-band for the lh-e transition.

the pump-probe wavelength (λ=1.51 μm) is below band for the lh-e transition (λ=1.38 μm) and the hh-e transitions are forbidden. This result confirms that the effects of band-mixing at bias current levels below 20 mA are weak. The limited tuning range of our APM color center laser, 1.47 μm to 1.52 μm, restricts above-band pump-probe measurements to the TE polarization.

The TE polarized results show similar dynamics to those observed previously in bulk and MQW diodes (Chapter 5). The three regimes are distinguished by the step change in probe transmission due to stimulated emission (gain) or absorption (absorption) of the pump. At the transparency point, there are no net stimulated transitions and no step change in probe transmission. All three regimes show a gain compression that recovers with a time constant of $\sim$ 1 ps. This compression is associated with the heated carrier distribution cooling back to the lattice temperature. In the absorption and transparency regimes, there is an intermediate transient increase in probe transmission recovering with a time constant of approximately 150 fs. Also, there is an instantaneous decrease in gain, present in all regimes of operation, associated with TPA. This instantaneous gain compression

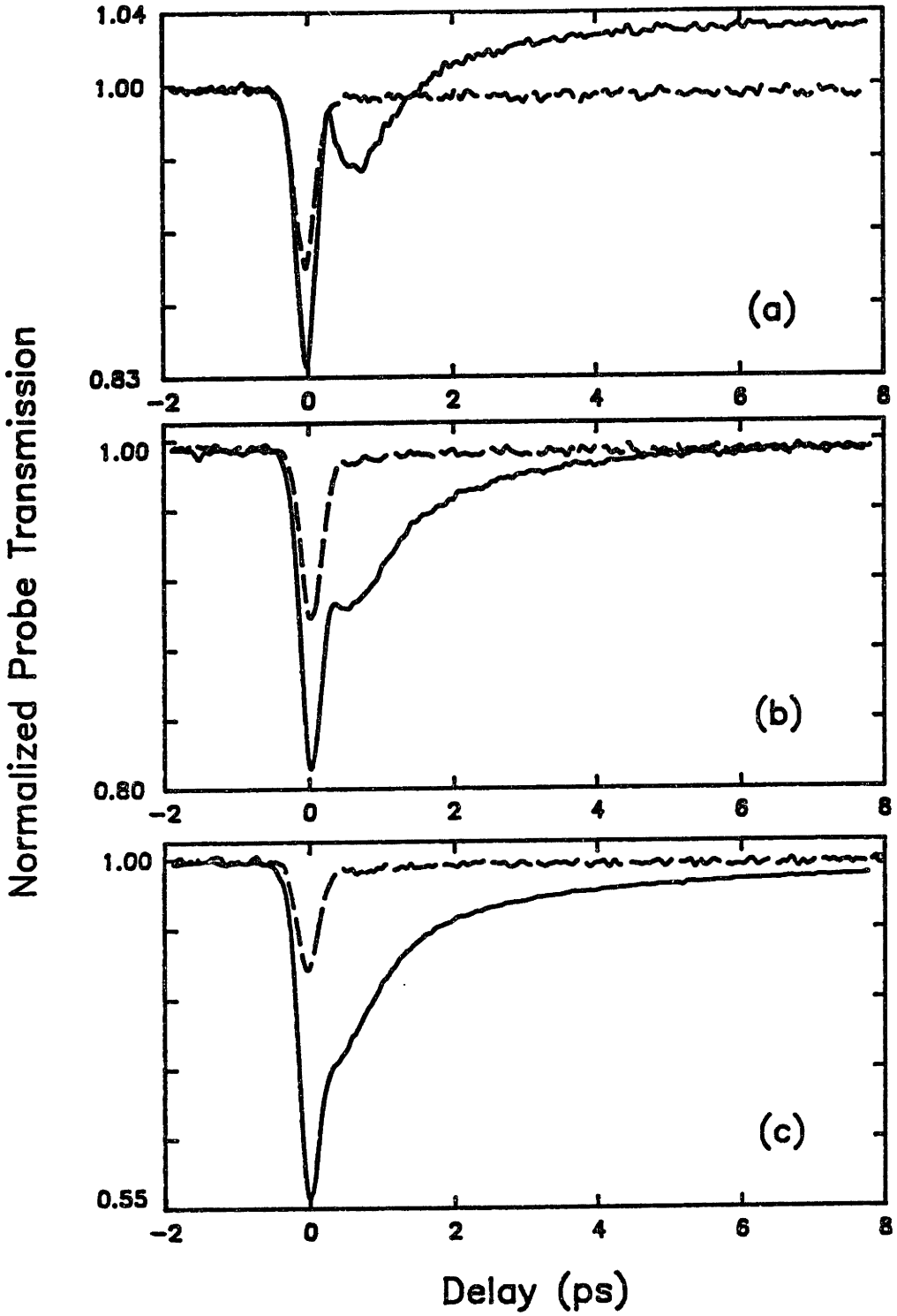

Figure 7.8: Change in probe transmission as a function of copolarized pump-probe delay. The solid lines are for TE polarized pump-probe pulses and the dashed lines are for the TM polarized pulses. The pump-probe center wavelength is 1.51 μm. The bias current is (a) 10 mA in the absorption regime, (b) 12 mA in the transparency regime, and (c) 18 mA in the gain regime.

is a significant fraction of the total response but is not attributed to spectral hole burning because it does not disappear at the transparency point and it does not cause a transient increase in transmission in the absorption regime.

Using orthogonally polarized (cross-polarized) pump and probe pulses, we take further advantage of the large valence subband energy separation ($\sim$ 100 meV) and the polarization selection rules to pump below band for one transition while probing above band for another. When the pump is TM polarized, it is "below-band" for lh-e transitions and is able to stimulate only intraband transitions. However, the TE polarized probe can monitor the carrier distribution via the interband hh-e transition. Note that since the pump cannot stimulate interband transitions, there should be no observed change in gain associated with a change in carrier number. Also, nonlinearities due to interband transitions, like spectral hole burning, should not be observed in this case. In other words, when the pump and probe are TE polarized, nonlinearities due to both intraband [e.g., carrier heating due to free carrier absorption (FCA)] and interband [e.g., spectral hole burning and carrier heating or cooling due to stimulated transitions] effects may be observed. But, when pump (TM) and probe (TE) are cross-polarized, only nonlinearities associated with intraband processes are possible. Figure 7.9 shows the pump-probe result for a SLMQW diode biased in the absorption regime when the pump-probe pulses are (a) copolarized and (b) cross-polarized. The solid lines are the data and the dashed lines are the fits. The step increase in probe transmission in the copolarized data, associated with carrier generation by stimulated absorption of the pump, is almost absent in the cross-polarized data. The small step increase observed in the cross-polarized case is an order of magnitude smaller than that observed in the copolarized case and may be due to either band-mixing effects or imperfect polarization decoupling between pump and probe. Note that both sets of data show the heated carrier distribution cooling to an equilibrium temperature with a time constant of $\sim$ 1 ps. Also, both show a transient increase in gain, recovering with a time constant of $\sim$ 150 fs. In the cross-polarized data, this dynamic cannot be due to spectral hole burning but can be explained by a delay in the turn-on of carrier heating.

Figure 7.10 shows the measured probe transmission as a function of cross-polarized pump-probe delay. The bias conditions for the diode are the same as those for the data shown in Figure 7.8. Notice that the three curves are almost

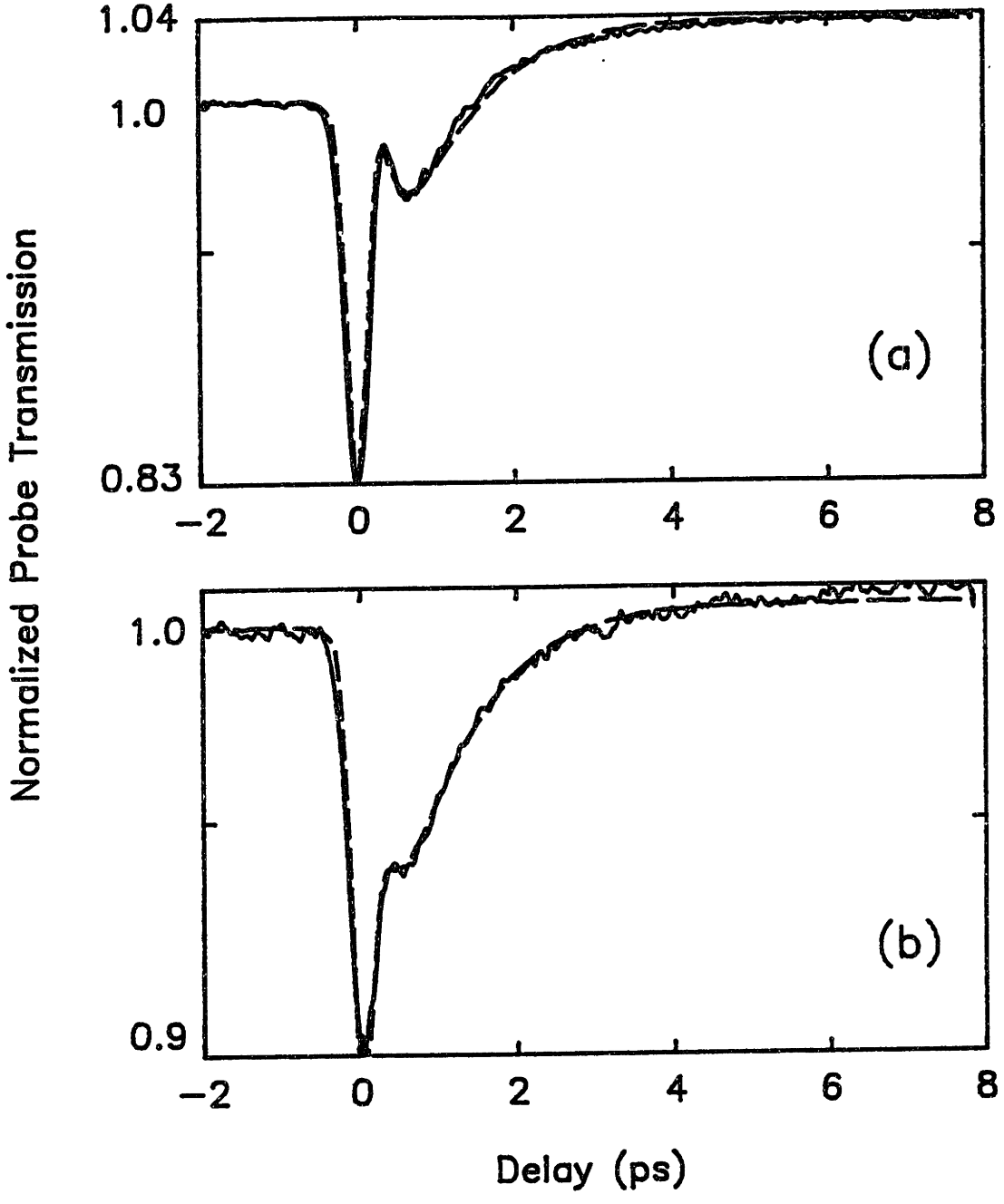

Figure 7.9: Measured change in probe transmission (solid line) and fit (dashed line) as a function of pump-probe delay for the SLMQW diode biased in the absorption regime when (a) the pump and probe are TE polarized and (b) the pump is TM polarized and the probe is TE polarized. The bias current is 8 mA.

identical. There is no step change in transmission associated with pump-induced stimulated transitions distinguishing the different regimes of operation. Notice also that the real change in probe transmission due to carrier heating for the cross-polarized results is approximately half that measured in the copolarized results. These carriers are heated by FCA (and possibly TPA). When we fit these data by convolving the impulse response function with the experimentally determined autocorrelation function, we find that the transient bleaching term is opposite in sign, but nearly equal in amplitude to the carrier heating term. We can combine these two opposing exponential terms into a single term that describes a delayed gain compression term. Physically, we are suggesting that there is a delay of 100-200 fs associated with the time it takes the initial nonequilibrium carrier distribution to evolve into a new hot Fermi distribution. This hot distribution then cools back to the lattice temperature with a time constant of $\sim$ 1 ps.

We rewrite Eq. (5.15) so that it includes a delay in the onset of carrier heating explicitly,

$$h(t) = u(t)\left[a_2 e^{-t/\tau_2}(1 - e^{-t/\tau_{eff}}) + (a_1 + a_2)e^{-t/\tau_1}\right] + a_3\delta(t) \qquad (7.6)$$

where $1/\tau_{eff} = (1/\tau_1) - (1/\tau_2)$. By forcing Eq. (5.15) into this form, we create a residual term whose amplitude changes sign, depending on the relative magnitudes of a_1 and a_2. To the extent that this term changes sign at the transparency point, it behaves like spectral hole burning.

Figure 7.11 shows the amplitude of the residual term, $a_1 + a_2$, as a function of the bias current for the copolarized (open circles) and cross-polarized (solid circles) pump-probe results. Both amplitudes a_1 and a_2 are normalized to a_3, the magnitude of the TPA term. Normalizing all terms with respect to a_3 automatically eliminates discrepancies due to the presence of a coherent coupling term in the copolarized data. Notice that in the cross-polarized data, $a_1 + a_2 \simeq 0$ for all bias currents, as we would expect when spectral hole burning is absent. In this case, heating occurs via FCA. That is, some carriers are excited to high lying states by FCA and there is some delay associated with the transfer of their excess energy to the rest of the carrier distribution. For the co-polarized data, there is, in addition to the delay in carrier heating, a transient bleaching ($a_1 + a_2 > 0$) in the absorption regime that goes away at transparency. This behavior is consistent

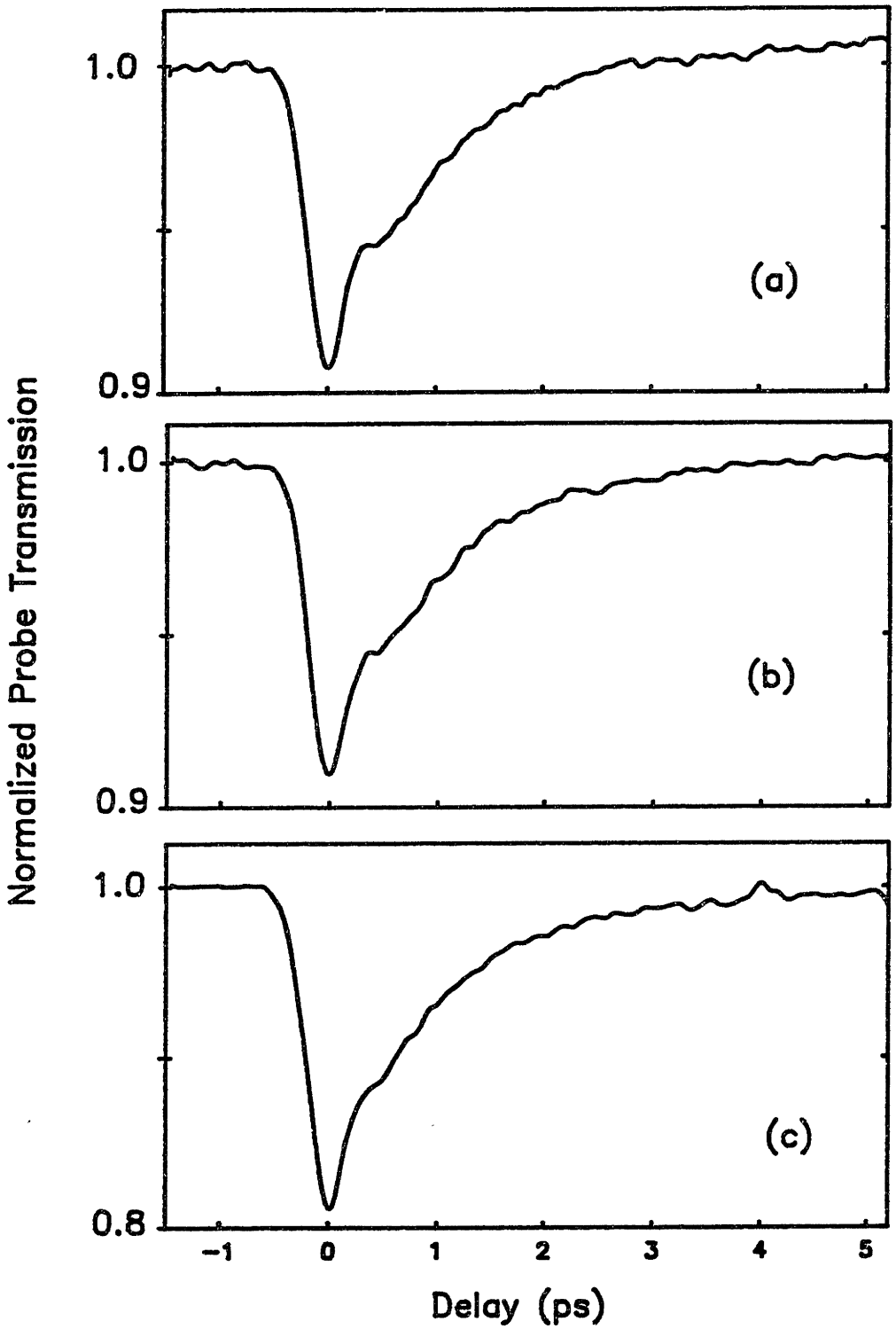

Figure 7.10: Measured change in probe transmission as a function of cross-polarized pump-probe delay for the SLMQW diode biased in the (a) absorption (I=10 mA), (b) transparency (I=12 mA), and (c) gain (I= 13 mA) regimes.

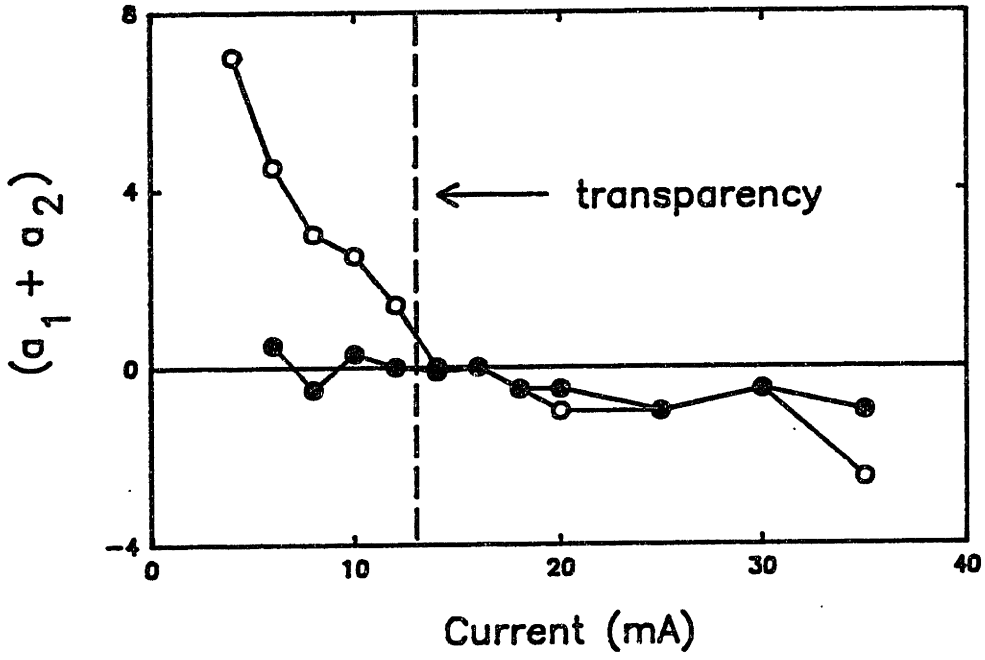

Figure 7.11: Amplitude of $(a_1 + a_2)$, the spectral hole burning component of the impulse response function, as a function of bias current for copolarized (open circles) and cross-polarized (solid circles) measurements. In this case, τ_1=170 fs and τ_2=1ps.

with spectral hole burning. However, in the gain regime, the magnitude of this component is small. We expect the amplitude of the spectral hole burning component to scale with the amplitude of the step. Figure 7.12 shows the measured amplitude of step, a_0, normalized to a_3, as a function of diode bias current. The step change in gain is leveling off at high bias currents because the gain coefficient is effectively saturated (Figure 2.4).

We can fit the cross-polarized pump-probe data for bulk and MQW diodes, presented in Chapter 5, using this new impulse response function that includes explicitly the delay in the onset of carrier heating. The results are shown in Figure 7.13. Notice that the results for these diodes also show a residual term that behaves like spectral hole burning. However, the sign of the residual term does not always flip right at transparency. There are a number of possible explanations for this behavior. First, the two opposing terms that represent the carrier heating and the delay are large, and their time constants can be determined accurately. However, the spectral hole burning component is buried in the total response and

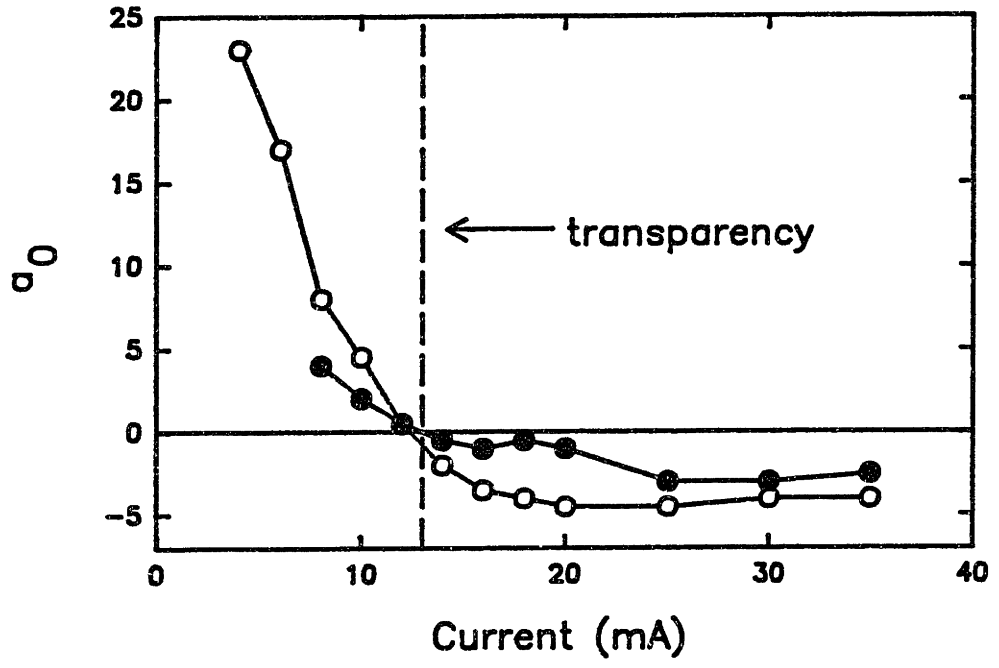

Figure 7.12: Amplitude of a_0, the step component of the impulse response function, as a function of bias current for copolarized (open circles) and cross-polarized (solid circles) measurements. These components are from the same impulse functions used in Figure 7.11.

is observed only after two much larger terms have been subtracted from the data. There are usually substantial errors associated with attaching physical significance to terms that result from the subtraction of two large numbers. Besides errors in the amplitude of the spectral hole burning component, it is possible that there are errors in the determination of the time constant as well. It appears that the 100-200 fs component we originally called the transient absorption bleaching is really a delay in the carrier heating. However, to make the impulse functions consistent, we forced the spectral hole burning term to take on this time constant. Since we have verified the delay in the onset of carrier heating, we should allow the three exponential terms, delayed carrier heating, carrier cooling, and spectral hole burning, in the impulse response function to have independent time constants.

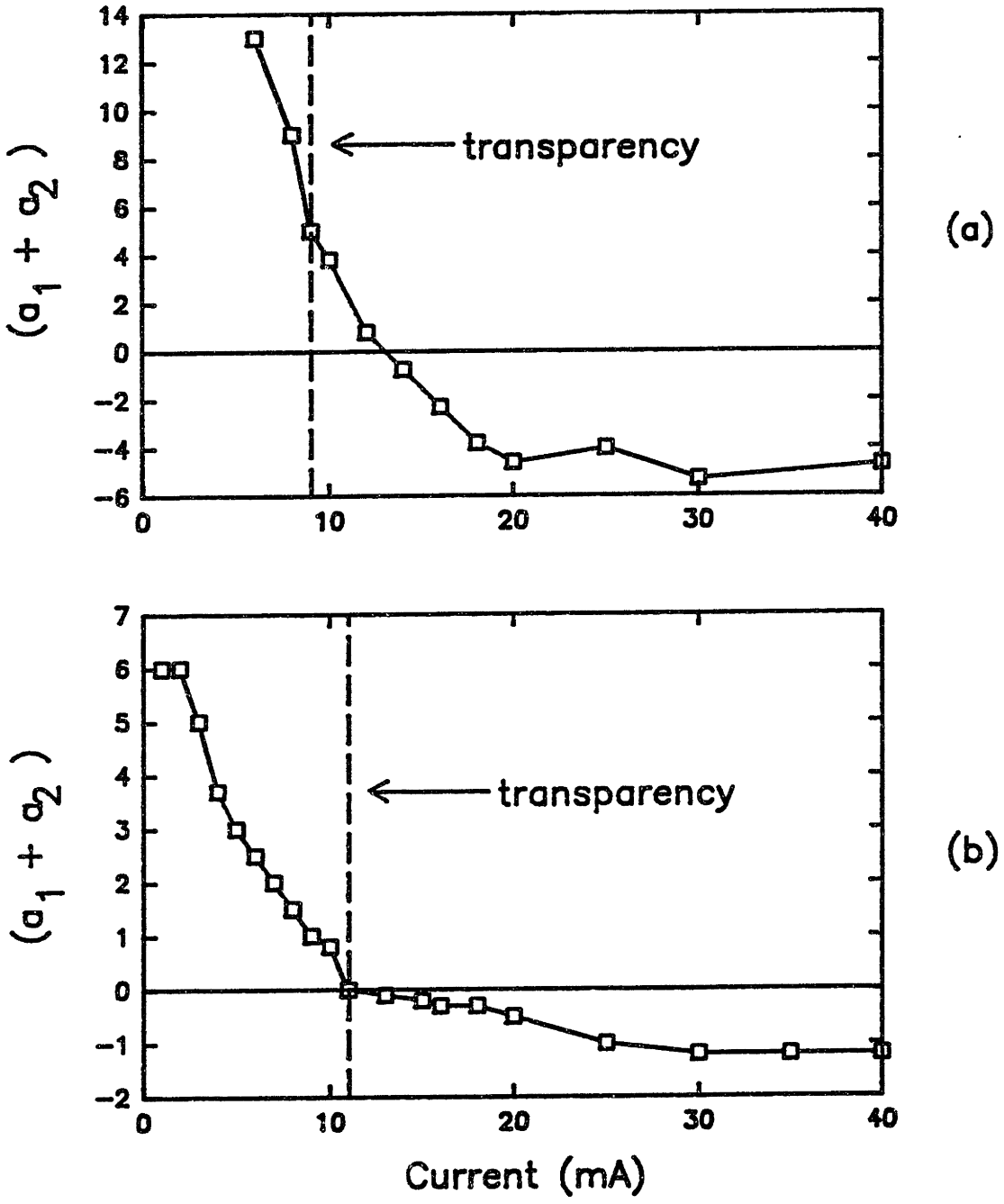

Figure 7.13: Amplitude of $(a_1 + a_2)$, the spectral hole burning component of the impulse response function, as a function of bias current for cross-polarized pump-probe measurements for (a) a bulk amplifier and (b) a MQW amplifier.

7.3 Index Nonlinearities

Ultrafast refractive index changes are important because they affect the chirp [143] and the spectrum [144] [145] of short pulses propagating in the waveguide. Refractive index nonlinearities might also be exploited in an all-optical switch. While these ultrafast refractive index changes have been studied in the time domain in active [61] [67] and passive [64] [65] AlGaAs waveguides, there have been no time-resolved studies of InGaAsP waveguides. We will use the heterodyne technique described in this chapter to measure the subpicosecond refractive index nonlinearities in InGaAs/InGaAsP diodes at 1.5 μm.

The experimental technique is similar to that used to measure the gain nonlinearities described above. The set-up is shown in Figure 7.2. In these experiments, the pump beam is chopped and the ham radio receiver is used as an FM receiver. When the probe precedes the pump, its phase is not modulated and the radio receiver output is zero. However, when the probe lags the pump, its phase is modulated (chopped). The radio receiver detects this modulation in phase and generates an output signal that is proportional to its derivative. The lock-in detects this signal, integrates it, and yields an output voltage that is proportional to the pump-induced phase change. This measured phase change is then calibrated with respect to a known optical phase change. In our case, one of the mirrors in an interferometer arm (Figure 7.2) is modulated by a piezoelectric transducer (PZT) and the phase shift is obtained by observing fringes.

There are a few important points regarding the calibration of the heterodyne receiver. First, the rise time of the chopped signal must be fast enough that the phase-locked loop (PLL) in the FM receiver can not follow it. If the PLL can follow the rising slope of the chopped signal, it can start to correct the phase before the phase has reached its maximum value. In this situation, the measured phase shift will vary as a function of chopper frequency (risetime). Figure 7.14 shows the measured probe phase shift at an arbitrary value of pump-probe delay for different chopper frequencies. Note that for chopper frequencies greater than 700 Hz, (or a rise time steeper than $\sim$ 0.3 ms), the measured signal is independent of chopper frequency. All the measurements we report are performed with chopper frequencies greater than 700 Hz. We will not choose chopper frequencies that are much higher than 2 KHz because we want to take advantage of the narrow, cw

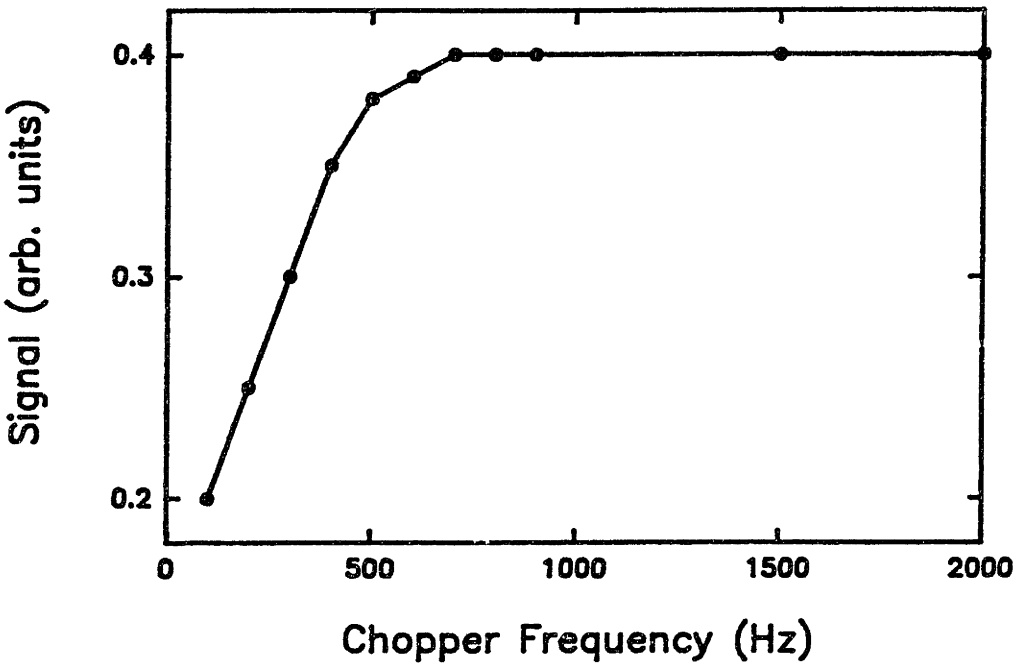

Figure 7.14: Signal from the FM radio receiver as a function of chopper frequency. The signal is the measured change in probe transmission at an arbitrary pump probe delay.

filters (2.4 KHz) in the radio receiver.

Second, to observe fringes, (and calibrate the PZT), we couple the two arms of the Michelson interferometer into a short length of fiber (Figure 7.15). Coupling both arms into the fiber insures that the phase fronts for the two beams are matched. Also, we adjust the length of the two arms to be equal so that we can measure the interference of like pulses (probe with probe, or pump with pump, etc.). We measure the interference of like pulses because they beat at DC. If we measure the interference between probe and pump for example, they beat at their difference frequency, 39 MHz. We could calibrate the PZT in this manner, but experimentally, it is easier for us to measure the fringes at DC. The fiber output is monitored by a slow detector. As the length of the arm containing the PZT is varied, we observe a sinusoidal variation in the power incident on the detector. In our case, applying 4 V across the PZT changes that arm's path length by $\lambda/2$, corresponding to a phase shift of π. We can calibrate the sign of the phase shift by knowing that positive voltages applied to the PZT shorten the interferometer arm. We remove the fiber and slow detector and replace the high-speed (25

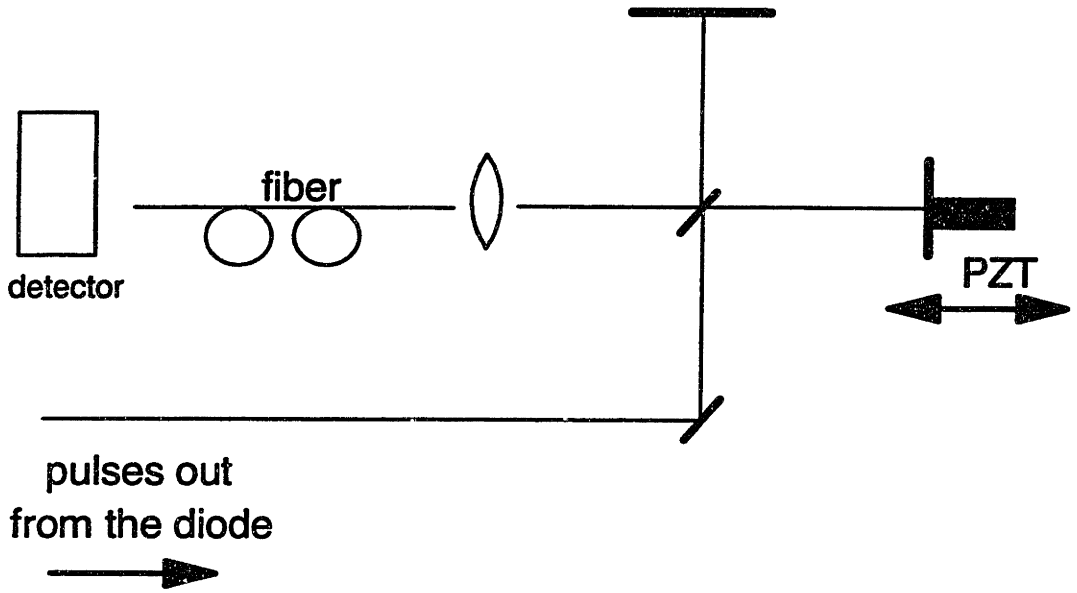

Figure 7.15: Interferometer set-up used to calibrate the ham radio receiver.

MHz) detector used in the pump-probe experiments. Then we apply a square-wave voltage to the PZT. The phase change due to the moving PZT simulates the probe phase change due to the chopped pump. The signal generated at the output from the ham radio receiver when the applied square-wave voltage is 4 V corresponds to a π phase shift.

Note that in FM operation, the radio receiver detects frequency changes, or the derivative of the phase changes ($f \sim \frac{d\Phi}{dt}$). A lock-in amplifier can be used to integrate the signal to obtain the desired phase change. Also note that a heterodyne pump-probe technique and an FM receiver has a number of advantages over the single-frequency time domain interferometer (TDI) used in previous experiments [61] [64] [65] [67] [139] [146] [147]. First, the phase-locked loop in the FM receiver automatically stabilizes the interferometer against slow phase drifts due to thermal and acoustic fluctuations. No additional stabilization of the interferometer arms is required. Second, the pump pulse can be either co-polarized or cross-polarized with respect to the probe pulse without affecting the heterodyne detection scheme. Third, we do not need to use a balanced detector scheme because the limiter in the FM receiver eliminates signals due to amplitude changes of the probe. Finally, this technique can be used with collinear pump and probe

beams.

7.3.1 Fiber

We can test the accuracy of this new experimental technique by measuring a known nonlinear refractive index. The instantaneous nonlinear refractive index, $n_{2\|}$, in optical (silica) fibers, is $n_2 = 3.2\times 10^{-16}$ cm^2/W [91]. This nonlinear index can be used to describe self-phase and cross-phase modulation and the optical Kerr effect, for example. Silica is isotropic and the nonlinear index is instantaneous and can be described by the third order polarizability via:

$$\mathbf{P}_x^{(3)} = \frac{\epsilon_0}{4}\chi^{(3)}\left(3|\mathbf{E}_x| + 2|\mathbf{E}_y|^2\right)\mathbf{E}_x = 2\epsilon_0 n n_2 |\mathbf{E}(\omega)|^2\mathbf{E}(\omega) \tag{7.7}$$

where $\mathbf{E}_x = |\mathbf{E}_x|e^{j(\omega t+\phi_x)}$, the linearly polarized field in the x direction and so on for $|\mathbf{E}_y|$ [148] [149]. In this equation, the self-phase modulation (SPM) term is proportional to

$$\text{SPM} \propto 3|\mathbf{E}_x|^2\mathbf{E}_x, \tag{7.8}$$

and the cross-phase modulation (XPM) term is proportional to

$$\text{XPM} \propto 2|\mathbf{E}_y|^2\mathbf{E}_x. \tag{7.9}$$

Comparing the two terms yields the well know ratio of SPM/XPM=3/2. In a pump-probe experiment where the pump and probe are cross-polarized ($\mathbf{E}_{pump} = \mathbf{E}_x, \mathbf{E}_{probe} = \mathbf{E}_y$), the measured response is described by Eq. (7.9) and the measured index change is given by,

$$\Delta n_\perp \propto \frac{1}{2}\epsilon_0\chi_{xxxx}|\mathbf{E}_{pump}|^2 \tag{7.10}$$

where we have used the identity [149]

$$\mathbf{P}_x^{(3)}(\omega) = 2\epsilon_0 n\Delta n = 2\epsilon_0 n n_2|\mathbf{E}(\omega)|^2\mathbf{E}(\omega). \tag{7.11}$$

If the pump and probe are copolarized, $\mathbf{E}_{pump} + \mathbf{E}_{probe} = \mathbf{E}_x$, and we can show that the measured index change is given by

$$\Delta n_{\parallel} \propto \frac{3}{2}\epsilon_0 \chi_{xxxx} |\mathbf{E}_{pump}|^2. \tag{7.12}$$

Therefore, in a pump-probe experiment, the ratio of $\Delta n_{\parallel}/\Delta n_{\perp}$ is 3/1 [139] [149]. We can understand the difference between the SPM/XPM ratio and the pump-probe ratio in terms of the coherent artifact. In calculating SPM and XPM, the coherent coupling term is automatically included by the conventional mathematical formalism [149]. However, in that formalism, the coherent coupling term does not contribute to the magnitude of the SPM term because there is only one field. In a copolarized pump-probe experiment there are two fields, pump and probe, and a coherent artifact is present. Therefore, we must double the magnitude of the SPM term when relating it to a copolarized pump-probe results. XPM is calculated assuming two fields are present and is an accurate representation of the cross-polarized pump-probe results.

Figure 7.16 shows the measured probe phase shift as a function of copolarized (solid line) and cross-polarized (dashed line) pump-probe delay. In this case, the waveguide is a 23 cm length of dispersion shifted fiber. We can use the measured probe phase shift to determine $n_{2\parallel}$ in this fiber via

$$\Delta n_{\parallel} = \frac{\lambda}{2\pi L}\Delta\Phi = 2n_{2\parallel}I \tag{7.13}$$

where λ is the pump-probe wavelength (1.5 μm), L is the fiber length, $\Delta\Phi$ is the measured phase shift, I is the intensity and $\Delta n = 2n_{2\parallel}I$ has the factor of two to account for the coherent artifact. The diameter of the dispersion shifted fiber is approximately 5 μm. The effective mode area, given by πr_{eff}^2, is assumed to be 35 μm^2. The pulse peak power is 67 W giving a measured $n_{2\parallel}$ =2.6 $\times$ 10^{-16} cm^2/W. This measured $n_{2\parallel}$ is in good agreement with the commonly used value of $n_{2\parallel}$ =3.2 $\times$ 10^{-16} cm^2/W.

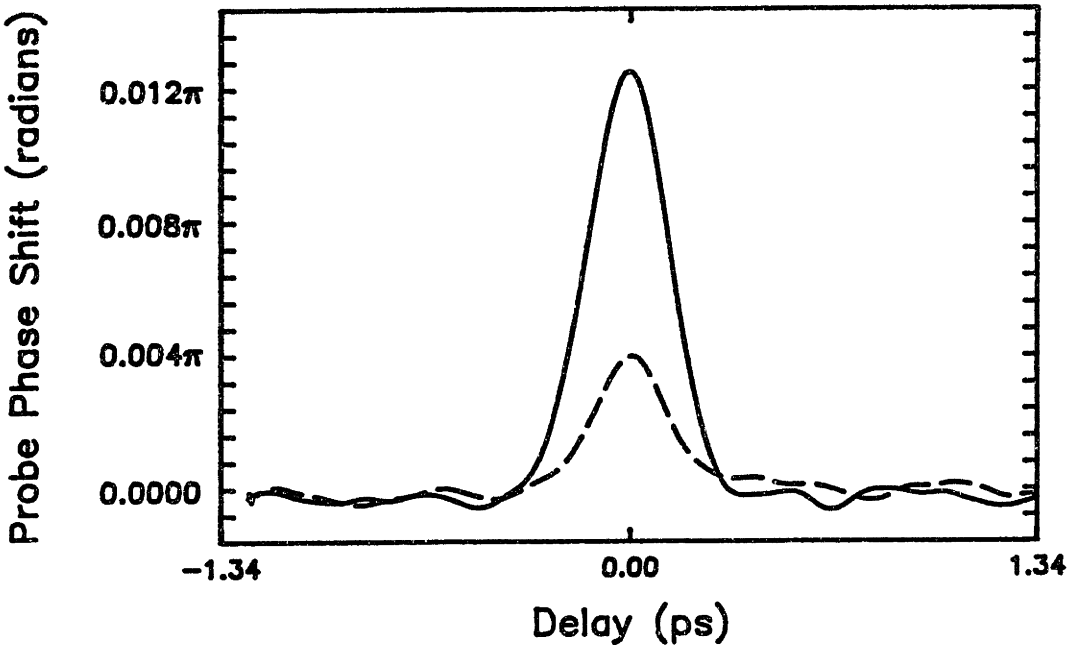

Figure 7.16: Measured probe phase shift as a function of pump-probe delay for copolarized (solid line) and cross-polarized (dashed line) pump-probe beams. The waveguide is a 23 cm length of dispersion shifted fiber.

7.3.2 Bulk Diodes

The results from the fiber measurements verify that the heterodyne technique and the ham radio receiver can be used to measure the ultrafast refractive index nonlinearities in waveguides. Figure 7.17 shows the measured probe phase shift as a function of copolarized (dashed lines) and cross-polarized (solid lines) pump-probe delay for a bulk diode biased in the (a) absorption, (b) transparency, and (c) gain regimes [150]. Notice again that the fast dynamics occurring near zero time delay are not as sharp in the cross-polarized data as in the co-polarized data. This blurring of the response is due to a combination of effects; pump-probe pulse walk-off, anisotropy in the nonlinearity and differences in the coherent coupling term. However, both sets of data are qualitatively the same.

The long-lived change or step change in refractive index is associated with pump-induced carrier density changes. In agreement with previous results [54] [61] [67], a decrease in carrier density increases the refractive index. A simple physical picture that confirms this behavior is given by the Drude model. If the electrons and holes in a semiconductor can be treated as free, noninteracting

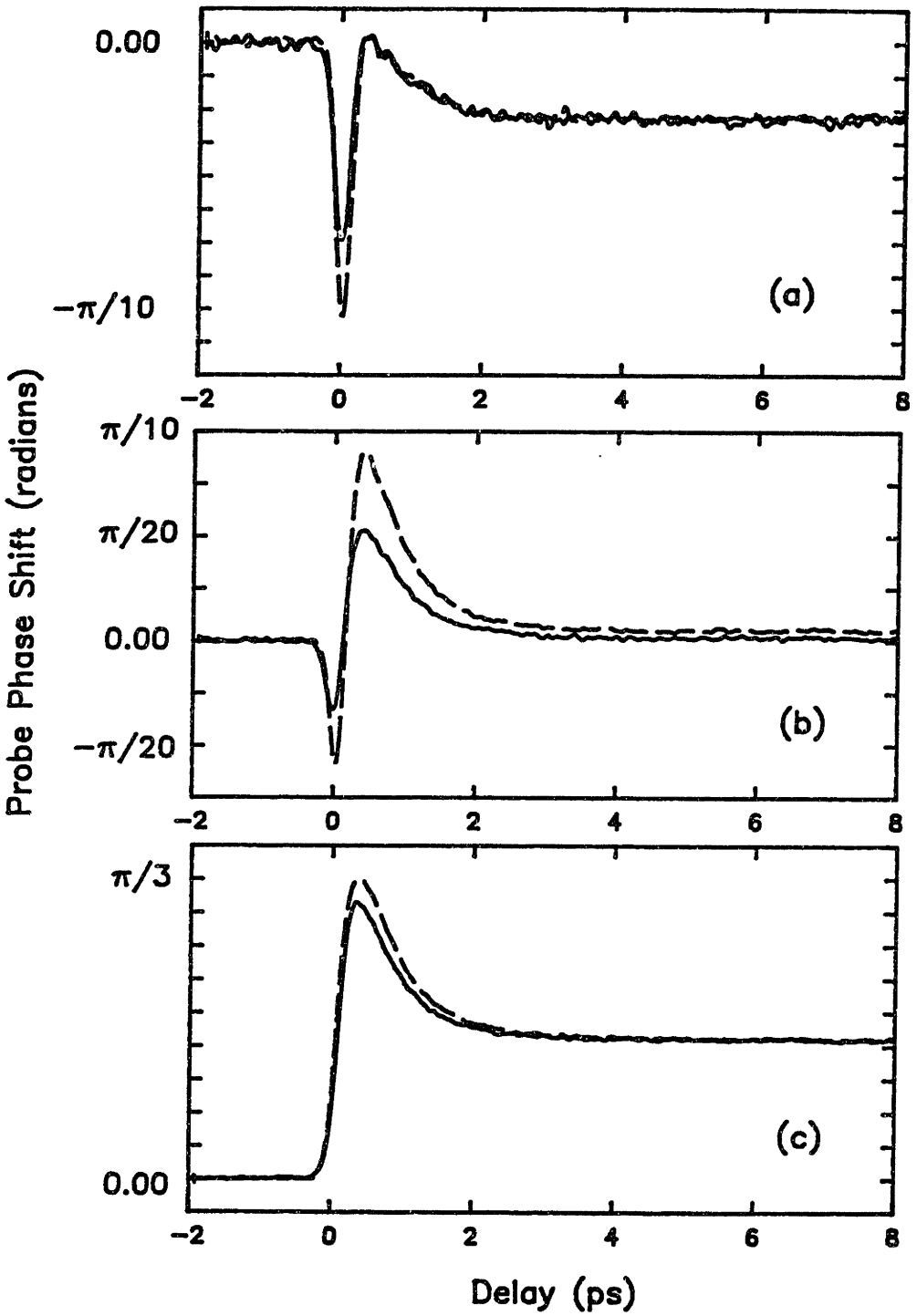

Figure 7.17: Measured probe phase shift as a function of pump-probe delay for copolarized (dashed line) and cross-polarized (solid line) pump-probe beams for a bulk diode biased in the (a) absorption, (b) transparency, and (c) gain regimes.

particles [21], then their influence on the material refractive index can be related to the plasma frequency, ω_P, via

$$\omega_P^2 = \frac{Nq^2}{\epsilon_0 m} \tag{7.14}$$

where N is the free carrier density, q is the electronic charge, ϵ_0 is the permittivity of free space, and m is the mass of the carriers. The refractive index, n, is given by

$$n^2 = \epsilon(\omega) = 1 - \frac{\omega_P^2}{\omega^2}. \tag{7.15}$$

In the absorption regime, the carrier density, N, is increased by stimulated absorption of the pump. Therefore, the plasma frequency increases and the refractive index decreases. Conversely, in the gain regime, stimulated emission caused by the pump decreases the carrier density, decreasing the plasma frequency and increasing the refractive index. At the transparency point, there is not net carrier density change and no long-lived change in refractive index.

In addition to the long-lived change in refractive index, there is a transient increase in refractive index observed in all three regimes of diode operation, recovering with a time constant of $\sim$ 600 fs, consistent with the delayed carrier heating signal we observed in the gain data. This result agrees with previous studies of AlGaAs devices that showed that for photon energies near the band-gap energy, heating the carrier distribution increases the refractive index [61]. To the extent that carrier heating causes a temporary decrease in the gain experienced by the probe, the increase in refractive index is also consistent with the Drude picture. Finally, in all three regimes of operation we observe an instantaneous decrease in the refractive index. This component has been attributed to a rapid electronic, or virtual, process [51] [61] [67].

7.3.3 Strained-Layer Multiple Quantum Well Diodes

Figure 7.18 shows the measured probe phase shift as a function of copolarized (dashed lines) and cross-polarized (solid lines) pump-probe delay for a SLMQW diode biased in the (a) absorption, (b) transparency, and (c) gain regimes [151].

In these diodes, differences between copolarized and cross-polarized results are attributed to the polarization selection rules as well as to pump-probe pulse walk-off and differences in the coherent artifact. Note that these pump-probe results are qualitatively similar to those obtained for the bulk diodes. In the copolarized data, there is a long-lived change in index due to pump-induced carrier density changes. In all three regimes, for both the copolarized and cross-polarized results, there is a transient increase in index that recovers with a 1 ps time constant and is associated with the heated carrier distribution cooling back to the lattice temperature. Also, in all cases we observe an instantaneous decrease in the refractive index.

We analyze the ultrafast refractive index data the same way we analyzed the nonlinear gain data. We assume a form for the impulse response function, $h(t)$, and then convolve it with an experimentally determined autocorrelation function. The difference between the $h(t)$ used to fit the gain data and the $h(t)$ used to fit the index data is the value of the various a_i's. For instance, in the refractive index data, $a_0 < 0$ in the absorption regime and $a_0 > 0$ in the gain regime because increasing the carrier density decreases the refractive index and vice versa. Also, carrier heating increases the refractive index so that $a_2 > 0$ and the delay causes $a_1 < 0$. The instantaneous change in refractive index is modeled by a_3, and is negative in all three regimes.

We can fit all the data in Figures 7.17 and 7.18 using the impulse response function given by Eq.(7.6). Table 7.1 lists the values of the amplitudes (a_i's) and time constants (τ_i's) used in the fits. In these data, we have not subtracted the coherent coupling term from the copolarized data. The reason is that in these index data, the magnitude of the pump-probe signal at zero time delay is almost zero, due to the offsetting behavior of the instantaneous and delayed carrier components. Therefore, the amplitude of the coherent coupling term (proportional to the half the value of the pump-probe signal at zero time delay) is small. Also, the slope of the pump-probe signal at zero time delay is so large, that small errors in defining the zero time delay position will result in relatively large changes in the estimation of the amplitude of the coherent artifact. Note that we are interested in understanding the amount of phase change one pulse induces on another. Therefore, the impulse response function, including the coherent artifact, is the most accurate predictor. For this reason, we have not subtracted the coherent coupling term from the instantaneous portion of the cross-polarized data either.

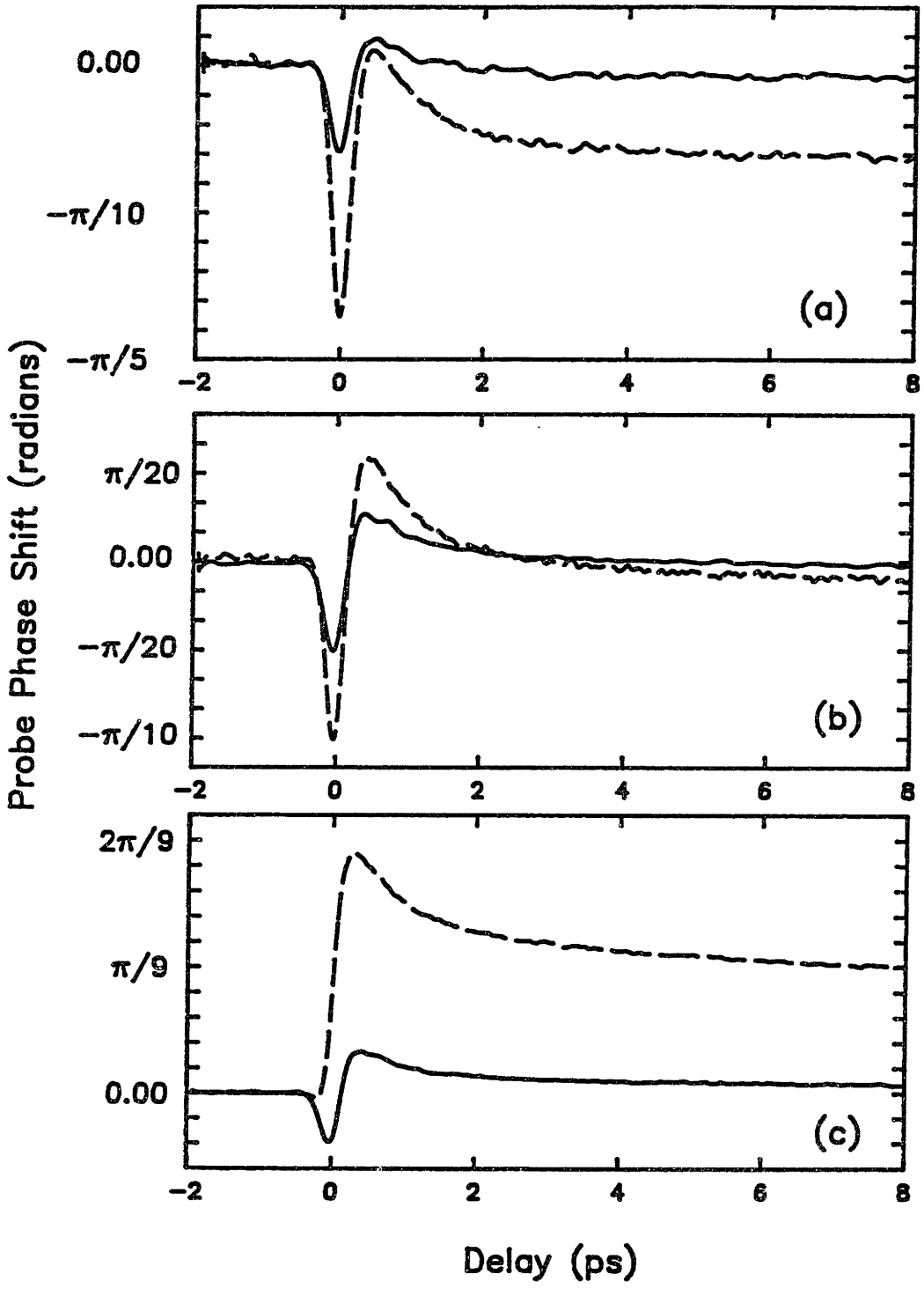

Figure 7.18: Measured probe phase shift as a function of pump-probe delay for copolarized (dashed line) and cross-polarized (solid line) pump-probe beams for a SLMQW diode biased in the (a) absorption, (b) transparency, and (c) gain regimes.

DIODE	a_1	τ_1	a_2	τ_2	a_3
BULK (gain)	-1	0.2 ps	1	0.6 ps	0
(transparency)	-9	0.2 ps	9	0.6 ps	-1
(absorption)	-2.8	0.2 ps	2.8	0.6 ps	-1
SLMQW (gain)	-7.5	0.15 ps	7.5	1 ps	-1
(transparency)	-3.5	0.15 ps	3.5	1 ps	-1
(absorption)	-2.5	0.15 ps	2.5	1 ps	-1

(a) Copolarized pump-probe

DIODE	a_1	τ_1	a_2	τ_2	a_3
BULK (gain)	-1	0.2 ps	1	0.6 ps	0
(transparency)	-9	0.2 ps	9	0.6 ps	-1
(absorption)	-4.2	0.2 ps	4.2	0.6 ps	-1
SLMQW (gain)	-3.5	0.15 ps	3.5	1 ps	-1
(transparency)	-2.5	0.15 ps	2.5	1 ps	-1
(absorption)	-2.5	0.15 ps	2.5	1 ps	-1

(b) Cross-polarized pump-probe

Table 7.1: Components in the impulse response function fits for the (a) copolarized and (b) cross-polarized data shown in Figures 7.17 and 7.18.

It is interesting to note that the amplitude of the residual, or spectral hole burning component in the fits, (a_1+a_2), is always zero for the index data. Spectral hole burning is not expected to contribute to the refractive index measurements if the spectral hole is symmetric around the pump-probe wavelength. This behavior is a property of the Kramers-Kronig transformation. Transforming an absorption (or gain) curve that is symmetric around λ_0 gives zero index change at λ_0. Our measurements of the gain nonlinearities suggest there is spectral hole burning in these diodes. The measurements of the index nonlinearities suggest the spectral hole is symmetric. Behavior consistent with symmetric spectral holes has also been observed in active AlGaAs devices [67].

From these measurements, we can deduce the intensity dependent portion of the refractive index, Δn. The measured change in phase is related to the change in refractive index by, $\Delta n = \frac{\lambda}{2\pi L}\Delta\Phi$, where λ is the wavelength, $\Delta\Phi$ is the measured phase change, and L is the length of the diode. To compare the relative magnitudes of the various components, we use the data fitting procedure to separate out each of the components' contribution to the total response [61] (Figure 5.8). Figure 7.19 shows the fit (solid line), along with the separate components of the fit (dashed lines) for the co-polarized data in Figure 7.18 (c). The instantaneous portion of the signal gives index changes proportional to the intensity, I, according to $n_2 = \Delta n_i/I$ where $I = P_p/A_{eff}$. In the gain regime, we estimate $n_{2\|} = -1.8\times10^{-12}$ cm^2/W for the co-polarized pump-probe case and $n_{2\perp} = -0.8\times10^{-12}$ cm^2/W for the cross-polarized pump-probe case. Assuming the position of zero time delay is correct, these values of n_2 are twice the amplitude of the real n_2 for the material, due to the coherent artifact. The long-lived refractive index change due to pump-induced carrier changes recovers on a nanosecond time scale and is proportional to the subpicosecond pump pulse energy, $\mathcal{E}_p$, rather than the peak power. We will characterize this index change by a term $\Delta n_{step}/E_p$, where $E_p = \mathcal{E}_p/A_{eff}$ is the pulse energy density. For our data, $\Delta\Phi_{step\|}$=0.08 π radians, yielding $\Delta n_{step\|}/E_p$ = 8 cm^2/J. There is no step change in index for the cross-polarized data because stimulated transitions are forbidden for the TM-polarized pump. Since our pulses are also much shorter than the 1 ps carrier heating lifetime, the amplitude of that induced index change is also proportional to the pulse energy density. We calculate the index change due to delayed carrier heating as $\Delta n_{CH}/E_p$ and obtain $\Delta\Phi_{CH\|}$=0.07 π radians and $\Delta\Phi_{CH\perp}$=0.02 π radians, yielding $\Delta n_{CH\|}/E_p$ = 6.7

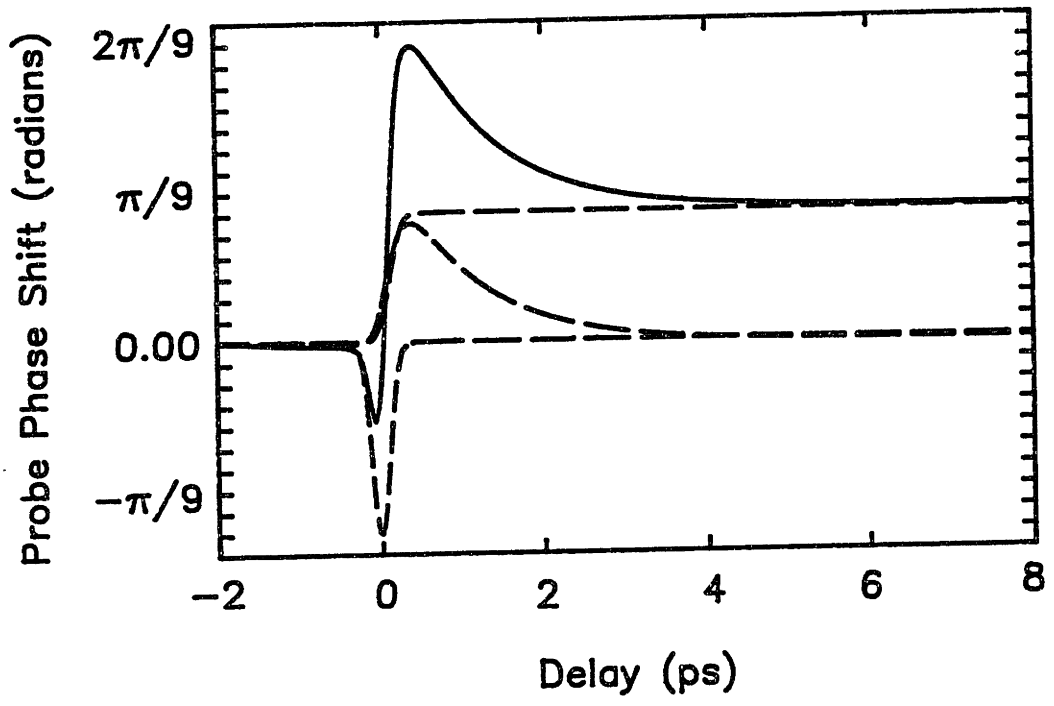

Figure 7.19: The solid line shows the fit to the copolarized data in Figure 7.18 (c). The dashed lines are the separate components in the fit.

cm^2/J and $\Delta n_{CH\perp}/E_p = 1.5$ cm^2/J. Thus, in our experiments the delayed carrier heating induced index change can be as large as the other measured index changes. In fact, at higher applied bias currents, the dominant index nonlinearity is that due to carrier heating. Note that for pulses longer than 1 ps, the delayed carrier heating index changes can be characterized by $n_{2ch} = \Delta n_{CH}/I = (\Delta n_{CH}\tau_{CH})/E_p$, where $n_{2ch\parallel} = 1 \times 10^{-12}$ cm^2/W and $n_{2ch\perp} = 0.22 \times 10^{-12}$ cm^2/W. A summary of the calculated Δn's for the bulk and SLMQW diodes in the three regimes of operation is given in Table 7.2.

Note that the amplitudes of the refractive index nonlinearities change in the different regimes of operation. This behavior suggests that the nonlinearities are carrier density dependent. In the nonlinear gain measurements, we observed that the amplitude of the step change due to pump-induced stimulated transitions and the carrier heating term were related to the free carrier density, N. In fact, in the rate equation model, both terms scale with N. Therefore, it is not surprising that the contributions of these components to the total index nonlinearity change in the various regimes of operation. However, the instantaneous term, that was only weakly dependent on carrier density in the gain measurements, depends

strongly on N in the index measurements. At high carrier densities, n_2 approaches zero. This behavior is consistent with a virtual process and has been previously attributed to the optical Stark effect [63] [67].

We point out that the Δn's we calculate are modal index changes. Any index change induced in the active region of the diode will be averaged across the spatial extent of the mode. Our estimation of the effective mode area in the diode, 3×10^{-8} cm^2, should be considered accurate to within a factor of 2. It is difficult to compare our measurements of n_2 to those in the literature because the calculated values depend very sensitively on approximations for A_{eff}. However, within an order of magnitude, our results agree with those reported for passive [64] [65] [66] and active [61] [67] AlGaAs devices. However, our results are inconsistent with those of Grant et al. [145]. The order of magnitude of their deduced n_2 agrees with our measured value, but the sign of n_2 does not agree. Further investigations are needed to clarify this discrepancy.

In conclusion, we have developed a novel heterodyne pump-probe technique in which the pump and probe pulses are collinear, copolarized, nominally at the same wavelength, but are still distinguishable. This technique uses heterodyne detection of femtosecond pulses whose spectra have been shifted by deflection at an acousto-optic modulator. Using a high-frequency (ham) radio receiver to detect the probe-reference beat, we are able to measure both gain and index nonlinearities in the InGaAsP diode amplifiers. The new technique improves the time resolution of some experiments by circumventing the group velocity walk-off associated with cross-polarized pump-probe beams and it allows the study of anisotropy in the waveguide nonlinearity.

Comparing copolarized and cross-polarized pump-probe transmission results in a SLMQW diode revealed a delay in the onset of carrier heating. When included explicitly in the impulse response function, a residual term whose amplitude flips sign at the transparency point was revealed. This residual term, while small compared to the carrier heating term, is the first clear time domain evidence for spectral hole burning in InGaAsP diodes. Measurements of the pump-induced index changes were used to calculate n_2 and Δn_{CH}, the instantaneous and carrier heating index nonlinearities. Our results agree well with previous results for active AlGaAs devices.

DIODE	n_2 ($\times 10^{-12}$ cm^2/W)	Δn_{step} (cm^2/J)	Δn_{CH} (cm^2/J)	n_{2CH} ($\times 10^{-12}$ cm^2/W)
BULK (gain)	0	42	43	6.5
(transparency)	-1.5	0	5.0	0.8
(absorption)	-3.5	-7.7	5.3	0.8
SLMQW (gain)	-1.8	8.0	6.7	1.0
(transparency)	-1.6	0	3.3	0.5
(absorption)	-2.0	-4.8	2.7	0.4

(a) Copolarized pump-probe

DIODE	n_2 ($\times 10^{-12}$ cm^2/W)	Δn_{step} (cm^2/J)	Δn_{CH} (cm^2/J)	n_{2CH} ($\times 10^{-12}$ cm^2/W)
BULK (gain)	0	33	33	5.0
(transparency)	-0.8	0	2.7	0.4
(absorption)	-2.0	-5.6	4.7	0.7
SLMQW (gain)	-0.8	0	1.5	0.2
(transparency)	-0.9	0	1.0	0.1
(absorption)	-0.7	-0.5	1.0	0.1

(b) Cross-polarized pump-probe

Table 7.2: Calculated values for the nonlinear index coefficients.

Chapter 8

Conclusion

Through a series of time domain studies, we have characterized the ultrafast nonlinearities in InGaAs/InGaAsP diode lasers and amplifiers at 1.5 μm. Our results suggest that delayed carrier heating, two photon absorption and spectral hole burning contribute to the gain nonlinearities and delayed carrier heating and an instantaneous electronic, or virtual process contribute to the index nonlinearities in these diodes. In this chapter, we will consider the importance of these nonlinearities to applications such as high-speed laser modulation, diode modelocking, short pulse amplification, and all-optical switching. We will show that our results are consistent with a number of other experiments, both in the time and frequency domains. Finally, we will discuss some future experiments and present conclusions.

8.1 Summary of Our Results

Measurements of the group velocity dispersion (GVD) in the 1.5 μm diodes led to a number of interesting conclusions. First, we observed the polarization dependence of the group velocity [105] [106] and learned that cross-polarized pump-probe pulses were walking-off from each other as they traveled through the diode. Pump-probe pulse walk-off gives an effective pulse broadening that can limit the time resolution of some experiments. As a result, we developed the heterodyne pump-probe technique. The GVD measurements also showed that critical pulsewidths for 0.5 mm to 1 mm long devices were less than 90 fs. Therefore, pulses longer than

$\sim$ 150 fs experienced negligible broadening while passing through the diodes. We also found that the dispersion in the diode is dominated by material dispersion. The material in the bulk and MQW active regions is similar, consistent with the similar GVD measured in the two structures.

We reviewed some of our earlier measurements of gain nonlinearities in diode amplifiers at 1.5 μm [114] [121]. Those data showed strong gain nonlinearities due to two photon absorption (TPA) and carrier heating. In addition to these nonlinearities, we observed a transient increase in probe gain in all three regimes of operation that recovered with a 100-200 fs time constant. Using a novel heterodyne pump-probe technique to study the gain nonlinearities in strained-layer multiple quantum well (SLMQW) diodes, we found that most of the transient increase in probe gain can be associated with a delay in the onset of carrier heating [141] [152]. This delay is attributed to the thermalization time for highly excited free carriers in a dense carrier sea. Analyzing the data with an impulse response function that included the delay in carrier heating explicitly revealed the presence of a component of the total nonlinear response whose amplitude changed sign at the transparency point. This component of the response has been attributed to spectral hole burning. In the gain regime, the amplitude of the spectral hole burning component is small compared to the delayed carrier heating and two photon absorption components. Using this explicit impulse response function to analyze our original pump-probe results for bulk and MQW diodes also revealed a small component in the total nonlinear response due to spectral hole burning.

Besides the study of more complex structures such as the SLMQW diodes, the heterodyne pump-probe technique allowed us to compare results of copolarized and cross-polarized pump-probe experiments. Differences between the copolarized and cross-polarized responses may be due to differences in the amplitude of the coherent artifact, effective pulse broadening in the cross-polarized experiments and anisotropy in the waveguide nonlinearity. Data analysis suggested that the effects of the coherent artifact and effective pulse broadening accounted for most of the observed differences in the copolarized and cross-polarized results.

Short pulse gain saturation measurements showed that the output saturation energies for subpicosecond pulses differed significantly from those for multipicosecond pulses [42] [120]. In fact, the saturation behavior for 20 ps pulses was essentially the same as for a cw beam with the same average power. To model

the saturation behavior, we altered the standard set of rate equations for carrier density and photon flux to include the effects of carrier heating. This model predicted output saturation energies for the 150 fs and 15 ps pulses that agreed very well with the measured energies. We point out that the calculated difference in the output saturation energies is governed only by the carrier heating (cooling) time constant. Therefore, the excellent agreement between the predictions of the simple model and the experimental results suggest that carrier heating is the dominant gain nonlinearity for diodes biased above the transparency point.

We also performed the first subpicosecond pump-probe studies of refractive index nonlinearities in these long wavelength diodes by extending the heterodyne pump-probe technique to measure pump-induced probe phase changes [151]. We measured the nonlinear probe phase shift for bulk and SLMQW diodes biased in the absorption, transparency, and gain regimes. Our results revealed pump-induced index changes due to stimulated transitions, delayed carrier heating, and an instantaneously recovering process. This instantaneous process has been observed in passive [64] [65] [66] and active [67] [142] AlGaAs waveguides and has been attributed to a rapid electronic, or virtual process. Theoretical predictions have suggested that such a response may be due to TPA, electronic Raman, and the optical Stark effect [63]. We showed that the n_2 associated with the rapid electronic or virtual process is on the order of -10^{-12} cm^2/W. The n_{2CH} associated with delayed carrier heating for picosecond pulses has the opposite sign, but is of the same order of magnitude as n_2. These values of the nonlinear index are carrier density, and pump-probe wavelength, dependent. For instance, n_{2CH} increases with increasing carrier density, whereas n_2 decreases with increasing carrier density. We will show that the relative importance of index nonlinearities due to carrier heating and the instantaneous process will depend also on the optical pulsewidths used to induce and sense the nonlinearities.

Much hope has been held out for the application of semiconductor waveguides to all-optical switching. One possible advantage of semiconductor waveguides, compared to optical fibers for instance, is the large magnitude of n_2 (four orders of magnitude greater in the semiconductor waveguides than in optical fibers). We have performed initial investigations into the applicability of these InGaAsP active waveguides to all optical switching. For some time, researchers have proposed using the below-band (no linear loss) index nonlinearities to build all-optical

switches. However, pulse intensities large enough to produce significant index changes also induce TPA. In some cases, this nonlinear absorption completely attenuates (limits) the signal. Even in cases where there is not complete absorption of the signal pulse, the carrier generation associated with TPA has limited switching speeds to a few nanoseconds [65] [66]. Our results suggest that better switches may be designed using above-band index and gain nonlinearities. First, there is a resonant enhancement of n_2 above the band-edge [61]. Second, the diode can be biased to the transparency regime, where there is no net carrier generation due to stimulated transitions. For high intensity pump pulses, where significant numbers of carriers can be generated via TPA, the diode bias current can be tuned so that on average, there is no net carrier generation. With no net carrier generation, the switching speed should be limited only by the recovery times of the nonlinearities that are producing the phase shifts. In our diodes, pumped with subpicosecond optical pulses, we expect the nonlinearities to have recovered completely within approximately 5 ps.

Figure 8.1 shows the measured pump-induced probe phase shift for a bulk diode biased at the transparency point. (Note that in a switching application, the pump would be called the control pulse and the probe would be called the signal pulse.) In this case, the pump pulse energy was $\sim$ 10 pJ, and the pulsewidth was 150 fs. Note that very large index changes are observed, even for this modest pump pulse energy. However, for these short pulses, the sign of the nonlinear index varies, depending on the relative delay between the pump and probe pulses. For all-optical switching applications, it may be desirable to have an index nonlinearity that doesn't change sign. One way to accomplish this is to lengthen the optical pulse. Figure 8.2 shows the probe phase shift predicted by convolving the appropriate impulse response function determined in Chapter 7 with autocorrelation functions that represent pulses of various pulsewidths but the same pulse energy. Note that as the pulsewidth increases, carrier heating dominates the nonlinear response. For pulses longer than 600 fs, the nonlinear index change is always positive. Note also that in these calculations, we have held the pump pulse energy constant. As a result, the peak phase shift induced by the longer pulses is less than that induced by the shorter pulses (because the pulse peak power is less). Increasing pump energy in the longer pulses should produce larger peak phase shifts.

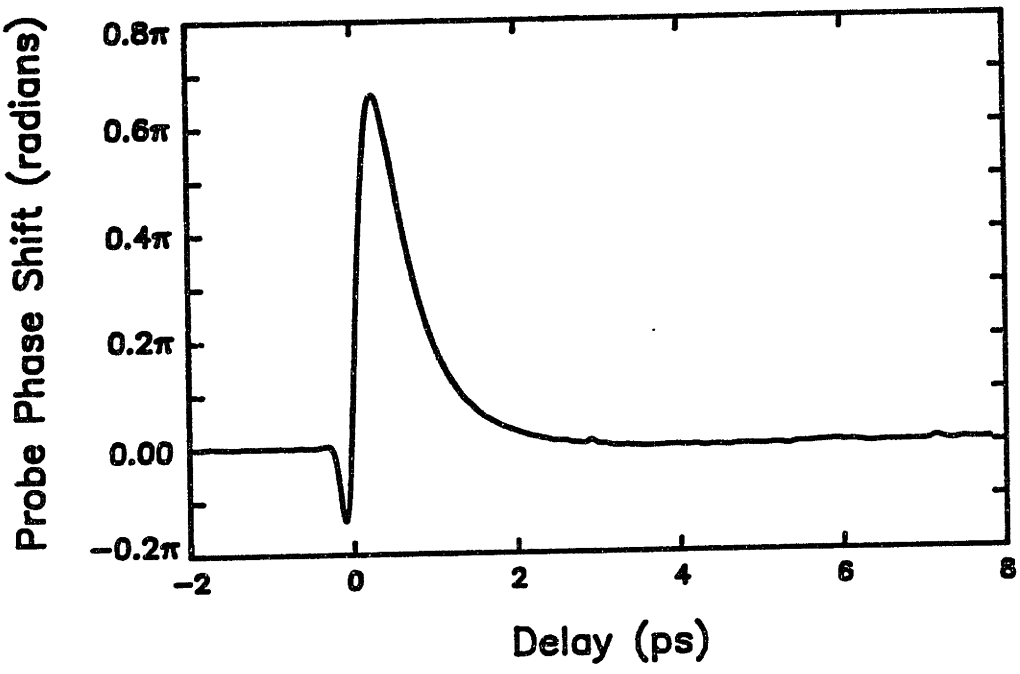

Figure 8.1: Measured probe phase shift versus copolarized pump-probe delay for a pump pulse energy of ~ 10 pJ and pulsewidth of 150 fs. The bulk diode is biased at the transparency point.

We have measured the changes in probe phase shift as a function of copolarized pump-probe delay for pump pulses with ~ 10 pJ pulse energy and pulsewidths ranging from 160-700 fs. Figure 8.3 shows the measured probe phase shifts. Note the excellent agreement between the measured and calculated (Figure 8.2) responses. Note also, that the largest observed probe phase shifts are 0.7 π. This phase shift may be too small for practical switching devices which would require a phase shift of π to turn completely on or off. Presumably, we could increase the probe phase shift if we increased the pump pulse energy. Unfortunately, ~ 10 pJ was the highest pulse energy attainable at the time. Also note that the effective n_2 for the semiconductor waveguide is pulsewidth dependent. Figure 8.4 shows the measured index nonlinearities (solid lines) along with the experimentally determined pump-probe autocorrelation functions for the 160 fs and 700 fs pump-probe pulses. For pulses shorter than ~ 150 fs in duration, the "instantaneous" nonlinearities dominate and the effective n_2 is negative. However, for pulses greater than 1 ps in duration, the carrier heating nonlinearities dominate and the effective n_2 is positive. For pulsewidths between 150 fs and 1 ps, n_2 is

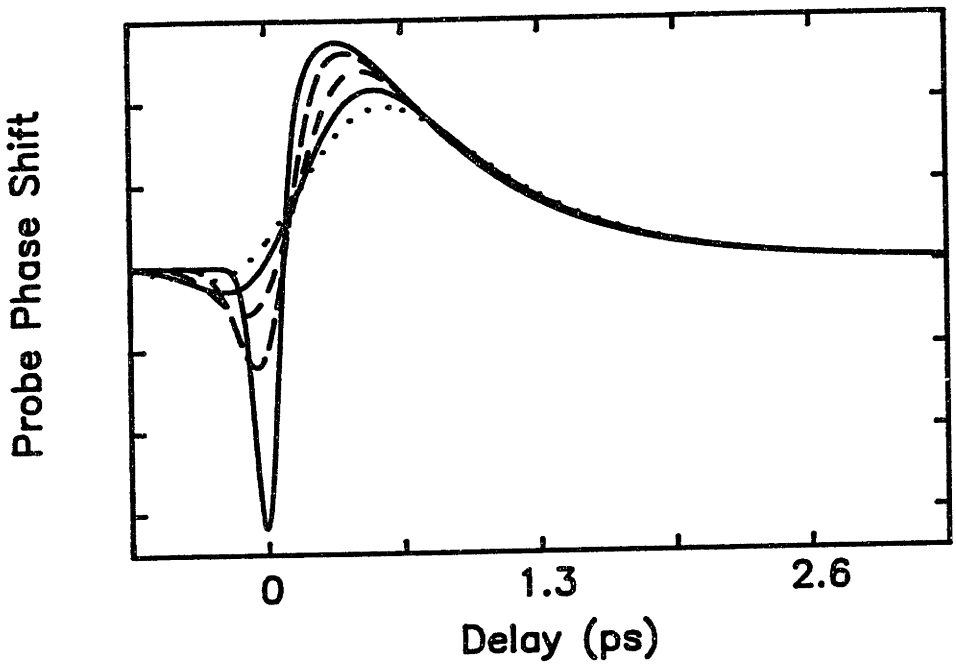

Figure 8.2: Calculated probe phase shift as a function of pump-probe delay. The curves are generated by convolving an experimentally determined impulse response function with autocorrelation functions representing pulses of constant pulse energy but varying pulse width (τ=100, 200, 300, 400 and 500 fs).

undefined.

There are large gain nonlinearities associated with the index nonlinearities shown in Figures 8.3 and 8.4. Figure 8.5 shows the change in probe transmission associated with the probe phase shift shown in Figure 8.3. Even for these modest pump pulse energies, the probe transmission is changing by more than 95%. Thus, the probe pulse is almost completely absorbed in the waveguide. Note that both TPA and carrier heating contribute significantly to the nonlinear gain. These large gain changes can be utilized in an absorptive switch. However, reactive switches, based on index nonlinearities, rather than resistive switches, based on gain nonlinearities, may be preferable because absorptive nonlinearities generate heat.

These results suggest that subpicosecond picojoule pulses can be exploited in designing nonlinear devices based on optically-induced gain changes. However, all-optical switches based on index nonlinearities may be more difficult to design because we must find a way to take advantage of the large index nonlinearities

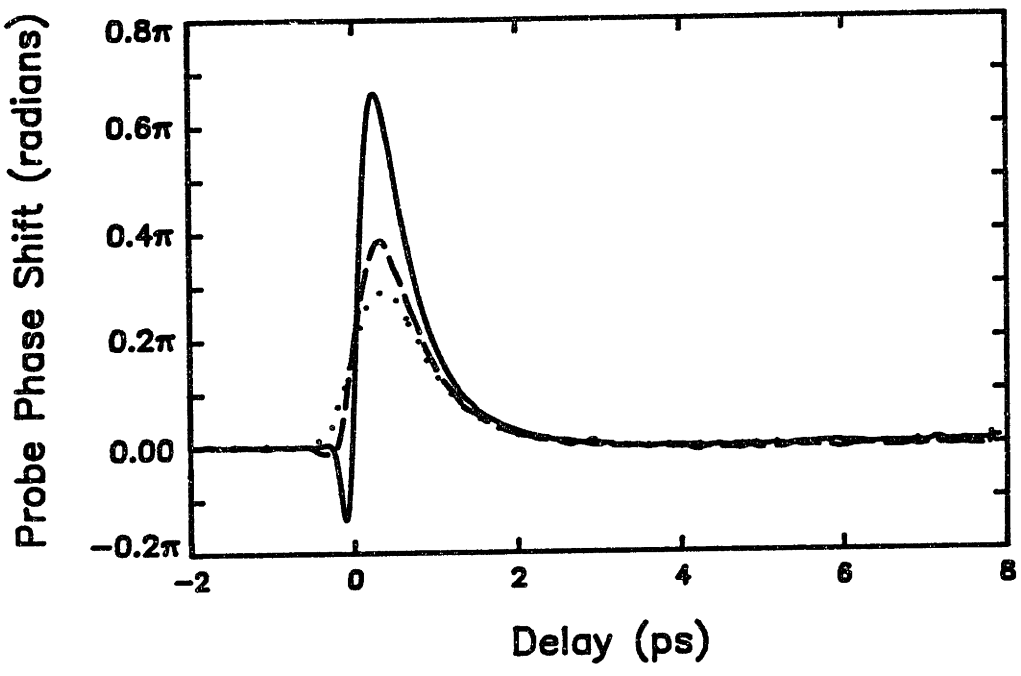

Figure 8.3: Measured probe phase shift versus copolarized pump-probe delay for pump pulse energies of ~ 10 pJ and pulsewidths of 160 fs (solid line), 420 fs (dashed line) and 700 fs (dotted line). The diode is biased at the transparency point.

while avoiding the large gain nonlinearities. One way to avoid the gain nonlinearities in an SLMQW device is to use TE-polarized pump pulses to stimulate large, above-band nonlinearities that will be sensed by a TE-polarized (below band) probe. Theory (Figure 2.11) and experiment [67] have shown that below-band probe pulses are sensitive to index changes induced above-band. In our case, we can imagine a TM-polarized probe delayed by -0.5 ps with respect to a TE-polarized pump. In a SLMQW diode, the only induced nonlinearity in probe transmission is TPA. The TPA nonlinearity is instantaneous and has recovered completely for pump-probe delays greater than 0.5 ps. Therefore, the 0.5 ps offset is enough to insure that the probe transmission is unaffected by the presence of the pump. However, the pump-induced index nonlinearities are still significant at a pump-probe delay of 0.5 ps (Figure 7.18). Therefore, by experimenting with pump-probe delays, polarizations, and pulsewidths, it may be possible to design an all-optical switch based on index nonlinearities, using devices that exist today. Further research is needed to determine the relative strengths and weaknesses of

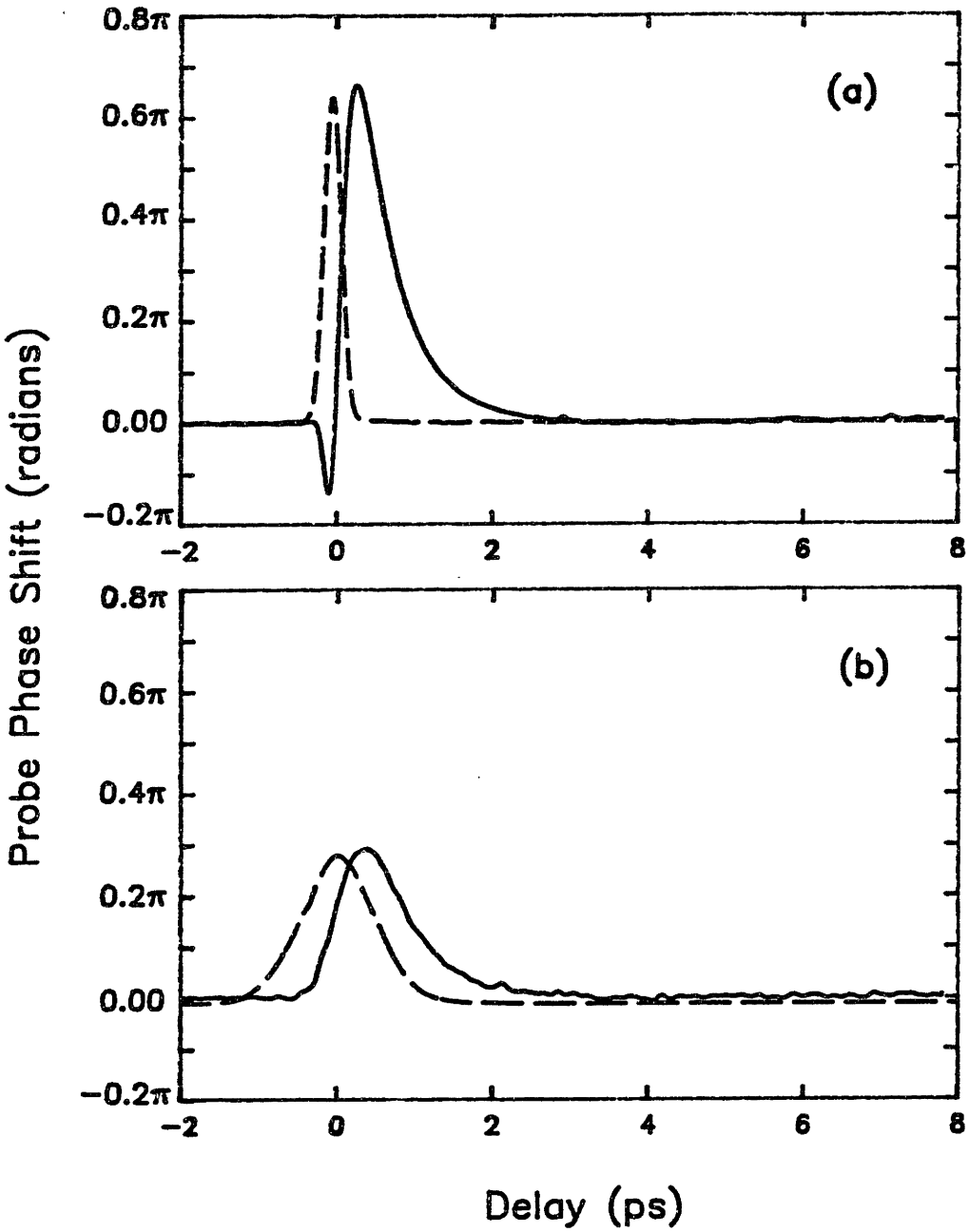

Figure 8.4: Measured probe phase shift as a function of copolarized pump-probe delay (solid lines) for pump pulse energies of ~ 10 pJ and pulsewidths of (a) 160 fs and (b) 700 fs. The dashed lines show the experimentally determined pump-probe autocorrelation functions. The diode is biased at the transparency point.

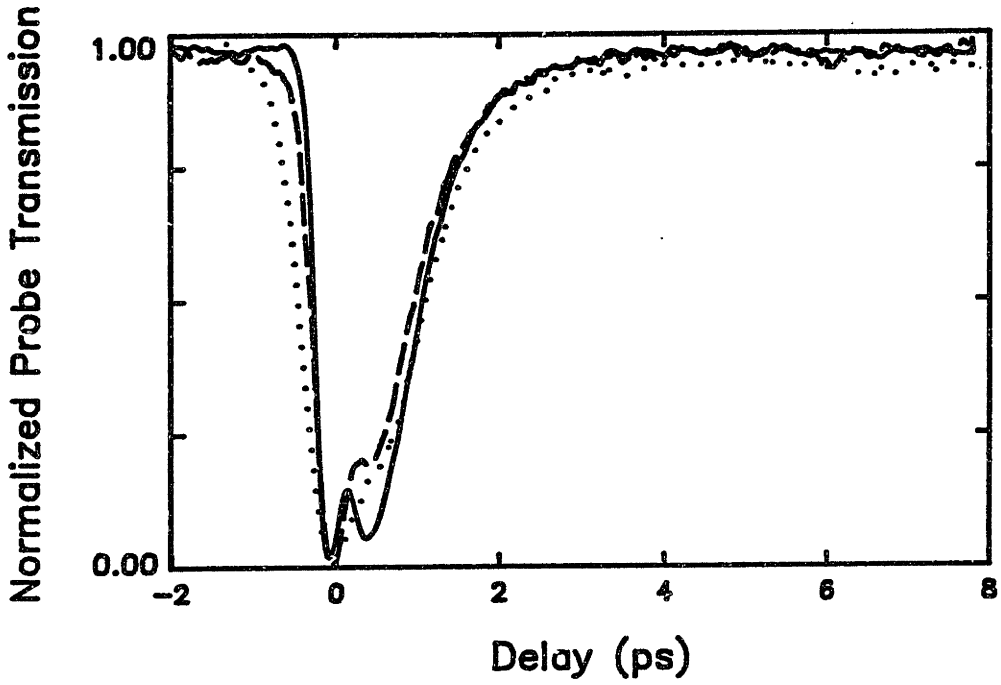

Figure 8.5: Measured change in probe transmission versus copolarized pump-probe delay for a pump pulse energies of ~ 10 pJ and pulsewidths of 160 fs (solid line), 420 fs (dashed line), and 700 fs (dotted line). The diode bias conditions are the same as in Figure 8.3.

all-optical switches based on gain and index nonlinearities in these diodes.

8.2 Summary of Other Results

Recently, there have been a number of experiments by other research groups that have confirmed the importance of carrier heating and TPA to the nonlinear gain in InGaAsP lasers and amplifiers. In the time domain, cross-polarized pump-probe measurements of gain nonlinearities in bulk diodes have agreed qualitatively with our cross-polarized results [116]. In those experiments, the authors varied the pump-probe wavelength rather than the diode bias current to reach the three regimes of operation. Their experimental results agree qualitatively with ours [115]. They attribute the nonlinear changes in probe transmission to carrier heating, TPA and spectral hole burning. However, there are discrepancies between the theoretical model and the data. These discrepancies may be due to the delay in the onset of carrier heating. Still, it is clear from their experimental plots, as

well as from other experiments with longer pump-probe pulses in MQW amplifiers [26], that carrier heating causes significant nonlinear gain compression and that the gain nonlinearity recovers with a limiting time constant of $\sim$ 1 ps.

Pump-probe experiments on active AlGaAs devices have confirmed the importance of carrier heating to the diode's total nonlinear response as well. Below band measurements of the nonlinear refractive index were the first to suggest the importance of free carrier absorption (FCA) in heating the distribution, and to show clearly, the delay in the onset of carrier heating [67]. Subsequent experiments on strained AlGaAs devices have suggested that the carriers are heated mainly by stimulated transitions [153]. It is clear from the calculations plotted in Figures 2.5 and 2.7 that the relative magnitudes of the stimulated and free carrier effects depend on a number of parameters. First, they depend on the ratio of the gain coefficient to the FCA coefficient. Also, they depend on the carrier density and the pump-probe wavelength (energy), relative to the average wavelength (energy) of the carrier distribution. There are diode bias conditions (low carrier densities and short pump-probe wavelengths) where stimulated carrier cooling should become the dominant effect. Therefore, carrier heating due to FCA and carrier heating or cooling due to stimulated transitions can cause nonlinear gain compression in these diodes. Which effect dominates depends on the bias conditions to the diode, the diode structure, and the optical wavelength.

Besides the time domain experiments described above, frequency domain experiments have attributed some portion of the diode's nonlinear response to carrier heating. In four wave mixing (FWM) experiments, two detuned optical signals (f_1 and f_2) are coupled into the waveguide under test. These two optical signals beat at their difference frequency ($f_1 - f_2$). When this beat frequency is less than 100 GHz, (nearly-degenerate FWM) the dominant effect is the modulation of the carrier density. However, the carrier density can not respond to driving frequencies greater than $\sim$ 100 GHz (nondegenerate FWM), and the response due to the nonlinear gain takes over. The modulation of the nonlinear gain can be thought of as a modulation of the intraband carrier energy distributions. This modulation of the gain (and the associated modulation of the index) will generate sideband signals at $2f_1 - f_2$ and $2f_2 - f_1$. The power in these sidebands is related to [154]

$$\Sigma K_i \frac{1}{1+(2\pi\tau_i)^2(f_1-f_2)^2} \tag{8.1}$$

where K_i is the strength of the physical effect responsible for the nondegenerate FWM signal and τ_i is the time constant. Measurements of the relative sideband power versus frequency detuning have shown a roll-off in the frequency detuning range of 200-500 GHz [62] [154] [155] [156]. Tiemeijer and Vahala et al. showed that their data could be fit by including the effect of nonlinear gain with a characteristic time constant of 650 fs [154] [155]. Kikuchi et al. show a similar plot of relative sideband power versus frequency detuning. However, their maximum detuning frequency was only 400 GHz (compared to Tiemeijer's 600 GHz and Vahala's 1.7 THz). They saw a resonance due to nonlinear gain but did not observe a clear roll-off in the generated sideband power. Therefore, they concluded that the nonlinearity time constant must be shorter than 400 fs ($1/[2\pi\Delta f]$ where Δf=400 GHz). Further experiments are needed to resolve the discrepancies in these results.

There are other reports in the literature that attribute some portion of an observed nonlinear response to carrier heating. However, these reports are unconvincing either because they use carrier heating to explain the leftover portion of the signal not explained by spectral hole burning [157] [158] or because the index changes or gain changes they observe are not consistent with those due to carrier heating [145]. There are other reports in the literature that may be explained by carrier heating. For instance, to date, the shortest optical pulses produced directly from a modelocked semiconductor laser have a pulsewidth of 640 fs [159]. This pulsewidth is consistent with the measured carrier cooling time. As we showed in Chapter 6, short pulses saturate the gain more easily than longer pulses. This gain saturation may limit the attainable pulsewidth in modelocked diode systems.

8.3 Future Work

While we have shown extensive time domain evidence for gain nonlinearities due to delayed carrier heating and TPA, and for index nonlinearities due to delayed carrier heating and an instantaneous electronic, or virtual process, there is still much work to be done. First, we should characterize our diodes, under the same

bias conditions, in the time and frequency domains. The strength of, and the time constants for, the nonlinearities measured in the pump-probe experiments should be verified by highly nondegenerate FWM experiments. Because the color center lasers have very wide tuning ranges, compared to temperature-tuned diode lasers for example, we should be able to measure the relative sideband ratio for frequency detunings greater than 500 GHz. Such a study would clarify the relationship between pump-probe and FWM experiments. Also, we should map out the behavior of the various components in the nonlinear response as a function of wavelength. In that case, the carrier density, N, would be constant. Then it may be possible to determine the relative importance of FCA induced heating and stimulated heating or cooling.

The measurements of the nonlinear index presented in this thesis are preliminary. There again, careful studies of how the different components in the nonlinear response scale with pump-probe wavelength and carrier density may illuminate some of the different mechanisms responsible for the total response. As we mentioned before, further experiments are needed to determine the maximum phase shift attainable in such a device. Such a study may determine the strengths and weaknesses of various all-optical switching architectures.

8.4 Final Word

In conclusion, we have reported the results of an extensive experimental study of the ultrafast gain and index nonlinearities in InGaAsP diode lasers and amplifiers operating in the 1.5 μm region of the spectrum. We have studied the physical mechanisms responsible for linear and nonlinear changes in gain and refractive index. We have described the operation of the Additive Pulse Modelocked color center laser that generates the 100-200 fs optical pulses used in the experiments. We have employed a variety of time domain techniques to characterize the diodes. Pulse echo experiments measured values of the GVD that ranged from -0.6 to -0.95 μm^{-1}. Cross-polarized and bias-lead monitoring pump-probe experiments revealed large gain nonlinearities due to carrier heating, TPA, and an unidentified transient increase in probe transmission. A novel heterodyne pump-probe technique was developed to study strained quantum well structures and to study copolarized as well as cross-polarized pump-probe results. Measurements using

this new technique showed a delay in the onset of carrier heating. Most of the previously unidentified transient increase in probe transmission was attributed to this delay in the onset of carrier heating. A residual component of the nonlinear response was attributed to spectral hole burning. The heterodyne technique was extended to measure refractive index nonlinearities. Large index nonlinearities due to delayed carrier heating and an instantaneous electronic, or virtual process were observed. Pulsewidth-dependent output saturation energies in these diodes were explained by the delayed carrier heating and TPA nonlinearities. The measured carrier cooling times were 650 fs for the bulk diodes, 700 fs for the MQW diodes and 1 ps for the SLMQW diodes. The hot carrier thermalization time was 100-250 fs in all three diode structures.

Bibliography

[1] L. F. Tiemeijer, "Optical properties of semiconductor lasers and laser amplifiers for fiber optical communications." Doctoral Thesis, 1992.

[2] D. P. Wilt, R. F. Karlicek, K. E. Strege, W. C. Dautremont-Smith, N. K. Dutta, E. J. Flynn, W. D. Johnson, and R. J. Nelson, "Channelled-substrate buried hetrostructure InGaAsP/InP lasers with vapor phase epitaxy base structure and liquid phase epitaxial regrowth," *J. Appl. Phys.*, vol. 56, pp. 710–712, 1984.

[3] G. P. Agrawal and N. K. Dutta, *Long Wavelength Semiconductor Lasers*. Van Nostrand Reinhold; New York, 1986.

[4] U. Koren, B. I. Miller, Y. K. Su, T. L. Koch, and J. E. Bowers, "Low internal loss separate confinement heterostructure InGaAs/InGaAsP quantum well laser," *Appl. Phys. Lett.*, vol. 51, no. 21, pp. 1744–1746, 1987.

[5] U. Koren, M. Oron, M. G. Young, B. I. Miller, J. L. D. Miguel, G. Raybon, and M. Chien, "Low threshold highly efficient strained quantum well lasers at 1.5 micrometer wavelength," *Electron. Lett.*, vol. 26, no. 7, pp. 465–467, 1990.

[6] T. Saitoh and T. Mukai, "Recent progress in semiconductor laser amplifiers," *J. Lightwave Technol.*, vol. 6, pp. 1656–1664, 1988.

[7] R. S. Tucker, "High-speed modulation of semiconductor lasers," *J. Lightwave Technol.*, vol. LT-3, pp. 1180–1192, 1985.

[8] K. Inoue, T. Mukai, and T. Saitoh, "Nearly degenerate four-wave mixing in a travelling-wave semiconductor laser amplifier," *Appl. Phys. Lett.*, vol. 51, pp. 1051–1053, 1987.

[9] R. M. Jopson, T. E. Darcie, K. T. Gayliard, R. T. Ku, R. E. Tench, T. C. Rice, and N. A. Olsson, "Measurement of carrier-density mediated intermodulation distortion in an optical amplifier," *Electron. Lett.*, vol. 23, no. 25, pp. 1394–1395, 1987.

[10] I. W. Marshall, D. M. Spirit, and M. J. O'Mahoney, "Picosecond pulse response of a travelling-wave semiconductor laser amplifier," *Electron. Lett.*, vol. 23, no. 16, pp. 818–819, 1987.

[11] G. Eisenstein, P. B. Hansen, J. M. Wiesenfeld, R. S. Tucker, and G. Raybon, "Amplification of high repetition rate picosecond pulses using an InGaAsP traveling-wave optical amplifier," *Appl. Phys. Lett.*, vol. 53, pp. 1539–1541, 1988.

[12] A. Lattes, H. A. Haus, F. J. Leonberger, and E. P. Ippen, "An ultrafast all-optical gate," *IEEE J. Quantum Electron.*, vol. 19, no. 11, p. 1718, 1983.

[13] H. A. Haus, E. P. Ippen, and F. J. Leonberger, "Nonlinear optical waveguide devices," in *Optical Signal Processing (J. L. Horner, ed.)*, pp. 245–277, Academic Press, Inc., New York, 1987.

[14] G. I. Stegeman, E. M. Wright, N. Finlayson, R. Zanoni, and C. T. Seaton, "Third order nonlinear integrated optics," *IEEE J. Lightwave Technol.*, vol. 6, no. 6, p. 953, 1988.

[15] M. S. Stix, M. P. Kesler, and E. P. Ippen, "Observations of subpicosecond dynamics in GaAlAs laser diodes," *Appl. Phys. Lett.*, vol. 48, pp. 1722–1724, 1986.

[16] M. P. Kesler and E. P. Ippen, "Subpicosecond gain dynamics in GaAlAs laser diodes," *Appl. Phys. Lett.*, vol. 51, pp. 1765–1767, 1987.

[17] E. P. Ippen and C. V. Shank, "Techniques for measurement," in *Ultrashort Light Pulses, Picosecond Techniques and Applications (S.L. Shapiro, ed)*, New York: Springer, 1977.

[18] M. P. Kesler and E. P. Ippen, "Femtosecond time-domain measurements of group velocity dispersion in AlGaAs diode lasers," *Electron. Lett.*, vol. 25, no. 10, pp. 640–641, 1989.

[19] R. N. Hall, G. E. Fenner, J. D. Kingsley, T. J. Soltys, and R. O. Carlson, "Coherent light emission from GaAs junctions," *Phys. Rev. Lett.*, vol. 9, p. 366, 1962.

[20] M. I. Nathan, W. P. Dumke, G. Burns, F. H. Dill, and G. Lasher, "Stimulated emission of radiation from GaAs p-n junctions," *Appl. Phys. Lett.*, vol. 1, p. 62, 1962.

[21] T. M. Quist, R. H. Rediker, R. Keyes, W. E. Krag, B. Lax, A. L. McWhorter, and H. J. Zeiger, "Semiconductor masers of GaAs," *Appl. Phys. Lett.*, vol. 1, p. 91, 1962.

[22] N. Holonyak and S. F. Bevacqua, "Coherent (visible) light emission from $Ga(As_{1-x}P_x)$ junctions," *Appl. Phys. Lett.*, vol. 1, p. 82, 1962.

[23] H. C. Casey and M. B. Panish, *Heterostructure Lasers, Part A: Fundamental Principles.* Academic Press : New York, 1978.

[24] N. W. Ashcroft and N. D. Mermin, *Solid State Physics.* Saunders College; Philadelphia, 1976.

[25] P. Rees, H. D. Summers, and P. Blood, "Gain-current calculations for bulk GaInP lasers including many body effects," *Appl. Phys. Lett.*, vol. 59, no. 27, pp. 3521–3523, 1991.

[26] N. K. Dutta, "Gain-current relation for $In_{0.72}Ga_{0.28}As_{0.6}P_{0.4}$ lasers," *J. Appl. Phys.*, vol. 52, no. 1, pp. 55–60, 1981.

[27] N. K. Dutta, "Calculated absorption, emission and gain in $In_{0.72}Ga_{0.28}As_{0.6}P_{0.4}$," *J. Appl. Phys.*, vol. 51, no. 12, pp. 6095–6100, 1980.

[28] G. Eisenstein, R. S. Tucker, J. M. Wiesenfeld, P. B. Hansen, G. Raybon, B. C. Johnson, T. J. Bridges, F. G. Storz, and C. A. Burrus, "Gain recovery time of traveling-wave semiconductor optical amplifiers," *Appl. Phys. Lett.*, vol. 54, no. 5, pp. 454–456, 1989.

[29] G. Eisenstein, J. M. Wiesenfeld, M. Wegener, G. Sucha, D. S. Chemla, S. Weiss, G. Raybon, and U. Koren, "Ultrafast gain dynamics in 1.5 μm multiple quantum well amplifiers," *Appl. Phys. Lett.*, vol. 58, no. 2, pp. 158–160, 1991.

[30] B. Sermage, H. Eichler, J. Heritage, R. Nelson, and N. Dutta, "Photoexcited carrier lifetime and Auger recombination in 1.3-μm InGaAsP," *Appl. Phys. Lett.*, vol. 42, no. 3, pp. 259–261, 1983.

[31] E. Wintner and E. Ippen, "Nonlinear carrier dynamics in $Ga_xIn_{1-x}As_yP_{1-y}$ compounds," *Appl. Phys. Lett.*, vol. 44, no. 10, pp. 999–1001, 1984.

[32] W. Rideout, W. F. Sharfin, E. S. Koteles, M. Vassell, and B. Elman, "Well-barrier hole burning in quantum well lasers," *IEEE Photon. Technol. Lett.*, vol. 3, no. 9, pp. 784–786, 1991.

[33] R. Nagarajan, T. Fukushima, S. W. Corzine, and J. E. Bowers, "Effects of carrier transport on high-speed quantum well lasers," *Appl. Phys. Lett.*, vol. 59, no. 15, pp. 1835–1837, 1991.

[34] N. Tessler, R. Nagar, D. Abraham, G. Eisenstein, U. Koren, and G. Raybon, "Coupling between barrier and quantum well energy states in a multiple quantum well optical amplifier," *Appl. Phys. Lett.*, vol. 60, no. 6, pp. 665–667, 1992.

[35] S. Weiss, J. M. Wiesenfeld, D. S. Chemla, G. Raybob, G. Sucha, M. Wegener, G. Eisenstein, C. A. Burrus, A. G. Dentai, U. Koren, B. Miller, H. Temkin, R. Logan, and T. Tanbun-Ek, "Carrier capture times in 1.5 μm quantum well optical amplifiers," *Appl. Phys. Lett.*, vol. 60, no. 1, pp. 9–11, 1992.

[36] R. Nagarajan, T. Fukushima, M. Ishikawa, J. E. Bowers, R. S. Geels, and L. A. Coldren, "Transport limits in high-speed quantum-well lasres: Experiment and theory," *IEEE Photon. Technol. Lett.*, vol. 4, no. 2, pp. 121–123, 1992.

[37] N. Tessler and G. Eisenstein, "Distributed nature of quantum-well lasers," *Appl. Phys. Lett.*, vol. 62, no. 1, p. 10, 1993.

[38] A. Grabmaier, M. Schofthaler, A. Hangleiter, C. Kazmierski, M. Blez, and A. Ougazzaden, "Carrier transport limited bandwidth of 1.55 μm quantum-well lasers," *Appl. Phys. Lett.*, vol. 62, no. 1, p. 52, 1993.

[39] W. H. Knox, D. S. Chemla, and G. Livescu, "High density femtosecond excitation of nonthermal carrier distributions in intrinsic and modulation doped GaAs quantum wells," *Sol. St. Electron.*, vol. 31, no. 3, pp. 425–450, 1988.

[40] W. H. Knox, D. S. Chemla, G. Livescu, J. E. Cunningham, and J. E. Henry, "Femtosecond carrier thermalization in dense fermi seas," *Phys. Rev. Lett.*, vol. 61, no. 11, p. 1290, 1988.

[41] J. L. Oudar, D. Hulin, A. Migus, A. Antonetti, and F. Alexandre, "Subpicosecond spectral hole burning due to nonthermalized photoexcited carriers in GaAs," *Phys. Rev. Lett.*, vol. 55, p. 2074, 1985.

[42] H. Lobentanzer, W. Stolz, J. Nagle, and K. Ploog, "Cooling of hot carriers in three- and two-dimensional $Ga_{0.47}$ $In_{0.53}$ As," *Phys. Rev. B*, vol. 39, p. 5234, 1989.

[43] C. R. Pidgeon, B. S. Wherrett, A. M. Johnston, J. Dempsey, and A. Miller, "Two-photon absorption in zinc-blende semiconductors," *Phys. Rev. Lett.*, vol. 42, no. 26, pp. 1785–1788, 1979.

[44] A.Villenueve, M. Sundheimer, N. Finlayson, G. I. Stegeman, S. Morasca, C. Rigo, R. Calvani, and C. D. Bernardi, "Two-photon absorption in InGaAlAs/InP waveguides at communications wavelengths," *Appl. Phys. Lett.*, vol. 56, pp. 1865–1867, 1990.

[45] Y. Lai, K. L. Hall, E. P. Ippen, and G. Eisenstein, "Short pulse gain saturation in InGaAsP diode laser amplifiers," *IEEE Photon. Technol. Lett.*, vol. 2, no. 10, pp. 711–713, 1990.

[46] R. Olshansky, P. Hill, V. Lanzisera, and W. Powazinik, "Frequency response of 1.3 μm InGaAsP high speed semiconductor lasers," *IEEE J. Quantum Electron.*, vol. QE-23, no. 9, pp. 1410–1418, 1987.

[47] T. Fukushima, J. E. Bowers, R. A. Logan, T. Tanbun-Ek, and H. Temkin, "Effect of strain on the resonant frequency and damping factor in InGaAs/InP multiple quantum well lasers," *Appl. Phys. Lett.*, vol. 58, no. 12, pp. 1244–1246, 1991.

[48] C. B. Su, J. Eom, C. H. Lange, C. B. Kim, R. B. Lauer, W. C. Rideout, and J. S. LaCourse, "Characterization of the dynamics of semiconductor lasers using optical modulation," *IEEE J. Quantum Electron.*, vol. 28, no. 1, pp. 118–127, 1992.

[49] C. B. Su and V. Lanzisera, "Effect of doping level on the gain constant and modulation bandwidth of InGaAsP semiconductor lasers," *Appl. Phys. Lett.*, vol. 45, no. 12, pp. 1302–1304, 1984.

[50] K. Uomi, T. Tsuchiya, M. Aoki, and N. Chinone, "Oscillation wavelength and laser structure dependence of nonlinear damping effect in semiconductor lasers," *Appl. Phys. Lett.*, vol. 58, no. 7, pp. 675–677, 1991.

[51] L. F. Tiemeijer, P. J. Thijs, P. J. de Waard, J. J. Binsma, and T. v. Dongen, "Dependence of polarization, gain, linewidth enhancement factor, and K factor on the sign of the strain of InGaAs/InP strained-layer multiquantum well lasers," *Appl. Phys. Lett.*, vol. 58, no. 24, pp. 2738–2740, 1991.

[52] W. F. Sharfin, J. Schlafer, W. Rideout, B. Elman, R. B. Lauer, J. LaCourse, and F. D. Crawford, "Anomalously high damping in strained InGaAs-GaAs single quantum well lasers," *IEEE Photon. Technol. Lett.*, vol. 3, no. 3, pp. 193–195, 1991.

[53] P. A. Morton, H. Temkin, D. L. Coblentz, R. A. Logan, and T. Tanbun-Ek, "Enhanced modulation bandwidth of strained multiple quantum well lasers," *Appl. Phys. Lett.*, vol. 60, no. 15, pp. 1812–1815, 1992.

[54] M. Sheik-Bahae, D. C. Hutchings, D. J. Hagan, and E. W. V. Stryland, "Dispersion of bound electronic nonlinear refraction in solids," *IEEE J. Quantum. Electron.*, vol. 27, no. 6, pp. 1296–1309, 1991.

[55] C. T. Hultgren, "Ultrafast refractive index changes in AlGaAs diode lasers." MIT Master's Thesis, January 1991.

[56] The computer program to calculate the Kramers-Kronig transformation was written by C. T. Hultgren.

[57] C. H. Henry, R. A. Logan, and K. A. Bertness, "Spectral dependence of the change in refractive index due to carrier injection in GaAs lasers," *J. Appl. Phys.*, vol. 52, no. 7, pp. 4457–4461, 1981.

[58] B. R. Bennett, R. A. Soref, and J. A. D. Alamo, "Carrier-induced change in refractive index of InP, GaAs, and InGaAsP," *IEEE J. Quantum Electon.*, vol. 26, pp. 113–122, 1990.

[59] J. Manning, R. Olshansky, and C. B. Su, "The carrier-induced index change in AlGaAs and 1.3 μm InGaAsP diode lasers," *IEEE J. Quantum Electron.*, vol. 19, no. 10, pp. 1525–1530, 1983.

[60] C. H. Henry, "Theory of the linewidth of semiconductor lasers," *IEEE J. Quantum Electron.*, vol. 18, no. 2, pp. 259–264, 1982.

[61] M. Osinski and J. Buus, "Linewidth broadening factor in semiconductor lasers-an overview," *IEEE J. Quantum Electron.*, vol. QE-23, no. 9, p. 9, 1987.

[62] A. Yariv, *Quantum Electronics, Third Ed.* John Wiley and Sons, New York, 1989.

[63] M. P. Kesler, "Ultrafast dynamics in GaAlAs laser diodes." MIT Doctoral Thesis, May 1988.

[64] C. T. Hultgren and E. P. Ippen, "Ultrafast refractive index dynamics in AlGaAs diode laser amplifiers," *Appl. Phys. Lett.*, vol. 59, no. 6, pp. 635–637, 1991.

[65] K. Kikuchi, M. Kakui, C. E. Zah, and T. P. Lee, "Observation of highly nondegenerate four-wave mixing in 1.5 μm traveling-wave semiconductor optical amplifiers and estimation of nonlinear gain coefficient," *IEEE J. Quantum Electron.*, vol. 28, no. 1, pp. 151–156, 1992.

[66] M. Sheik-Bahae and E. W. V. Stryland, "Theory of ultrafast nonlinear refraction in semiconductor optical amplifiers," in *Conference on Lasers and Electro-optics Technical Digest 1992*, p. QThD19, 1992.

[67] M. J. LaGasse, K. K. Anderson, H. A. Haus, and J. G. Fujimoto, "Femtosecond all-optical switching in AlGaAs waveguides using a time division interferometer," *Appl. Phys. Lett.*, vol. 54, no. 21, pp. 2068–2070, 1989.

[68] K. K. Anderson, M. J. LaGasse, C. A. Wang, J. G. Fujimoto, and H. A. Haus, "Femtosecond dynamics of the nonlinear index near the band edge in AlGaAs waveguides," *Appl. Phys. Lett.*, vol. 56, no. 19, pp. 1834–1836, 1990.

[69] M. J. LaGasse, K. K. Anderson, C. A. Wang, H. A. Haus, and J. G. Fujimoto, "Femtosecond measurements of the nonresonant nonlinear index in AlGaAs," *Appl. Phys. Lett.*, vol. 56, no. 5, pp. 417–419, 1990.

[70] C. T. Hultgren, D. J. Dougherty, and E. P. Ippen, "Above- and below-band femtosecond nonlinearities in active AlGaAs waveguides," *Appl. Phys. Lett.*, vol. 61, no. 23, pp. 2767–2769, 1992.

[71] J. I. Pankove, *Optical Processes in Semiconductors*. Dover Publications, Inc.; New York, 1971.

[72] P. N. Butcher and D. Cotter, *The Elements of Nonlinear Optics*. Cambridge University Press; Cambridge, 1991.

[73] G. Eisenstein, G. Raybon, and L. W. Schulz, "Deposition and measurements of electron-beam-evaporated SiO_x antireflection coatings on InGaAsP injection laser facets," *J. Lightwave Technol.*, vol. 6, pp. 12–16, 1988.

[74] B. I. Miller, E. F. Schubert, U. Koren, A. Ourmazd, A. H. Dayem, and R. J. Capik, "High quality narrow GaInAs/InP quantum wells grown by atmospheric organometallic vapor phase epitaxy," *Appl. Phys. Lett.*, vol. 49, no. 20, pp. 1384–1386, 1986.

[75] G. Bastard, *Wave Mechanics Applied to Semiconductor Heterostructures*. Halsted Press; New York, 1988.

[76] R. M. Jopson, G.Eisenstein, K. L. Hall, G.Raybon, C. A. Burrus, and U. Koren, "Polarisation-dependent gain spectrum of a 1.5 μm travelling-wave optical amplifier," *Electron. Lett.*, vol. 22, no. 21, pp. 1105–1107, 1986.

[77] E. Yablonovitch and E. O. Kane, "Band structure engineering of semiconductor lasers for optical communications," *J. Lightwave Technol.*, vol. 6, no. 8, pp. 1292–1299, 1988.

[78] E. Yablonovitch and E. O. Kane, "Reduction of lasing threshold current density by the lowering of valence band effective mass," *J. Lightwave Technol.*, vol. 4, no. 5, pp. 504–506, 1986.

[79] J. P. V. der Ziel, "Modelocking of semiconductor lasers," in *Semiconductors and Semimetals*, pp. 1–68, Academic Press, Inc, 1985.

[80] L. F. Mollenauer and R. H. Stolen, "The soliton laser," *Optics Letters*, vol. 9, pp. 13–15, January 1984.

[81] M. N. Islam, E. R. Sunderman, C. E. Soccolich, I. Bar-Joseph, N. Sauer, T. Y. Chang, and B. I. Miller, "Color center lasers passively mode locked by quantum wells," *IEEE J. Quantum Electron.*, vol. 25, no. 12, p. 2454, 1989.

[82] K. Tamura, E. P. Ippen, H. A. Haus, and L. E. Nelson, "77-fs pulse generation from a stretched pulse mode-locked all-fiber ring laser." to be published in Opt. Lett.

[83] P. N. Kean, R. S. Grant, X. Zhu, D. W. Crust, D. Burns, and W.Sibbett, "Enhanced mode-locking of colour centre lasers by coupled-cavity feedback control," in *Conference on Lasers and Electro-optics Technical Digest 1988*, p. 468, 1988.

[84] K. J. Blow and B. P. Nelson, "Improved modelocking of an F-center laser with a nonlinear external cavity," in *Ultrafast Phenomena Technical Digest 1988*, p. 446, 1988.

[85] J. Mark, L. Y. Liu, K. L. Hall, H. A. Haus, and E. P. Ippen, "Femtosecond pulse generation in a laser with a nonlinear external resonator," *Opt. Lett.*, vol. 14, pp. 48–50, January 1989.

[86] "Quantronix technical manual.".

[87] L. F. Mollenauer, N. D. Vieira, and L. Szeto, "Optical properties of the $Tl^0(1)$ center in KCl," *Physical Review B*, vol. 27, pp. 5332–5346, May 1983.

[88] L. F. Mollenauer, "Color center lasers," in *Laser Handbook*, pp. 143–228, Elsevier Science Publishers B.V., 1985.

[89] H. W. Kogelnik, E. P. Ippen, A. Dienes, and C. V. Shank, "Astigmatically compensated cavities for CW dye lasers," *IEEE J. Quantum Electron.*, pp. 373–379, March 1972.

[90] K. Naganuma, G. Lenz, and E. P. Ippen, "Variable bandwidth birefringent filter for tunable femtosecond pulses," *IEEE J. Quantum Electron.*, vol. 28, no. 10, pp. 2142–2150, 1992.

[91] R. H. Stolen and C. Lin, "Self-phase modulation in optical fibers," *Physical Review A*, vol. 17, pp. 1448–1453, April 1978.

[92] E. P. Ippen, H. A. Haus, and L. Y. Liu, "Additive pulse mode locking," *J. Opt. Soc. Am. B*, vol. 6, no. 9, pp. 1736–1745, 1989.

[93] H. A. Haus, J. G. Fujimoto, and E. P. Ippen, "Structures for additive pulse mode locking," *J. Opt. Soc. Am. B*, vol. 8, no. 10, pp. 2068–2076, 1991.

[94] H. A. Haus, J. G. Fujimoto, and E. P. Ippen, "Analytic theory of Additive Pulse and Kerr Lens mode locking," *IEEE J. Quantum Electron.*, vol. 28, no. 10, pp. 2086–2096, 1992.

[95] F. M. Mitschke and L. F. Mollenauer, "Stabilizing the soliton laser," *IEEE J. Quantum Electron.*, pp. 2242–2250, December 1986.

[96] E. P. Ippen, L. Y. Liu, and H. A. Haus, "Self-starting condition for additive-pulse mode-locked lasers," *Opt. Lett.*, vol. 15, no. 3, pp. 183–185, 1990.

[97] H. A. Haus and E. P. Ippen, "Self-starting of passively modelocked lasers," *Opt. Lett.*, vol. 16, no. 17, pp. 1331–1333, 1991.

[98] D. Marcuse, *Theory of Dielectric Optical Waveguides*. Academic Press; Boston, 1991.

[99] C. A. Brackett, "Second-order dispersion in oscillating GaAs junction lasers," *IEEE J. Quantum Electron.*, vol. 8, no. 2, pp. 66–69, 1972.

[100] J. P. V. der Ziel and R. A. Logan, "Dispersion of the group velocity refractive index in GaAs double heterostructure lasers," *IEEE J. Quantum Electron.*, vol. 19, no. 2, pp. 164–168, 1983.

[101] C. Cali and E. P. Ippen, "Technique for second order dispersion measurement in diode lasers," in *Proc. Second European Conference on Integrated Optics, Florence, Italy*, 1983.

[102] L. D. Westbrook, "Measurements of dg/dN and dn/dN and their dependence on photon energy in λ=1.5 μm InGaAsP laser diodes," *IEE Proc. J. Optoelectron.*, vol. 133, no. 2, pp. 135–142, 1986.

[103] L. D. Westbrook, "Dispersion of linewidth-broadening factor in 1.5 μm laser diodes," *Electron. Lett.*, vol. 21, no. 22, pp. 1018–1019, 1985.

[104] L. Zenteno, "Group delay dispersion measurements in InGaAsP 1.3-μm optical amplifiers," *J. Lightwave Technol*, vol. 7, pp. 39–44, 1989.

[105] K. Naganuma and H. Yasaka, "Group delay and α-parameter measurement of 1.3 μm semiconductor traveling-wave optical amplifier using the interferometric method," *IEEE J. Quantum Electron.*, vol. 27, no. 6, pp. 1280–1287, 1991.

[106] K. L. Hall, G.Lenz, and E. P. Ippen, "Femtosecond time-domain measurements of group velocity dispersion in diode lasers at 1.5 μm," *J. Lightwave Technol.*, vol. 10, no. 5, pp. 616–619, 1992.

[107] These calculations were performed by Gadi Lenz.

[108] G. Raybon, P. B. Hansen, U. Koren, B. I. Miller, M. G. Young, M. Newkirk, P. P. Iannone, C. A. Burrus, J. C. Centanni, and M. Zirngibl, "Two contact, 1 cm long, monolithic extended cavity laser actively mode-locked at 4.4 GHz," *Electron. Lett.*, vol. 28, no. 24, pp. 2220–2221, 1992.

[109] M. J. Adams, *An Introduction to Optical Waveguides.* John Wiley and Sons;New York, 1981.

[110] S. Adachi, "Optical properties of $In_{1-x}Ga_xAs_yP_{1-y}$ alloys," *Phys. Rev. B.*, vol. 39, no. 17, pp. 12612–12621, 1989.

[111] Z. Vardeny and J. Tauc, "Picosecond coherence coupling in the pump and probe technique," *Opt. Comm.*, vol. 39, no. 6, pp. 396–400, 1981.

[112] A. L. Smirl, T. F. Boggess, B. S. Wherrett, G. P. Perryman, and A. Miller, "Picosecond transient orientational and concentration gratings in Germanium," *IEEE J. Quantum Electron.*, vol. 19, no. 4, pp. 690–700, 1983.

[113] K. L. Hall, E. Ippen, J. Mark, and G. Eisenstein, "Subpicosecond gain dynamics in InGaAsP diode laser amplifiers," in *Conference on Lasers and Electro-optics Technical Digest 1989*, p. 280, April 1989.

[114] K. L. Hall, J. Mark, E. P. Ippen, and G. Eisenstein, "Femtosecond gain dynamics in InGaAsP optical amplifiers," *Appl. Phys. Lett.*, vol. 56, pp. 1740–1742, 1990.

[115] K. L. Hall, E. P. Ippen, J. Mark, and G. Eisenstein, "Ultrafast nonlinearities in InGaAsP diode laser amplifiers," in *Picosecond Electronics and Optoelectronics Conference Technical Digest 1989*, p. WA5, March 1989.

[116] J. Mark and J. Mork, "Subpicosecond gain dynamics in InGaAsP optical amplifiers: Experiment and theory," *Appl. Phys. Lett.*, vol. 61, no. 19, pp. 2281–2283, 1992.

[117] M. P. Kesler and E. P. Ippen, "Subpicosecond spectral gain dynamics in AlGaAs laser diodes," *Electron. Lett.*, vol. 24, no. 17, pp. 1102–1103, 1988.

[118] P. J. Delfyett, Y. Silberberg, and G. A. Alphonse, "Hot-carrier thermalization induced self-phase modulation in semiconductor traveling wave amplifiers," *Appl. Phys. Lett.*, vol. 59, pp. 10–12, 1991.

[119] K. L. Hall, E. P. Ippen, G. Eisenstein, U. Koren, and G. Raybon, "Short pulse gain saturation in a 1.5μm multiple quantum well optical amplifier," *Conference on Lasers and Electro-optics Technical Digest 1990*, p. 532, 1990.

[120] K. L. Hall, Y. Lai, E. P. Ippen, G. Eisenstein, and U. Koren, "Femtosecond gain dynamics and saturation behavior in InGaAsP multiple quantum well optical amplifiers," *Appl. Phys. Lett.*, vol. 57, pp. 2888–2890, 1990.

[121] K. L. Hall, E. P. Ippen, and G. Eisenstein, "Bias-lead monitoring of ultrafast nonlinearities in InGaAsP diode laser amplifiers," *Appl. Phys. Lett.*, vol. 57, pp. 129–131, 1990.

[122] A. Alping, B. Bentland, and S. T. Eng, "100 Mbit/s laser diode terminal with optical gain for fiber optic local area networks," *Electron. Lett.*, vol. 20, no. 19, pp. 794–795, 1984.

[123] P. A. Andrekson, P. Andersson, A. Alping, and S. T. Eng, "In situ characterization of laser diodes from wideband electrical noise measurements," *J. Lightwave Technol.*, vol. LT-4, pp. 804–811, 1986.

[124] M. Gustavsson, A. Karlsson, and L. Thylen, "A travelling wave semiconductor laser amplifier for simultaneous amplification and detection," in *Optical Fiber Conference Technical Digest 1989*, pp. MEE8–1, 1989.

[125] C. Harder, J. Katz, S. Margalit, J. Shacham, and A. Yariv, "Noise equivalent circuit of a semiconductor laser diode," *IEEE J. Quantum Electron.*, vol. QE-18, pp. 333–337, 1982.

[126] W. B. Joyce and R. W. Dixon, "Electrical characterization of heterostructure lasers," *J. Appl. Phys.*, vol. 49, no. 7, pp. 3719–3726, 1978.

[127] V. V. Luc, P. G. Eliseev, M. A. Manko, and G. T. Mikaelian, "Electrical diagnostics of the amplifier operation and a feasibility of signal registration on the basis of the voltage saturation effect in junction laser diodes," *IEEE J. Quantum Electron.*, vol. QE-19, no. 6, pp. 1080–1083, 1983.

[128] Y. Mitsuhashi, J. Shimada, and S. Mitsutsuka, "Voltage change across a self-coupled semiconductor laser," *IEEE J. Quantum Electron.*, vol. QE-17, no. 7, pp. 1216–1225, 1981.

[129] J. M. Wiesenfeld, G. Eisenstein, R. S. Tucker, G. Raybon, and P. B. Hansen, "Distortionless picosecond pulse amplification and gain compression in a travelling-wave InGaAsP optical amplifier," *Appl. Phys. Lett.*, vol. 53, pp. 1239–1241, 1988.

[130] P. B. Hansen, J. M. Wiesenfeld, G. Eisenstein, R. S. Tucker, and G. Raybon, "Repetition-rate dependence of gain compression in InGaAsP optical amplifiers using picosecond optical pulses," *IEEE J. Quantum Electron.*, vol. QE-25, pp. 2611–2620, 1989.

[131] T. Saitoh, H. Itoh, Y. Noguchi, S. Sudo, and T. Mukai, "Pulse energy gain saturation in subpico- and picosecond pulse amplification by a traveling-wave semiconductor laser amplifier," *IEEE Photon. Technol. Lett.*, vol. 1, no. 10, pp. 297–299, 1989.

[132] C. H. Lee and P. J. Delfyett, "Limits on amplification of picosecond pulses by using semiconductor laser traveling-wave amplifiers," *IEEE J. Quant. Electron.*, vol. 27, no. 5, pp. 1110–1114, 1991.

[133] T. Saitoh and T. Mukai, "Gain saturation characteristics of traveling-wave semiconductor laser amplifiers in short optical pulse amplification," *IEEE J. Quantum Electron.*, vol. 26, no. 12, pp. 2086–2094, 1990.

[134] A. Dienes, J. P. Heritage, M. Y. Hong, and Y. H. Chang, "Time- and spectral-domain evolution of subpicosecond pulses in semiconductor optical amplifiers," *Opt. Lett.*, vol. 17, no. 22, pp. 1602–1604, 1992.

[135] G. Eisenstein, U. Koren, G. Raybon, T. L. Koch, J. M. Wiesenfeld, M. Wegener, R. S. Tucker, and B. I. Miller, "Large- and small-signal gain characteristics of 1.5 μm multiple quantum well optical amplifiers," *Appl. Phys. Lett.*, vol. 56, pp. 1201–1203, 1990.

[136] A. E. Siegman, *Lasers*. University Science Books; Mill Valley, CA, 1986.

[137] A. Icsevgi and J. W. E. Lamb, "Propagation of light pulses in a laser amplifier," *Physical Review*, vol. 185, no. 2, pp. 517–545, 1969.

[138] K. Inoue, T. Mukai, and T. Saitoh, "Gain saturation dependence on signal wavelength in a travelling-wave semiconductor laser amplifier," *Electron. Lett.*, vol. 23, no. 7, p. 328, 1987.

[139] C. C. Chamon, C. K. Sun, H. A. Haus, and J. G. Fujimoto, "Femtosecond time division interferometry technique for measuring the tensor components of $\chi^{(3)}$," *Appl. Phys. Lett.*, vol. 60, no. 5, pp. 533–535, 1992.

[140] H. A. Haus, *Waves and Fields in Optoelectronics*. Englewood Cliffs, NJ: Prentice-Hall, 1984.

[141] K. L. Hall, G. Lenz, E. P. Ippen, U. Koren, and G. Raybon, "Carrier heating and spectral hole burning in strained-layer quantum-well laser amplifiers at 1.5 μm," *Appl. Phys. Lett.*, vol. 61, no. 21, pp. 2512–2514, 1992.

[142] C. T. Hultgren, K. L. Hall, G. Lenz, D. J. Dougherty, and E. P. Ippen, "Spectral-hole burning and carrier heating nonlinearities in active waveguides," in *Picosecond Electronics and Optoelectronics Conference Technical Digest 1993*, p. MA1, January 1993.

[143] T. L. Koch and R. A. Linke, "Effect of nonlinear gain reduction on semiconductor laser wavelength chirping," *Appl. Phys. Lett.*, vol. 48, p. 613, 1986.

[144] G. P. Agrawal and N. A. Olsson, "Self-phase modulation and spectral broadening of optical pulses in semiconductor laser amplifiers," *IEEE J. Quantun Electron.*, vol. 25, p. 2297, 1989.

[145] R. S. Grant and W. Sibbett, "Observation of ultrafast nonlinear refraction in an InGaAsP optical amplifier," *Appl. Phys. Lett.*, vol. 58, no. 11, pp. 1119–1121, 1991.

[146] K. Oka and Y. Ohtsuka, "Polarization heterodyne interferometry using another local oscillator beam," *Opt. Comm.*, vol. 92, pp. 1–5, 1992.

[147] E. Tokunaga, A. Terasaki, and T. Kobayashi, "Frequency-domain interferometer for femtosecond time-resolved phase spectroscopy," *Opt. Lett.*, vol. 17, no. 16, pp. 1131–1133, 1992.

[148] H. A. Haus, "Derivation of instantaneous third order polarizability." Quantum Electronics and Femtosecond Optics Memo No. 13, September 1988.

[149] E. P. Ippen, "Nonlinear Optics-MIT Course 6.634 Notes.".

[150] K. L. Hall, A. M. Darwish, E. P. Ippen, U. Koren, and G. Raybon, "Subpicosecond index nonlinearities in InGaAsP diode laser amplifiers," in *Conference on Lasers and Electro-optics Technical Digest 1993*, p. JThA2, May 1993.

[151] K. L. Hall, A. M. Darwish, E. P. Ippen, U. Koren, and G. Raybon, "Femtosecond index nonlinearities in InGaAsP optical amplifiers," *Appl. Phys. Lett.*, vol. 62, no. 12, pp. 1320–1322, 1993.

[152] K. L. Hall, G. Lenz, E. P. Ippen, and G. Raybon, "Hetrodyne pump-probe technique for time-domain studies of optical nonlinearities in waveguides," *Opt. Lett.*, vol. 17, no. 12, pp. 874–876, 1992.

[153] C. K. Sun, H. K. Choi, C. A. Wang, and J. G. Fujimoto, "Studies of carrier heating in InGaAs/AlGaAs strained-layer quantum well diode lasers using a multiple pump probe technique," *Appl. Phys. Lett.*, vol. 62, no. 7, pp. 747–749, 1993.

[154] L. F. Tiemeijer, "Effects of nonlinear gain on four-wave mixing and asymmetric gain saturation in a semiconductor laser amplifier," *Appl. Phys. Lett.*, vol. 59, no. 5, pp. 499–501, 1991.

[155] K. J. Vahala, J. Zhou, N. Park, J. Dawson, M. A. Newkirk, and B. I. Miller, "Tera-Hertz four-wave mixing spectroscopy of intraband dynamics in quantum-well amplifiers," *Conference on Lasers and Electro-Optics Technical Digest*, p. CPD2, 1993.

[156] J. Zhou, N. Park, J. W. Dawson, K. J. Vahala, M. A. Newkirk, U. Koren, and B. I. Miller, "Highly nondegenerate four-wave mixing and gain nonlinearity in a strained multiple-quantum-well optical amplifier," *Appl. Phys. Lett.*, vol. 62, p. 2301, 1993.

[157] R. Frankenberger and R. Schimpe, "Measurement of the gain saturation spectrum in InGaAsP diode lasers," *Appl. Phys. Lett.*, vol. 57, no. 24, pp. 2520–2522, 1990.

[158] R. Frankenberger and R. Schimpe, "Origin of nonlinear gain saturation in index-guided InGaAsP laser diodes," *Appl. Phys. Lett.*, vol. 60, no. 22, pp. 2720–2722, 1992.

[159] Y. K. Chen, M. C. Wu, T. Tanbum-Ek, R. A. Logan, and M. A. Chin, "Subpicosecond monolithic colliding-pulse mode-locked multiple quantum well lasers," *Appl. Phys. Lett.*, vol. 58, p. 1253, 1991.